MELTING TRANSITION MEASUREMENTS

IN URANIUM DIOXIDE

by

Dario Manara

Thesis

Submitted to the University of Warwick

For the degree of

Doctor of Philosophy

Department of Physics

January 2004

TABLE OF CONTENTS

Acknowledgements

International co-operation, just like scientific research, is a way to higher civilisation. Thus the fruitful co-operation of people of different nationalities can be seen as a first, fundamental success in a scientific project. People coming from more than fifteen different countries are hereby acknowledged, and I am most thankful to the European Commission that has made all this possible by sponsoring this project through its Human Capital and Mobility Program.

I would like to convey my gratitude to Dr. R. Schenkel and Prof. G. Lander, Directors of the Institute for Transuranium Elements (Joint Research Centre, ITU, Karlsruhe, Germany) during the first and second half of this project respectively, for giving me the opportunity to carry out most of this research in such a prestigious facility, and for encouraging me throughout the duration of the work. I am also particularly grateful to Dr. Hj. Matzke, who first invited me to work in the Materials Research Unit of the ITU.

Very special thanks go to my supervisors: at the University of Warwick Prof. M. Lewis, to whom I feel deeply indebted for his supervision, constant help and most valuable advice, and also for his enduring patience in correcting my English in the whole manuscript, and Dr. G. Hyland, who was my adviser in the first year of this project and has always kept following with interest the development of it; at the ITU Karlsruhe Dr. C. Ronchi - Head of the Materials Research Unit since 2002 - who has guided me through the whole research project with his sound experience in Materials Science and Computing and with his hearty and constant encouragement, and Prof. M. Sheindlin, who patiently passed me part of his vast knowledge in high-temperature and high-pressure experimental techniques, and made the realisation of this work feasible with his precious advice and ideas.

I am particularly thankful to all the ITU staff, and in particular to:

- Dr. V.V. Rondinella who, besides giving important advice in the revision of the first chapter of this thesis, has always provided help and useful discussions, both scientific and non-scientific, as well as the relief of a Valda pastille whenever needed;

- Dr. J. P. Hiernaut and Dr. T. Wiss for their friendly encouragement and support over the whole duration of this project;

- Dr. J. Spino, whose help and advice was indispensable in the material preparation, and who gave me the opportunity to work in his laboratory for long periods;

- Dr. M. Betti, Dr. D. Bottomley, Dr. D. Papaioannou, Dr. J. Somers and Dr. G. Tamborini, who helped me in the sample preparation and characterisation;

- Dr. J.-F. Babelot and Prof. J. Leroy, who helped me with their advice and experience in the discussion of the results;

- The whole ITU technical staff, without whom the realisation of this work would not have been feasible: I am especially thankful to W. Heinz and U. Zweigner, who daily helped me in the experimental work for over two years, and R. Selfslag, true pillar of the high-temperatures laboratory until the end of the first year of this project. Among the several people working at the ITU, whose help was often indispensable, I am especially indebted to (in alphabetic order): C. Brossard, F. Capone, J.-Y. Colle, B. Cremer, M. Jörgensen, M. Martellenghi, J. McGilney, V. Meyritz, M. Murray, R. Nasyrow, G. Pagliosa, R. Beukers, V. Tebaldi, A. Thiele.

- The ITU grant-holders group, being part of which has always been of support, help, and fun to me. Many thanks to all my PhD-fellows, with special mention to those who in some way participated with their help in the realisation of this project: M. Amme, M. Cinta Pujol, P. Damen, S. Lutique, R. Pflieger.

- The administrative staff of the ITU, in particular Mrs. I. Neumann-Schölles, who more than once has helped me solve complicated bureaucratic issues, Mrs. G. Martelleghi, always present whenever I needed help in binding and archive work, and Dr. R. Richter, precious

whenever a bibliography search was required. Special thanks to Mrs. P. Strube, who has been of great help in the final part of this project.

Special acknowledgements go to Profs. I. Iosilevski and E. Yakub; this latter, in particular, revised the conclusions of this Thesis and contributed with his most valuable advice to its final version. Prof. M. Brykin gave also a fundamental support by providing the code used for the simulation of the experiments.

Special thanks to Dr. B. Renker of the Institute für Festkörper Physik (IFP)- FZK Karlsruhe, who made possible the Raman characterisation of UO_{2+x} samples in his laboratory.

Although more fundamental than any other kind of help, true friendship is sort of "unofficial" support, and therefore seldom "officially" acknowledged. I am immensely grateful to all my friends, some of whom have already been mentioned here, for their tremendous support in these years. I particularly mean to thank Liubashka, who patiently supported me in the worst moments of the writing, Nicola, Magnus, Andrea and all the "Karlsruhe pirates" gang, who made my stay in Germany really pleasant and unforgettable. Special gratitude goes to Laura, Eric, Monica and Stéphane who have been to me family, friends, cooks, mechanics, in a word most of what a single man far from home may need. I also wish to thank Elisa, with whom I have shared the same office for over two and a half years, and the Blue Docs, my band-fellows: music has always been real fun and relief during my stay in Karlsruhe.

Special gratitude goes to Ann-Marie, my Irish pen-mate and first teacher of written English.

Last, but definitely not least, I am sincerely and deeply thankful to my family back in Italy. This Thesis is dedicated to my parents and my sister, who have always motivated and encouraged me heartily and enthusiastically despite the distance, and to my aunt Alma and uncle Adriano, who first induced me to undertake this unique experience, and on whose constant (even independently of considerable health problems - get better soon!-) and loving listening and support I could rely all the time. Thank you again!

Declarations

This Thesis is based on joint research carried out at the Institute for Transuranium Elements, Karlsruhe, Germany. My work consisted of managing the experimental part of the project, analysing and critically assessing the data obtained. During the research, I contributed with original ideas to the development of the experimental apparatus and to the interpretation of the results obtained. Furthermore, I made use of a computer code, developed at the Joint Institute for High Temperatures of RAS, Moscow (Russia), in order to simulate laser-induced surface melting experiments.

Part of the work was presented at the following conferences:

1. 6th International Workshop on Subsecond Thermophysics, September 26 - 28 2001, Leoben (Austria): *"Dependence of the Freezing Temperature on Pressure in Uranium Dioxide by a Two-Pulse Laser Method"*, D.Manara, C.Ronchi, M.Sheindlin; *"Multichannel Pyrometry Applications in High- Temperature Thermophysics"*, W. Heinz, D. Manara, C. Ronchi, M. Sheindlin.
2. 14th European Conference on Thermophysics, September 1 - 4 2002, London (UK): *"High- Pressure Melting Behaviour of Non- Stoichiometric Uranium Dioxide"*, D. Manara, C. Ronchi, M. Sheindlin.
3. 15th Symposium on Thermophysical Properties, Boulder, Colorado, June 22- 27 2003: "*Advances in Measurements of the Melting Transition in Non- Stoichiometric UO_2*", D. Manara, M. Sheindlin, M. Lewis.

Some of the work was published or is now in press under the titles:

1. *"Dependence of the Freezing Temperature on Pressure in Uranium Dioxide by a Two-Pulse Laser Method"*, D. Manara, C. Ronchi, M. Sheindlin, Int. J. Thermophys. **23-5** (2002), 1171.
2. *"Raman Spectra of Stoichiometric and Hyperstoichiometric Uranium Dioxide"*, D. Manara and B. Renker, J. Nucl. Mater. **321** (2003), 233.
3. *"Solidus and Liquidus of UO_{2-x} from High- Pressure Melting Experiments"* D. Manara, C. Ronchi, M. Sheindlin, High Temperatures- High Pressures **35 / 36** (2003 / 2004), 25.
4. *"Advances in Measurements of the Melting Transition in Non- Stoichiometric UO_2"*, D. Manara, M. Sheindlin, M. Lewis, in press on the International Journal of Thermophysics.

No part of the work described in this Thesis has been submitted in support of an application for a higher degree or qualification in this or in any other University.

Dario Manara

Abstract

The broad objective of research described in this thesis was the experimental determination of the solid / liquid transition in both stoichiometric and hyperstoichiometric uranium dioxide. Experimental information in this field constitutes a necessary reference for the analysis of hypothetical nuclear reactor accidents and, in particular, for the formulation of an equation of state (EOS) for uranium dioxide.

A review of previous research on the same topic revealed that only few and uncertain experimental data were available prior to this work, obtained with conventional thermal analysis techniques in which it was not possible, at temperatures close to melting, to prevent sample contamination from the containing material and non- congruent evaporation.

The experimental approach in the current research consisted mainly of the development of a laser heating method that enabled fast (tens of ms) melting / freezing experiments under containerless conditions, during which the sample could be kept under a buffer gas at high pressure (tens of MPa) in order to suppress any evaporation. In this way, the main difficulties encountered by previous researchers were overcome. UO_{2+x} samples with $0 \leq x \leq 0.21$ were prepared starting from original nuclear-grade pellets and analysed. Thermograms were recorded with fast pyrometers and interpreted with the help of a one-dimensional code-simulation of the measurements. In addition, a novel method for measurement of phase transition points was developed, based on the precise detection of surface reflectivity variations. The point of congruent melting was determined for the stoichiometric oxide in the pressure range between 0.1 and 250 MPa. *Liquidus* and *solidus* lines were established, for pressures between 50 and 250 MPa, in the hyperstoichiometric range investigated. The results obtained, which in a number of cases significantly differed from the existing data, were finally used for a better assessment of the phase diagram of the system UO_{2+x} in the vicinity of the melting transition.

List of the main Symbols and Abbreviations used in this work

A	Optical spectral absorbivity of a surface.
a	Lattice parameter.
C	Composition.
c	Velocity of light in vacuum.
D	Diffusion coefficient.
D_c	Chemical diffusion coefficient.
D_s	Self- diffusion coefficient.
ΔH_m	Latent heat of melting.
ΔH_{vap}	Latent heat of evaporation.
$\Delta \tau_i$	Integrating time.
ε	Spectral emissivity.
ε_0	Dielectric constant in vacuum.
EMF	Electro- Motive Force.
E	Hemispherical radiative energy density.
FZK	*Forschungszentrum Karlsruhe* (Karlsruhe Research Centre).
$G_{(i)}$	Gibbs free energy (of the component i).
$g_{(i)}$	Specific Gibbs free energy (of the component i).
$H_{(i)}$	Enthalpy (of the component i).
$h_{(i)}$	Specific enthalpy (of the component i).
i	Electrical current intensity.
IFP	*Institut fuer Festkoerper Physik* (Institute of Solid State Physics).
INTAS	International Association for Promotion of Cooperation with Scientists from the New Independent States of the Former Soviet Union.
ITU	*Institut fuer Transurane* (Institute for Transuranium Elements).
IVTAN	Institute of High Temperatures of the Russian Academy of Sciences.
JRC	Joint Research Centre.
λ	Wavelength of the electromagnetic radiation.

λ	Heat conductivity (clear from the context).
m	Mass.
$M_{(xy)}$	Molar mass of the compound xy.
MW	Molar weight.
n	Refractive index.
O/U	Ratio between O and U atomic concentrations (O/U ≡ [O]/[U]).
P	Total pressure.
p_i	Partial pressure of the component i.
q	Heat flux.
ρ	Density.
RLS	Reflected Light Signal.
SEM	Scanning Electron Microscope.
SIMS	Secondary Ion Mass Spectrometry.
S_m	Melting slope (gradient of the melting line).
T	Absolute temperature.
τ_i	Optical transmittance of the element i.
t	Time.
TG	Thermogravimetry.
T_m	Melting point (melting temperature).
x	Non-stoichiometry parameter in uranium dioxide: $x = (O/U) - 2$.
XRD	X-Ray Diffraction.
V	Voltage.
v	Specific volume.
W	Weight.
z	Depth.

Illustrations List

Tables List

Chapter 1

Introduction-

Nuclear Engineering scenario and role of fuel response in reactor accidents

Since the discovery of nuclear fission (Meitner, Hahn and Strassmann 1939) and the first nuclear pile (Fermi 1942), its application as an advantageous source of energy for civil needs has been the concern of a great number of researchers in the field.

Based on today's technology, nuclear fission constitutes the most effective energy source known, though some aspects still interfere with its full public acceptance. The most widespread fears about the civil use of atomic energy concern two main points: disposal of the radioactive waste and safety of nuclear installations, namely of nuclear plants and related facilities. These are therefore two topics of great importance in today's nuclear fission energy research and on them significantly depends the future itself of nuclear fission plants.

Within the research field related to the safety of nuclear installations, the present work is aimed at providing experimental information on the behaviour of the nuclear fuel at high temperature and high pressure. Such information is of basic importance in the analysis and prediction of possible nuclear reactor accidents.

The following description of some mishaps happened in the history of nuclear reactors gives an idea of the conditions that could lead to or take place take place during an accident.

1.1 Nuclear reactor accidents

Among the hypothetical accidents that could befall a nuclear reactor, the worst conceivable and most fearful one is a supercritical nuclear excursion leading to uncontrolled power transient with explosive

release of a large amount of energy and disassembly of the core. Such kind of mishap unfortunately happened once, in Chernobyl, USSR, in 1986 [1,2].

1.1.1 Chernobyl

The Chernobyl plant included four units, each one being a nuclear reactor RBMK-1000 (ordinary water reactor graphite-moderated). In this kind of plant, existing at the time in the URSS only, ordinary non-pressurised water is used as refrigerant, the steam of which directly activates the turbines without introduction of any heat exchanger, and graphite rods are employed as neutron-moderators. Uranium dioxide is used as nuclear fuel. Such reactors suffer from instability at low power, due to the fact that they possess a "positive void coefficient". This means that the larger amount of steam, produced if the power increases or the water flux diminishes, results in an increased fission rate since liquid water absorbs neutrons, but steam does not. If the power is high enough, the high temperature reduces the nuclear cross section in the fuel, balancing the positive void coefficient effect, and avoiding any uncontrolled power excursion during the normal functioning of the reactor. But if the plant works at low power, it becomes unstable, and the positive void coefficient effect can cause sudden uncontrollable power peaks.

On April the 25th, 1986, Reactor Four was to be shutdown for routine maintenance, and it was decided to take advantage of this to run a test: to check whether, in the event of a shutdown, enough electrical power was available to operate the emergency equipment and core cooling pumps until the diesel power supply came online. For the test the reactor was to be stabilised at 1000 MW prior to shutdown, however, due to operational error, the power fell to about 30 MW, a level at which the reactor could not be considered stable. The operators tried to raise the power by freeing all the control rods manually and at 1am on April the 26th the reactor stabilised at 200 MW. But an increase in the coolant flow and the following drop in the steam pressure slowed the turbine, hence decreasing the power to the cooling system pumps. This resulted in additional steam in the cooling channels (positive void coefficient) and the operators could not control the situation any longer. A terrific power surge estimated to be 100 times the nominal power rose, and the sudden increase in temperature caused part of the fuel to rupture. Fuel particles then reacted with the water creating a steam explosion that destroyed the reactor core. A second explosion added to the destruction two

minutes later. Fragments of the core at high temperature spread into the surroundings, setting fire to some buildings nearby. At the same time a huge radioactive cloud was produced and dispersed into the atmosphere, bringing randomly distributed contamination to several other countries in the northern hemisphere, depending on the winds and on the weather conditions. Thirty lives were lost during the accident or shortly thereafter. Figures from the Ukraine Radiological Institute suggest that over two thousand five hundred deaths were caused by the Chernobyl accident due to cancer or other illnesses related to high radiation exposure, without taking into account further damage to people and environment that can hardly be evaluated.

1.1.2 Collapse due to overheating of the reactor core

Even if such an unfortunate sequence of events, which caused an accident like Chernobyl, looks quite unlikely to take place again, one should always take into account the risk of a simpler coolant leakage. In most of the cases this could lead to overheating of the reactor core. Mishaps due to coolant leakage took place, for example, on the Soviet nuclear submarines K-8 in 1960 and K-19 in 1961 [3] and in the Three Mile Island (TMI) nuclear plant (Pennsylvania, 1979)[4].

Nuclear submarines accidents

On October the 13th, 1960, a leak in the primary steam generator system developed in the PWR aboard the Soviet submarine K-8 on exercise in the Barents Sea, and subsequent damage occurred in the piping of the reactor coolant circuit. Unfortunately, large amounts of radioactive gas leaked from the reactor even though the heroic efforts of the crew prevented a reactor meltdown. Three sailors suffered visible radiation injuries, and others were exposed to potentially fatal radiation doses.
Less than a year later on July the 4th, 1961, the missile submarine K-19 was in the north Atlantic when a leak developed in a pipe in the pressure regulating circuit of the primary cooling system of the PWR. The sudden drop in pressure as a result of the leak triggered the reactor emergency alarms as the coolant supply diminished and excess heat began to build within the reactor core. The crew had to do whatsoever they could to repair the leak, and they succeeded as the temperature of the core was maintained below 1000°C throughout the duration of the emergency. At the time nobody was aware of

the possible consequences of a core overheating at higher temperatures. Actually the leakage, if left unchecked, could have led to a core meltdown. Although it could not explode like a nuclear bomb, as there was no risk of a supercritical nuclear excursion, a reactor core meltdown could have produced an intense vapour explosion, followed by the uncontrollable diffusion of huge radioactive contamination into the sea. Amid the tensions at the peak of the Cold War, such an explosion (the K19 was cruising just close to a NATO facility) might well have resulted in an uncontrollable confrontation between the Super Powers. The price needed to avoid such a catastrophe was extremely high: seven members of the crew died of exposure to radioactivity almost immediately, and fourteen died shortly thereafter.

Three Mile Island

On March the 28th, 1979 a pump used to supply water to the PWR secondary circuit steam generator in the Unit 2 of the Three Mile Island (TMI) pressurised water reactor (PWR) (Pennsylvania, USA) stopped operating. The safety system of the plant automatically shut down the steam turbine and the electric generator it powered, and as the coolant temperature rapidly increased, its pressure increased too. Then a pilot-operated relief valve (PORV) opened to release the overpressure and steam and water began flowing out of the reactor coolant system through a drain pipe to a tank on the floor of the containment building. As pressure still kept increasing, the control rods mechanically dropped down into the reactor core to halt its nuclear reaction. This all happened within 8 seconds after the first pump malfunctioning. As in any nuclear reactor, though, the decaying radioactive materials left from the fission process continued to produce heat that was to be removed. Unfortunately, at this stage another malfunction affected the PORV. This valve stuck open for almost two and a half hours, without the operators to realize it. In the first 100 minutes of the emergency, over one third of the water capacity of the reactor coolant system escaped out of the let-down system. The core became largely uncovered and reached in several points temperatures above melting, as verified in later checks. Finally, as the malfunction was eventually detected, the emergency high-pressure pumps were activated. Unluckily, though, since the accident had probably caused much damage over the whole system, also to the pumps that had been running dry, it took several hours more to cover the core with water. As a consequence, the core collapsed, as the UO_2 fuel merged with

the zircalloy cladding, and fifty percent of it was destroyed or melted and something of the order of twenty tons of uranium dropped to the bottom of the pressure vessel.

Luckily, conditions for any explosion were not met. Due to the spread of contaminated steam and water from the leak, the accident produced high radiation levels that were detected in the containment building and in the reactor auxiliary building, which was promptly evacuated. The main consequences of the TMI mishap were, apart the obvious closure of the plant itself, the suspected release of radioactive gas inside the reactor, and the panic among the population nearby, not to speak of all the unavoidable controversies and charges that have continued up till now.

1.2 Nuclear and Materials Engineering scenario.

Several scientists, both theoreticians and experimentalists, have undertaken important efforts in the analysis of such kinds of accidents since the beginning of the nuclear plant era.

In a nuclear mishap materials can undergo physico-chemical conditions among the most extreme that one could imagine in any technological application. Thus researchers in this field have had to deal with quite complicated issues involving physics, chemistry, engineering, nuclear and materials sciences.

As reported in the description of the mishaps mentioned above, during a severe accident the fuel can melt, and interact with several other materials of which the core parts are made: mainly zircalloy (of the cladding), steel, silver, cadmium, indium, boron carbide (control rods), fission products, concrete, air and water. The overall material mass resulting from a core melting is designated as "corium".

Bethe and Tait [5, 6] developed a simplified analysis providing an estimate of the energy release in case of the most fearful accident that could take place in a nuclear plant, namely the explosive disassembly of the core in a Fast Breeder Reactor (FBR). Such an accident could be caused, for example, by a loss of coolant leading to overheating of the reactor core to a temperature where both fuel and cladding melt. In this case, the uranium-plutonium oxide fuel and its cladding would collapse to the bottom of the core, and in the worst case the atoms

compaction could lead to a supercritical configuration, with an even higher release of fission energy. This would result in even higher temperatures and also in high pressures. Both high temperature and high pressure would tend to terminate the power transient - the high temperature reducing the fission rate due to the drop in the nuclear cross section, the pressure pulse, if large enough, leading to the hydrodynamic dispersal of the fuel. All this could happen very rapidly, and the fission energy released during the reactivity ramp would result from the competition between the lifetime of prompt and delayed neutrons, and the rate of expansion of the core, governed by the vapour pressure of the molten fuel [7]. A pictorial overview of the Bethe- Tait accident is given in Fig. 1.1 (after [6]).

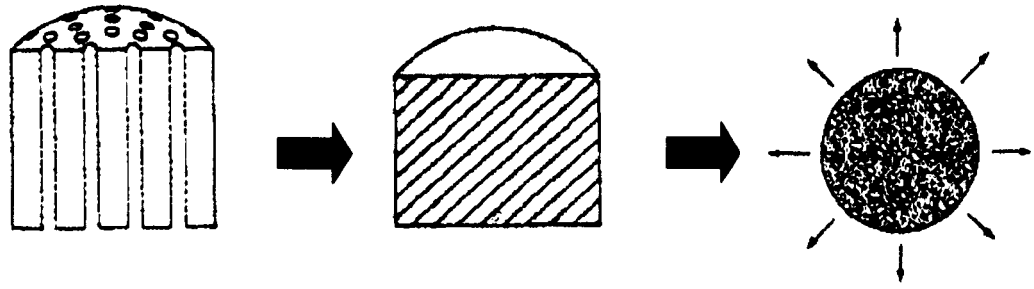

1)
A leakage of coolant causes overheating of the reactor core.

2)
Core meltdown: nuclear fuel and cladding collapse to the bottom of the core.
If a supercritical configuration is reached, even more fission energy is released, resulting in very high temperature and pressure.

3)
The high pressure produced leads to the disassembly of the core, terminating the power transient.

Fig 1.1: Pictorial overview of the Bethe-Tait accident (after [6]).

Although the Bethe –Tait analysis gives only an order-of-magnitude-estimate of the energy released in case of core meltdown, their approach has been used for many years in the entire world to establish a conservative upper bound for FBR containment requirements.

The risk prediction of potential mishaps in a nuclear plant needs a sound formulation of the equation of state (EOS) for the materials forming the corium [8]. The EOS provides basic information necessary to determine a relation between the energetic aspects and the dynamic response of the core during an accident. In particular, knowledge of the corium temperature (T) as a function of internal energy (U) and volume (V) would permit control of the nuclear cross section through the Doppler coefficient, while the relation P (U, V), P being the total pressure, would be needed for the evaluation of the total mass geometry evolution with time via the equations of hydrodynamics [7].

Sound thermodynamic modelling is necessarily based on the critical assessment of the main binary and multi-component subsystems that constitute the corium, for which the availability of reliable experimental data under extreme conditions is therefore fundamental.

The U-O binary subsystem is definitely the most important, as uranium dioxide constitutes the nuclear fuel in the majority of the nuclear reactors. This compound has been preferred to uranium metal and to uranium carbide (UC_2) among possible nuclear fuels, due to its higher melting point and lower chemical reactivity towards O_2. However, UO_2 reactivity towards O_2 is still considerably high. Uranium dioxide can easily change its oxidation state in the presence of even low oxygen pressure and exist over a wide range of compositions around the exact stoichiometry. Oxygen content is a parameter that affects many properties of the fuel, specially its phase transition points.

Knowledge about the melting transition in the nuclear fuel is particularly important in the analysis of hypothetical meltdown accidents, as it defines the structural limit of a combustible element. Moreover, due to a possible failure of the cladding during an accident, the fuel could come into contact with the coolant. If this latter is water, as in most reactors, strongly oxidising conditions can be produced, under which the oxygen content of the fuel can be significantly increased. Hence precise knowledge of the fuel melting point

dependence on the oxygen content is also of primary importance for the analysis of hypothetical mishaps.

1.3 Contents of the current research

This work deals with the experimental investigation of the melting behaviour of the system UO_{2-x} at several degrees of oxidation.

This is a topic where few experimental data are available, due to the extreme conditions created during the melting experiments. In the present investigation, great importance is given to the influence of external pressure and oxygen potential on melting. A new experimental method is presented, aimed at overcoming difficulties that hindered the measurements previously performed in the same field by other researchers, namely the very high rate of non-congruent evaporation and the low chemical stability shown by uranium dioxide at high temperature. Laser heating was used to bring the sample surface up to a temperature above melting, the temperature of the specimen being detected by a high-speed two-channel pyrometer and separately by an additional multichannel spectrometer. This latter also allowed a fine spectral analysis of the heated surface, from which data on the spectral emissivity of the sample surface could be obtained. Thermal arrests were observed during the cooling stage of the recorded thermograms at the temperatures corresponding to the phase transition points. Phase transition points were also studied through the changes induced in the sample surface reflectivity, monitored simultaneously with an additional probe laser. In order to suppress non-congruent evaporation phenomena, the specimen was held in an autoclave filled with high-pressure buffer gas (up to 0.25 GPa). In this way, also the pressure dependence of the UO_{2-x} melting could be studied.

This method was proved to be quite effective in the determination of high-temperature properties of compounds, such as UO_{2-x}, that are chemically unstable under extreme temperature-pressure conditions.

Chapter 2 contains an overview of the information available on the binary system U-O, particularly on the phase diagram region concerning the compound UO_{2+x}. Particular interest is directed at the few high-temperature data available.

An overview of the experimental methods for melting investigation available prior to this work is presented in Chapter 3, together with a discussion on the difficulties implied by the various techniques. The experimental methods devised and employed in the current research are described in detail in Chapter 4, the preparation and characterisation of the investigated uranium dioxide samples in Chapter 5.

Chapter 6 reports the melting point measurements performed on stoichiometric uranium dioxide, and also an exhaustive study on the pressure dependence of the melting transition. The experimental determination of the *solidus* and *liquidus* lines for the system UO_{2+x}, described in Chapter 7, constituted a quite complex issue especially due to the onset of fast oxygen diffusion between solid and liquid. A better understanding of this latter phenomenon was obtained by simulating the laser- induced melting/freezing process by means of a computer code based on a one-dimensional model. Thermograms yielded by the simulation were used to interpret the experimental data better. The one-dimensional model is presented in Chapter 8 together with the results of the simulation and the interpretation of the experimental curves.

In Chapter 9 the final results of this research are summarised, critically discussed and compared with previous studies performed in the same field.

Some conclusions are presented in Chapter 10, concerning the improvements, obtained in this work, to the UO_{2+x} phase diagram and the applicability of the new experimental method to other physico- chemical systems.

References Chapter 1

1. *Summary Report on the Post-Accident Review Meeting on the Chernobyl Accident*, INSAG No.1, IAEA Publication, Vienna 1986.
2. *Radionuclide Source Terms from Severe Accidents to Nuclear Power Plants with Light Water Reactors*, INSAG No.2, IAEA Publication, Vienna 1987.
3. T. Nielsen, I. Kudrik and A. Nikitin, *"The Russian Northern Fleet"*, Report 2 (1996), The Bellona Foundation, Oslo 1996.
4. Sergio Curoni *et al.*, *"Energia Nucleare. Problemi degli Anni '80"*, Patrón Editore, Bologna, 1980.
5. H.A. Bethe and J.H. Tait, *"An Estimate of the Order of Magnitude of the Explosion When the Core of a Fast Reactor Collapses"*, RHM 56- 113, April 1956.
6. A.E. Waltar and A.B. Reynolds, *"Fast Breeder Reactors"*, Pergamon Press, New York 1981.
7. C.Ronchi, I.L. Iosilevski, E. Yakub, *"Equation of State of Uranium Dioxide"*, in press.
8. D. R. Olander: " *Fundamental Aspects of Nuclear Reactor Fuel Elements*", Technical Information Center, Office of Public Affairs-Energy Research and Development Administration, 1976, p.100.

Chapter 2

The uranium – oxygen system in the domain of UO_{2+x}

2.1 Phase diagram

2.1.1 Introduction

The O-U binary system has been widely studied in the last forty-five years, since the beginning of the utilisation of uranium dioxide as a commercial nuclear fuel. Although a large amount of experimental information has been collected in constructing the phase diagram, data are still rather limited especially near the melting transition where measurements are difficult due to the very high temperature and to the low chemical stability of the material itself. Basically, six solid uranium oxides are known at room temperature and atmospheric pressure, having the ideal compositions UO_2, U_4O_9, U_3O_7, U_2O_5, U_3O_8, and UO_3; each one of them is characterised by a variable range of existence as a function of the O/U ratio[1].

Quite complete experimental data collections over the whole O-U system were compiled recently by Guéneau *et al.* [1], Chevalier and Fisher [2], and Chevalier *et al.* [3]. Figure 2.1 reports the O-U phase diagram as calculated in [1] with a free-energy model calibrated on the basis of the available experimental data.

Most of the experimental information on the O-U binary system has been collected within the region of the solid solution UO_{2-x}, where x, which can assume both positive and negative values, indicates the deviation from the uranium dioxide stoichiometric

[1] *In this work O/U = [O]/[U]= ratio between the atomic concentrations of O and U.*

composition. The high-temperature part of the state diagram of UO_{2+x} constitutes the domain of interest of the present work.

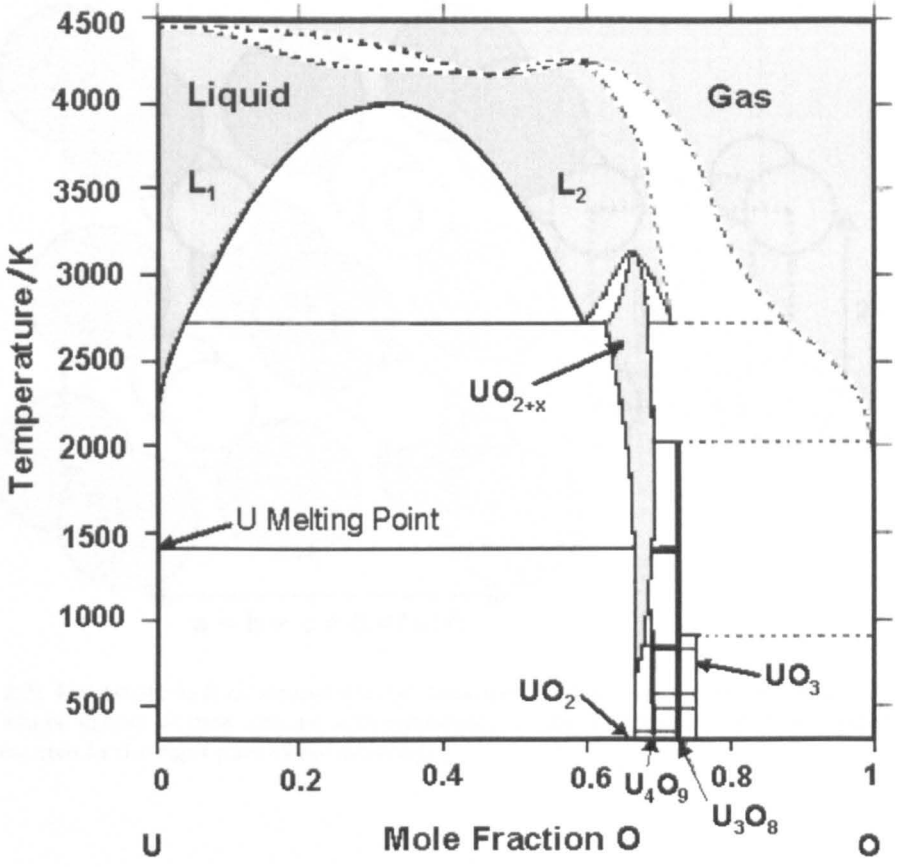

Fig. 2.1: U-O phase diagram at 1 atm as calculated in [1]. Grey fields indicate the single-phase regions. Dotted phase boundaries indicate uncertain regions of the state diagram, where results are only extrapolated and not supported by any experimental datum.

A detailed summary of the urania phase thermodynamic properties can be found in a report written by Rand *et al.* [4] as part of an early IAEA project.

It is well known that urania crystallises in the fluorite structure, space group Fm3m (O^5_h), similar to the rocksalt structure with one more atom in the primitive unit cell (Fig. 2.2).

At high temperature, this crystal form can be found over a remarkably broad range of non-stoichiometric compositions. For instance, the species UO_{2+x} can exist in the form of a solid solution for approximately $-0.4 < x < +0.3$ at temperatures higher than 2000 K. This occurs by accommodation of oxygen vacancies or interstitial atoms. This feature is made possible

by the easy shift of the U valence states +3, +4, +5 and +6 due to the presence of an odd number of electrons in the 5*f* orbital.

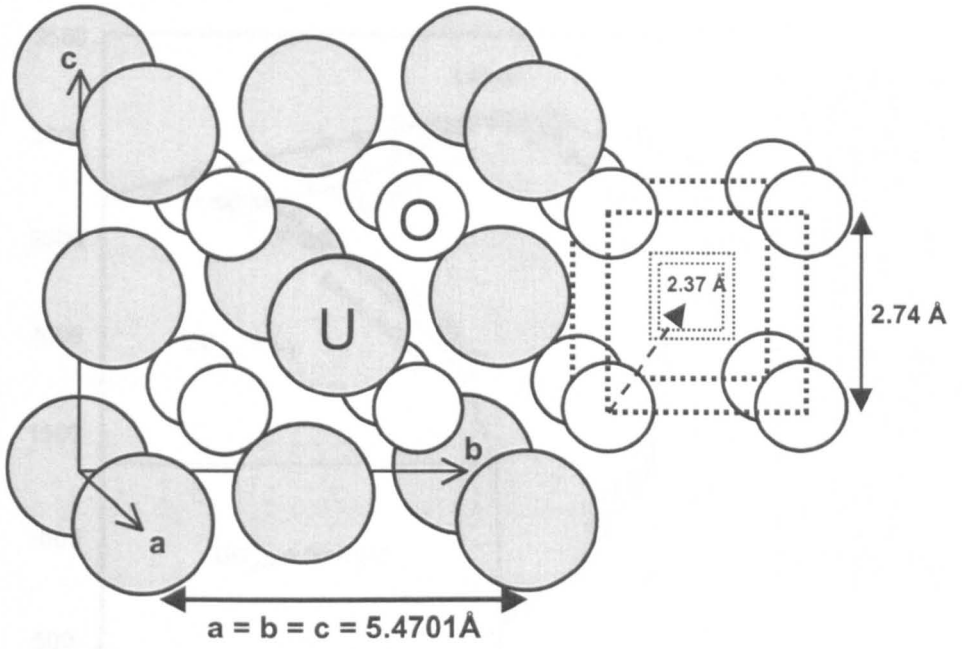

Fig. 2.2: Fcc lattice cell of stoichiometric uranium dioxide. An octahedral interstitial site where excess oxygen can be accommodated in the hyperstoichiometric oxide is represented in the right part of the drawing.

2.1.2 Temperatures below the monotectic

Fig. 2.3 shows an enlarged view of the O-U phase diagram centred on the dioxide domain, along with the available experimental data. Oxygen vacancies are the predominant defects in hypostoichiometric urania. At temperatures below 1500 K approximately, the presence of these high- energy defects makes hypostoichiometric urania unstable with respect to the dissociation into metallic uranium and stoichiometric UO_2, hence in this part of the phase diagram the value of x remains very close to zero along the homogeneity range boundary. The substoichiometric homogeneous domain broadens at $T > 1500$ K, where a significant amount of uranium atoms occupy the interstitial sites. As uranium melts at 1405 K, and the melting temperature increases in the oxidised metal, the hypostoichiometric boundary of

urania above 1405 K represents a *solidus* line, indicating the temperature at which the first sign of melting appears.

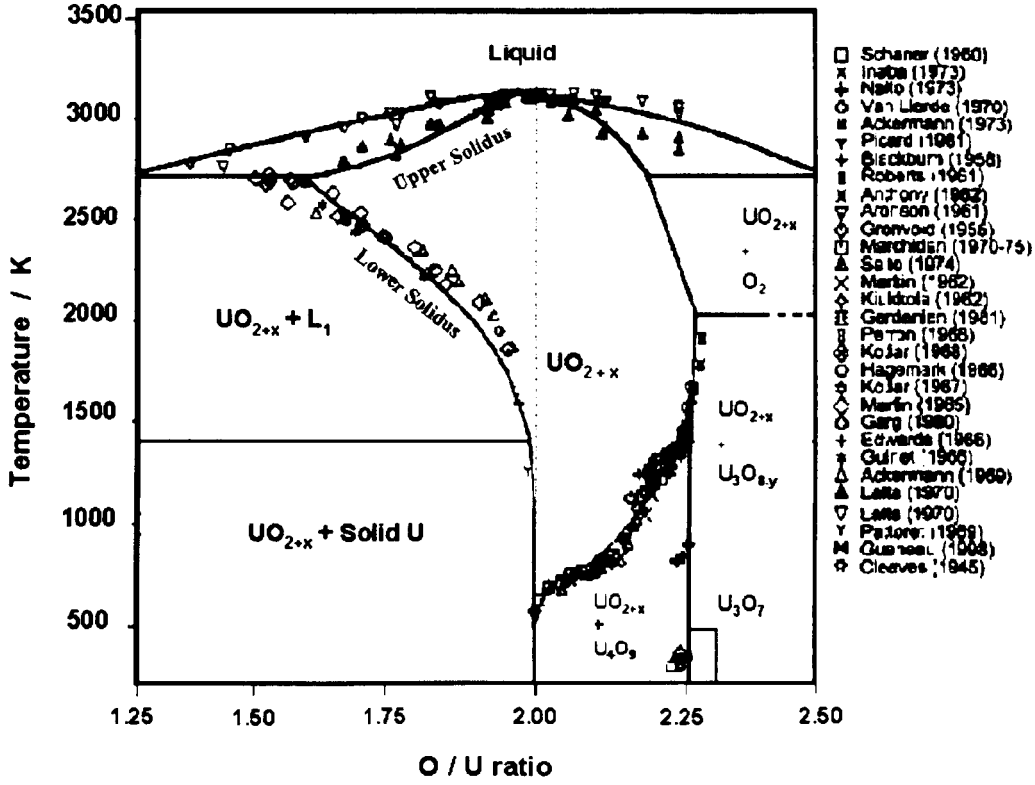

Figure 2.3: U-O phase diagram as calculated in [1] around the UO_{2+x} domain. Experimental points available are also indicated.

The initially formed liquid has a composition different from the solid. This hypostoichiometric UO_{2+x} (solid) / UO_{2+x} (solid) + UO_y (liquid) boundary was firstly studied by Bates [5] through metallographic observations. One year later it was determined by Martin and Edwards [6] by equilibrating uranium melts with uranium dioxide in helium atmosphere, and subsequently quenching to room temperature where the composition was analysed. The same authors also established the existence of an important liquid miscibility gap by metallographic examination of arc-melted alloys in a wide range of compositions. Such a feature implies the existence of two different liquid phases, L_1 richer in uranium and L_2 richer in oxygen, and of a monotectic reaction (L_1 + solid $UO_{2+x} \Leftrightarrow L_2$) at an invariant temperature. The monotectic was established by Martin and Edwards from experiments in

which pure uranium was heated in uranium dioxide crucibles, at 2773 ± 30 K at L_2 composition $UO_{1.30}$ and urania phase composition $UO_{1.64}$. The *solidus* line below the monotectic temperature was called "lower *solidus*". Guinet *et al.* [7] by the saturation method located the monotectic at 2743 ± 30 K with L_2 composition $UO_{1.18}$ and urania composition $UO_{1.60}$. Further determinations of the monotectic reaction were included in the studies on UO_{2-x} melting discussed in the next section. Bannister [8] obtained interesting results by heating hypostoichiometric urania samples in an electric furnace under inert atmosphere, making use of optical pyrometry and microscopy to detect the specimen temperature and state. Latta and Fryxell [9] performed a comprehensive study of urania melting using a thermal arrest technique. The value of 2693 ± 15 K suggested by Latta and Fryxell was in excellent agreement with that previously measured by Bannister and has been accepted as the best estimate for the monotectic temperature, with urania composition $UO_{1.66}$ and L_2 composition about $UO_{1.5}$.

Hyperstoichiometric urania preserves the fluorite-like symmetry up to $x = +0.25$ even at room temperature. In disordered UO_{2+x} the lattice accommodates excess oxygen atoms as interstitials without significantly affecting the cations position. Interstitials may be considered as randomly distributed for values of x close to zero. At higher oxidation levels evidence of cluster formation has been provided by neutron diffraction experiments confirmed by simulation- based calculation. An interstitial 2:2:2 cluster type was proposed in particular on the basis of the neutron diffraction experiments conducted by Willis [10-13] and its stability was studied by Catlow [14,15] and by Catlow and Lidiard [16]. The propagation of such cluster chains in different crystallographic directions was investigated by Allen and Tempest [17]. Willis [18] also studied the slight displacement of the oxygen atoms from the perfect tetrahedral site symmetry. Below 1400 K the regularly clustered excess oxygen atoms tend to precipitate as an ordered compound of composition U_4O_{9-y}. This latter is characterised by a fluorite-like superlattice, and some slight movements of the

uranium atoms from the original fcc positions are suggested by the results of x-ray and neutron scattering measurements.

Temperature strongly affects the solid solution range of the urania phase. Also, at room temperature, a narrow UO_{2-x} single-phase domain is likely to exist, as the lattice parameter of UO_{2+x} in equilibrium with U_4O_{9-y} is lower than that for the pure UO_2, as established by Ishii *et al.* [19]. The O/U ratio at the UO_{2-x} upper phase boundary starts to deviate significantly from 2 only above 600 K. It rises to about 2.24 at 1400 K, where the three phases UO_{2-x}, U_4O_{9-y}, and U_3O_{8-z} are in equilibrium. The UO_{2+x} / U_4O_{9-y} phase diagram was established by Schaner [20] making use of metallography techniques; by Saito [21] and by Nakamura and Fujino [22] from electromotive force measurements; by Aronson *et al.*[23] by thermoelectric power and thermal conductivity measurements. Van Lierde *et al.* [24] determined, by X-ray analysis, metallography, chemical analysis and electron microscopy, that the homogeneity range of the U_4O_{9-y} phase covers the composition interval $0.235 < x < 0.245$ at room temperature and $0.2235 < x < 0.24$ at 1373 K. The point where U_4O_{9-y} transforms to UO_{2-x} was measured to be 1398 K. The same point was measured by Roberts and Walter [25] at 1396 ± 5 K, where they located the invariant reaction $U_4O_{9-y} \Leftrightarrow UO_{2-x} + UO_{2.61}$. With their tensimetric experiments, they also determined the equilibrium oxygen pressures in the range $0 < x < 0.3$, $1273\ K < T < 1723\ K$ and hence the UO_{2+x} /U_3O_{8-z} / $U_8O_{21-\xi}$ phase boundaries, the latter species existing only above 1400 K. At higher temperature Anthony *et al.* [26] established the phase boundary at $1500\ K < T < 2000\ K$ by quenching UO_{2+x} samples at fixed temperature and known oxygen partial pressure. They determined the O/U ratio by thermogravimetry and the different phases by X ray diffraction, but in considering their results one should not forget that measurements performed on hyperstoichiometric urania quenched samples are not fully reliable due to the extremely high mobility of the anions. However, x is likely to increase slightly up to 0.27 at 2000 K along the phase boundary. No further experimental data are available on the hyperstoichiometric urania phase diagram at higher temperatures, up to the melting

measurements performed by Christensen [27] and by Latta and Fryxell (op. cit. [9]) that cover the range 2837 K < T < 3138 K, and will be discussed in the next section.

2.1.3 High temperatures

Few authors have investigated the melting behaviour of uranium dioxide, and most of them obtained data on the hypostoichiometric compositions only, for which the experimental investigation is facilitated by the better physico- chemical stability of the compound.

As mentioned in the previous section, the lower *solidus* was well established by Martin and Edwards. Hypostoichiometric urania melting behaviour was first investigated by Bates [28], who made use of an electric furnace with purified inert atmospheres to measure, using optical pyrometry and microscopy, the phase boundary UO_{2-x} / L_1+UO_{2-x} / L_1. However, in his report it is not clearly explained whether he recorded the first sign of melting, i.e. the *solidus* transition, or rather just an estimate of the temperature above which the liquid phase was certainly there. Bannister (op. cit. [8]), in using a technique of the same kind, managed to distinguish *solidus* and *liquidus* (i.e. the point of first appearance of the solid phase in the liquid). The most complete work was due to Latta and Fryxell (op. cit. [9]), who used a thermal arrest technique on urania samples heated within an inductively heated furnace and held in sealed tungsten or rhenium capsules. This method will be described in the next Chapter. The resulting accuracy was ±15 K, far better than the previous attempts. *Liquidus* and *solidus* lines as well as the monotectic temperature were successfully established for hypostoichiometric uranium dioxide. The congruent melting temperature (CMT), where *solidus* and *liquidus* intersect, was measured at 3138 K with good agreement among the cited works. The 15 K temperature gap between solidus and liquidus reported at this point by Latta and Fryxell, probably attributable mainly to temperature gradients over the sample, was considered as an indication of the precision limit of their method. Stoichiometric $UO_{2.00}$ was established to be the congruent melting composition; on the other hand, the method was

not accurate enough to ascertain whether the congruent melting occurred instead at $UO_{1.98}$, which was estimated as the congruent vaporisation composition.

Latta and Fryxell extended their investigation to the hyperstoichiometric domain up to the composition $UO_{2.23}$, where only one published indication of the melting point variation with O/U ratio was given by Christensen (op. cit. [27]) within a report describing a study of the effects of high irradiation on $UO_{2.00}$ fuel rods. In this work, the temperature was monitored both on the periphery and on the centre of the rod. The molten centre was highly enriched in oxygen, due to the massive oxygen diffusion that occurred between solid and liquid phases. From that Christensen could roughly estimate the melting point variation with oxidation, and the features of the phase diagram upon melting.

Latta and Fryxell performed the only systematic experimental study of the *solidus* and *liquidus* of hyperstoichiometric uranium dioxide. Unfortunately, the measured transition points were significantly affected by the strong interaction between the tungsten or rhenium [29] crucible and the urania samples, as detected by the authors themselves. One of the main consequences of the sample contamination was the loss of the excess oxygen that extensively reacted with the crucible metal. But even neglecting such phenomena, one should consider that significant oxygen losses probably occurred due to the large non-congruent evaporation rate characteristic of the oxygen- enriched phase at high temperature. The laser method presented in this thesis was employed to measure, in an original way, the melting transition of hyperstoichiometric urania, overcoming difficulties such as those mentioned in the review of Latta and Fryxell's research.

2.2 Oxygen potential and equilibrium vapour pressure

2.2.1 Oxygen Potential

The "oxygen potential" (see [30]) of a condensed phase indicates the partial molar free energy of oxygen in the phase itself and is denoted as:

$$\Delta G_{O2} = RT \ln p_{O2} = 2\mu_O(\text{solution}) - \mu^0_{O2} \qquad (2.1)$$

In Eq. (2.1), R is the ideal gas constant, p_{O2} the oxygen partial pressure expressed in atmospheres, μ_O the chemical potential of oxygen dissolved in the condensed phase, and μ^0_{O2} the chemical potential of pure gaseous oxygen at the same temperature and at 1 atm.

ΔG_{O2} expresses the equilibrium oxygen pressure over the material. It constitutes a most significant chemical property in an oxide nuclear fuel in determining the behaviour of the fuel so far as features like cladding corrosion, coolant interaction, fission product retention, creep and matter transport are concerned [31-34].

In 1985 Lindemer and Besmann [35] published the first extensive database on the oxygen potential of the urania phase. They also interpreted the data by least-squares analysis using equations based on the classical thermodynamic theory of the solid. Their final output was an accurate ΔG_{O2} - $T - x$ diagram (Fig. 2.4) that still constitutes an important reference for the O-U system, largely used also in this work. Some interesting later research, specially the accurate electromotive force (emf) measurements published by Nakamura and Fujimo (op. cit. [22]), obtained an entire set of partial molar thermodynamic functions of oxygen in urania. A good data review, more recent than that of Lindemer and Besman, is compiled in the work of Chevalier *et al.* (op. cit. [3]) already quoted above with reference to the U-O phase diagram. The oxygen partial pressure on urania increases by several orders of magnitude (depending on the temperature) on passing from the hypostoichiometric to the hyperstoichiometric compositions, justifying the lower physico- chemical stability of compositions richer in oxygen.

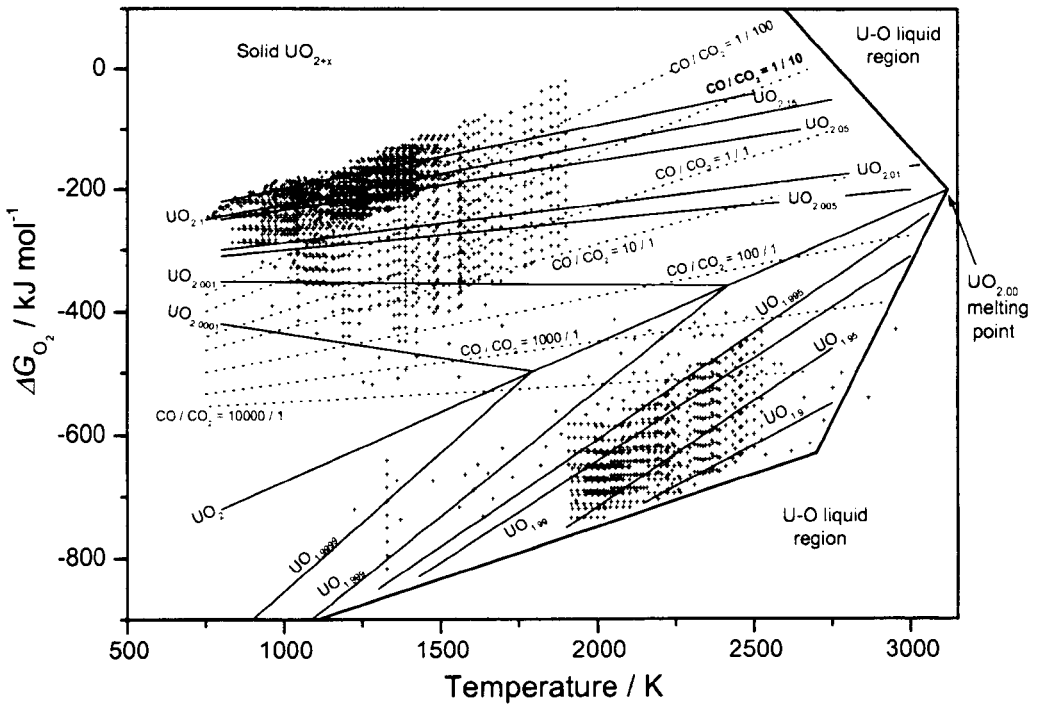

Fig. 2.4: Oxygen potential calculated for the system UO_{2+x} plotted together with available experimental data (after [35]).

Fig. 2.5 exemplifies some $p_{O2} - x$ diagrams reported by Guéneau *et al.* (op. cit. [1]).

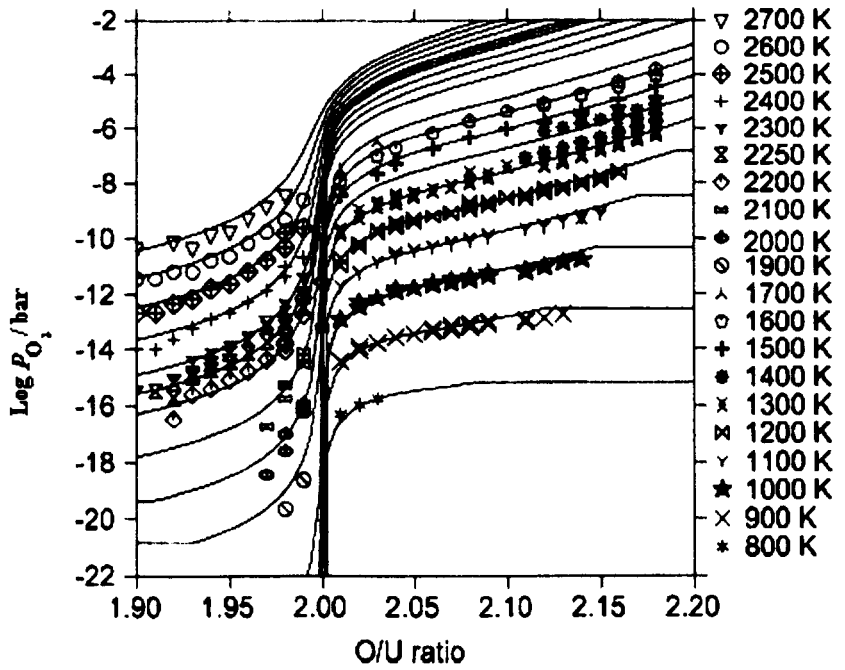

Fig. 2.5: Urania $p_{O2} - x$ diagram as reported in [1] at different temperatures. The oxygen potential increases by several orders as the composition changes from hypo- to hyper-stoichiometry.

An important thermodynamic model concerning oxygen vapour pressure over the urania fuel is due to Blackburn [36], based on his calculations of a free energy and mass action. Blackburn's results were compared with the experimental data obtained by Tetenbaum and Hunt [37]. Because of the sharp increase in the oxygen partial pressure at O/U = 2, the oxygen potentials in the hypo- and hyperstoichiometric domains have been investigated in very different temperature regimes and by different techniques.

For hypostoichiometric UO_{2-x} compositions, ΔG_{O2} was measured by gas equilibration, beside Tetenbaum and Hunt, by Markin *et al.* [38], Wheeler and Jones [39] and Javed [40]. Pattoret *et al.* [41] have derived p_{O2} values from mass-spectrometric measurements of the UO and UO_2 intensities. Aitken *et al.* [42] determined the limiting composition under free vaporisation as a function of temperature and oxygen partial pressure.

The gas equilibration technique was also used on hyperstoichiometric urania by Markin and by Wheeler and Jones within the studies quoted above, and by Adamson and Carney [43].

Electromotive force measurements and thermogravimetry are the techniques most frequently used to investigate the oxygen potential for hyperstoichiometric oxides. These methods have also been used within this work, and are presented in Chapter 5. Several authors have published data obtained via emf measurements; apart from the already cited work of Nakamura and Fujimo, this technique was used by Aronson and Belle [44], Une and Oguma [45] and Schleifer *et al.* [46]. Marchidan *et al.* [47-50], Saito [51] and Markin *et al.* [52] extended their measurements to U_4O_{9-y}.

The thermogravimetric technique was used by Une and Oguma [53] along with gas equilibration for low values of x, by Chapman and Meadows [54] and by Hagemark and Broli [55] in the range $0.01 < x < 2.63$.

Blackburn [56] used a Knudsen-diffusion method to analyse compositions from $UO_{2.0}$ to $UO_{2.6}$; in the same domain Picard and Gerdanian determined the partial molar mixing enthalpy of oxygen, ΔH_{O2} making use of a microcalorimetrc method [57].

Chapman *et al.* [58] published interesting work where they extrapolated oxygen isobars up to melting from Hagemark and Broli's (op. cit. [55]) data and measured the oxygen pressure over liquid urania at a temperature of 3150 K by a gas equilibration technique. Their results, the only experimental reference at high temperature, are illustrated in Fig. 2.6, along with Latta and Fryxell's phase diagram and Hagemak and Broli's high temperature data.

As far as the present work is concerned, oxygen potential is a parameter of great significance insofar as it is related to the equilibrium vapour pressure and composition, hence to the O/U ratio and the nuclear fuel stability upon melting.

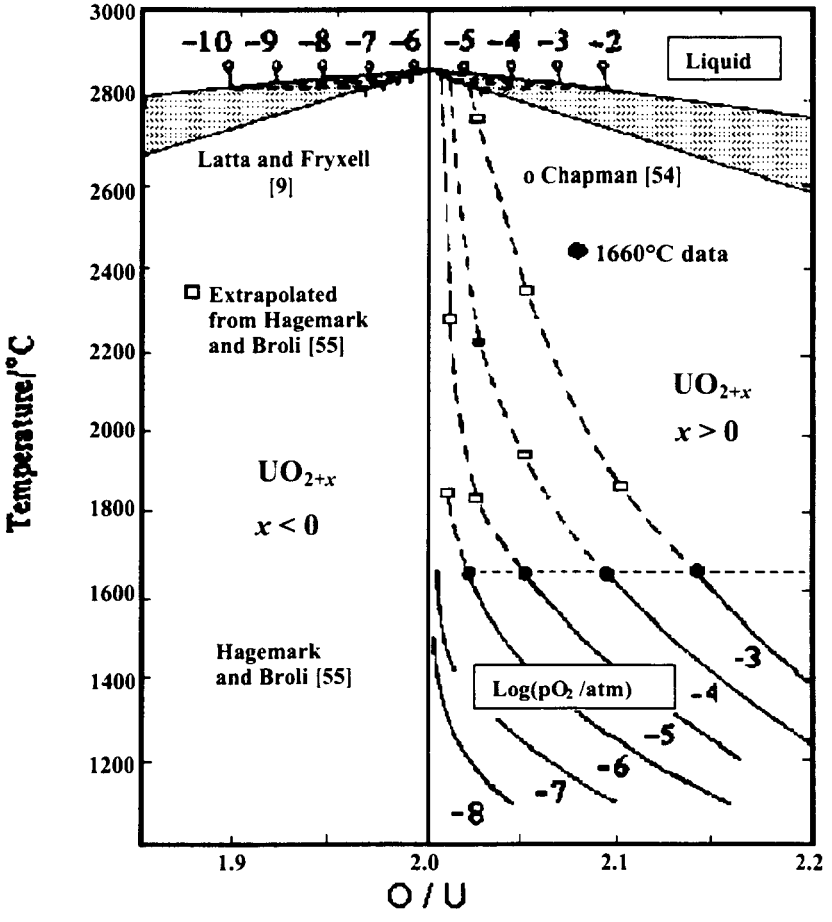

Fig. 2.6: *T–x* phase diagram and oxygen potential of the hyperstoichiometric Oxygen–Uranium system. White circles indicate the measurements of oxygen potential performed by Chapman *et al.* [58] over liquid urania (figure from [58]).

2.2.2 Equilibrium vapour composition and pressure

The main species present in the gas phase in equilibrium with the condensed uranium dioxide are U(g), O, O_2, UO(g), UO_2(g) and UO_3(g). Chapman and Meadows (op. cit. [54]) studied the volatility of urania with a thermogravimetric technique. Their results required that UO_4 (g) be the uranium-bearing vapour species above hyperstoichiometric UO_{2+x}. However, successive mass spectrographic attempts to detect UO_4 were unsuccessful, suggesting that such a molecule has only transient stability before the formation of UO_3(g). At temperatures well above melting the existence of the dimer $(UO_2)_2$(g) had been postulated by Ackermann *et al.* [59]. Congruent vaporisation occurs at one definite composition only, depending on the temperature. The congruent vaporising composition (CVC) was found by Edwards *et al.* [60], by Drowart *et al.* [61] and by Tetenbaum and Hunt [62] to be slightly hypostoichiometric.

The deviation of CVC from stoichiometry increases with temperature. According to Edwards *et al.* [60] the condensed urania phase changes its stoichiometry on evaporation until CVC is attained. These authors also provided the following equation for the temperature dependence of the CVC:

$$x \ln x = (-0.850 \pm 0.100) + (3.832 \pm 0.396)\ 10^{-4}\ T. \qquad (2.2)$$

In Eq. (2.2) x is the non-stoichiometry in UO_{2+x} at the CVC, T is the absolute temperature ($2218 < T < 3058$ K), and the uncertainties in the coefficients represent the standard deviation for the regression on experimental data. The plot of Eq. (2.2) reported in Fig. 2.7 shows that even at temperatures well below melting stoichiometric uranium dioxide produces a vapour phase with O/U > 2.

Edwards *et al.* provided a diagram (Fig. 2.8) showing the partial pressures of the species listed above as functions of x at 2185 K, based on a fit of the data measured by Tetenbaum and Hunt (op. cit. [62]) and by Ackermann *et al.* (op. cit. [59]).

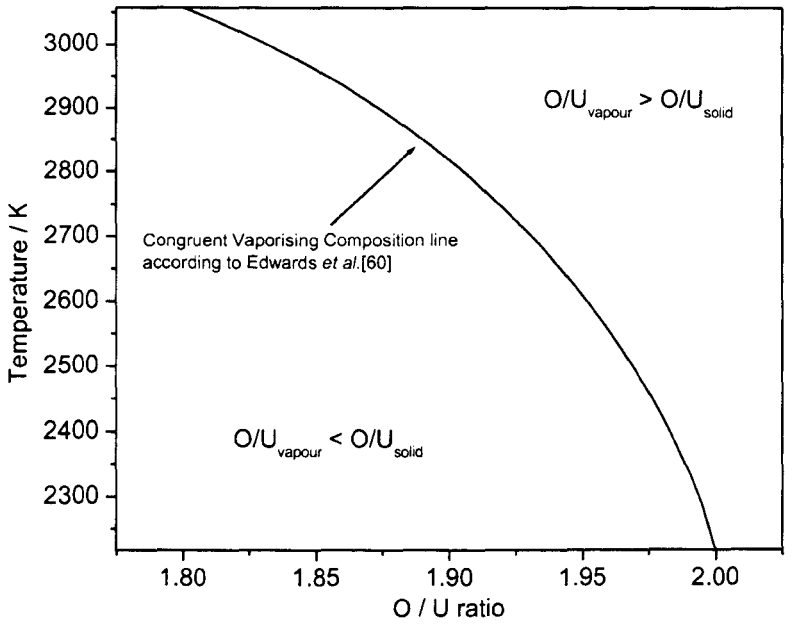

Fig. 2.7: Plot of equation (2.2): Congruent Vaporising Composition line [60].

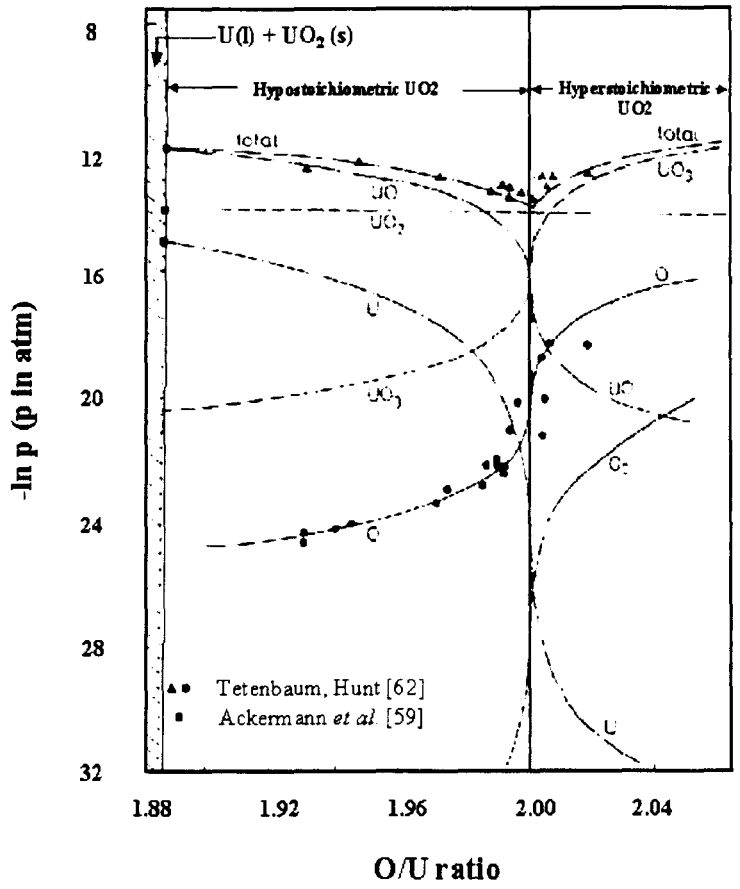

Fig. 2.8: Total and partial pressure curves calculated for uranium dioxide at 2185 K (from [60]).

The vapour above stoichiometric urania consists mainly of UO_2, but at 2185 K it already contains 10 to 15% of UO and UO_3, and the fraction of this latter significantly increases with temperature.

In the hyperstoichiometric range, the pressure of UO_3 rises quickly with the O/U ratio, and soon exceeds that of UO_2. Likewise the partial pressure of U and UO exceeds that of UO_2 in the hypostoichiometric region, while p_{UO2} remains practically independent of the composition. Punni and Mason [63], proposed the same type of diagram at 2700 K, where both total pressure and UO_3 (g) partial pressure already increased by four orders of magnitude. An extensive data collection on this subject can be found in [64].

Tetenbaum and Hunt (op. cit. [62]) plotted the total pressure of uranium-bearing vapour species over solid urania as a function of inverse temperature on the basis of the experimental data obtained by themselves and by Alexander *et al.* [65] via a transpiration technique, by Ackermann *et al.* (op. cit. [59]) and by Ivanov *et al.* [66] via an effusion technique. This graph is reported in Fig. 2.9 together with the data obtained by Ohse *et al.* [67] by effusion.

Equilibrium total vapour pressure over liquid urania represents an important factor for the prediction of the nuclear excursion yield in hypothetical whole-core accident analysis, as an increase in vapour pressure decreases significantly the energy release. Beitung and Reil [68] derived the following equation for the total vapour pressure over liquid urania from their in-pile equation-of-state measurements:

$$\mathrm{Log}_{10} P = 15.961 - 26974\, T^{-1} - 2.7600 \log_{10} T\,, \qquad (2.3)$$

where P is in MPa. Eq. (2.3) is in good agreement with the pressures measured by Ohse *et al.* from laser-vaporisation experiments in 1985 [69], with the low-temperature 1972 transpiration data of Reedy and Chasanov [70], with the high-temperature data presented in 1981 by Limon *et al.* [71], and with the boiling - point data published in 1987 by Bober and Singer [72], who used a novel laser heating technique to measure the saturated vapour pressure curve of liquid UO_2 for $3500 < T < 4500$ K. They established the atmospheric -

pressure boiling point at 3809 K, in excellent agreement with Eq. (2.3) that gives a boiling temperature of 3815 K.

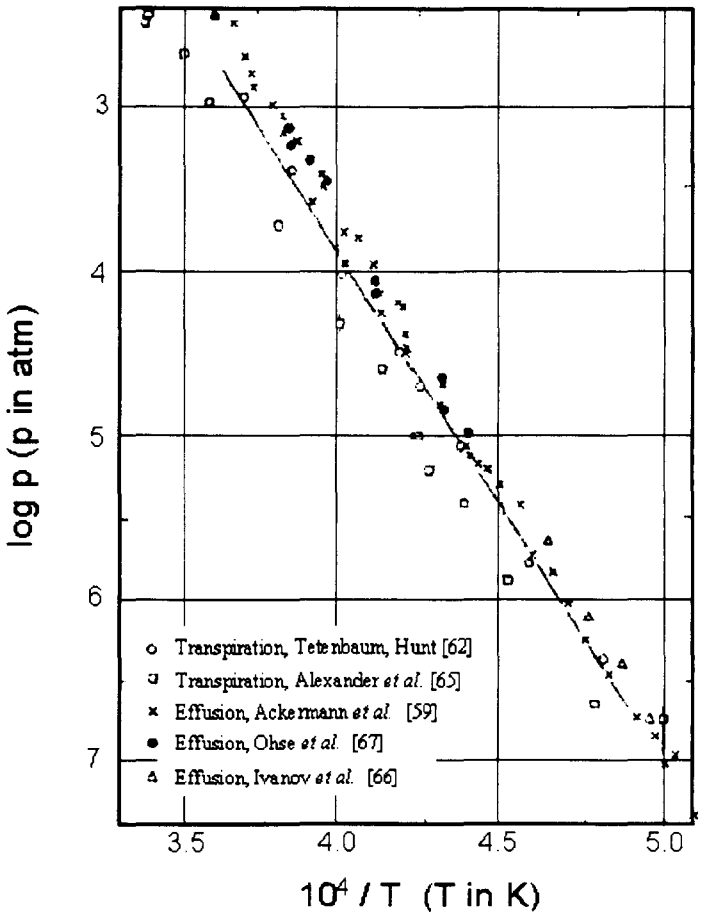

Fig. 2.9: Total pressure of uranium-containing species over solid UO_2 (after [62]).

Fig. 2.10 shows the most relevant data reported in the review paper by Fink [73], where Eq. (2.3) is recommended as representing the best experimental measurements on liquid urania vapour pressure. The sensitivity of vapour pressure to the composition of the condensed phase is rather well determined only up to the melting point; at higher temperatures experimental data on the O/U ratio dependence are missing.

According to Bober and Fischer [74] the vapour composition over stoichiometric UO_2 is highly enriched in oxygen above the melting point: the O/U ratio was calculated to be 2.5 at

3500 K (predominant presence of UO_3), and 2.8 at 4500 K (O_2 and O produced in abundance).

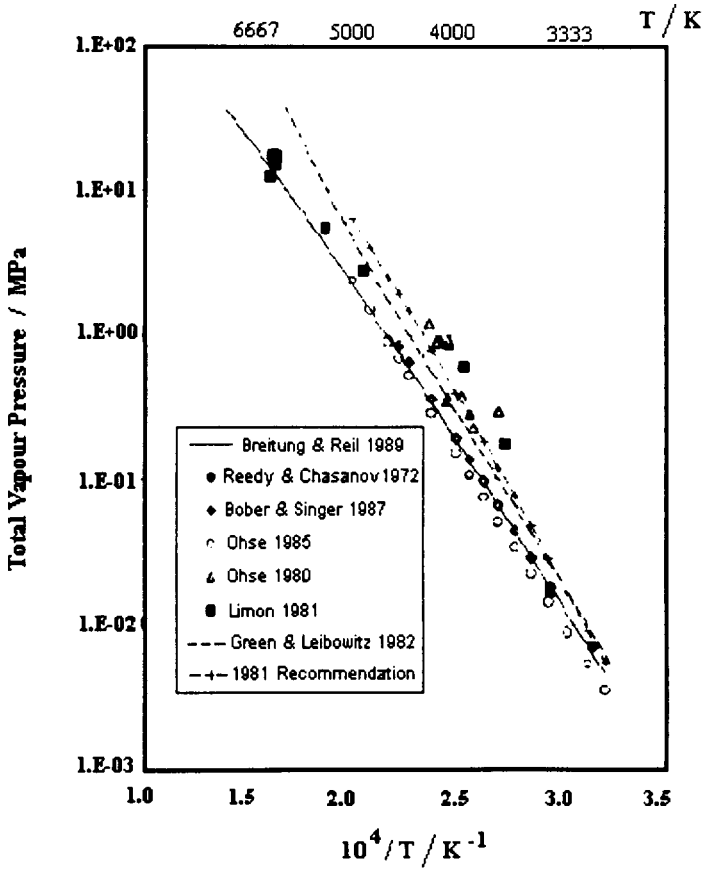

Fig. 2.10: Equations and data for the total vapour pressure over liquid UO_2 as a function of inverse temperature (after [73]).

Data on the vapour composition over hyperstoichiometric urania have mainly been calculated within theoretical work on the equation of state (EOS). The model used by Babelot *et al.* [75] for composition close to stoichiometry, based on the Schottky – Wagner [76] disorder model, provided data for slightly stoichiometric oxides (up to O/U = 2.01). A comprehensive thermodynamic database for liquid and gaseous urania was calculated by Iosilevski *et al.* [77]. These latter authors used a "chemical model" for the theoretical description of liquid urania, thus considered as a multicomponent mixture of chemically reactive, strongly interacting neutral and charged molecules and atoms. A high-temperature (up to the critical point calculated at about 10120 K) phase diagram was obtained for the

system UO_{2-x}. Very high maximum vapour pressure ($P_{max} \approx 1$ GPa) and oxygen enrichment of the vapour phase over boiling UO_{2-x} ($(O/U)_{max} \approx 7$) were found as a consequence of the strongly non-congruent vaporisation.

Non-congruent vaporisation of uranium dioxide constitutes one of the main issues in the experimental determination of the melting transition. This feature hinders melting point measurements, by causing changes in the composition of the sample. Moreover, the vapour generated in large amount at high temperature could interfere with the optical measurement of the temperature. Melting transition measurements presented in Chapters 5 and 6 of this work were performed under inert buffer gas at high pressure (order of kbar) in order to suppress vaporisation from the sample surface.

2.3 Relevant thermodynamic and thermophysical properties

The cited works of Chevalier *et al.* [3] and of Rand *et al.* [4] both contain a broad data collection on the thermodynamic properties of the urania phase, although the most exhaustive review on the thermophysical properties of uranium dioxide was compiled by Fink in [73].

2.3.1 Thermodynamic functions

Integral thermodynamic data for the urania phase are rather consistent. Enthalpy of formation, entropy and heat capacity of the stoichiometric oxide at standard conditions (298.15 K, 1 atm, fluorite-like lattice) are accepted as ΔH_f° = -1084.9112 kJ mol^{-1}, S_f° = 77.02744 J mol^{-1}, C_P° = 63.5968 J K^{-1} mol^{-1}.

UO_2 undergoes a λ-phase transition at 2670 K, which was first observed by Ackermann *et al.* (op. cit. [59]), then studied in detail by Bredig [78], that identified it as a "textural" change [79-81]. Hiernaut, Hyland and Ronchi [81] developed a model for the transition as a function

of stoichiometry and temperature. The heat capacity of UO_2 was measured up to 8000 K on laser-heated microspheres by Ronchi *et al.* [82].

Starting from the interpretation of these experimental data, Ronchi and Hyland [83] provided an extensive description of the contributions from each physical process to the heat capacity. Fig. 2.11 shows the temperature dependence of uranium dioxide heat capacity as reported by these latter authors. They suggested that harmonic lattice vibrations, approximately described by a single effective Debye model, govern the increase in heat capacity from room temperature up to about 1000 K. From 1000 to 1500 K, the weak C_P increase with temperature was attributed to the progressive increase in the anharmonicity of the lattice vibrations, as reflected in the thermal expansion of the material.

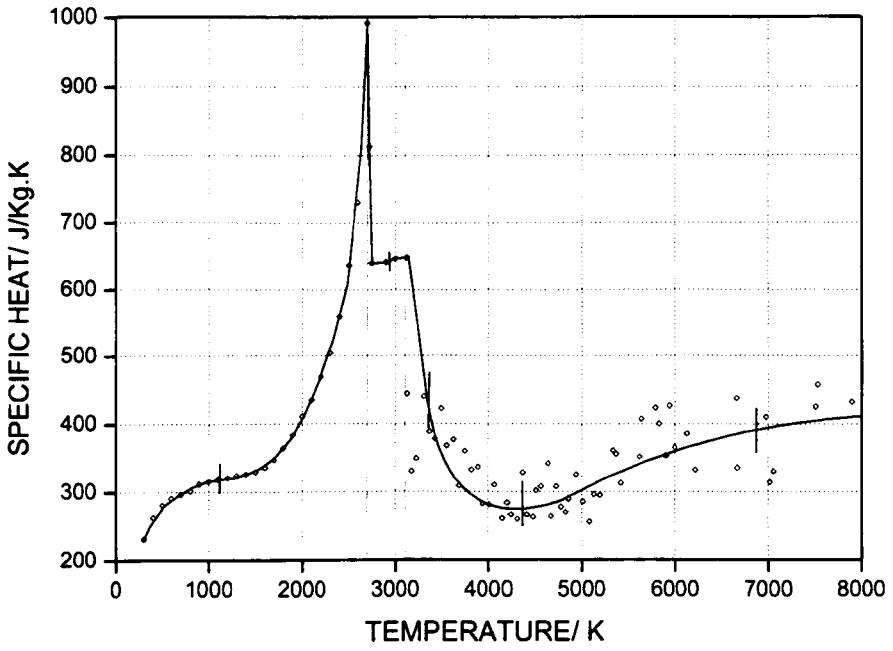

Fig. 2.11: Heat capacity of nominally stoichiometric UO_2: experimental points and least-square fitting curve obtained by Ronchi *et al.* [82]. The ranges corresponding to the different heat transfer mechanisms analysed by Ronchi and Hyland [83] are evidenced.

The increased heat capacity from 1500 to 2670 K is due to the formation of Frenkel point defects. Above the λ-phase transition and up to the melting point Schottky defects prevail after the Frenkel defect concentration becomes saturated, and this gives a slightly increasing stage. From the melting temperature to about 4500 K, C_P stabilises around the level attained at 1000 K, indicating that all the thermally activated processes have entirely saturated, and only atomic vibrations support further heat exchanges. At higher temperatures, where data appeared to be quite scattered, a further slight increase in C_P was observed, with an activation energy of the same order as what needed in the solid to excite the valence electrons of the deeper 2p-based band.

The above-mentioned review by Fink [73] reports a combined fitting of selected enthalpy and heat capacity data with the constraints:

$H(T) - H(298.15\ K) = 0$ at $T = 298.15$ K

$(\partial H / \partial T)_P = C_P$

The following 7-term polynomial was recommended as a best fit to enthalpy data:

$H(T) - H(298.15\ \text{K})$ (kJ mol^{-1}) =

$$-21.1762 + 52.1743\ t + 43.973\ t^2 - 28.0804\ t^3 + 7.88552\ t^4 - 0.52668\ t^5 + 0.7139\ t^{-1}, \quad (2.4)$$

where $t = T / 1000$, T being the absolute temperature. Equation (2.4) derivative provides the best fitting for C_P in J K^{-1} mol^{-1}:

$$C_P(T) = 52.1743 + 87.951\ t - 84.24\ t^2 + 31.542\ t^3 - 2.6334\ t^4 - 0.7139\ t^{-2}. \quad (2.5)$$

For liquid urania, at 3138 K ≤ T ≤ 4500 K, the suggested equations are:

$$H(l, T) - H(s, 298.15\ \text{K})\ (\text{J mol}^{-1}) = 8.0383 \cdot 10^5 + 0.25136\ T - 1.3288 \cdot 10^9\ T^{-1}, \quad (2.6)$$

yielding

$$C_P\ (\text{J K}^{-1}\ \text{mol}^{-1}) = 0.25136 + 1.3288 \cdot 10^9\ T^{-2}. \quad (2.7)$$

The enthalpy of fusion proposed by Fink is 70 ± 4 kJ mol^{-1}, obtained from the difference between solid and liquid enthalpies as provided by equations (2.4) and (2.6) at the melting point. However, the value of 74.814 kJ kg^{-1} recommended by Harding *et al.* [84] is preferable in practice as based on enthalpy experimental data near the melting point, rather

than being extrapolated from the fitting of enthalpy and thermal capacity data over wide temperature ranges.

As for the enthalpy of vaporisation, Breitung and Reil in their work cited above [68] recommended the following expression:

$$\Delta H_{vap} = 516.382 - 22.946 \cdot 10^{-3}\, T, \tag{2.8}$$

obtained by applying the Clausius – Clapeyron equation to their vapour pressure equation (Eq. (2.3)). Eq.(2.8) is valid for 3138 K ≤ T ≤ 8000 K and ΔH_{vap} is expressed in kJ mol^{-1}.

2.3.2 Thermal conductivity

Thermal conductivity is an important property of the samples investigated in the current research, because it constitutes one of the main factors determining the shape of the thermograms recorded during the melting / freezing experiments. In Nuclear Technology, nuclear fuel thermal conductivity λ (T) enters in the "in- reactor conductivity integral to melt" (CIM), defined as

$$CIM = \int_{773K}^{T_{melt}} \lambda(T)dT, \tag{2.9}$$

The CIM represents the reactor linear power at which melting begins on the centreline of a fuel pellet, the outer surface of which is assumed to be at 773 K.

Experimental values for CIM range from 5.5 to 7.5 kW m^{-1}, which can be compared with values calculated by substituting in Eq. (2.9) the thermal conductivity λ (T) experimentally obtained by different authors. On the basis of such a comparison Fink [73] recommended that the following equation was the best fit to the thermal conductivity data in 95% dense UO_2 at temperatures between 1000 and 3120 K:

$$\lambda(T) = \frac{100}{7.5408 + 17.692\,T + 3.614\,T^2} + \frac{6400}{T^{\frac{5}{2}}} \exp\left(-\frac{16.35}{T}\right) \text{ kW m}^{-1}, \tag{2.10}$$

where T is the absolute temperature expressed in kK. Eq. (2.10) takes into account the most recent advances in understanding the heat transport mechanisms in UO_2, especially the work, both experimental and theoretical, of Ronchi *et al.*[85]. Uranium dioxide thermal conductivity both measured and fitted by Ronchi *et al.* is reported in Fig. 2.12 (after [73]) together with the plot of Eq. (2.10) and other experimental data. The value of λ at the melting point is about 3.0 W $m^{-1} K^{-1}$ (Ronchi *et al.* [85] suggested $2.4 \leq \lambda \leq 3.1$ W $m^{-1} K^{-1}$). Available data on thermal conductivity of liquid uranium dioxide were reviewed by Ronchi in an extended work [86], where the value $\lambda_{liquid} = 2.5 \pm 1$ $Wm^{-1}K^{-1}$ was finally recommended. Fink also recommended such a value in [73]. Finally, although uranium dioxide thermal conductivity in the liquid is likely to be slightly smaller than in the solid, the difference is contained within the data uncertainty. Data on thermal conductivity of non-stoichiometric uranium dioxide are not available.

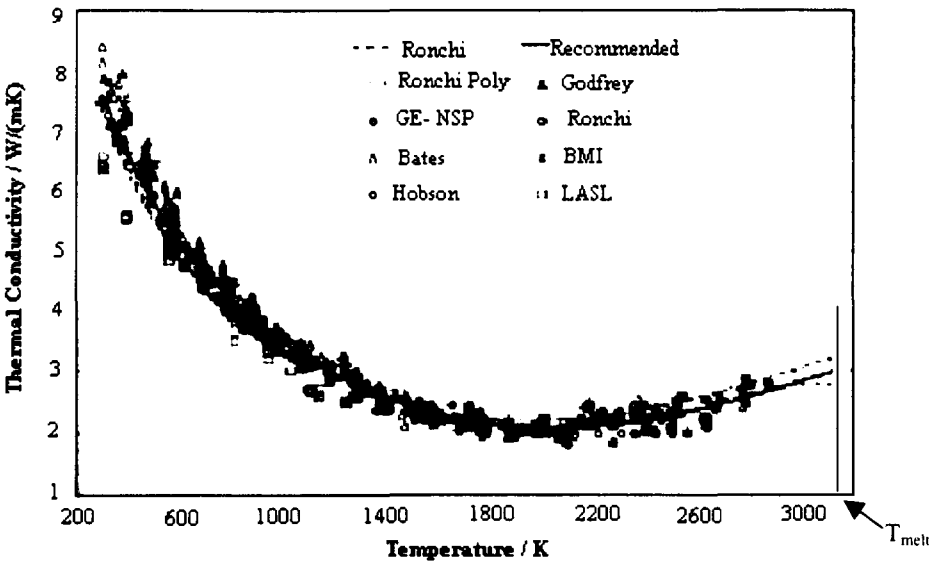

Fig. 2.12: Thermal conductivity of solid stoichiometric uranium dioxide [73].

2.3.3 Density and thermal expansion

The coefficient of thermal expansion at constant pressure $\alpha_p = V^{-1}(\partial V / \partial T)_p$ and the density $\rho = MW / V$ (V = molar volume; MW = molar weight) of urania are significant properties in the study of the equation of state of the material, and in the design of the reactor core. On the difference between thermal expansions of the fuel and the cladding depends the variation of the initial fuel-cladding gap as the fuel element is brought to power (see, for instance, [30]). As for the present work, such data are important in the study of the UO_2 melting line reported in Chapter 6.

Martin [87] compiled an exhaustive review of UO_2 thermal expansion data, based on lattice parameter measurements and on observed macroscopic length changes.

Martin obtained a satisfactory fitting of the chosen data with the following polynomials expressing the linear thermal expansion:

$$L_T = L_{273}\,(9.9734\cdot10^{-1} + 9.802\cdot10^{-6}\,T - 2.705\cdot10^{-10}\,T^2 + 4.391\cdot10^{-13}\,T^3) \qquad (2.11)$$

for 273 K ≤ T ≤ 923 K, and

$$L_T = L_{273}\,(9.9672\cdot10^{-1} + 1.179\cdot10^{-5}T - 2.429\cdot10^{-9}\,T^2 + 1.219\cdot10^{-12}\,T^3) \qquad (2.12)$$

for 923 K < T ≤ 3138 K,

where L_T = length of a material element at the temperature T.

The coefficient of linear thermal expansion $\alpha_p(l) = L^{-1}(\partial L / \partial T)_p$ ($\alpha_p(l) = \alpha_p/3$ supposing the material to be isotropic) could then be determined by differentiating equations (2.11) and (2.12), but it is also well represented by the polynomials:

$$\alpha_p(l) = 9.828\cdot10^{-6} - 6.930\cdot10^{-10}\,T + 1.330\cdot10^{-12}\,T^2 - 1.757\cdot10^{-17}\,T^3 \qquad (2.13)$$

for 273 K ≤ T ≤ 923 K, and

$$\alpha_p(l) = 1.1833\cdot10^{-5} - 5.013\cdot10^{-9}\,T + 3.756\cdot10^{-12}\,T^2 - 6.125\cdot10^{-17}\,T^3 \qquad (2.14)$$

for 923 K < T ≤ 3138 K.

Martin's investigation extended also to the data available within the hyperstoichiometric domain, where no significant deviation from the linear thermal expansion described by the above equations could be appreciably detected.

Original studies on the variation of cubic urania lattice parameter a with the deviation from stoichiometry x date back to the fifties and are due to Groenvold [88] and Perio [89].

Fig. 2.13, after Groenvold's paper, reports values of a measured as a function of T and x in the domains UO_{2+x} and U_4O_9.

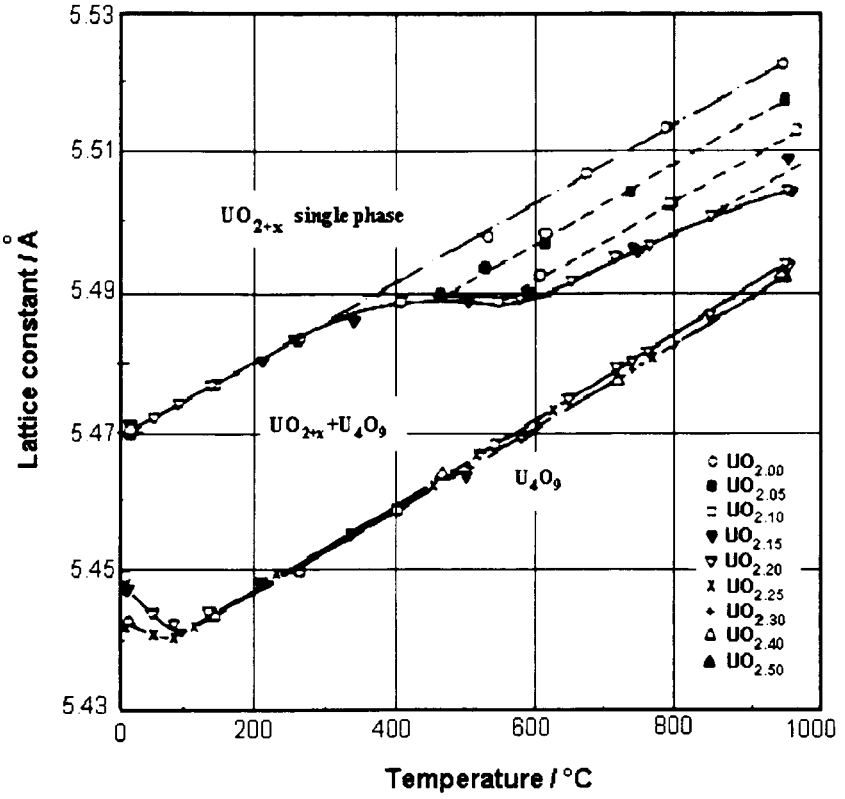

Fig.2.13: Lattice parameter of the phase UO_{2+x} as a function of temperature and composition (after [88]).

Perio proposed the equation

$$a\,(\text{Å}) = 5.4690 - 0.12\,x\,, \tag{2.15}$$

that can be considered valid in the one-phase region only.

The density of $UO_{2.00}$ at room temperature is $\rho_{273} = 10.963$ g cm^{-3} (see, for instance, [90]), and its decrease with temperature can be obtained from equations (2.11) and (2.12), as

$$\rho_T = \rho_{273} (L_{273} / L_T)^3. \quad (2.16)$$

The dependence of ρ on non-stoichiometry has been measured on the urania samples used in the present work. Density increases with x in the hyperstoichiometric domain as reported in Chapter 5.

The coefficient of linear thermal expansion for liquid urania was recommended by Breitung and Reil [90] as

$$\alpha_P(l) = \frac{0.9285}{8860 - 0.9285(T - 3120)}, \quad (2.17)$$

Breitung and Reil performed in-pile measurements from the melting point up to 7600 K. They also proposed an equation for the density of liquid urania:

$$\rho = 8.860 - 9.285 \cdot 10^{-4} (T - 3120) \text{ g cm}^{-3} \quad (2.18)$$

in agreement with the data obtained by Drotning using the gamma- attenuation technique [91]. These latter were the most precise experimental points among those reviewed by Fink [73]. The recommended density at the melting point is 8.860 g cm^{-3}.

2.4 Conclusion

The short overview of uranium dioxide properties presented in this chapter provides a physico- chemical background for the current research. Most of the thermodynamic and thermophysical uranium dioxide properties reviewed were used in the design, analysis and simulation of the experiments performed within the present work.

The experimental and calculated data reported in this chapter give an idea of the great amount of work performed in the last decades aimed at understanding the behaviour of the nuclear fuel under different conditions, but also reveal areas where experimental information is still limited. In particular, the behaviour of hyperstoichiometric uranium dioxide is known only with large uncertainty in the vicinity of the melting transition, where sound experimental data would be needed in the analysis and prediction of hypothetical core-

meltdown accidents. The main goal of the present research is to provide this kind of empirical data using a novel experimental technique aimed at overcoming the difficulties encountered by previous researchers.

References Chapter 2

1. C. Guéneau, M. Baichi, D. Labroche, C. Chatillon, B. Sundman, J. Nucl. Mater. **304** (2002), 161.
2. P.-Y. Chevalier, E. Fischer, J. Nucl. Mater. **257** (1998), 213.
3. P.-Y. Chevalier, E. Fischer, B. Cheynet, J. Nucl. Mater. **303** (2002), 1.
4. M.H. Rand, R.J. Ackermann, F. Groenvold, F.L.Oetting, A. Pattoret, Rev. Int. Hautes Tempér. Réfract. Fr., **15** (1978), 355.
5. J.L. Bates, US At. Energy Comm. HW-81603 (1964), 2.
6. A.E. Martin, R.K. Edwards, J. Phys. Chem. **69-5** (1965), 1788.
7. P. Guinet, H. Vaugoyeau, P.L. Blum, C.R. Acad. Sci. Série C 263 (1966), 17, Rapport CEA - R3060, CENG, Section de Metallurgie, Nov. 1966.
8. M.J. Bannister, J. Nucl. Mater. **24** (1967), 340.
9. R.E. Latta, R.E. Fryxell, J. Nucl. Mater. **35** (1970), 195.
10. B.T.M. Willis, Nature (London) **197** (1963), 755.
11. B.T.M. Willis, J. Phys. Radium **25** (1964), 431.
12. B.T.M. Willis, Acta Crystallogr., Sect. A, **34** (1978), 88.
13. B.T.M. Willis, Proc. Roy. Soc. (London), Ser. A **274** (1963), 122
14. C.R.A. Catlow, J. Phys. C **6** (1973), L64.
15. C.R.A. Catlow, Proc. R. Soc. London, Ser. A **353** (1977), 533.
16. C.R.A. Catlow and A.B. Lidiard, in "*Thermodynamics of Nuclear Materials (1974)*", IAEA, Vienna, Vol. II (1975), 27.
17. G.C. Allen and P.A. Tempest, J. Chem. Soc. Dalton Trans. (1983), 2673.

18. B.T.M. Willis, Proc. Brit. Ceram. Soc. No. **1** (1964), 9.

19. T. Ishii, K. Naito, K. Oshima, Solid State Commun. **8** (1970), 677.

20. B.E. Schaner, J.Nucl.Mater. **2** (1960), 110.

21. Saito, J. Nucl. Mater. **51** (1974), 112.

22. A. Nakamura, T. Fujimo, J. Nucl. Mater. **149** (1987), 80.

23. S. Aronson, J.E. Rulli, B.E. Schaner, J.Chem.Phys. **35-4** (1961), 151.

24. W. Van Lierde, J. Pelsmaekers, A. Lecocq-Robert, J. Nucl. Mater. **37** (1973), 276.

25. L.E.J. Roberts, A.J. Walter, J. Inorg. Nucl. Chem. **22** (1961), 213.

26. A.M. Anthony, R. Kiyoura, T. Sata, J. Nucl. Mater. **10-1** (1963), 8.

27. J.A. Christensen, *Stoichiometry Effects in Oxide Nuclear Fuels*, Battelle Northwest (USA) Laboratory Report 536, 1967, 1.

28. J.L. Bates, J. Am. Ceram. Soc. **49-7** (1966), 395.

29. R. E. Fryxell, *High Temperature Nuclear Fuels*, Gordon and Breach Publ., New York, 1968, 211.

30. D. R. Olander: " *Fundamental Aspects of Nuclear Reactor Fuel Elements*", Technical Information Center, Office of Public Affairs-Energy Research and Development Administration, 1976.

31. C.M. Mari, S. Pizzini, L. Manes and F. Toci, J. of Electrochem. Soc. Vol. **124-12** (1977), 1831.

32. F.T. Ewart, C.M. Mari, L.Manes, Hj. Matzke, F. Toci, R. Schreiber, J. Nucl. Mater. **81** (1979), 185.

33. F.T. Ewart, C.M. Mari, S. Fourcaudot, Hj. Matzke, L.Manes, F. Toci, Thermodyn. Nucl. Mater. 1979, vol. I, IAEA SM 236/07, 369.

34. Hj. Matzke, J. Nucl. Mater. **208** (1994), 18.

35. B. Lindemer and T. Besman, J. Nucl. Mater. **130** (1985), 473.

36. P.E. Blackburn, J. Nucl. Mater. **46** (1973), 244.

37. M. Tetenbaum and P.D. Hunt, J. Chem. Phys. **49** (1968), 4739.

38. T.L.Markin, V.J. Wheeler, R.J. Bones, J. Inorg. Nucl. Chem. **30** (1968), 807.

39. V.J. Wheeler, I.G. Jones, J. Nucl. Mater. **42** (1972), 117.

40. N.A. Javed, J. Nucl. Mater. **43** (1972), 219.

41. A. Pattoret, J. Drowart, S. Smoes, Thermodyn. Nucl. Mater. 1967, IAEA Vienna 1968, 613.

42. E.A. Aitken, H.C. Brassfeld, R.E. Fryxell, Proc. Symp. Thermodyn. Nucl. Mater., vol. II, IAEA, Vienna, 1966, 435.

43. M.G. Adamson and R.F.A. Carney, J. Nucl. Mater. **54** (1974), 121.

44. S. Aronson and J. Belle, J. Chem. Phys. **29** 1 (1958), 151.

45. K. Une and M. Oguma, J. Nucl. Mater. **110** (1982), 215.

46. F. Schleifer, A. Naoumidis and H. Nickel , J. Nucl. Mater. **115** (1983), 143.

47. D.I. Marchidan and S. Matei, Rev. Roum. Chim. **17 - 9** (1972), 1487.

48. D.I. Marchidan and S. Matei-Tanasescu, Rev. Roum. Chim. **18 - 10** (1973), 1681.

49. D.I. Marchidan and S. Tanasescu, Rev. Roum. Chim. **19-9** (1974), 1435.

50. D.I. Marchidan and S. Tanasescu, Rev. Roum. Chim. **20 - 11/12** (1975), 1365.

51. Y. Saito, J. Nucl. Mater. **51** (1974), 112.

52. T.L. Markin, L.E.J. Roberts and A. Walter, Proc. Symp. Thermodyn. Nucl. Mater., IAEA, Vienna (1962), 693.

53. K. Une and M. Oguma, J. Nucl. Mater. **115** (1983), 84.

54. A.T. Chapman and R.E. Meadows, J. Amer. Ceram. Soc. **47 - 12** (1964), 614.

55. K. Hagemark and M. Broli, J. Inorg. Nucl. Chem. **28** (1966), 2837.

56. P.E. Blackburn, J. Phys. Chem. **62 – 8** (1958), 897.

57. C. Picard and P. Gerdanian, J. Nucl. Mater. **99** (1981), 184.

58. A.T. Chapman, J. Brynestad, G.W. Clark, High Temp. High Press. **12** (1980), 447.

59. R.J. Ackermann, P.W. Gilles, R.J. Thorn, J. Chem. Phys. **25** (1956), 1089.

60. R.K. Edwards, M. S. Chandrasekharaiah, P.M. Danielson, High Temp. Sci. **1** (1969), 98.

61. J. Drowart, A. Pattoret, S. Smoes, Proc. Brit. Ceram. Soc. **8** (1967), 67.

62. M. Tetenbaum, P. D. Hunt, J. Nucl. Mater. **34** (1970), 86.

63. J. S. Punni and P.K. Mason, *UO_2 Oxidation and Volatilisation*, AEAT-1277, ST: MP (1997), 1.

64. Gmelin Handbook of Inorganic Chemistry, Springer Verlag Berlin 1986, *Uranium*, suppl. Vol. **C5**, Uranium Dioxide, UO_2. Physical Properties. Electrochemical Behaviour (1986), 74.

65. C.A. Alexander, J.S. Ogden, G.W. Cunningham, Report Battelle Memorial Institute (USA) **1789** (1967), 1 (cited by [62]).

66. V.E. Ivanov, A.A. Kroolich, V.S. Pavlov, *et al.* Thermodyn. Nucl. Mater. Proc. Symp., Vienna 1962 (1963), 733.

67. R.W. Ohse, P.G. Berrie, H.G. Bogensberger, E.A. Fischer, J. Nucl. Mater. **59** (1976), 112.

68. W. Breitung, K.O. Reil, Nucl. Scie. Eng. 101 (1989), 26.

69. R.W. Ohse, J.F. Babelot, C. Cercignani, J.P. Hiernaut, M. Hoch, G.J. Hyland, J. Magill, J. Nucl. Mater. **130** (1985), 165.

70. G.T. Reedy, M.G. Chasanov, J. Nucl. Mater. **42** (1972), 341.

71. R. Limon, G. Sutren, P. Combetter, F. Barbry in: Proceedings of the ENA / ANS Topical Meeting on Reactor Safety Aspects of Fuel Behaviour, Sun Valley, Idaho, USA, 2-6 August 1981, CEA-CONF-5816, American Nuclear Society **2** (1981), 2-576.

72. M. Bober and J. Singer, Nucl. Scie. Eng. **97** (1987), 344.

73. J.K. Fink, J. Nucl. Mater. **279** (2000), 1.

74. M. Bober, E.A. Fisher, Report Kern Forschungszentrum Karlsruhe (Germany) **13** (1981), 88.

75. J.F. Babelot, R.W. Ohse and M. Hoch, J. Nucl. Mater. **137** (1986), 144.

76. C. Wagner and W. Schottky, Z. Phys. Chemie **B11** (1931), 163.

77. I. Iosilevski, G. J. Hyland, C. Ronchi and E. Yakub, Int. J. Thermophys. **22-4** (2001), 1253.

78. M.A. Bredig, *Colloque Int. sur l'étude des transformations crystallines á haute témperature*, Odeillo 1971, 183.

79. J.K. Fink, M.G. Chasanov, L.Leibowitz, J. Nucl. Mater. **102** (1981), 17.

80. M.T. Hutchings, J. Chem. Soc. Faraday Trans. II **83** (1987), 1083.

81. J.P. Hiernaut, G.J. Hyland, C. Ronchi, Int. J. Thermophys. **14** (1993), 259.

82. C. Ronchi, J.P. Hiernaut, R. Selfslag, G.J. Hyland, Nucl. Sci. Eng. **113** (1993), 1.

83. C.Ronchi and G.J. Hyland, J. Alloys Compounds **213 / 214** (1994) 159.

84. J.H. Harding, D.J. Martin, P.E. Potter, *Thermophysical and Thermochemical Properties of Fast Reactor Materials*, Harwell Laboratory UKAEA Report EUR 12402, 1989.

85. C. Ronchi, M. Sheindlin, M. Musella and G.J. Hyland, J. Appl. Phys. **85** (1999), 776.

86. C. Ronchi, J. Phys.: Condens. Matter **6** (1994), L561.

87. D.G. Martin, J. Nucl. Mater. **152** (1988), 94.

88. F. Groenvold, J. Inorg. Nucl. Chem. **1** (1955), 357.

89. P. Perio, *Contribution to the Crystallography of the Uranium-Oxygen System*, Doctoral Dissertation, University of Paris, (1955) CEA-363.

90. W. Breitung, K.O. Reil, Nucl. Sci. Eng. **105** (1990), 205.

91. W.D. Drotning, in: *Proceedings of the Eighth Symposium on Thermophysical Properties,* Gaithersburg, MD, National Bureau of Standards 1981, 15- 18 June 1981.

Chapter 3

Techniques for high- temperature melting point measurements

3.1 Introduction

Much can be learned about a physico- chemical system if its thermophysical and thermodynamic properties are experimentally studied under extreme conditions, up to the limits of existence of the system itself. In this respect, the investigation of high-temperature and high-pressure regions has appeared particularly promising in the last decades, as more and more sophisticated experimental facilities have been developed. However, the high measuring accuracy and precision needed in order to rule out the risk of an inadequate interpretation of experimental results can be obtained by present-day techniques over a limited range of pressures and temperatures only. Such a range narrows even more if the behaviour of a certain substance is to be studied *simultaneously* at high-pressure and at high-temperature. Upon closer analysis of the experimental possibilities, one could estimate that present experimental investigation can be carried out up to hydrostatic pressures of about 1 GPa (≈ 10000 atm) and 10000 K [1]. Much higher pressures (tens of GPa) can be reached by means of diamond anvil techniques (e.g. [2]) but under such conditions accurate temperature measurements are practically impossible.

The experimental method developed in this work constitutes a challenge to the high-temperature high- pressure range. Such a method is aimed at investigating the melting behaviour of refractory materials, in particular of non- stoichiometric uranium dioxide, characterised by strongly non-congruent evaporation at high temperature. The experimental

setup was developed in order to optimise the measuring conditions. Measurements under high buffer gas pressure were found adequate to face incongruent evaporation. Moreover, measurements had to be carried out under containerless conditions in order to avoid any contamination of the sample. As for the choice of a suitable heating technique, laser heating was finally chosen as the most convenient method. The present chapter contains a brief introduction to the experimental determination of the melting behaviour of materials in general. Some available methods of melting investigation are described in order to give an idea of the scenario in which the technique employed in this work was devised.

Previous attempts to measure the melting / freezing transition of both stoichiometric and non-stoichiometric uranium dioxide are then described. Limits and difficulties of the methods employed in such attempts are identified, and used in developing a suitable new experimental technique.

The experimental method finally devised and used in this work is then described in detail in the next chapter.

3.2 Available methods of melting investigation

The accuracy with which a phase diagram is experimentally determined largely depends on two main issues: the accuracy in the measurement of temperature and the accuracy in the characterisation of the sample composition at the exact moment when the phase transitions occur.

In principle, any physical or chemical difference among phases or effects occurring on the appearance or disappearance of a phase can be employed to determine phase equilibria.

Measurements can be performed under static or dynamic conditions.

In static methods the sample is held under specific conditions (temperature, pressure, volume) until equilibrium is reached, then the number and composition of the phases present are determined. This can be done either by measurements at temperature (e.g. with high

temperature X-ray diffraction or microscopy) or by quenching the system so rapidly that the high temperature phases are maintained for examination at room temperature. Measurements at temperature are feasible only in systems stable enough not to decompose before reaching equilibrium conditions. On the other hand, the method of quenching is feasible only when the diffusion phenomena controlling the formation of the crystalline phase are slow enough to be "frozen" by the practicable cooling rate (e.g., as in the case of silicates).

Systems like hyperstoichiometric uranium dioxide do not meet any of the requirements for static methods to be feasible, as this material tends to decompose by fast incongruent evaporation at high temperature, and oxygen diffusion occurs too rapidly for quenching to be feasible. Thus dynamic methods have to be used for substances of this type.

Dynamic methods detect changes in the properties of a system when the system itself is cooled or heated (or its pressure changed) so that new phases appear. Thermal analysis is the most used dynamic method of this kind. In such a method, the temperature at which a certain phase transition occurs is determined by detecting the changes in the rate of the sample heating or cooling caused by the latent heat of reaction. Changes brought about by the phase transition in other properties, such as electrical conductivity, thermal expansion, radiant emissivity /reflectivity etc. can also be used.

3.2.1 Thermal analysis

In condensed materials, phase changes are generally characterised by absorption or release of latent heat (ΔH_t) that stems from the discontinuity in the state functions over the transition. For instance, a latent heat of melting (ΔH_m) is absorbed by a material that melts, and released upon freezing. When a sample is heated or cooled through a structural transition, a thermogram describing the temperature of the specimen as a function of time will show either a change in gradient or a complete thermal arrest, depending on the variance of the system under investigation.

According to Gibbs' phase- rule, the variance of a system, i.e., the number of intensive variables necessary to fully describe the state of the system, is given by

$$V = C + 2 - P, \tag{3.1}$$

C being the number of independent components of the system and P the number of coexisting phases. If one of the intensive variables is fixed, like pressure in the experiments reported in this work, Eq. (3.1) becomes

$$V = C + 1 - P. \tag{3.2}$$

During the melting / freezing process, two phases coexist and $P = 2$. In the case of a single-component or any congruently melting material, $C = 1$ and $V = 0$ on melting, therefore temperature must stay constant over the whole phase transition. Fig. 3.1a shows a typical equilibrium thermal arrest corresponding to freezing of a congruent-melting material.

The situation is somewhat more complicated when the material is not homogeneous, i.e., when it contains more than one component. In this case, liquid and solid will in general coexist in equilibrium with different compositions, and in the phase- rule as written in Eq. (3.2) $C = 2$ will yield $V = 1$. This means that the temperature does not remain constant when liquid and solid coexist, although the thermogram slope will decrease during the phase transition due to the absorption (on melting) or release (on freezing) of the latent heat (Fig. 3.1b). Thus the melting/freezing transition will occur over a range of temperature, rather than at a definite point. On the heating stage of an experiment, the temperature at which the first drop of liquid appears is called the *solidus*, whilst the temperature at which the whole specimen becomes liquid is the *liquidus*. During the cooling stage of a liquid mass, at the *liquidus* temperature the first nucleus of solid forms in the molten pool, and at the *solidus* the last drop of liquid freezes over. At thermodynamic equilibrium, the phase transition temperature constitutes an invariant of the material under investigation, but structural changes often show temperature hysteresis or thermal lag.

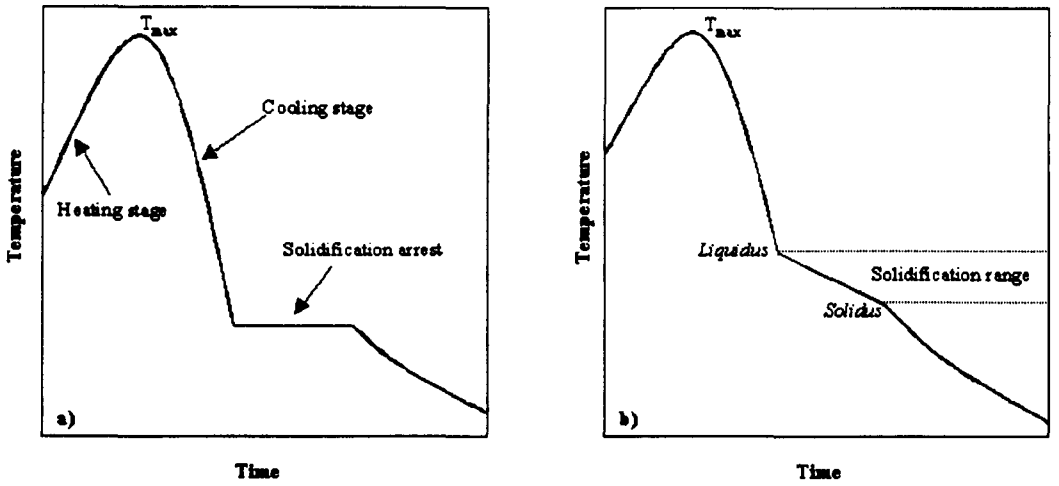

Fig. 3.1: Thermograms showing the solidification (freezing) transition. a) Single-component or congruently melting sample. b) Non-congruently melting sample. V = variance of the system.

A well-known example, given in [3] is that of liquid tin. The freezing temperature of tin is known with great precision to be 505.05 K, the temperature at which a thermal arrest would be observed on slow cooling of the specimen. In actual practice, however, it is always possible to cool liquid tin for 20 or 30 K *below* the equilibrium freezing point before crystallisation begins, depending on the speed of cooling. This phenomenon, called *supercooling* or *undercooling*, is due to the fact that crystallisation proceeds from small nuclei of the solid phase. If the equilibrium freezing temperature is indicated with T_m, whenever an embryo of solid is formed within the melt at $T \leq T_m$, the new phase will be characterised by a volume free energy g_s smaller than the free energy of the liquid g_l. However, the superficial tension of the newly formed solid nucleus, having large surface-to-volume ratio, will lead to a positive free energy contribution g_{sup}. Therefore, the total free energy of the solid nucleus will be given by $g_{tots} = g_s + g_{sup}$, and at each temperature $T \leq T_m$ there will be a critical nucleus size below which the spontaneous growth of the new solid phase does not occur, because $g_{tots} \geq g_l$. Supposing that the solid nuclei are spherical, the critical radius size as a function of temperature is given by

$$r^* = \frac{2\gamma_{sl}T_m}{\Delta H_m(T_m - T)}, \tag{3.3}$$

where γ_{sl} is the solid-liquid interfacial free energy and ΔH_m the latent heat of melting [4].

The critical nucleus size tends to infinity at the equilibrium melting temperature, but decreases rapidly as the temperature falls. Producing solid nuclei larger than the critical size requires a certain characteristic time depending on the speed of diffusion from the liquid into the solid phase. There is thus a range of temperatures lower than, but very close to T_m where the phase transformation proceeds extremely slowly or not at all unless crystal nuclei are somehow introduced. Nucleation is usually heterogeneous, promoted by impurities or by the walls of the vessel containing the sample; homogeneous nucleation can occur, resulting from free energy fluctuations in the liquid, only when the impurity concentration is extremely low. The described phenomenon of undercooling is an important source of error if a cooling thermogram is to be used in order to determine the equilibrium freezing point of a material, and must therefore be avoided. Depending on the interfacial energy and the speed of diffusion typical of each system, in most materials (and uranium dioxide among them) undercooling can be prevented by a simple reduction of the cooling rate. However, in some cases- for instance in the case of tin- this is not sufficient, and it may be necessary to induce crystallisation by the introduction of small particles of solid in the liquid. Fig. 3.2a displays a thermogram where undercooling precedes the freezing plateau in a congruently- melting sample.

When a homogeneous material is heated, the liquid formation will not proceed by this nucleation scheme, and will therefore occur at the true equilibrium melting point, without any "superheating".

Also in a multi- component system characterised by *solidus* and *liquidus* transitions the freezing process can be affected by undercooling, depending on the kinetics of nucleation of the solid phase (Fig. 3.2b).

Fig. 3.3a illustrates a system in which a solid state solubility gap intersects the *liquidus* and *solidus* lines. For the sake of simplicity, we discuss in such a case the cooling of the liquid only. During the freezing process, when the system reaches the temperature at which the formed solid exists as a mixture of two distinct phases α and β, the number of phases in Eq. (3.3) becomes $P = 3$, yielding $V = 0$. Therefore a thermal arrest will be observed, as temperature must stay constant up to completion of freezing (Fig. 3.3b). The line on the phase diagram corresponding to such a constant temperature is the *monotectic*. Monotectic lines occur in many systems, included the system uranium-oxygen (see previous chapter).

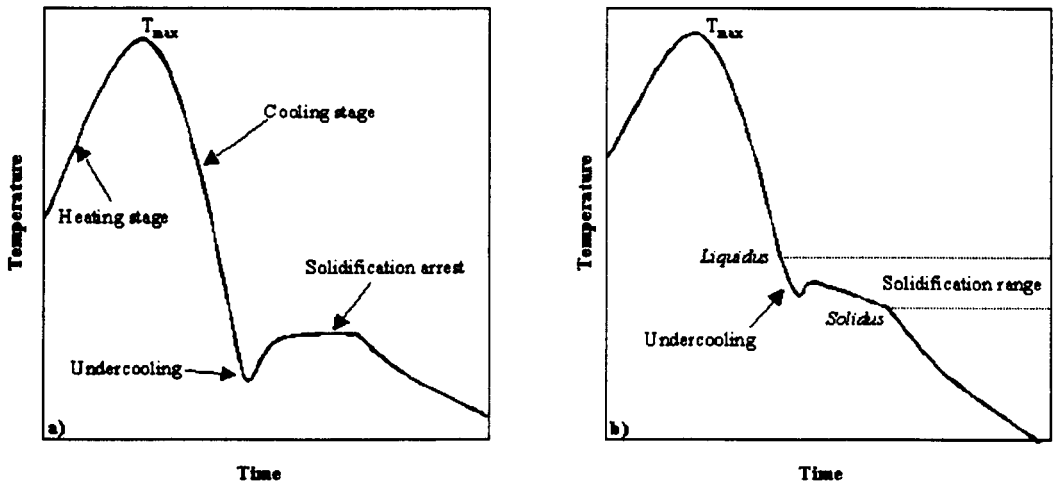

Fig. 3.2: Thermograms showing undercooling upon the freezing transition.
a) Single- component or congruently melting sample. b) Non-congruently melting sample.

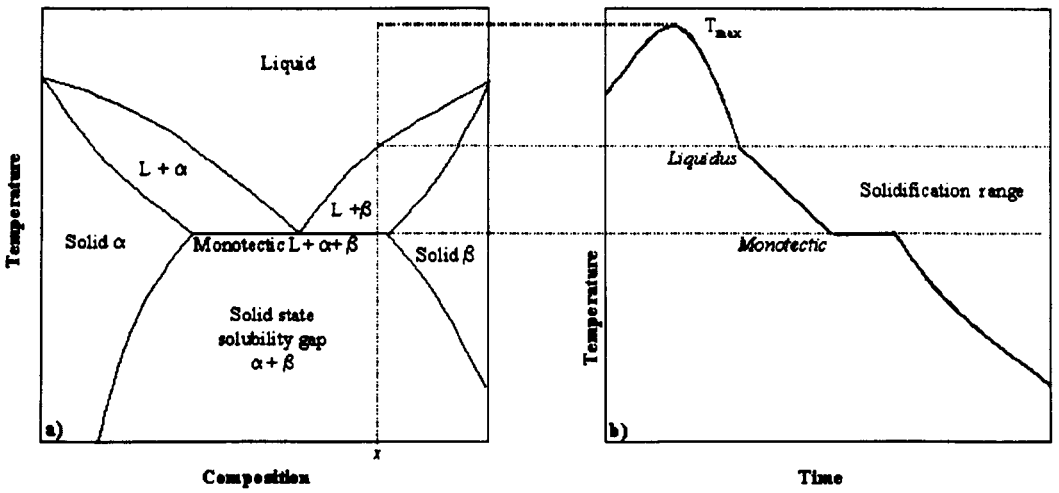

Fig. 3.3: a) Phase diagram showing a solid state solubility gap with monotectic line.
b)Thermogram showing the freezing transition in a sample of composition *x*.

3.2.2 Thermal arrest techniques

Phase transitions in condensed materials are determined through thermal arrest techniques by detecting the exact temperature at which the inflection occurs at a given sample composition. Reviews of experimental methods for determining the melting / freezing point of materials are given in [3] and [5].

In general, every material presents peculiar problems to be solved in order for its high-temperature phase transitions to be measured, and often experimental methods have to be devised *ad hoc* for a certain kind of substance, without being applicable for any other. So universal methods do not exist. Nonetheless, most of the traditional methods have common features.

In traditional thermal arrest techniques employed for metallic alloys and refractory materials melting below ~2700 K, electrical furnaces are normally used as heat sources. Direct high-frequency inductive heating furnaces can be used if the sample has sufficient electrical conductivity, or by use of a suitable metallic susceptor when a non-conductive sample is to be measured. In metallic samples, the use of inductive furnaces implies the advantage that the variable electromagnetic field induced in the specimen also acts as a stirrer of the liquid phase after the onset of melting. Stirring of the liquid is a key issue to ensure homogeneity of the process, and it must be provided by some other means when an inductive furnace cannot be employed. Temperature can be measured by means of suitable thermocouples, or with optical pyrometers, but only the latter systems are applicable above 2500 K. In this case, the specimen and the sample holder should be shaped in such a way that blackbody conditions be reproduced (optical emissivity as close as possible to unity). When a thermocouple is implemented, the melting points of the component metals and possible contamination of the specimen represent further problems. Suitable shields should be added to the system in order to minimise radiative thermal losses. Moreover, in many cases the measurements should be performed under vacuum or inert gas in order to maintain the composition of the specimen.

Measurements at high pressure are in general difficult with this kind of method, although Basset [6] and, later, Noda [7] managed to measure the melting point of graphite. Both authors used a complex furnace where it was possible to set internal buffer gas pressures up to 1 GPa, and to heat a graphite sample by direct electrical heating (DEH).

More sophisticated experimental techniques of thermal analysis have been developed in the last thirty years, operating under containerless conditions.

Levitation techniques appear to be the only steady- state methods of investigating the properties of refractory materials around their melting point under containerless conditions. Several levitation systems, in which it may be possible to melt and freeze materials, have been reported. These are based upon hydrodynamic (e.g. [8-12]), acoustic (e.g. [13-15]) and electromagnetic (e.g. [16-18]) techniques. In all these methods, a small specimen (usually bead-shaped of diameter 1-5 mm) is levitated at some 0.5 to 1 mm, avoiding contact with any external container. The sample is heated in a radiant furnace [14] or by means of a laser source [18], and its temperature detected by optical pyrometry. Levitation methods can be employed to determine thermophysical properties as well as phase boundaries of several classes of materials. Skaggs [11] reports that the melting boundary of a specimen can be well detected with this technique by visual examination, and this point makes levitation methods suitable for the melting point investigation, provided the sample emissivity differs significantly between solid and liquid state. An interesting study on thermophysical properties of containerless liquid iron aerodynamically levitated has been recently performed by Willie *et al.* [19].

A technique often used to bring a levitating sample to high temperature is *solar image heating* (see, for instance, [1 and 9]). Such a technique is illustrated in Fig. 3.4. The method is also applicable to samples contained in normal holders rather than levitating under containerless conditions.

The sample is placed at one of the foci of an ellipsoidal reflecting shell, the inner wall of which has a reflectivity close to one.

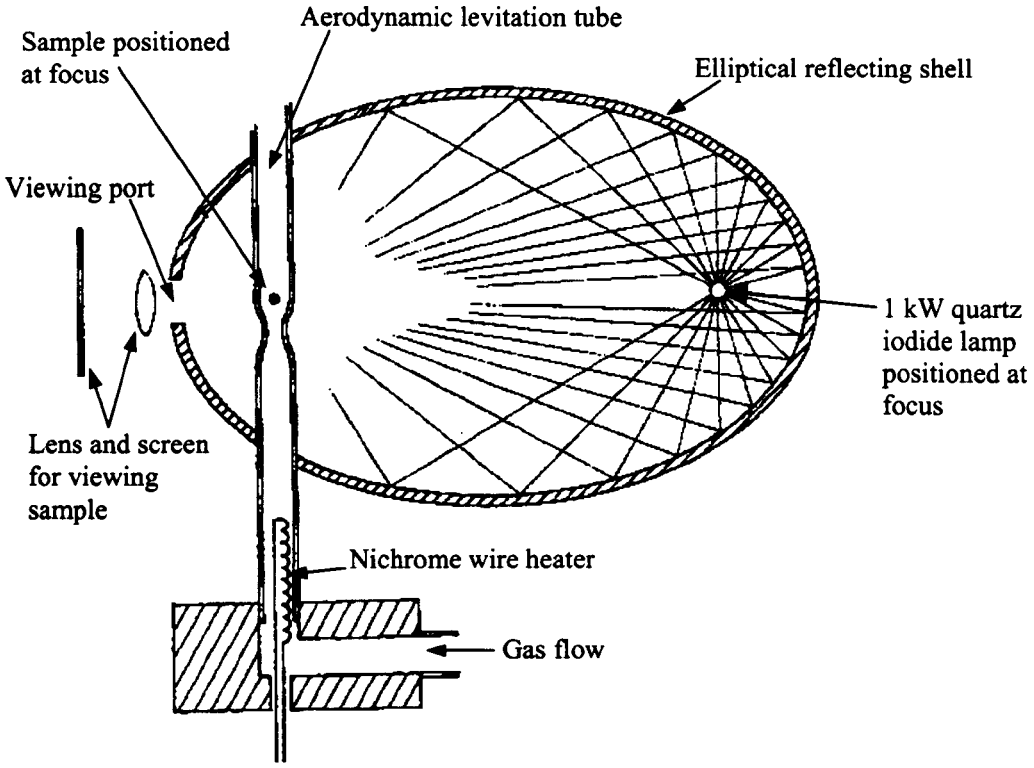

Fig. 3.4: Schematic of a solar image heating technique applied to samples aerodynamically levitated (after [10]).

A high- power lamp is set at the other focus of the ellipsoid. In this way, the light emitted by the lamp is concentrated on the sample, which can be heated up to several thousands of degrees Kelvin. This method presents several advantages. The sample can be heated without any electrical current crossing it, so the technique can be used equally for conductors and insulators. Experiments can be conducted under high pressure, and the specimen can be kept at high temperature under static equilibrium conditions, as there is in principle no time limit for the duration of an experiment. All these point seem to put forward the solar image heating as a good candidate technique for the investigation of the melting behaviour of uranium dioxide under high pressure. However, such method has a significant drawback in the fact that the sample is heated by white light that mixes up with thermal radiation emitted from the hot specimen. This latter point seriously inhibits the pyrometric measurement of temperature, and for such a reason the solar image heating technique was finally not used in

this work. Moreover, the main limitation of levitation techniques is the unfeasibility of measurements under pressures higher than some MPa [1]. This constraint makes any levitation method inapplicable to the experimental study of uncongruently vaporising materials. Thus levitation has to be excluded from the list of possible techniques applicable to containerless conditions in the investigation of hyperstoichiometric uranium dioxide.

Conventional steady- state and quasi steady- state techniques for measuring thermophysical properties are generally limited to temperatures below 2500 K. This limitation is due to problems (chemical reactions, heat losses, evaporation, specimen containment etc.) arising from the exposure of the sample at high temperature for the extended periods of time required to reach equilibrium conditions. The use of dynamic techniques permits a drastic reduction in the experiment duration, hence minimising the above problems. One of the most frequently used dynamic techniques for the investigation of refractory materials at temperatures near the melting point is the method of the *exploding wire*. In this DEH method, extensively described in a review by A. Cezairiliyan [20], a high-density current pulse passes through a wire- shaped sample that is heated by the Joule effect. The measurement system, schematically shown in Fig. 3.5, consists of an electric power- pulsing circuit and associated high- speed measuring circuits, able to detect current through and potential difference across the specimen with appropriate time resolution. The sample temperature is also measured, generally with a high- speed pyrometer. If measurements other than thermal analyses are to be performed with this method, additional variables will have to be detected (specific heat, heat capacity, electric resistivity, emissivity, thermal expansion etc.). The exploding wire technique allows performing measurements at high temperature and high pressure simultaneously. Furthermore, with such a technique the whole volume of the sample can be heated in a homogeneous manner, minimising undesirable temperature gradients. In spite of these clear advantages, such a method has important restrictions, as pointed out by Sheindlin [1].

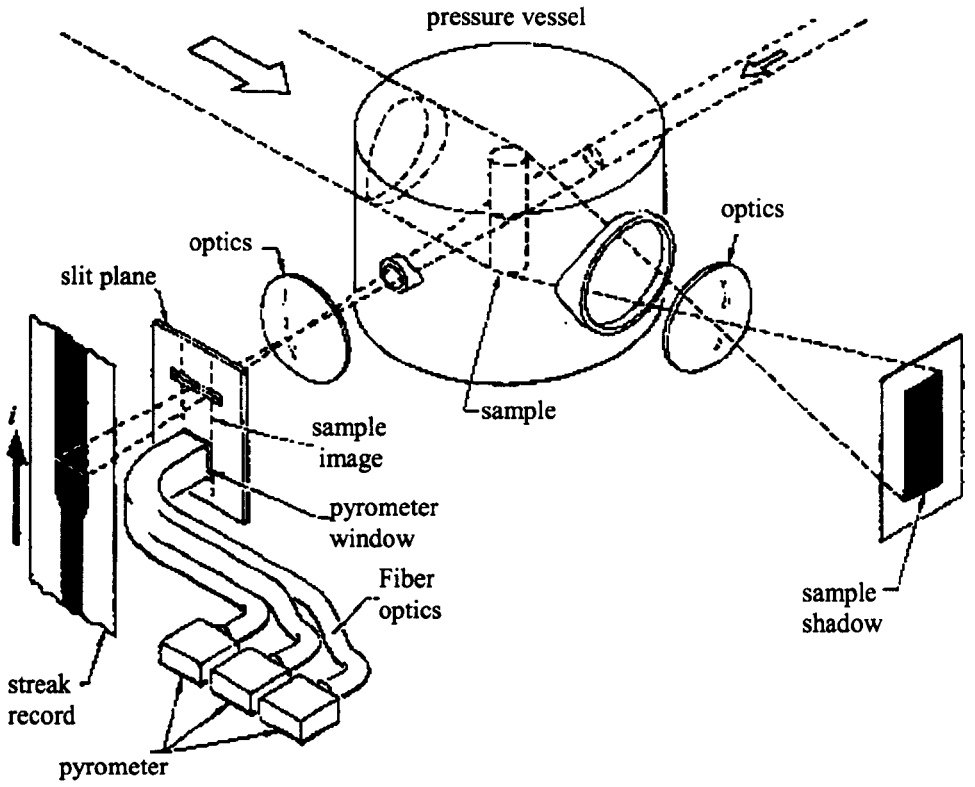

Fig.3.5: Schematic view of a typical wire explosion apparatus used by Gathers *et al.* [27].

The main restriction is obviously the need for the investigated material to be a homogeneous electrical conductor, and this made the method hardly applicable to ceramics. For uranium dioxide a heating technique had to be selected not involving the direct passage of electrical current through the sample. In fact, although uranium dioxide can be considered a semiconductor (conducting band- valence band gap $\approx$ 4 eV), heating by the Joule effect would involve the consumption of prohibitively high power.

Thermal arrest techniques are suitable for the measurement of the *liquidus* from the cooling thermogram. The *solidus* transition is preferably determined on the heating stage of an experiment, as undercooling and diffusion phenomena in the liquid may significantly alter the measurement during the cooling stage. However, in both cases equilibrium conditions and homogeneity of the material have to be ensured if very accurate measurements are to be made, and microscopical analysis of the samples is necessary, either at temperature or on

quenched specimens, in order to obtain accurate results. On the other hand, as stated above, this kind of *static* microscopical analysis is not feasible on high- temperature unstable materials or on substances characterised by fast diffusion phenomena. Finally, a simple thermal arrest technique alone cannot provide sufficient information in the investigation of unstable materials. In this case the analysis should always be completed with data obtained by some other independent technique.

3.2.3 Miscellaneous methods for determination of the liquidus

Liquidus determination based on changes produced by the phase transition in properties such as electrical conductivity, thermal expansion, radiant emissivity / reflectivity etc. is not feasible. A simple technique to determine the *liquidus* temperature of a substance can be realised by heating samples small enough (some tens of mg) for their complete melting to be directly observable via a long-distance-operating microscope. This technique was used by Bates [21] and by Bannister [22] in early studies on the melting point of hypostoichiometric uranium dioxide.

Another method for *liquidus* determination not based on a thermal arrest technique is reported in [3] as the method of cooling and sampling (Fig. 3.6). A liquid specimen is kept at a certain temperature between *liquidus* and *solidus*, and stirred properly, until equilibrium conditions are realised. In such conditions, liquid of composition *a* coexists with solid of composition *b*, and the two phases can be separated and independently analysed to obtain the *liquidus* and *solidus* curves. However, the separation procedure can present insurmountable difficulties at high temperature, therefore this technique can only be used for low-melting alloys and for amalgams.

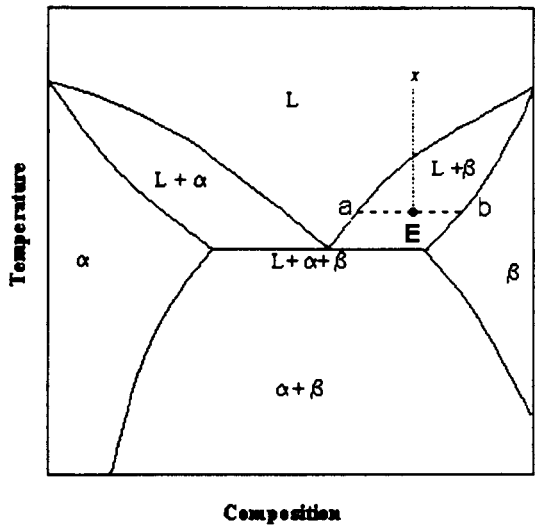

Fig. 3.6: Method of cooling and sampling: a liquid sample of composition *x* is cooled to the point E until equilibrium is reached with the coexistence of liquid *a* and solid *b*. Liquid is then removed and analysed (after [4]).

A novel method of *liquidus* determination was devised within the present work for the investigation of hyperstoichiometric uranium dioxide. A technique was developed, suitable for both *solidus* and *liquidus* determination in substances with very high melting point. This technique, described in detail in § 4.3.7, is based on detection of the reflectivity variation of the sample surface when the first liquid drop is produced on heating and when the first solid seed is formed on cooling.

3.2.4 Miscellaneous methods for the determination of the solidus

Contrary to the *liquidus*, in the *solidus* transition the first appearance of liquid phase when a sample is heated can be observed and detected in several ways, as it normally brings about a significant variation of most of the material properties.

An effective though rather old technique for determining the *solidus* temperature for electrical conductors is the Pirani and Alterthum method of directly observing the first formation of a liquid phase [23]. In this technique, the sample consists of a rectangular or cylindrical bar of metal heated by an electric current. A small hole is bored into the centre of

the bar, normal to its length (Fig. 3.7), so that the greatest heating takes place near the hole where the cross-section is the least, and the current density maximum. The centre of the hole is observed with an optical pyrometer. The hole can be considered to be with good approximation a black body, and will appear brighter than the rest of the sample if the temperature of the bar is increased. When the fusion point is reached, a drop of molten metal will be formed inside the hole, drastically reducing its emissivity, and making it appear dark. If a thermogram is drawn from the pyrometer reading, the last temperature at which no liquid (i.e., no hole darkening) could be seen should be taken as the *solidus*. The Pirani method was successfully used for high- melting platinum- tungsten [24], molybdenum- carbon [25] and thorium- carbon [26] alloys. Although this method is only applicable to conductive materials, and therefore not to uranium dioxide, it represents an interesting example of fusion point determination from direct observation of changes induced in the sample during the transition. In principle, a similar method could be used for non-conductive materials provided a different heating agent is employed.

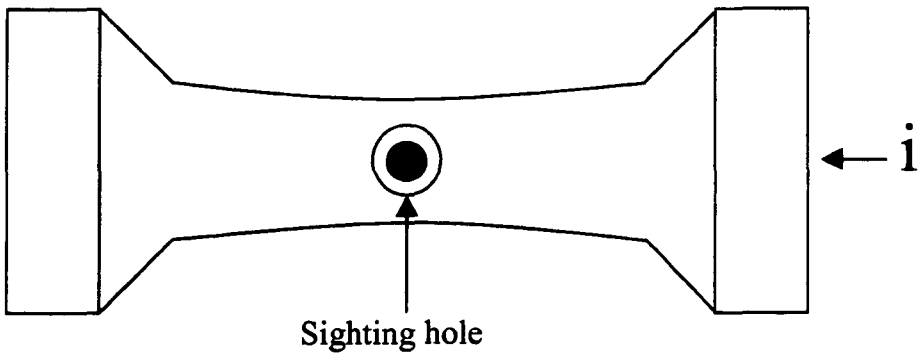

Fig. 3.7: Pirani method for the visual determination of *solidus*.

3.2.5 Previous studies on the melting behaviour of uranium dioxide

Experimental studies already performed on the melting behaviour of uranium dioxide were listed in the previous chapter. Bates [27] studied the lower *solidus* line for the hyperstoichiometric oxide by a static method based on the microscopical observation of quenched samples. Martin and Edwards [28] determined the lower *solidus* with better precision by employing an "equilibration technique" in which molten uranium metal was equilibrated with uranium dioxide. The composition obtained was then quenched to room temperature and analysed. It is worth recalling here that in the hyperstoichiometric oxide the very fast oxygen diffusion makes quenching practically impossible.

At higher temperatures, the melting boundary for the hypo-stoichiometric oxide was studied in previously mentioned papers by Bates, Bannister and by Latta and Fryxell [29].

Both Bates and Bannister used an electric tungsten V-shaped filament furnace under purified inert atmosphere. Bates measured the filament temperature by means of an optical pyrometer, whilst in Bannister's work the specimen temperature was kept under control by calibrating the furnace power. In both cases, the use of small ($\leq$ 100 mg) samples permitted the visual determination of the total liquefaction point at several compositions. In Bates' paper it is not clear whether this point should be regarded as a *solidus* or as a *liquidus*. Bannister clearly indicated the total liquefaction point as the *liquidus*, and then used two different empirical methods to determine the *solidus*. In the first, specimens of approximately 100 mg were positioned just above the base of a V- filament furnace wedge so that any liquid formed would flow down into the base. In the second technique specimens were heated until some liquid had appeared, then the liquid was left to vaporise at a constant temperature. Upon total disappearance of the liquid phase, the solid phase left had a composition equal to the *solidus* composition at the annealing temperature. Such a composition was determined by measuring its *liquidus* temperature, as the material volume was too small to permit any chemical analysis. This latter method was less accurate because

solidus points were influenced by errors in the *liquidus* curve. If both Bates' and Bannister's methods were somewhat empirical in nature, the only existing systematic study on melting of both hypo- and hyper- stoichiometric uranium dioxide samples was made by Latta and Fryxell with a traditional thermal-arrest technique. Although Latta and Fryxell's work was already presented in the previous chapter, a more detailed description of their experimental technique is at this point suitable in order to emphasize the difficulties associated with the uranium dioxide system at high temperature.

Latta and Fryxell built special equipment to conduct their experimental study with a traditional thermal arrest technique in order to create conditions as close to equilibrium as possible despite the very high temperatures involved and the poor stability of the investigated substance. Fig. 3.8a shows a sketch of their melting point furnace. The furnace was designed in order to have a homogeneous temperature over the entire body of the specimen whilst still retaining the ability to change temperature slowly or rapidly by means of an induction generator coupled by a copper coil to a current concentrator. The specimen was held in an isothermal chamber, consisting of a tungsten susceptor, tungsten end plates, and a number of tungsten heat shields. Heat was generated in an almost uniform manner in the hollow cylindrical susceptor, and its end caps by a low frequency electromagnetic field from the copper coil. Samples used were nuclear grade urania pellets approximately 2 cm in diameter by 3 cm height. A blackbody hole with depth / diameter ratio 9:1 was drilled on the sample upper surface. Specimens were then sealed in tungsten or rhenium capsules, of the type shown in Fig. 3.8b, in order to avoid long exposure to high temperature and massive evaporation. The resulting specimen capsule was placed in the centre of the susceptor, and thereby heated both by inward radiation from the susceptor and by the electromagnetic field. The temperature was measured by means of an automatic optical pyrometer focused on the sample black body hole. Measurements were carried out with a downward flow of an argon-hydrogen mixture at room pressure. The calibration of the pyrometer yielded an uncertainty of approximately ± 0.1% between 2100 and 3000 K. The power input to the furnace was

programmed to give linear heating and cooling on an empty capsule, so that in presence of a sample a change in slope of the recorded thermogram occurred at the inception of a phase change (fusion or solidification). Each sample was submitted to three to six heating/cooling cycles in the temperature range of 50 to 100 K below and above the expected *solidus* and *liquidus* points. Each cycle lasted about 30 minutes, thus during an experiment the sample was exposed to temperatures above 2300 K for several hours. The observed thermal arrest temperatures were averaged over all the cycles on a single specimen. The system was successfully calibrated by measuring the melting points of alumina, molybdenum and tantalum. A typical thermogram of those measured by Latta and Fryxell in stoichiometric UO_2 is shown in Fig. 3.9. A clear inflection accompanies both melting and freezing processes. The fact that an inflection is observed over a temperature range instead of a plateau at constant T gives an idea of the importance of thermal gradients in the sample.

Fig. 3.10 shows the graphical method used by Latta and Fryxell to determine *solidus* and *liquidus* points from a thermogram by minimising the indeterminacy due to thermal gradients across the sample.

Results were obtained by Latta and Fryxell on UO_{2+x} samples with $-0.5 < x < 0.20$. The phase diagram obtained near the melting temperature is reproduced in Fig. 3.11.

As already pointed out in § 2.1.2, this thermal arrest technique gave reliable results in the hyperstoichiometric part of the phase diagram, but *solidus* and *liquidus* measured at hyperstoichiometric compositions were doubtful, basically due to the poor chemical stability of the compound. Latta and Fryxell performed a detailed characterisation of the tungsten-encapsulated hyperstoichiometric urania samples after the melting experiments by means of x- ray and ceramographic analyses. Tungsten contamination up to 5.56 % wt. was detected. A ternary oxide U_xWO_3 was extensively formed, and the remaining pure urania phase had, according to the XRD analysis, perfectly stoichiometric composition. This last point was of great importance, as it indicated that, besides the W contamination, the whole amount of excess oxygen had either reacted with the crucible or evaporated.

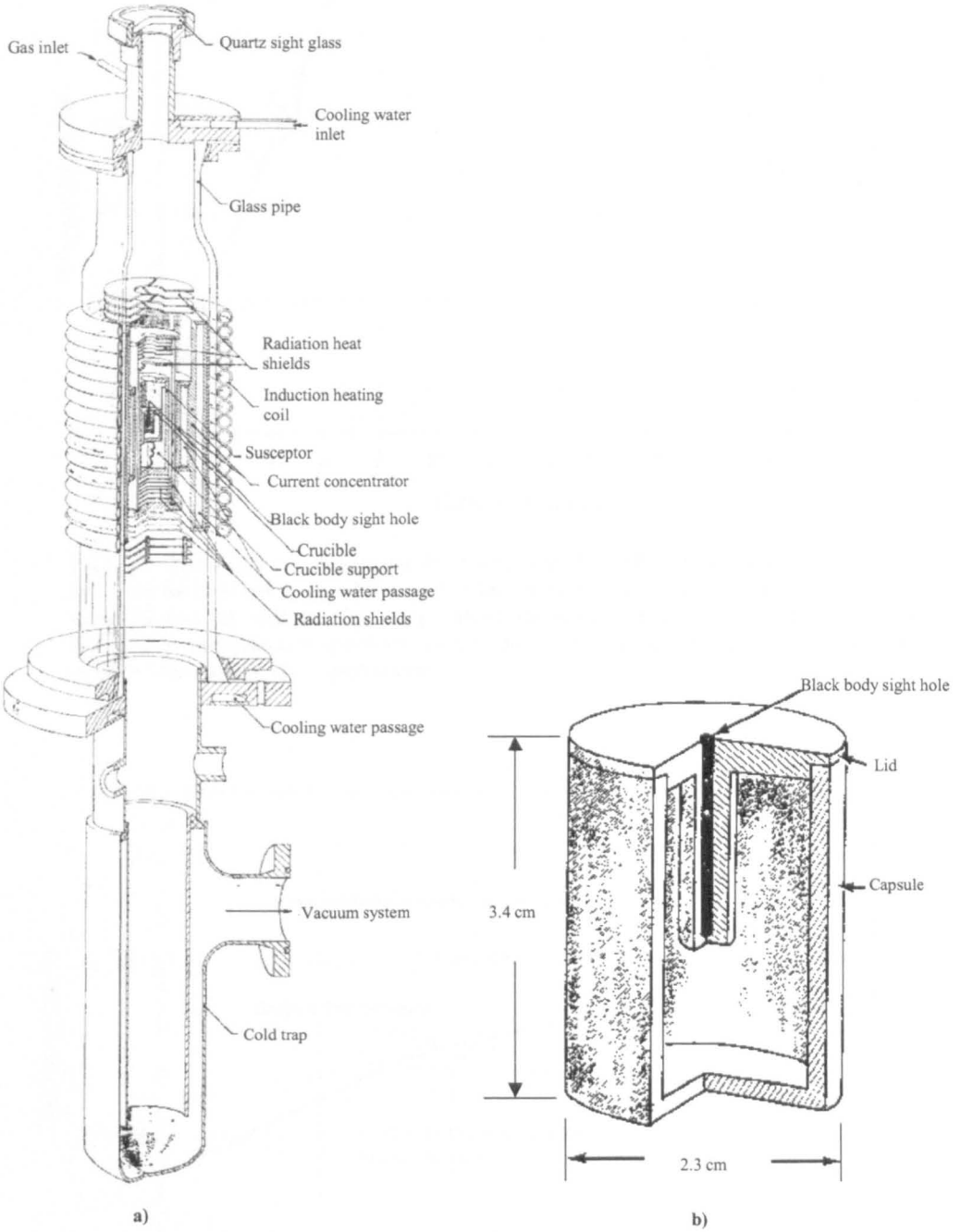

Fig. 3.8: a) Furnace used by Latta and Fryxell [29] for the determination of the *liquidus* and *solidus* lines of uranium dioxide via a traditional thermal arrest technique. b) Standard tungsten capsule sample holder used by the same authors.

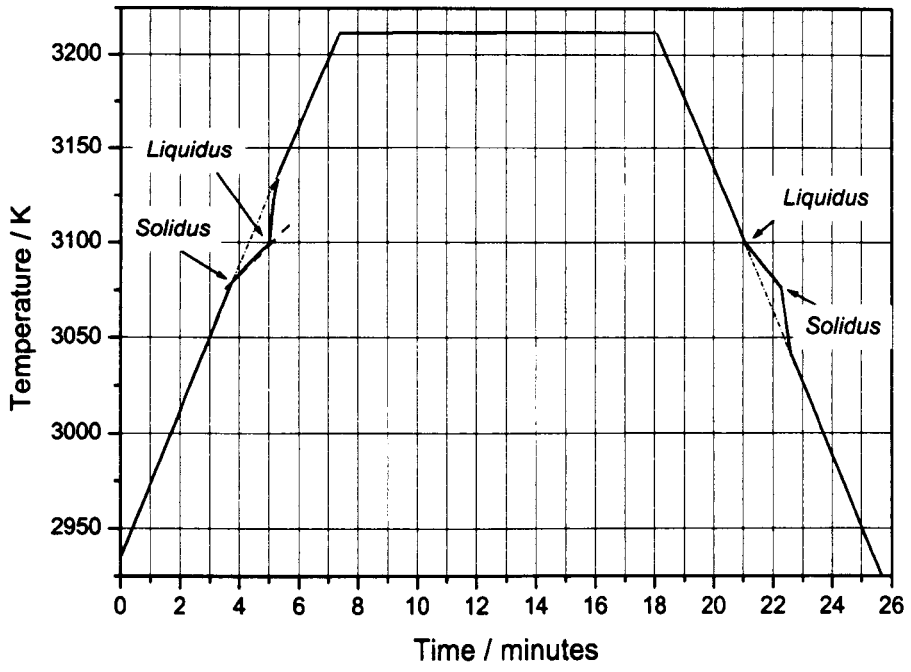

Fig. 3.9: Thermogram registered by Latta and Fryxell [29] on one heating-cooling cycle performed on a stoichiometric UO_2 sample. Three to six similar cycles were repeated on each sample. The temperature gap observed between *solidus* and *liquidus* was due to temperature gradients across the specimen, and to changes in the sample composition during the experiments.

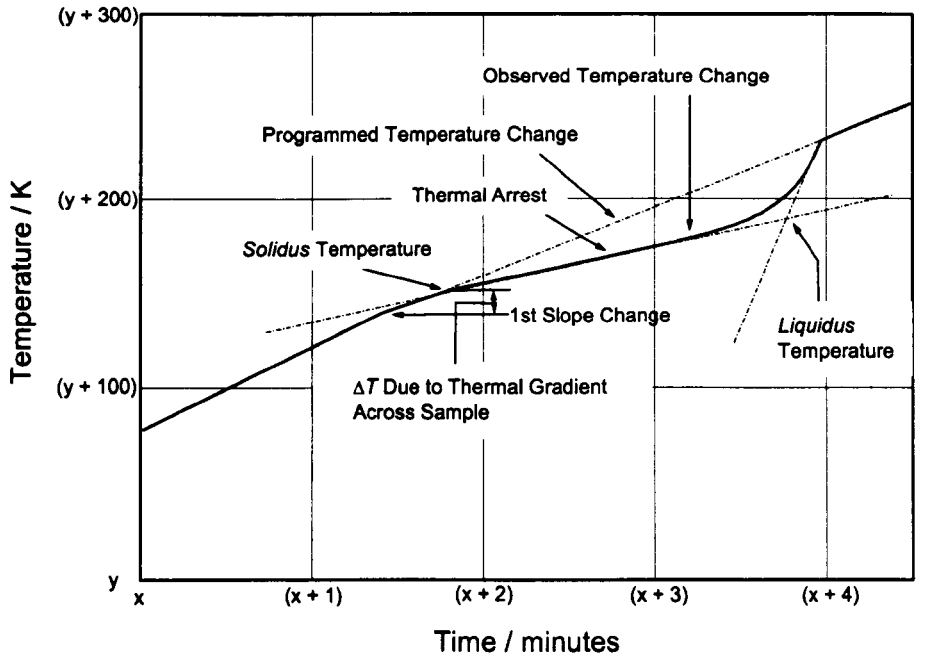

Fig. 3.10: Typical thermal arrest observed by Latta and Fryxell on heating, showing pre-curvature due to thermal gradient over the sample.

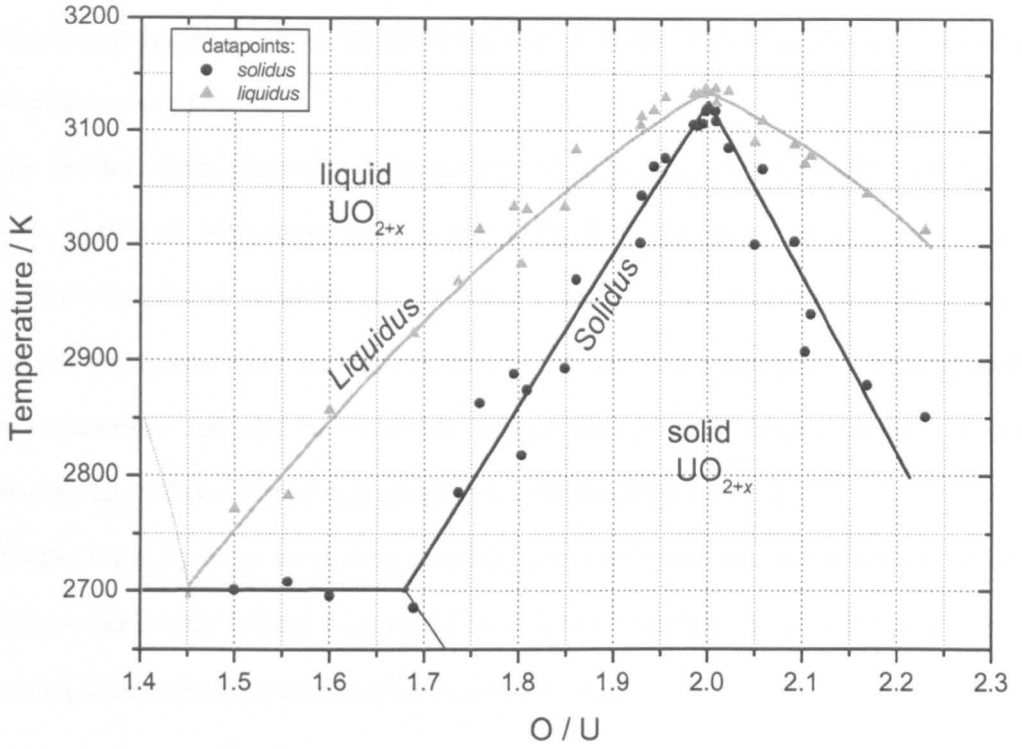

Fig. 3.11: UO_{2+x} *Solidus* and *Liquidus* lines as measured by Latta and Fryxell [29].

Moreover, it was not possible to determine at which stage of an experiment sample contamination and oxygen losses started. Possibly, these phenomena mostly occurred when the sample was liquid. However, at high temperature hyperstoichiometric uranium dioxide exhibits a high non-congruent evaporation rate even in the solid state (see, for example, Fig. 2.8), and the specimen could be significantly altered even before the first onset of melting, due to the long dwell- time at temperatures well above 2000 K. In these conditions, the rather slight, sometimes hardly detectable, thermogram inflection used by Latta and Fryxell to determine the *solidus* transition could be misleading. Samples sealed in rhenium capsules were less contaminated after melting, and also oxygen losses were minimised compared to those detected in W-contained specimens. Although Re was known to be more inert to both urania and oxygen, a Re contamination up to 2% was measured in molten samples. Moreover, one should not forget that in no case could the dynamics of oxygen evaporation/ diffusion during the experiments be determined. In fact, due to the very fast oxygen diffusion

rate in hyperstoichiometric uranium dioxide, specimen characterisation conducted after the experiments could be only partly indicative of the real state of the sample during the actual melting/freezing process.

The fact that results obtained by Latta and Fryxell on Re-encapsulated samples were in fairly good agreement with those from W-encapsulated specimens could be regarded as a confirmation of their reliability. On the other hand, such an agreement could alternatively indicate that in both cases results were strongly affected by the alteration of the samples due to uncontrolled diffusion of the excess oxygen during the prolonged exposure to high temperature, independently of the containing metal contamination rate.

Finally, due to the large uncertainty affecting Latta and Fryxell results, the development of a novel experimental method was needed in order to investigate in an alternative way the melting behaviour of hyperstoichiometric uranium oxide.

3.3 Conclusions

The investigation of the melting behaviour of chemically non- invariant refractory materials entails a number of experimental issues, as testified by experimental difficulties encountered in previous studies:

- A container is needed to hold the sample in the liquid state without contaminating it. Alternatively, a containerless method should be devised.
- Conditions should be created, which minimize any incongruent evaporation and sample decomposition at high temperature.
- An appropriate heating agent has to be chosen compatible with the optical temperature measurement.

With electrically non-conducting sample materials the listed requirements are met using laser heating only.

In laser melting techniques, a zone of the sample surface is subjected to strong heating by means of a high- power laser beam. In this way controlled melting under self-containment conditions can be obtained and the problem of sample contamination, that affected the measurements performed by Latta and Fryxell, solved. Moreover, the use of monochromatic radiation as heating agent does not interfere with the optical measurement of temperature, which can be carried out at wavelengths far from that of the heating laser. Keeping the sample under high pressure is also less problematic with this heating method.

Thus, a laser heating technique under high- pressure buffer gas was chosen in this work for the experimental study of the melting behaviour of hyperstoichiometric uranium dioxide. Similar techniques have recently been used in some experimental research concerned with the melting point of graphite and of other refractory substances [30, 31]. A detailed description of the method employed in this work is presented in the next chapter.

References Chapter 3

1. M.A. Sheindlin, Sov. Tech. Rev. B. Therm. Phys. **1** (1987), 139.
2. A. Jayaraman, A. Rev. Mod. Phys. **55** (1983), 65.
3. W. Hume- Rothery, J.W. Christian, W.B. Pearson, *"Metallurgical Equilibrium Diagrams"*, London, The Institute of Physics, Chapman & Hall 1953.
4. R.W. Cahn and P. Haasen, *„Physical Metallurgy"*, 3rd revised and enlarged edition, Elsevier Science Publisher BV, 1983. H. Biloni, Cap. 9, *„Solidification"*, 478.
5. W.D. Kingery, *"Property Measurements at High Temperatures"*, John Wiley and Sons, Inc., New York, Chapman & Hall, Limited, London, 1959.
6. M.J. Basset, J. de Phys. **5** (1939), 217.
7. T. Noda (results presented by Hisao Mii), in *Selection of papers on "Investigations at High Temperatures"*, Mir Publishers, Moscow 1962, 471.
8. D. A. Winborn, P.C. Nordine, D.G. Rosner and N.F. Marley, Metall. Trans. B **7B** (1976), 713.

9. W.A. Oran and L.H. Berge, Rev. Sci. Instr. **53** (1982), 851.

10. L.S. Nelson, N.L. Richardson, K. Keil and S.R. Skaggs, High Temp. Sci. **5** (1973), 138.

11. S.R. Skaggs, High Temp. Sci. **9** (1977), 197.

12. B. Granier and S. Heurtault, Rev Int. Hautes Temp. Refract. **20** (1983), 61.

13. R.R. Whymark, Ultrasonics **13** (1975), 251.

14. W.A. Oran, L.H. Berge and H.W. Parker, Rev. Sci. Instr. **51** (1980), 64.

15. J. Magill, F. Capone, R. Beukers, P.Werner, R.W. Ohse, High Temp.– High Press. **19** (1987), 461.

16. A. Ashkin and J.M. Dziedzic, Science **187** (1975), 1075.

17. W.-K. Rhim, S.-K. Chung, D. Barber, K.-F. Man *et al.*, Rev. Sci. Instr. **64** (1993), 2961.

18. P.-F. Paradis, T. Ishikawa, J. Yu and S. Yoda, Rev. Sci. Instr. **72** (2001), 2811.

19. G. Wille, F. Millot, J.C. Rifflet, Int. J. Thermophys. **23** (2002), 1197.

20. A. Cezairiliyan, High Temp.– High Press. **11** (1979), 9.

21. J.L. Bates, J. Am. Ceram. Soc. **49** (1966), 395.

22. M. J. Bannister, J. Nucl. Mater. **24** (1967), 340.

23. M. Pirani and H. Alterthum, Z. Electrochem. **29** (1923), 5.

24. R. I. Jaffee and H.P. Nielson, Trans. Amer. Inst. Min. Metall. Engrs. **180** (1949), 603.

25. H.A. Wilhelm and P. Chiotti, Trans. Amer. Soc. Mater. **42** (1959), 1295.

26. R.A. Oriani and T. S. Jones, Rev. Sci. Instr. **25** (1954), 248.

27. J.L. Bates, Report HW-81603 US Atomic Energy Comm. (1964), 2.

28. A. E. Martin, R.K. Edwards, J. Phys. Chem. **69-5** (1965), 1788.

29. R.E. Latta, R.E. Fryxell, J. Nucl. Mater. **35** (1970), 195.

30. M. Musella, C. Ronchi, M. Sheindlin, Int. J. Thermophys. **20** (1999), 1177.

31. C. Ronchi and M. Sheindlin, Int. J. Thermophys. **23** (2002), 293.

Chapter 4

Design and implementation of a new experimental technique for the *liquidus* / *solidus* determination

4.1 General description of the method

The experimental method used in this work was designed in order to meet the following requirements:

- The sample surface had to be heated over the melting point. Maximum temperatures of about 4000 K should be reachable, and possibly higher in order to investigate a wider set of materials.
- The sample should remain uncontaminated during the measurement.
- The sample had to be kept under high-pressure buffer gas in order to prevent non-congruent evaporation with consequent decomposition of the material at high temperature.
- The sample temperature should be measured with sufficient precision for the thermal arrests corresponding to the phase transitions to be clearly distinguishable. Phenomena of liquid undercooling should be avoided; hence the sample cooling should not be too fast.
- On the other hand, the whole experiment should be fast enough to avoid convection in the buffer gas and evaporation/ condensation phenomena that could interfere with the optical measurement of temperature.
- The phase transition points should be determinable independent of the complex non-equilibrium phenomena that could possibly occur in the sample due to the appearance of strong temperature/ concentration gradients.

To meet all the above requirements, an experimental apparatus was designed and put into operation in the High-Temperature Properties laboratory of the Institute for Transuranium Elements (ITU). The setup is sketched in Fig. 4.1, and shown in Fig. 4.2.

As for the heating method, the need to obtain fast heating rates to high temperature under high pressure required the employment of a pulsed laser. However, by using pulsed lasers it is generally difficult to suitably plan and keep under control the heating process parameters. Such an issue was encountered in previous investigations [1, 2] carried out with a similar laser heating technique, where significant undercooling of the liquid under the equilibrium freezing temperature affected the measured data. Therefore, LASAG® Nd: YAG lasers were chosen, in which pulse length and power were programmable. Moreover, a double- pulse laser technique was devised in order to have better control of the heating and cooling rates undergone by the sample. Thus, the laser beams of two Nd: YAG pulsed-lasers (total power of $\approx$ 3kW for several tens of milliseconds) were merged and channelled into the same optical fibre and hence simultaneously focused on the sample surface. The first laser head supplied the "power pulse", heating the sample above the melting point; the second one, separately controlled in intensity and duration, delivered a longer pulse of lower power, ensuring conditioning of the sample cooling-rate. In this way, the sample temperature was prevented from decreasing too rapidly. Homogeneous power density distribution was obtained over the focal spot of 3mm- diameter following the random mixing of the laser radiation inside the optical fibre. An energy detector was placed at the exit of the beam-mixing fibre in order to record the power-time profile of the laser pulse.

The sample was held vertically inside a high- pressure cell. Such a cell was usually filled with helium used as a "buffer gas" to minimise evaporation from the sample surface. Helium was chosen since among the inert gases it causes the least optical disturbance at high pressures and temperatures. It was experimentally determined that pressures of the order of 0.1 GPa were ideal to prevent evaporation from the surface, without interfering with the optical measurements of temperature.

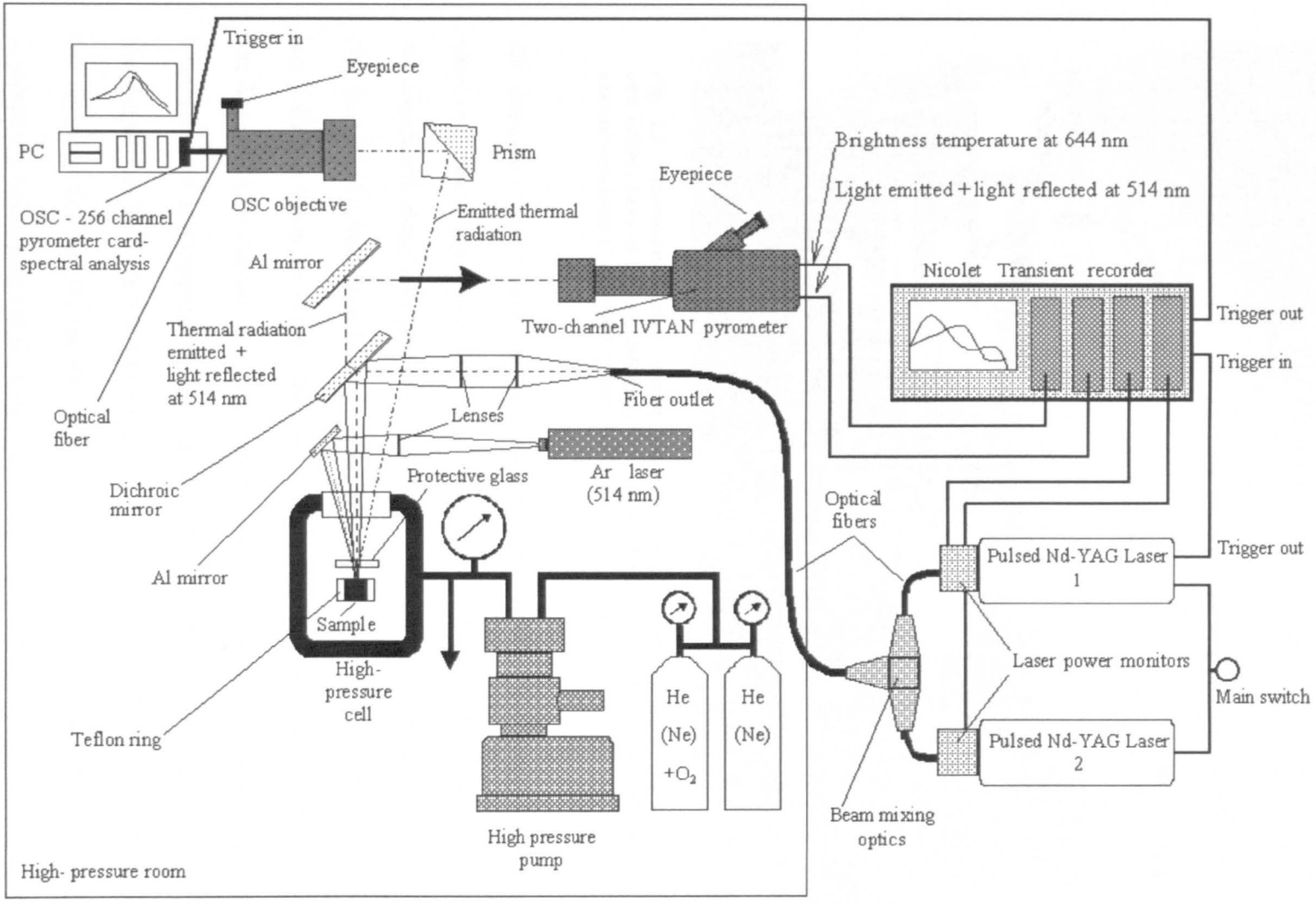

Fig. 4.1: Experimental equipment used in this work.

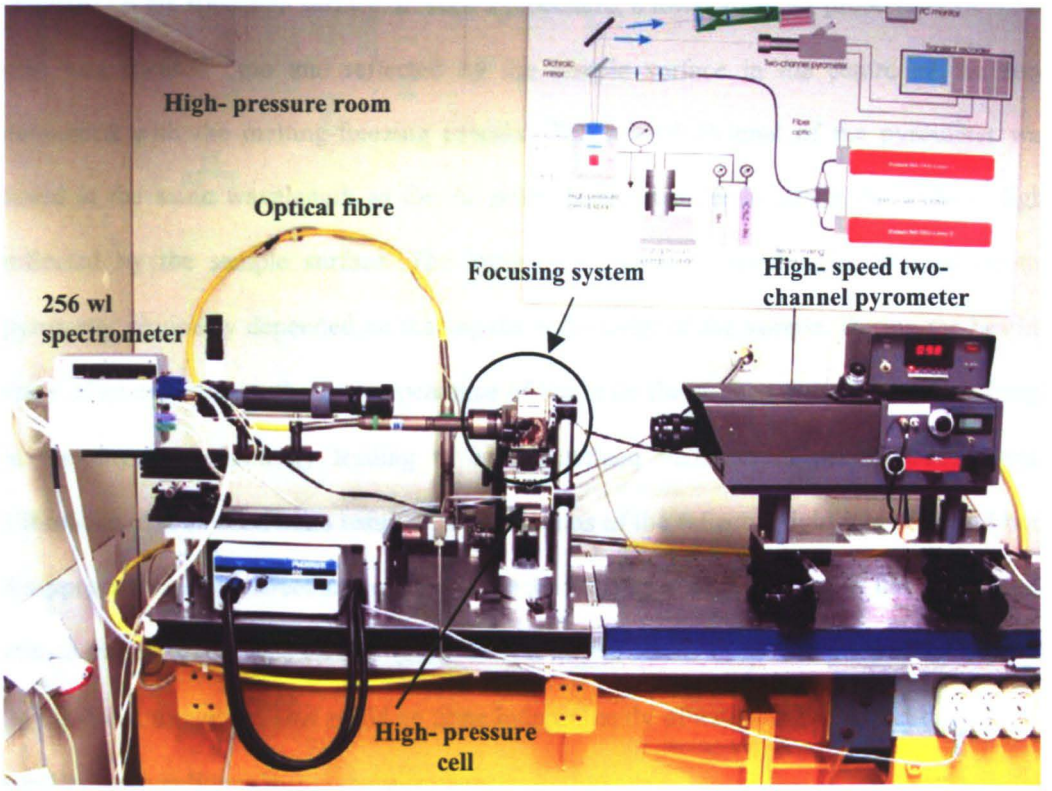

Fig. 4.2: Experimental setup used in this work for the measurement of the *liquidus* and *solidus* lines of hyperstoichiometric uranium dioxide. The Ar laser employed for the measurement of coherent reflected light is not shown in this picture.

The temperature of the sample surface heated by the laser beam was measured by a high-speed two-channel pyrometer. Each of the two channels produced an analogue signal that was transferred, along with the signals generated by the energy-detectors, to a Nicolet Pro 44C Transient Digitiser. This latter was externally triggered by the main switch of the two Nd: YAG laser heads. Finally, the digitised output curves were displayed on a PC screen.

The first pyrometer channel, operating at 644 nm and calibrated against a standard gas band-lamp, was used as a temperature reference. The brightness temperature was converted into true temperature by correcting it for the sample emissivity and for the total transmittance of the optical path. The second pyrometer channel, initially used to provide a further corroborating measurement of the temperature, was finally employed in a further procedure devised in order to independently determine the instant at which melting and solidification

occurred on the specimen surface. In such a procedure, a low- power Ar probe laser (λ = 514 nm) was focused onto and reflected by the sample surface in the centre of the zone concerned with the melting-freezing process. The second channel of the pyrometer was tuned at the same wavelength as the Ar probe laser, in order to detect the 514-nm light reflected by the sample surface. The intensity of such reflected light detected by the pyrometer obviously depended on the angular reflectivity of the sample. During the heating stage of an experiment, the first appearance of liquid on the surface caused a sudden change in the angular reflectivity leading to a well-defined variation in the recorded signal. Vibrations of the liquid mass resulted in oscillations of the reflected light intensity, and both disappeared when the freezing point was reached on the cooling phase. In this way, phase transition points could be clearly established from variations in the recorded reflected light signal. Most important, this could be done independently of any complex effect due to non-equilibrium conditions inside the specimen.

Finally, an additional multichannel (256 colours) pyrometer, triggered by the Nicolet Pro 44C Transient Digitiser, was also focused on the sample surface, through a slightly different optical path. This further means of measuring the sample temperature also permitted the emissivity of the molten surface to be measured. Although the relatively low time resolution constituted a limiting factor for such an instrument, data obtained were useful in order to estimate the superficial emissivity trend with temperature.

The whole high-pressure system, along with the pyrometers and the Ar probe laser were placed in a safety high- pressure room with reinforced explosion- proof walls. Experiments could be launched by starting the whole setup through the main switch of the Nd: YAG laser heads from outside the high- pressure room.

The different parts of the experimental setup are separately described in the next sections.

4.2 Different parts of the experimental equipment

4.2.1 High pressure system

The high-pressure cell where the sample was located during a melting point measurement is shown in Fig. 4.3.

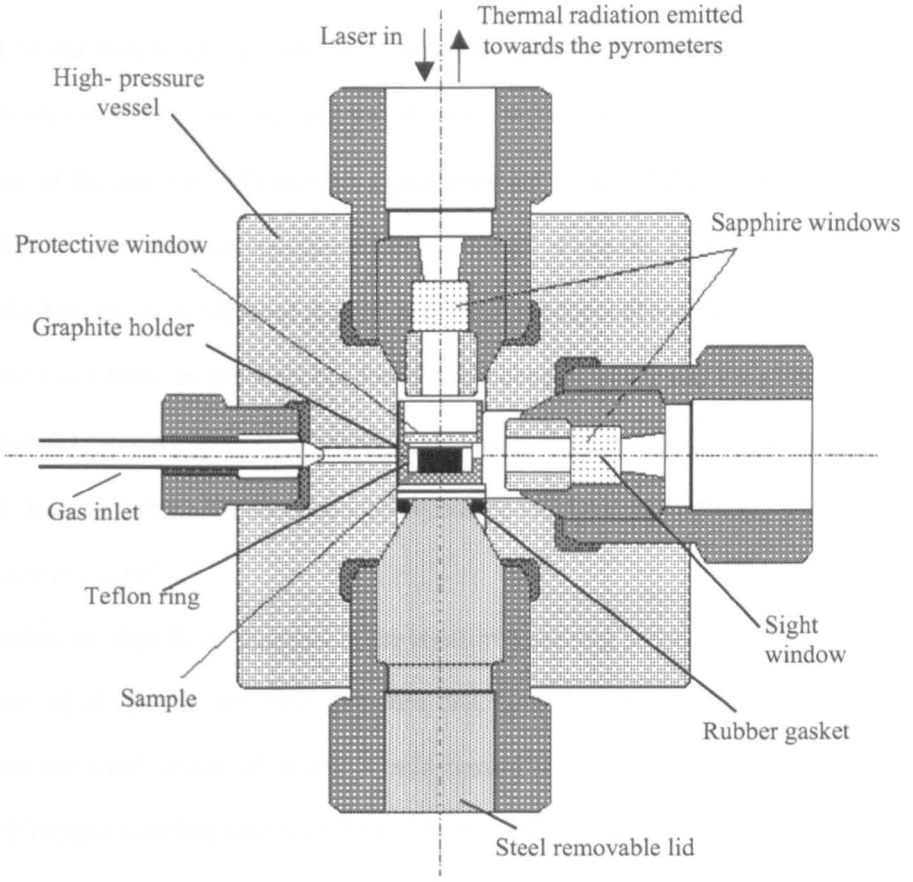

Fig. 4.3: High-pressure vessel used in this work.

In the direction of the pyrometer objective, the autoclave was closed by a sapphire window. Another thin sapphire window was placed just 1mm above the sample surface and protected the first window from possible vapour contamination. The main use of such a protective

window was to stop the development of convection streams in the high-pressure gas above the hot sample surface. Moreover, if significant evaporation took place, that was revealed by matter deposition on the thin protective window.

The sample was held vertically in a cylindrical graphite holder fixed on a stainless steel support that could be screwed in and out of the vessel bottom. In order to avoid rupture of the specimen under thermal stresses, its lateral surface was wrapped in an elastic Teflon ring. The high-pressure cell could be filled either with pure inert gas or, through a system of valves, with a mixture of inert gas and oxygen as illustrated in Fig. 4.1. Oxygen could be added to the buffer gas in order to compensate possible oxygen losses from the sample surface due to residual incongruent evaporation. Measurements were performed both in the absence of oxygen and with oxygen partial pressure up to 1 MPa (with a total pressure of 100 MPa). Nearly- anoxic conditions were obtained, if needed, by filling the high- pressure cell with helium at 10 MPa and then by opening the outlet valve until the inner pressure had decreased to 1 MPa. In this way, the atmospheric oxygen was flushed out from the cell along with helium. Starting from the oxygen partial pressure in air ($p_{O2atm} \approx 20$ kPa), the oxygen partial pressure left in the autoclave by repeating the "helium flushing" procedure n times was $p_{O2} \approx p_{O2atm}\, 10^{-n}$.

In practice, no significant changes in the measured melting points were observed due to the presence of oxygen in the high- pressure cell. This was due to the fact that under high pressure the small atoms of helium would immediately occupy the surface reaction sites, making oxygen-reaction kinetics slower. If one adds to this the relatively short duration of the experiments, it seems reasonable to consider the presence of oxygen in the autoclave as having a negligible influence.

High pressure was obtained with a Nova Swiss® electro-membrane compressor reaching pressures up to 0.3 GPa. The maximum pressure attainable with helium was 0.25 GPa (2500 bar). Helium was mainly used as buffer gas, as it has the best optical characteristics among the inert gases at high pressure, especially in the presence of a strong heat source. In

fact helium combines relatively high thermal conductivity and almost perfect optical transparency. Neon could also be employed for comparison, but only up to 0.15 GPa. Beyond that limit the measurements were affected by the turbulent convection inducted in the high-density gas by the very high temperature in proximity of the sample surface. For the same reason no heavier noble gas could be employed[1].

Under the transient conditions produced during a thermal pulse, vapour was formed on the hot sample surface, diffusing into the surrounding buffer gas. The regime with which a diffusion process of this kind occurs depends on the experimental conditions, and is described by the Knudsen layer thickness. If p^v_s is the vapour partial pressure on the hot surface at the temperature T ($p^v_s \leq p^v_E$ with p^v_E = equilibrium vapour pressure at the temperature T), the Knudsen layer is defined as the fluid region in contact with the sample surface where the vapour partial pressure is larger than p^v_s / k, k (>1) being a constant characteristic of the diffusion process. The definition of the Knudsen layer is related to the application limits of the differential equation of the mass transport in the gas. It provides a spatial separation between the initial fast evaporation regime, which takes place in the proximity of the sample surface and is only describable by gas dynamics, and the following slow classical diffusion. For a given material, the thickness of the Knudsen layer is a function of temperature and external pressure. For uranium dioxide at 3000 K and 0.1 GPa, this thickness was measured in [3] to be of the order of 100 μm, in agreement with the theoretical values calculated in [4].

In the experiments presented in this work, classical diffusion of the vapour into the buffer gas was practically suppressed by setting sufficiently high buffer gas pressures and sufficiently short experiment duration. However, within the Knudsen layer more significant mass transport could take place by laminar convection, which for this reason was particularly

[1] *Some exploratory tests carried out with Ar as buffer gas showed that the turbulence of this high-density gas inhibited the optical measurement of temperature at any pressure > 1 MPa.*

important, in the present experimental investigation, besides its optical effect. Only for a suitable buffer gas pressure and geometrical set-up, obtained by setting a protective window 1 mm above the sample surface, could these phenomena be controlled and their effects be kept under the required limits. The minimum pressure needed in order to prevent diffusion of the vapour into the gas and Knudsen layer convection was about 10 MPa, with a measurement duration of the order of 100 ms. Under these conditions the goal was satisfactorily achieved, as confirmed by the agreement of the experimental results with theoretical predictions based on the assumption of negligible evaporation (Chapter 6 and 8). In general, no signs of vapour condensation were detectable on the sapphire protective window above the sample surface, confirming that the Knudsen layer was maintained well below that reference. Slight halos of condensed vapour were occasionally visible on the protective window after experiments carried out on samples with a high degree of oxidation ($O / U > 2.10$), in general when some of the experimental parameters were not properly set. A significant amount of condensed vapour was observed on the protective window only when the sample surface was kept above the melting point for a long time (> 100 ms), for instance in the case of malfunctioning of the heating laser, and when the buffer gas pressure was lower than 10 MPa approximately. In these cases, experimental results were discarded.

4.2.2 Controlled laser-pulse melting (double-pulse technique)

Two laser pulses coming from two LASAG® Nd: YAG laser cavities (λ = 1060 nm) were mixed up in the same optical fibre and then focused on the sample surface.

The first laser head supplied a "power pulse", heating the sample up above the melting point; the second one, separately controlled in intensity and duration, delivered a longer pulse of lower power, ensuring conditioning of the sample cooling-rate. The maximum power reachable by each laser head was $\approx$ 1.5kW for up to 200 ms with the capacitors of the pumping system loaded at 350 V. Loading such capacitors at 700 V was also possible,

yielding double the output power. However, in this latter case it was hardly possible to keep under control the transient characteristics of the pulses, and only pulses lasting up to a few tens of milliseconds were realisable. Nonetheless, such a "high- power mode" was extremely useful in order to perform quick experiments (total duration < 20ms) with very high peak-temperature (up to 6000 K).

Power and duration of the single pulses were set each time in order to obtain optimal conditions for the detection of melting and freezing arrest points on the measured thermograms (see Chapter 6). Finally, the possibility to use two laser pulses instead of one permitted setting a considerable variety of cumulative pulse profiles, according to the need of any single experiment. For example, a simple but effective experiment was devised to visually determine the *solidus* point of a sample. The specimen was heated to increasingly higher maximum temperature, starting from a maximum temperature well below the expected *solidus*. When the maximum temperature reached during a shot was just above the *solidus*, traces of the first liquid formation were visible on the sample surface. Thus the *solidus* could be estimated in a simple and reliable manner (practically without any error source).

Fig. 4.4 shows the optical system devised in order to merge the two beams concentrically into a single ray successively channelled into an optical fibre and hence focused onto the sample surface. The laser electromagnetic field mode TEM_{00} would originally yield a Gaussian power profile on the beam front. However, laser modes were mixed up over the optical path inside the fibre, yielding constant power density on the 3mm- radius circular focal spot obtained on the sample surface.

An energy detector placed at the exit of the beam-mixing fibre recorded the power-time profile of the cumulative laser pulse. Such a profile was then displayed on the screen of the same Nicolet Transient Digitiser used for the pyrometer.

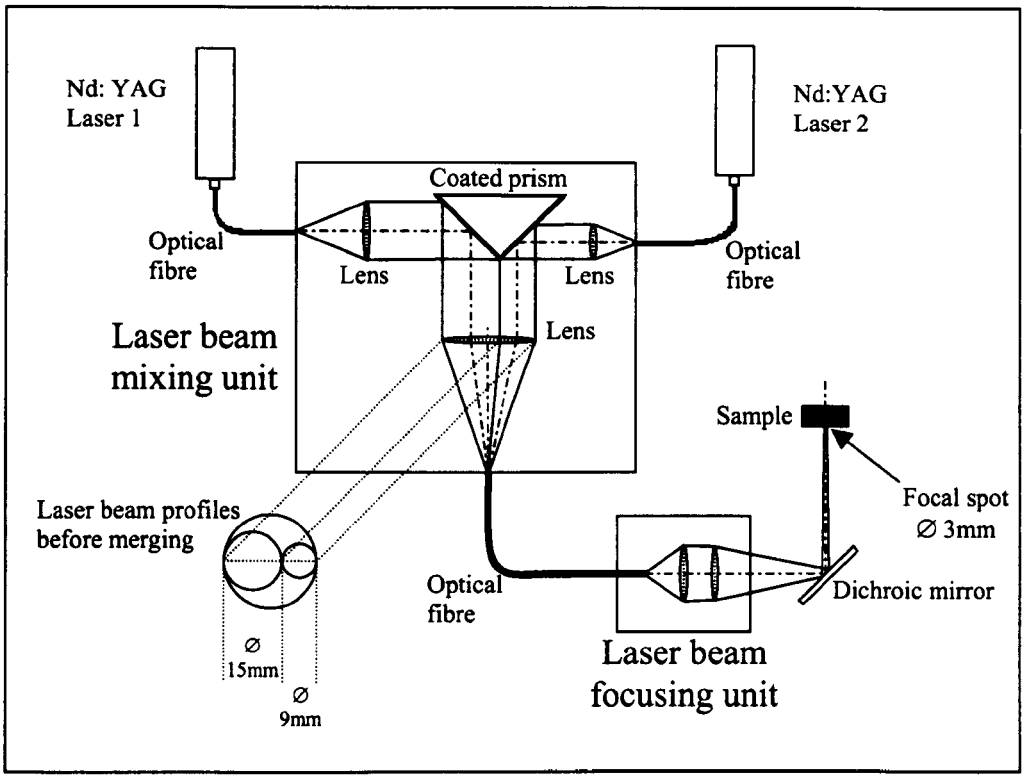

Fig. 4.4: Optical system devised in order to merge concentrically two laser beams into a single beam. The different diamters of the two beams were arranged in order to minimise power losses.

4.2.3 Problems of pyrometric application, calibration methods

Optical pyrometry

The first experimental issues to be faced in this work were the choice of means to measure the specimen temperature with a sufficient precision, and the calibration method.

Optical pyrometry is practically the only temperature measurement technique available for temperatures between 2000 and 10000 K [5]. This method consists of the measurement of the temperature of a sample through the detection of the electromagnetic energy intensity $E(\lambda, T)$ emitted by the sample surface in a unit solid angle at a wavelength λ and temperature T (see, for instance, [6]).

The radiation intensity I is defined as the energy irradiated per wavelength unit, per solid angle ω unit, per surface S unit:

$$I(\lambda,T,\varphi)=\frac{dq}{d\omega\, d\lambda\, dS\, \cos\varphi}, \tag{4.1}$$

where φ is the angle between the direction considered and the perpendicular to the sample surface (Fig. 4.5).

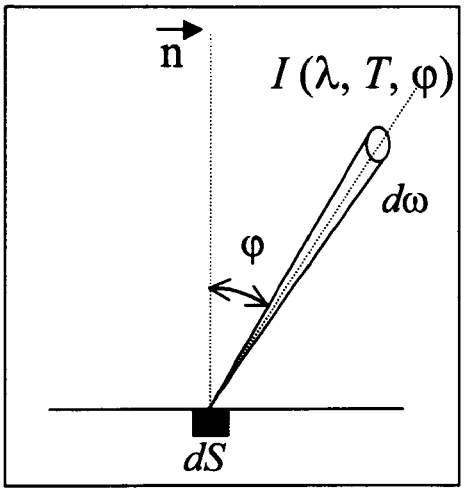

Fig. 4.5: Definition of radiation intensity emitted by a surface.

The energy irradiated from the whole hemisphere over the surface unit dS is given by

$$E(\lambda,T)=\int_{-\frac{\pi}{2}}^{\frac{\pi}{2}} I\cos\varphi\, d\varphi\,. \tag{4.2}$$

In a surface of an ideal isotropic body, I does not depend on φ, and $E=\pi I$. This is, however, in general not true for real specimens.

The hemispherical energy irradiated by an ideal blackbody per unit volume $E_b(\lambda, T)$ is given by Planck's radiation law

$$E_b(\lambda,T)=\frac{2\pi c^2 h}{\lambda^5\left[\exp\left(\frac{hc}{\lambda k_B T}\right)-1\right]}. \tag{4.3}$$

In (4.3), c is the speed of light ($2.997925 \cdot 10^8$ m s^{-1}), h the Planck constant ($6.6256 \cdot 10^{-34}$ Js), k_B the Boltzmann constant ($1.38047 \cdot 10^{-23}$J K^{-1}), T the absolute temperature. In practice, emitted radiation is measured perpendicularly to the sample surface ($\varphi = 0$). Fig. 4.6 reports the plot of Eq. (4.3) for some temperatures of interest in this work.

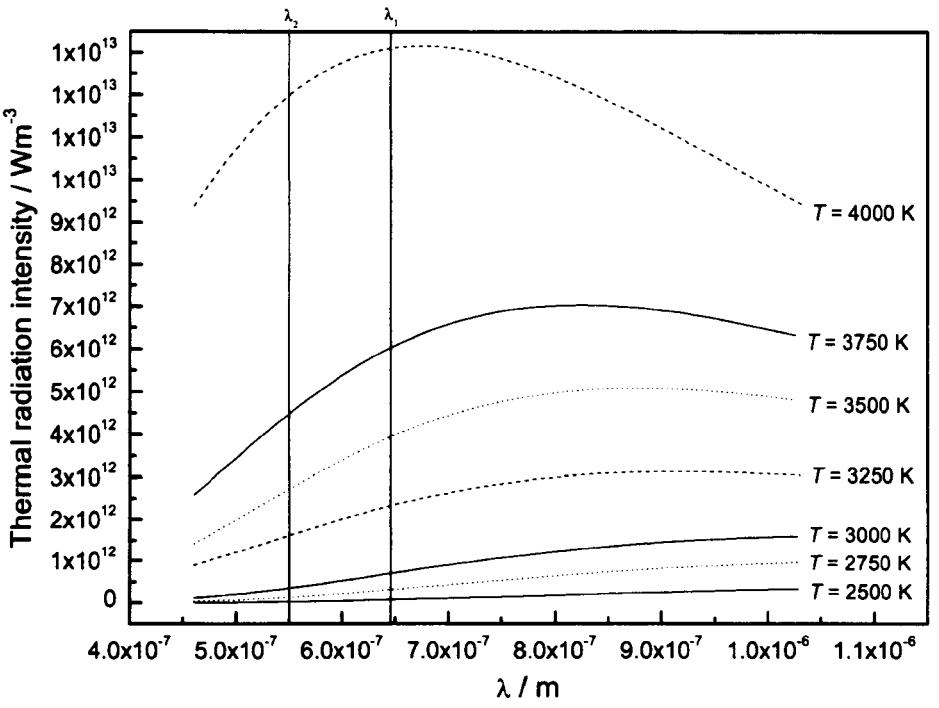

Fig. 4.6: Planck curves (thermal radiation intensity *vs.* wavelength) at several temperatures in the range of the melting transition of uranium dioxide. The effective wavelengths λ_1 and λ_2 at which the IVTAN pyrometer channels work are indicated by vertical lines.

Since ideal black body conditions are never realised in practice, formula (4.3) has to be corrected for the true normal emissivity ε of the investigated surface, defined as the ratio between the light intensity emitted by a certain sample perpendicularly to its surface at the temperature T and the light intensity emitted by an ideal black body at the same temperature ($0 \leq \varepsilon \leq 1$). Emissivity depends on the nature and the morphology of the surface, and is function of both λ and T. Moreover, when a specimen temperature is to be optically measured, the irradiated intensity is attenuated by the optical elements gone through by a

light beam between sample and detector. The factor by which the light intensity is attenuated is called transmittance τ ($0 \leq \tau \leq 1$). In general ε and τ depend on both temperature and wavelength. In this work, transmittance also depended on the pressure of the buffer gas in the high- pressure cell.

Finally the hemispherical energy density emitted by the sample surface and detected by the pyrometers used this work was:

$$E_{det}(\lambda,T)=\frac{C_1\,\varepsilon(\lambda,T)\,\tau(\lambda,P_{gas})}{\lambda^5\left[\exp\left(\frac{C_2}{\lambda T}\right)-1\right]}\,. \qquad (4.3')$$

In Eq. (4.3'), C_1 and C_2 regroup the universal constants written in Eq. (4.3), and in SI units have the values:

$C_1 = 3.74151 \cdot 10^{-16}$ W m^2

$C_2 = 0.0143886$ m K

The main problems involved in radiation pyrometry methods are linked to the investigated temperature range (Fig.4.6 shows that, from 2000 to 4000 K, the intensity of 0.65μm blackbody radiation changes by several orders of magnitude), the time resolution and the accuracy of the measurements. The basic elements of any radiation pyrometer include an optical system for the selection of emitted radiation flux from a certain area of the sample, a monochromatisation unit, a radiation detector with preamplifier and an analogue or digital unit to calculate the temperature.

High-speed two-channel Pyrometer used in this work

In the present work a particular optical pyrometer has been employed, designed at the Institute of High Temperatures of the Russian Academy of Sciences (IVTAN) [7] and described in detail in [8]. This pyrometer was developed to perform studies on samples subjected to fast (millisecond) heating. Primary attention was therefore given to the speed of

operation as well as to the elimination of possible exposure to powerful monochromatic radiation penetrating the sensitive region of the photodetectors employed. The use of photodiodes as photodetectors ensured a broad temperature range of operation (1700- 8000 K) and the linearity of the characteristic input light / output current, still maintaining a speed of operation sufficient to guarantee a good time resolution of the measurements. The need for investigating this large temperature range required the introduction of a device ensuring non-linear transformation of the photodiode signal, in order to adequately record such signal at both upper and lower limits using a fast analogue- digital converter (ADC). This problem was faced by using a fast logarithmic amplifier, enabling reduced swing of the signal at the ADC input and increased range of radiation intensity being recorded to approximately six decades, still maintaining a relatively high speed of operation (up to 500 kHz).

A schematic of the instrument is shown in Fig. 4.7. The focusing unit consisted of two lenses, a field diaphragm and a mirror for the eyepiece channel. A grating monochromator was used to spatially select the working wavelengths by separating the incoming light spectrum. The field diaphragm served as the "entrance slit" of the monochromator. The radiation was then directed onto two photodiodes, each defining a working channel. One of the two working wavelengths was fixed at λ_1 = 0.65 μm, the traditional wavelength for optical pyrometry. The second wavelength could be adjusted by moving the corresponding photodiode along the spectrum. The transmission band for each channel was $\Delta\lambda \approx 10$nm.

Calibration curves for the two channels were obtained starting from Planck's function $E(\lambda, T)$ as follows.

Equation (4.3') can be rewritten

$$E_{\text{det}}(\lambda,T) = \frac{C_1}{\lambda^5\left[\exp\left(\frac{C_2}{\lambda T_\lambda}\right)-1\right]}. \qquad (4.3'')$$

T_λ is the spectral radiance temperature, related to the true temperature T by the following equation, obtained by combining (4.3') and (4.3''), and supposing that exp $(C_2 / \lambda T) >> 1$:

$$\frac{1}{T} = \frac{1}{T_\lambda} + \frac{\lambda}{C_2} \ln(\varepsilon(\lambda, T)\tau(\lambda, P_{gas})) . \tag{4.4}$$

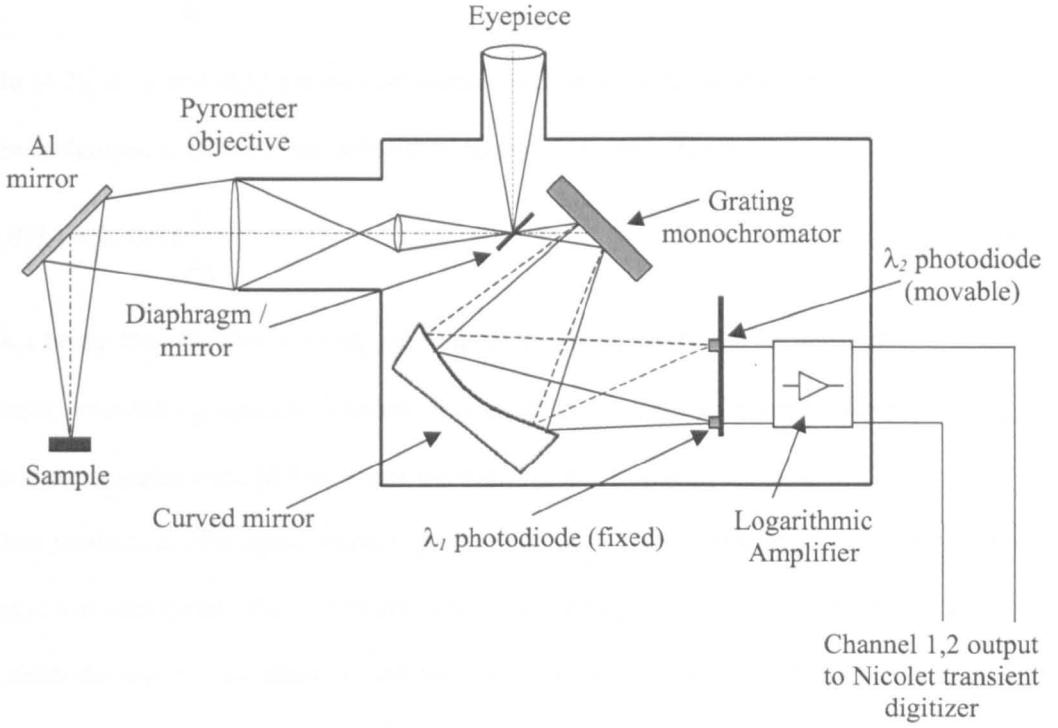

Fig. 4.7: Schematic of the IVTAN two- channel optical pyrometer.

The output current of each photodiode i_{pd} was directly proportional to the detected light,

$$i_{pd} = \alpha E(\lambda, T), \tag{4.5}$$

α being a constant that can be considered approximately independent of the device temperature (at least within the small ambient temperature variations, controlled by a thermostatic system included in the pyrometer equipment).

If i_{pd} is the logarithmic amplifier input and i_{ref} its reference current, the output voltage was given by:

$$V_{out} = k \, \mathrm{Log} \frac{i_{pd}}{i_{ref}} . \tag{4.6}$$

In (4.6) k is the logarithmic amplifier decimal coefficient (k=1 in our case).

From Eq. (4.6), (4.5) and (4.3'') one obtains:

$$V_{out} = A(\lambda) + \frac{B(\lambda)}{T_\lambda} . \tag{4.7}$$

In (4.7), $A(\lambda)$ and $B(\lambda)$ are two constants which have to be determined experimentally for each channel, to calibrate the pyrometer. In particular, one obtains

$$B(\lambda) = 0.4343 \frac{C_2}{\lambda_{eff}} . \tag{4.8}$$

λ_{eff} being the effective working wavelength of the pyrometer. The linear relation (4.7) is valid provided λ_{eff} remains constant. Therefore, at every recalibration of the pyrometer, λ_{eff} was recalculated from (4.8) to check the stability of the system.

The production of a signal linearly proportional to $1/T$ was extremely convenient from the practical standpoint. The λ_1 channel was calibrated against a 212P Polaron® gas lamp, for which the curve T vs. input current was very well established by KR Technologie GmbH-Stuttgart at a wavelength of 655.5 ± 0.2 nm. The uncertainty in the lamp spectral radiance temperature due to convection phenomena was ± 0.15 K at 1800 K and ± 0.5 K at 2400 K. The reproducibility of such temperature at 1800 K was better than ± 0.2 K over a three day period, and the same reproducibility was observed for the mean spectral radiance temperatures from 1800 to 2400 K. The lamp temperature, calibrated with the input current, was put in formula (4.7) as T_λ, in this case coinciding with T, as the calibrating lamp could be considered as an ideal blackbody. In Fig. 4.8a the pyrometer first channel output voltage V_{out} (measured by a digital voltmeter with a precision of 0.005%) is plotted against $1/T$. A straight line was obtained the parameters of which were $A(\lambda)$ and $B(\lambda)$ of formula (4.7). λ_{eff} was obtained from (4.8) to be 0.644 μm. The calibration was performed in the temperature

range 1800 – 2500 K. Thus a temperature scale was defined with an accuracy of ±0.5% up to 2500 K. The procedure was repeated several times, at intervals of several months. The effective wavelength remained constant within ± 1 nm over a period of three years.

The λ_2 channel was calibrated in the same way against a graphite blackbody light source up to 3300 K, the temperature of which was measured by the 0.644 μm channel (Fig.4.8b). This λ_2 channel was initially used, with λ_{eff} = 0.54 μm, only to test the λ_1 channel results.

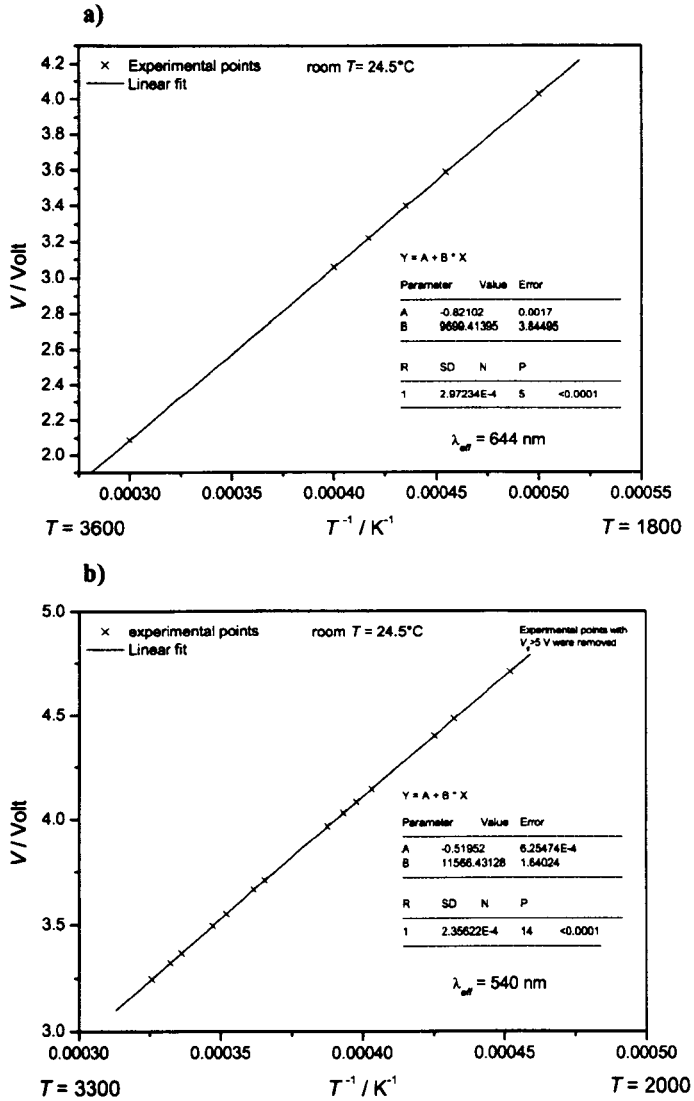

Fig. 4.8: Calibration of the IVTAN pyrometer. a) First channel, λ_{eff} = 644 nm, calibrated against a standard gas lamp. b) Second channel, λ_{eff} = 540 nm, calibrated against a black body source.

In order to check the validity of the temperature scale, constructed according to Eq. (4.7), linearity of the pyrometer opto- electronic circuit was checked at the Institute of High Temperatures of the Russian Academy of Sciences over a wide temperature range (2000- 8000 K) by using a He- Ne laser. The radiation of such a laser was fed, with appropriate attenuation, into the pyrometer optical circuit. At the upper limit of the instrumental range the error due to non- linearity did not exceed 0.5 %. The instrument drift was also investigated at the IVTAN using a temperature lamp set at different temperatures. The instrument drift at a constant source temperature of 2170 K, due to room temperature variations, supply instability and noise, for both channels did not exceed 0.3 K over 5h.

The instrument sensitivity was defined by the noise level and resolution of the 14- digit ADC. For the λ_1 channel the sensitivity, defined by the ADC, was about 1 K at 4500 K, and about 0.5 K at 3100 K. The sensitivity of the λ_2 channel was lower than that of the λ_1 channel at $T < 4100$ K, as obtained by differentiating Eq. (4.3) with respect to temperature at the two wavelengths (Fig.4.9).

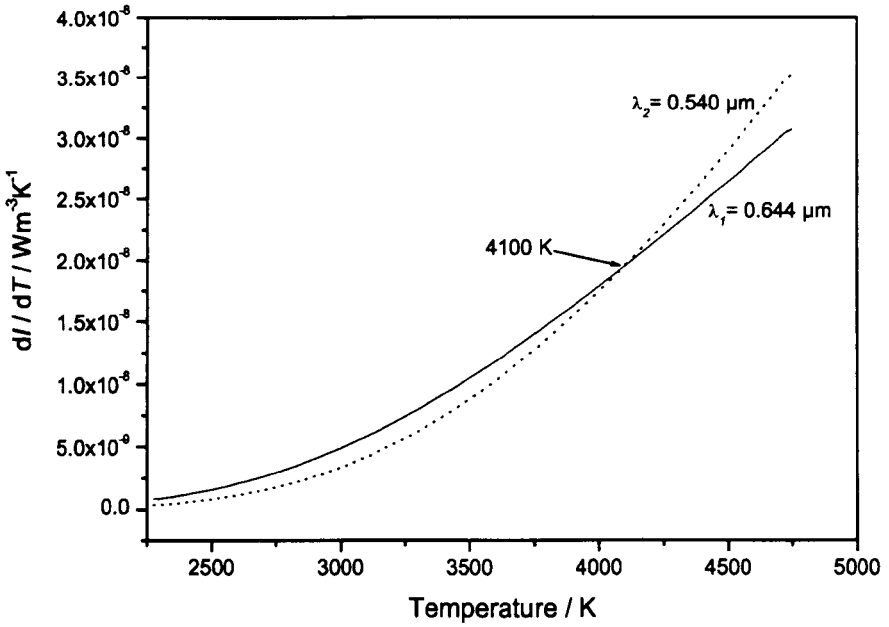

Fig. 4.9: Sensitivity of the two IVTAN pyrometer channels under ideal black body conditions.

Therefore under ideal black body or grey body conditions (i.e., with ε and τ in Eq. (4.3') independent of λ), in the temperature range around the melting point of uranium dioxide, the temperature measured by the 0.644 μm channel constituted a more precise reference.

The dynamic properties of the pyrometer were established on the basis of the detectable rate of temperature rise dT / dt and on the settling time $\Delta\tau_s$. This latter is defined as the time necessary for the output signal to stabilise at the higher level, when the input is instantly varied from a lower to a higher value. In order to study such transient characteristics, use was made of a light- emitting diode (LED) connected to a variable- amplitude nanosecond pulse generator, with $\Delta\tau_s \approx 10$ ns. Thus, variations in this light source intensity could be regarded as instantaneous from the viewpoint of the pyrometer. The pyrometer settling time to $\Delta T / T = 1\%$ was $\Delta\tau_s \approx 10$ μs, whilst dT / dt varied from $4 \cdot 10^8$ to 10^9 Ks^{-1} depending on the simulated T_{max} and T_{min}.

Finally, the main characteristics of the pyrometer are summarised in the table below.

Table 4.1: Some characteristics of the IVTAN microsecond pyrometer.

	Channel 1	Channel 2
Wavelength λ	0.644 μm	0.540 μm
Linearity range	Approx. 1600-8000 K	Approx. 1900-8000 K
Stability ($\Delta T / T$ at 2170 K)	< 0.02% for 3 days	< 0.02% for 3 days
Sensitivity (2500K)	1.5 K	Not measured
Sensitivity (5000K)	3 K	Not measured
Settling time ($\Delta T / T = 1\%$)	Approx.10 μs	Not measured

4.2.4 Multichannel pyrometry

Multichannel pyrometry is a unique solution to temperature and fast thermophysical properties measurements made in the vicinity of phase transitions where effective spectral emissivity of the surface cannot be evaluated with the required reliability. It essentially increases the information about thermal radiation in respect to the conventional single or double channel pyrometry, constituting a powerful mean of investigation for the previously introduced functions $\varepsilon(\lambda, T)$ and $\tau(\lambda, P)$. This type of technique has been presented and employed in the recent years in the investigation of high- melting point ceramics [2, 9].

In this work a 256- channel pyrometer was employed along with the IVTAN two- channel one presented in the previous section. As already mentioned, the time resolution yielded by this instrument was too poor to allow precise temperature measurements during millisecond-range experiments. On the other hand, such a multi- wavelength device was extremely useful in detecting the sample surface emissivity variations during the melting /freezing experiments as well as in measuring the transmittance of the optical path between sample surface and light intensity detectors.

Short description of the device

The Optical Spectrograph Card 488-1011 nm SNLC / 96 (OSC) is an integrated array of 256 photodiodes, and constitutes a board that can be directly installed in a suitable PC. This feature made it possible to display the output data and to perform their analysis in real time during the measurements. A focusing unit similar to the one implemented for the IVTAN pyrometer described in the previous section was used to collect the radiation emitted from the sample surface, and to channel it into an optical fibre directly connected to the integrated spectrometer. The sighting spot had a diameter of 0.3 mm at a distance of 500 mm.

Spatial spectral separation of the light signal was realised through a microscopic prism included in the system at the junction between fibre and photodiode array. Each photodiode of the array worked at one wavelength, defined with a precision of ± 2 nm. The working wavelengths spanned a spectral range from 0.487 to 1.012 μm. Each photodiode loaded a capacitor with a charge proportional to the light signal detected and to an integrating time τ_i, that could be set up before any measurement as an integer multiple of five times the minimum value 0.8 ms. Such a variable integrating time made it possible to find an optimal time resolution and signal level without recalibration of the instrument, constituting one of the main features of the OSC. This operating mode allowed averaging of the signal intensity collected during the integrating time, hence cleaning the output signal from the noise. The system is provided with a buffer memory that holds up to 256 signals per photodiode. Therefore, up to 256 spectra by 256 wavelengths each could be recorded in every measurement. If τ_i is the integrating time, the total duration spanned in a measurement was 256 τ_i. The integrating time τ_i also defined the time resolution of the pyrometer. The signals coming from the detectors were then converted into digital counts via an AD converter. The resulting spectrum in ADC counts vs. wavelength was displayed on the PC screen.

Linearity check: deviation from linearity and correction

Fig. 4.10a shows intensity measurements (in ADC counts) performed on the 755.014 nm photodiode. This photodiode was chosen because its wavelength was the closest to the spectrum maximum at the selected temperature, yielding the maximum number of ADC counts over the integrating time and therefore the "cleanest" averaged output signal. In fact, the higher the number of ADC counts, the better the system works in filtering the noise. The light source used was a P212c-gas lamp, the temperature of which was set at 2500 K. The OSC integrating time was changed every time after recording the counts number.

This kind of experiment was repeated several times at different temperatures. A capacitor was loaded by every pixel of the OSC with a charge proportional to the light detected and the integrating time. Such proportionality deviated from being linear, as shown in Fig. 4.10b, mainly because of the bias caused by the electronics between the light detector and the analogical- digital converter (ADC).

A routine was provided within the OSC software in order to linearise the ADC counts using a second order polynomial correction. The second order term coefficient was measured experimentally taking into account the relative deviation from linearity shown in Fig. 4.10b as a function of the number of counts measured.

The resulting correcting polynomial was:

$$Lc = rc + 6.98254 \cdot 10^{-7}\, rc^2, \tag{4.9}$$

where *Lc* stands for "linearised counts" and *rc* stands for "raw counts". The relative deviation from linearity after correction through formula (4.9) is shown in Fig. 4.10c. It is noticeable than this deviation is greater for measurements with less than 1000 ADC counts, where the error is randomly distributed and in any case contained within 2% of the value yielded by the linear dependence.

Calibration of the 0.6494 μm photodiode

The 0.6494 pixel was calibrated against the same P212c gas lamp used for the linearity check, because the wavelength of this pixel was the closest to 0.650 μm, at which the radiance temperature of the lamp was previously calibrated. Fig. 4.11 shows a schematic of the experimental set-up implemented for the OSC calibration and used for some measurements as well.

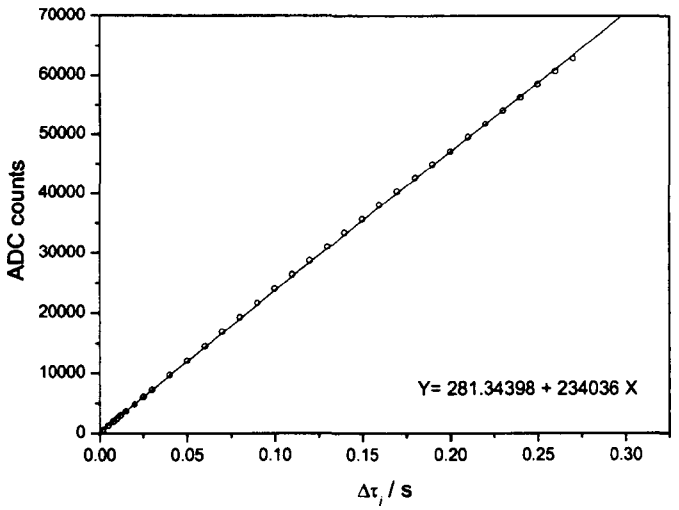

Fig. 4.10a: ADC counts as a function of the integrating time for the 755.014- nm OSC multichannel pyrometer pixel.

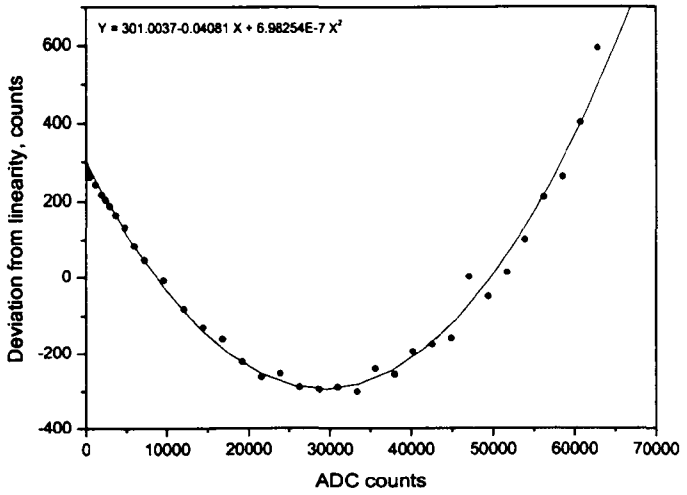

Fig. 4.10b: ADC counts measurements at different integrating times and λ =755 nm. The light source was a P212c gas lamp, at about 2500 K.

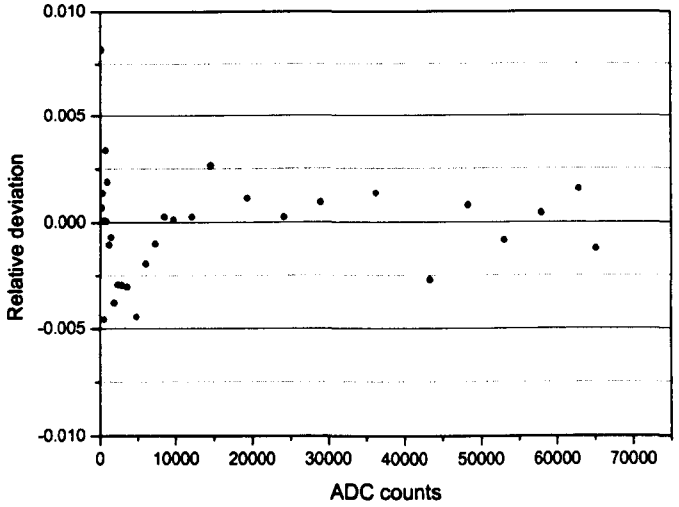

Fig. 4.10c: Relative deviation from linearity after correction through formula (4.9).

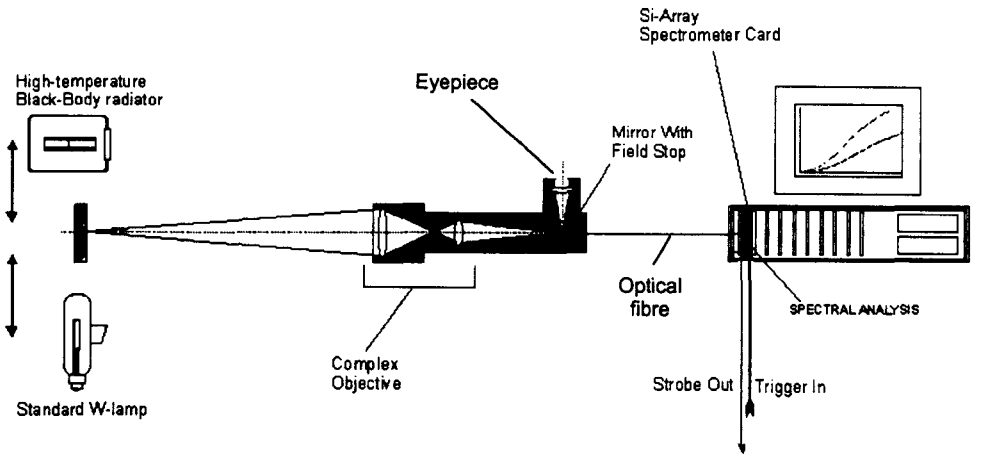

Fig. 4.11: Scheme of the experimental method used to calibrate the OSC multichannel pyrometer.

The calibration procedure was similar to the one implemented for the first channel of the IVTAN spectrometer. At each temperature of the lamp five measurements were carried out with the two shortest integrating times available, namely 0.8 ms and 4 ms.

The five values measured were then arithmetically averaged and the value obtained was used to calibrate the photodetector starting from Planck's function (4.3). According to this latter, since the ADC output counts were linearly dependent on the light intensity, the logarithm of their value had to be linearly dependent on $1/T$, T being the brightness temperature of the lamp:

$$\ln(I_{counts}) = A(\lambda) + \frac{B(\lambda)}{T} \tag{4.10}$$

$A(\lambda)$ and $B(\lambda)$ were the parameters to be determined.

Moreover, the following relation holds:

$$B(\lambda) = \frac{C_2}{\lambda_{eff}} \tag{4.11}$$

Thus, as in the case of the IVTAN pyrometer, λ_{eff} can be recalculated to check whether the calibration is self-consistent and the working wavelengths sufficiently stable. In this case,

however, slight displacements of the fibre optics as well as small variations in the ambient temperature were found to significantly affect the value of λ_{eff}. Thus the system was revised in order to reduce to a minimum the optical fibre length (less than 1 cm), making the fibre practically straight and rigid. Furthermore, a suitable miniaturised cooling system was added to the equipment in order to keep the photodiode temperature at a fixed value of 298 ± 1 K during operation. With these precautions, λ_{eff} of the calibrated channel could be maintained constant with long-term (several months) variations not exceeding 2nm.

In Fig. 4.12 the natural logarithm of the ADC counts corrected for linearity is plotted as function of $1/T$ with integrating time of 4 ms.

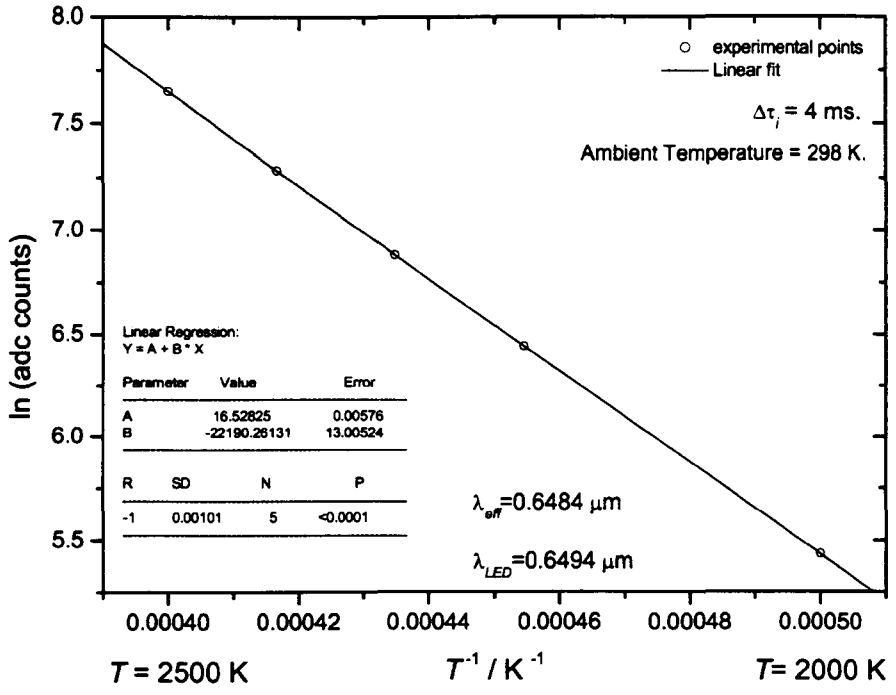

Fig. 4.12: Calibration of the 649.4 nm pyromter photodiode. Light source: standard gas lamp.

The parameters of the linear regression straight line are just A (λ) and B (λ). The first point of the graph, corresponding to the lowest temperature of the lamp, was removed as it was too far from the fitting straight line. This is easily explained remembering that the lower the

temperature of the light source, the lower is the intensity emitted and the higher is the (random) deviation from linearity.

Calibration of the whole 256 pixels spectrum

A graphite blackbody was finally used as a light source to calibrate all the remaining pixels. The 0.6494 μm pixel was used to measure the blackbody true temperature for eight values of the input power. To get the true temperature, the measured brightness temperature was corrected taking into account the transmittance of the blackbody quartz window. This latter was measured with an UV-Visible recording spectrophotometer (Shimadzu). It resulted in a good approximation to the straight line:

$$T_w(\lambda) = 0.9233974 + 7.0830 \cdot 10^{-3}\,\lambda\ (\mu m), \qquad (4.12)$$

which gave, at λ =649.4 nm, a T_w of 0.928.

The eight blackbody temperatures at which spectra were recorded were 2568, 2627, 2722, 2762, 2949, 3022, 3239 and 3406 K.

At each of these temperatures a spectrum spanning the 256 pixels was recorded with an integrating time of 0.8 ms. The spectrum registered at T = 3406 K is shown in Fig. 4.13 along with the theoretical Planck spectrum at the same temperature.

In each measurement the theoretical Planck spectrum was divided point by point by the spectrum measured in ADC counts, corrected with the window transmittance given by formula (4.12).

A resulting factor $K_{0.8}(\lambda)$[2] was calculated at each temperature, as

[2] *If a different integrating time τ_i was set in a measurement, the calibration function $K_{\tau i}(\lambda)$ had to be used*

$$K_{\tau_i}(\lambda) = K_{0.8}(\lambda)\frac{0.8}{\tau_i}, \qquad (4.13)$$

as a consequence of the linearity of the output signal with respect to the integrating time.

$$K_{0.8}(\lambda) = \frac{T_w(\lambda)}{ADC^{counts}{}_{0.8}(\lambda, T_{bb})} \frac{1}{\lambda^5 \left[\exp\left(\frac{C_2}{\lambda T_{bb}} \right) - 1 \right]}^3 . \quad (4.14)$$

$K_{0.8}(\lambda)$ constitutes the transfer function of the whole opto- electronical system of the OSC and contains all the information needed to obtain the true Planck spectrum from the ADC counts measurements.

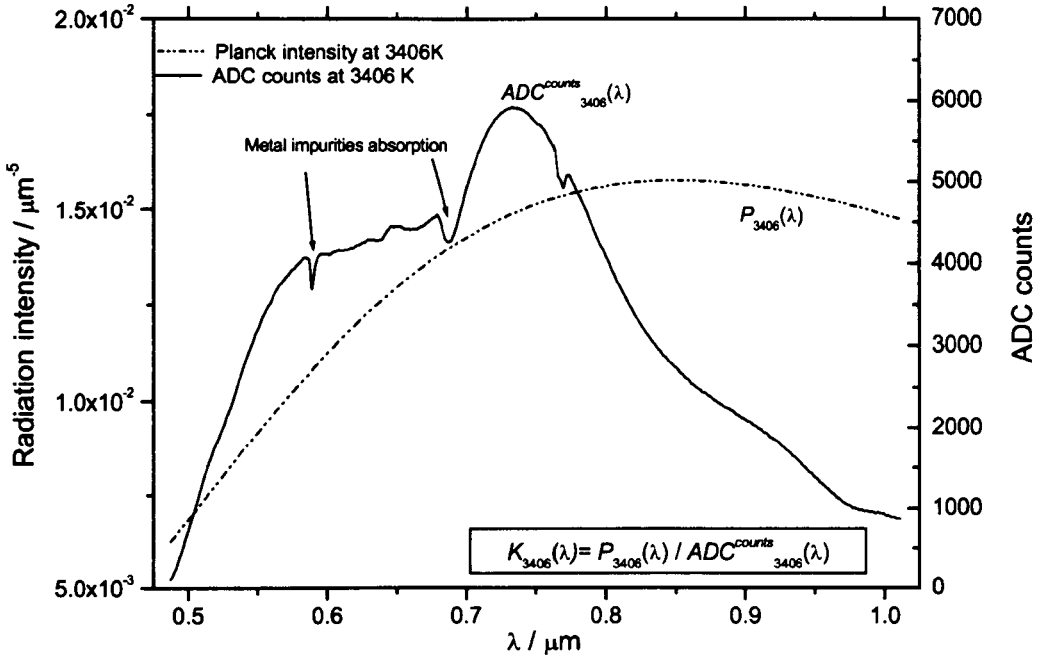

Fig. 4.13: Spectrum in ADC counts recorded at 3406 K with an integrating time of 0.8 ms. Comparison with the Planck spectrum at the same temperature. Light source: blackbody. Radiation intensity units are normalized to [L^{-5}] .

The resulting $K_{0.8}(\lambda)$ was independent of the temperature in the range 0.5 – 0.95 μm, whereas its values seemed not to be reliable at lower and higher wavelengths, where the signals were weaker due to both the low radiation intensity and the rather poor photodiodes sensitivities. Therefore the working range was restricted to 185 wavelengths between 515 and 900 nm.

[3] *In formula (4.14), as in all the following calculations, Planck intensity is divided by the constant $C_1=2\pi c^2 h$ for sake of simplicity. With this condition, radiation intensity dimensions are [L^{-5}], expressed in μm^{-5}.*

As one can identify from Fig. 4.14, moreover, the trend of $K_{0.8}(\lambda)$, like the one of the ADC counts, was affected by a much higher noise when the temperature was lower. This is clearly seen in the inset of Fig. 4.14: the values of $K_{0.8}(\lambda)$ deviated more from the regular trend at lower temperature, but at every second point recorded the values overlapped almost perfectly at each temperature. Such an effect was therefore thought to be due to some electronic noise in the system that was averaged out when the number of counts was large enough. For this reason the $K_{0.8}$ (λ) trend obtained at 3406 K (the maximum temperature at which the calibration was performed) was chosen as representative for $K_{0.8}(\lambda)$.

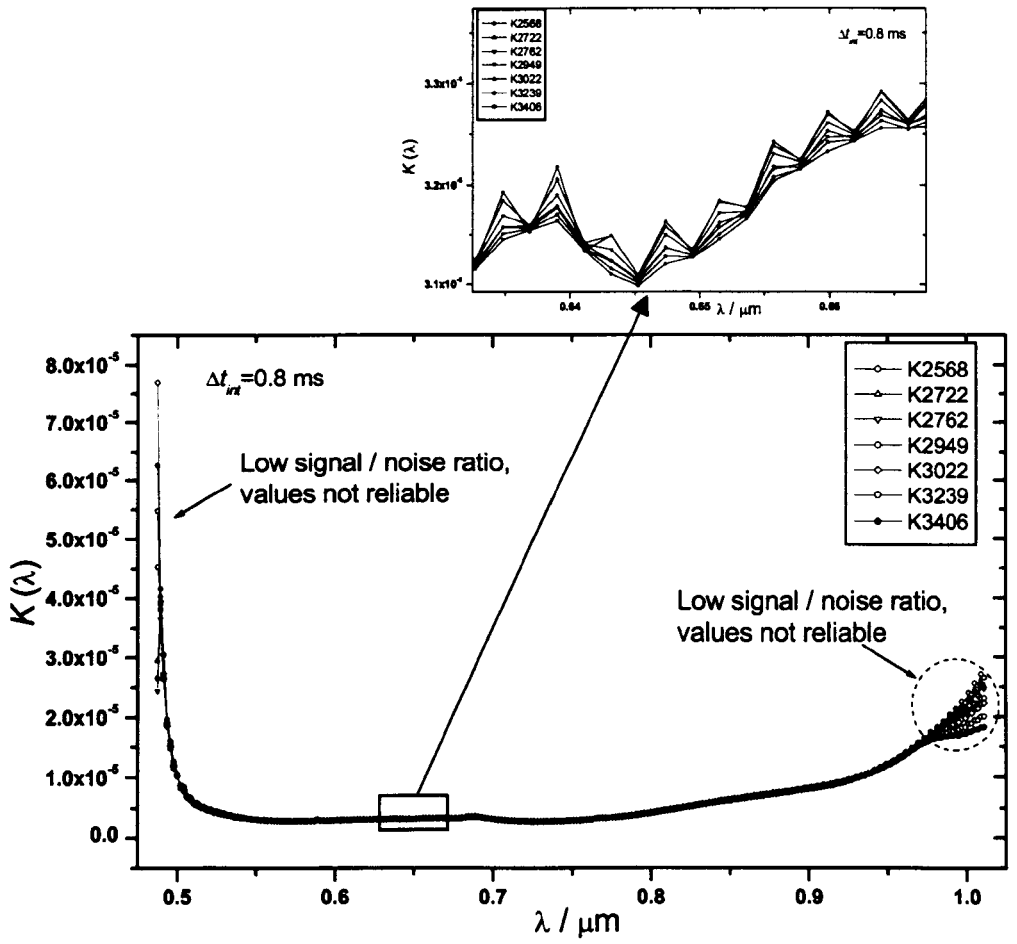

Fig. 4.14: $K(\lambda)$ curves at different temperatures. Inset: enlargement of the rectangle frame. Electric noise on the OSC output signal affects every second pixel, the more the lower the temperature.

Fig. 4.15 displays the ratio between $K_{0.8}(\lambda)$ at 3406 K and $K_{0.8}(\lambda)$ at 2568 K. The deviation between them remained within 2% of the average value over the central part of the spectrum, but it was much smaller considering only the "even" points.

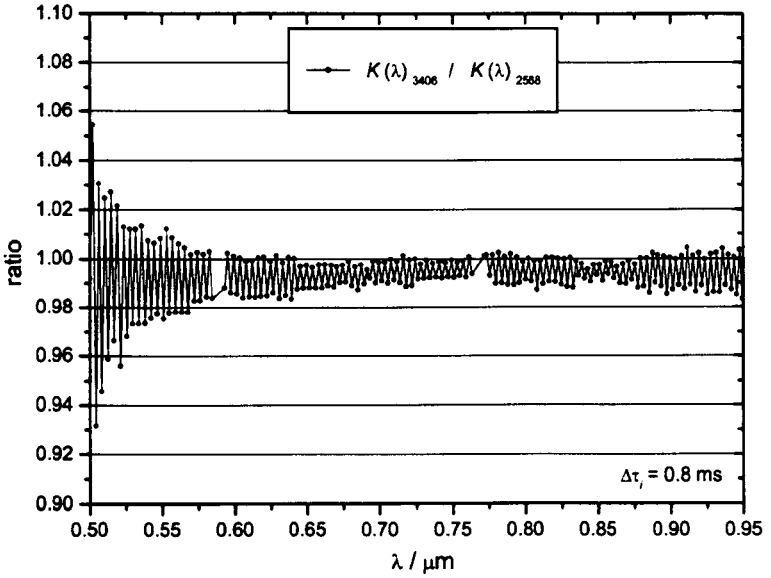

Fig. 4.15: Ratio between *K(λ)* at 3406 K and *K(λ)* at 2568 K.

Once $K(\lambda)$ was determined, the OSC was ready to operate. The Planck spectrum for the blackbody light emission was obtained by multiplying point by point the raw spectrum in ADC counts by $K(\lambda)$ and by $T_w(\lambda)$. To measure the exact spectrum of emission from a sample, $T_w(\lambda)$ had to be replaced with the transmittance $\tau(\lambda)$ of the optical system before the OSC multiplied by the emissivity $\varepsilon(\lambda, T)$ of the sample itself.

Functioning mode

Eq. (4.3') gives the thermal radiation intensity emitted by a surface at the temperature T and detected by the photodiodes. This radiation intensity was measured from the spectrum given by the OSC in ADC counts,

$$E_{det}(\lambda,T) = K_{\tau_i}(\lambda) ADC^{counts}(\lambda,T) \tag{4.15}$$

τ_i being the integrating time.

In Eq. (4.3') $\varepsilon(\lambda, T)$ is the surface emissivity. Generally it is unknown, and had to be determined by the following procedure:

1. The transmittance $\tau(\lambda, P_{gas})$ was measured separately before the experiment.
2. A function was selected to approximate the expected physical features of $\varepsilon(\lambda, T)$.
3. The product $\varepsilon(\lambda, T) E_b(\lambda,T)$ was parameterised as $\varepsilon_\lambda^{\alpha 1 \ldots \alpha k} . E_\lambda^{\ T}$, $k \geq 1$, and the functional

$$\Phi(\alpha_1..\alpha_k,T) = \int_{\lambda_{min}}^{\lambda_{max}} \left| E_{det}(\lambda,T) - \varepsilon(\alpha_1..\alpha_k,\lambda,T)\tau(\lambda,T)E_b(\lambda,T) \right|^2 d\lambda \tag{4.16}$$

was finally searched for a minimum in the R_{k+1} space $\{\alpha_1 \ldots \alpha_k, T\}$ by means of a computer programme.

4. The numerical robustness of the solution was checked and, if stability conditions were satisfied, k was increased by one, and the procedure restarted from step 3. Otherwise, the programme was stopped, giving the last calculated temperature and spectral emissivity function with the least uncertainty.

Steps 3. and 4. were repeated at each integration, being a full measurement composed of 256 integrations shifted by the integrating time τ_i. Thus values of $\varepsilon(\alpha_1 \ldots \alpha_k, \lambda, T)$, and of T were yielded by the analysis with a time resolution equal to τ_i.

During a single integration only one of the 256 LED pixels at the time produced a signal. Thus the signal coming from a pixel was time- shifted with respect to the previous pixel by τ_i /256. Such a shift could lead to significant errors in the analysis if the temperature change rate was high enough, i.e. comparable with the sensitivity of each pixel divided by τ_i / 256. For example, knowing that each LED had a sensitivity of ± 2 K at 2750 K, with τ_i = 0.8 ms a cooling rate ≈ 2 /(0.0008 / 256) = 640· 10^3 K s^{-1} would already cause a detectable effect. Since the cooling rate reached during a melting/freezing experiment normally reached

10^6 K s^{-1}, this effect could constitute an actual issue. Therefore the recorded signal $E_{det}(\lambda, T)$ used in Eq. (4.16) had to be linearly interpolated over the time for each pixel in order to obtain a simultaneous value for all the LEDs.

Tests of the method

Emissivity and temperature of the P212c gas lamp W filament were measured as a check in order to prove the validity of the depicted method. The lamp input current was set to a value higher than the maximum for which the lamp itself was calibrated. The results are shown in Fig. 4.16.

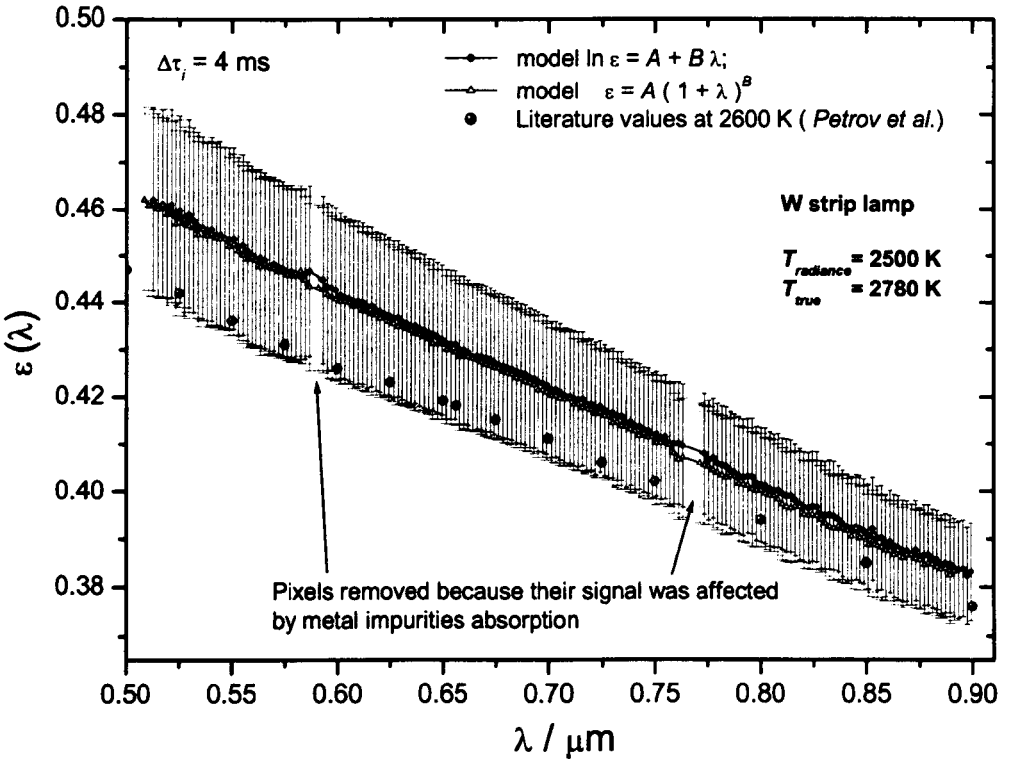

Fig. 4.16: Measurement of the W filament temperature and emissivity. The band around the experimental points indicates the standard deviation over 256 spectra.

The procedure for the calculation of ε and T was repeated for two different functions approximating the emissivity, representing a logarithmic- linear ($\ln\varepsilon = A + B\,\lambda$) and a polynomial ($\varepsilon = A\,(1 + \lambda)^B$) emissivity dependence on wavelength respectively. The congruence of the results confirmed the consistency of the method. The band around the experimental values represents the standard deviation over 256 successive spectra. The agreement with data reported in [10] was excellent. Fig. 4.17 shows a comparison between the true temperature measured by the 0.6494 μm diode used as a single channel pyrometer and the temperature fitted over the whole spectrum via steps 2.3.4. above. To obtain the true temperature at 0.6494 μm, the 0.65 μm average value of the fitted emissivity was employed. The agreement was excellent, and the noise affecting the fitted T gives an idea of the noise disturbance, both instrumental and numerical, arising from the whole procedure. Such disturbance was contained within ± 1% of the measured value.

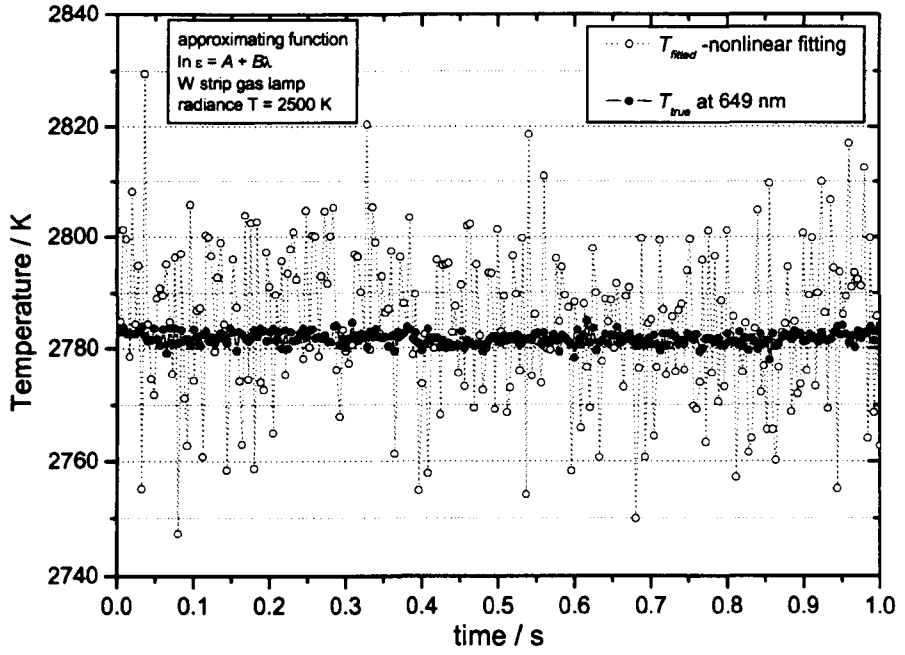

Fig. 4.17: Comparison between the temperature measured by the 649.4- nm photodiode and the temperature fitted over 185 wavelengths.

Other tests of the method were carried out by measuring the melting point of ZrO_2: Y_2O_3 samples, in a co-operation project between ITU and ENEA Bologna (Italy).

4.2.5 Temperature measurements

Spectral ratio temperature

In the initial scheme, the temperature was measured making use of both the IVTAN pyrometer channels. With the simultaneous measurement of the spectral radiance temperature T_λ at two distinct wavelengths one could obtain the sample true temperature from the λ_1 - λ_2 spectral ratio temperature, defined as:

$$T_{sr} = \frac{T_{\lambda 1} T_{\lambda 2} (\lambda_1 - \lambda_2)}{\lambda_1 T_{\lambda 1} - \lambda_2 T_{\lambda 2}}. \tag{4.17}$$

Combining Eq. (4.17) and (4.3'') one obtains

$$\frac{1}{T_{sr}} = \frac{1}{T} + \frac{\lambda_1 \lambda_2}{C_2 (\lambda_1 - \lambda_2)} \ln \frac{\varepsilon_1 \tau_1}{\varepsilon_2 \tau_2}. \tag{4.18}$$

$T_{sr} = T$ if $\varepsilon_1 \tau_1 = \varepsilon_2 \tau_2$, i.e. in the hypothesis- consistent for uranium dioxide- that the sample surface is a grey body and that also the optical path transmittance is independent of λ. Under such hypothesis, once $T_{\lambda 1}$ and $T_{\lambda 2}$ were measured, the true temperature T could be advantageously obtained through Eq. (4.17) with no need for the complicated determination of sample emissivity and optical path transmittance. Unfortunately, due to its definition as a ratio, the value of T_{rc} was largely affected by the least variation in the emitted thermal radiation intensity, and its determination was therefore extremely sensitive to any error or noise in the values of $T_{\lambda 1}$, $T_{\lambda 2}$, λ_1 and λ_2. Hence it was concluded that the ratio colour temperature method could not be successfully applied.

True temperature from the spectral radiance temperature

As a consequence of the unfeasibility of the above approach, the true temperature of the sample surface had to be obtained for each pyrometer channel from the spectral radiance temperature through Eq. (4.4):

$$\frac{1}{T} = \frac{1}{T_\lambda} + \frac{\lambda}{C_2} \ln(\varepsilon(\lambda, T)\tau(\lambda, P_{gas})) . \tag{4.4}$$

Therefore, the determination of the function $\varepsilon(\lambda, T)$ and of the optical system transmittance $\tau(\lambda, P_{gas})$ became a fundamental operative issue.

Sample effective emissivity

Effective emissivity of stoichiometric and hyperstoichiometric uranium dioxide samples was determined by means of the OSC multichannel pyrometer described in § 4.2.4. However, the precision of these measurements was limited by the low time resolution of the employed device with respect to the high heating and cooling rates produced during the experiments. Moreover, values of emissivity were not fully trustworthy at the beginning of the heating stage, where the temperature increase rate was very high and, because the specimen temperature was still relatively low, the signal intensity was weak with respect to the background noise. On the other hand, in spite of such limitations these *in situ* emissivity measurements yielded results in good agreement with those reported in literature. Two of these measurements are shown in Fig. 4.18a-b. Values of emissivity measured on liquid hyperstoichiometric uranium dioxide samples did not significantly differ from those obtained with the stoichiometric compound. Such results ensured that the values of $\varepsilon(\lambda, T)$ measured by Bober *et al.* [11, 12] and recommended by Fink [13] could be used in this work without adding any significant error to the results.

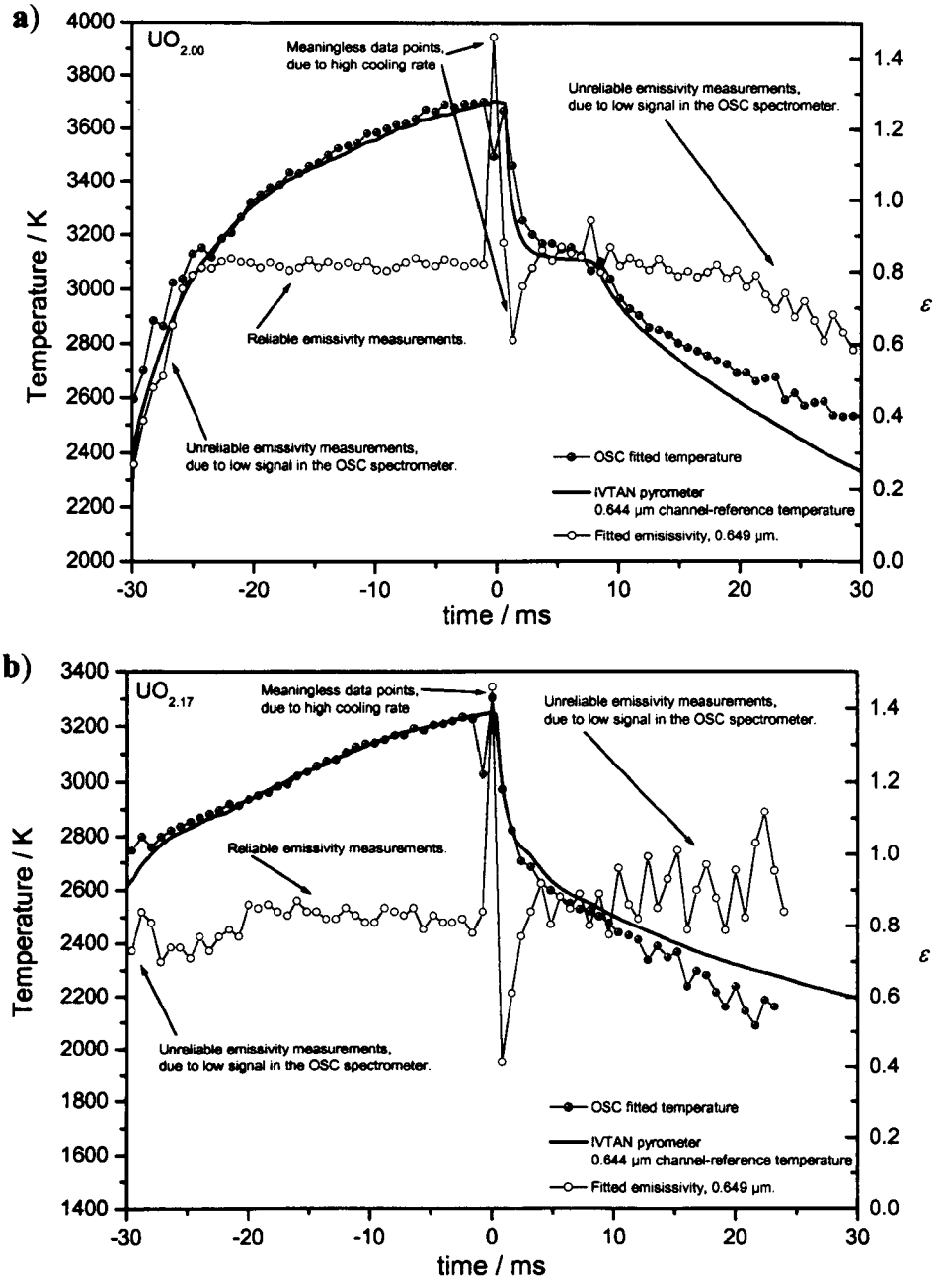

Fig. 4.18: Simultaneous measurements of surface emissivity and temperature on uranium dioxide samples subjected to laser heating:
a) $UO_{2.00}$ stoichiometric sample;
b) $UO_{2.17}$ hyperstoichiometric sample.
No significant difference was detected between emissivity values in stoichiometric samples and hyperstoichiometric samples.

According to the paper of Fink, where several sets of experimental data were critically assessed and fitted, emissivity for solid uranium dioxide in the range 1000 K ≤ T ≤ 3120 K

could be considered constant with wavelength, and only slightly dependent on temperature as in the following equation:

$$\varepsilon = 0.836 + 4.321 \cdot 10^{-6} (T - 3120). \quad (4.19)$$

Similarly, emissivity dependence on wavelength in liquid uranium dioxide for 3120 K ≤ T ≤ 4200 K and 400 nm ≤ λ ≤ 700 nm was recommended as:

$$\varepsilon = 1 - 0.16096 \exp[3.7897 \cdot 10^{-4} (T - 3120) - 3.2718 \cdot 10^{-7} (T - 3120)^2]. \quad (4.20)$$

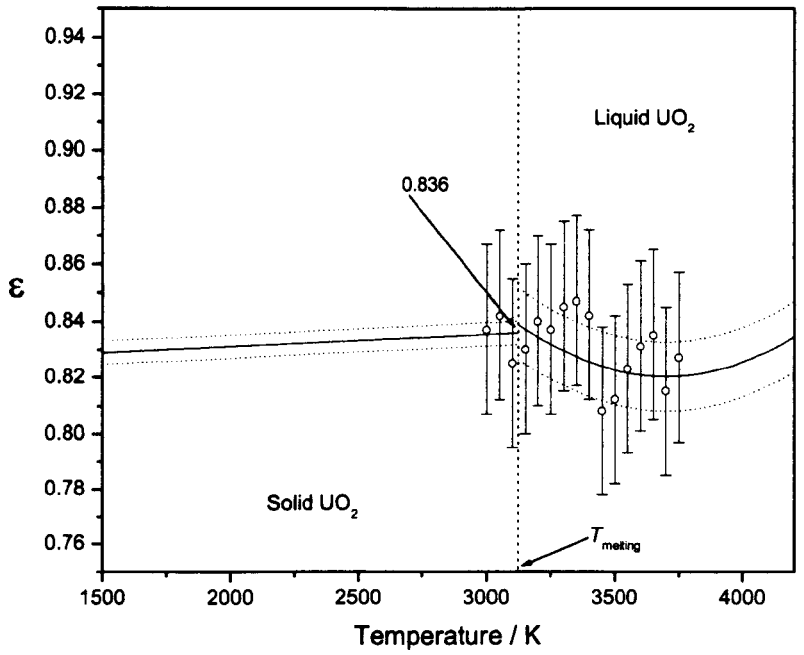

Fig. 4.19: Emissivity of uranium dioxide. Straight line: fitting of literature data [13]. Open circles: experimental points obtained in this work with related uncertainty.

Eqs. (4.19- 4.20) are plotted in Fig. 4.19, along with the uncertainty bands recommended in [13], and with values of emissivity determined in this work on liquid urania samples.

According to Eq. (4.4), an uncertainty of ± 2.5 % in the value of the factor ε (λ, T) would yield an uncertainty of approximately ± 0.25% in the true temperature T in the range 2000 K ≤ T ≤ 3800 K. This error could not be distinguishable within the temperature scale uncertainty implied by the pyrometer calibration itself (± 0.5%). Therefore, for the sake of

simplicity, the mean value ε = 0.836 was taken for all the temperatures and all the compositions. It was supposed that such an approximation would in no case generate any error larger than ± 0.25 % in the true temperature.

Total transmittance of the optical system

The optical system transmittance $\tau(\lambda, P_{gas})$ was determined for the optical paths between the sample surface and the temperature detectors.

The total transmittance of the optical path including the high-pressure buffer gas in the vessel and *n* optical elements (Fig. 4.3) between the specimen and the pyrometer (windows, lenses, mirrors, etc.) was given by

$$\tau(\lambda, P_{gas}) = \tau_{gas}(P_{gas}) \cdot \prod_{i=1}^{n} \tau_i(\lambda). \qquad (4.21)$$

The term $\tau_{gas}(P_{gas})$ represents the transmittance of the high- pressure buffer gas layer above the sample surface. In the case of the IVTAN two- channel pyrometer (see Fig. 4.3), the thermal radiation emitted by the hot sample surface came to the pyrometer objective through the protective sapphire glass above the specimen, the sapphire window of the high- pressure cell, the YAG dichroic mirror and by reflection from the Al mirror. The reflectivity of this latter could be written in Eq. (4.21) as a transmittance factor.

As for the OSC multichannel pyrometer, the optical path included crossing two sapphire windows in the high- pressure cell and reflection from a glass prism.

In both cases, a transmittance factor had to be determined for each of the listed optical elements, along with the term τ_{gas}, in order to obtain τ from Eq. (4.21).

Spectral transmittance of the high-pressure cell windows and of the YAG dichroic mirror at 45° incidence was measured with an UV-Visible recording spectrophotometer (Shimadzu) around the pyrometer channels wavelengths. Resulting transmittances are shown in Fig. 4.20. The multilayer YAG dichroic mirror, nearly transparent at the wavelengths of the

pyrometer, reflected almost perfectly the wavelengths close to the YAG laser (λ = 1.06 μm) at an incidence angle of 90°. The standard Al multilayer mirror reflectivity is reported in [14] as a function of λ.

In the case of the OSC multichannel pyrometer, the transmittance of the glass prism was determined by measuring the ratio between the light intensities of a standard lamp- generated beam before and after a 90° reflection in the prism itself.

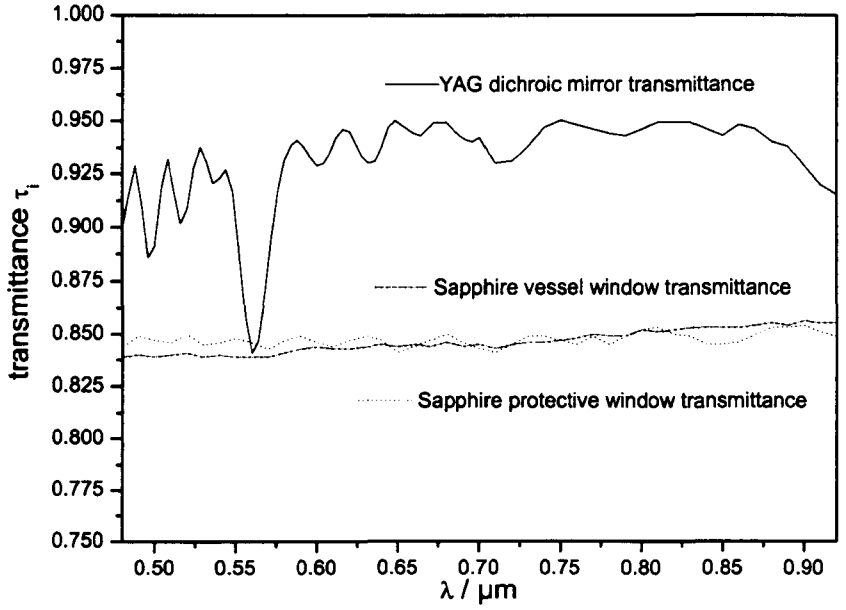

Fig. 4.20: Transmittance of some optical elements between the sample surface and the IVTAN optical pyrometer objective.

The whole attenuation of intensity due to all the optical elements was also directly measured at atmospheric pressure with two He-Ne probe lasers, with λ = 0.632 μm and λ = 0.540 μm by measuring with a Newport Optical Power Meter (model 835) the carried power density before and after crossing the optical path. With the same probe lasers and the same procedure the Al mirror reflectivity was also measured, confirming the literature data. Comparing the laser-measured transmittance of the whole optical path with the product of the transmittances obtained for each single element yielded a 2.5% uncertainty in the

absolute value of τ, accounting for an uncertainty of about 0.25 % in the final measurement of the true temperature.

Explicit temperature dependence of τ has not been considered in Eq. (4.21), as generally one can assume that all the optical elements involved remained at room temperature throughout an experiment. This is not true for the buffer gas layer in contact with the specimen surface, the transmittance of which implicitly depends on temperature, as also does the local gas density. This latter point is treated in the next subsection.

Transmittance of the high-pressure gas system

This subsection deals with the determination of the dependence of the term τ_{gas} in Eq. (4.21) on the gas pressure in the experimental chamber. More precisely, the term τ_{gas} does not indicate the transmittance of the gas itself, but rather the effect brought about by variations in the buffer gas pressure on the total transmittance of the whole high-pressure system. Such an effect, mainly due to the radiation reflection at the gas/sapphire interfaces, resulted in an apparent gas transmittance factor larger than 1.

The total transmittance changes with gas pressure for the system (buffer gas + high-pressure vessel employed in the melting experiments) was measured by means of the OSC multichannel pyrometer described in § 4.2.4. The autoclave used in the high-pressure melting experiments was provided with two sapphire windows (see Fig. 4.3), the protective window immediately above the sample surface and the autoclave window. A thick buffer gas layer was included between the two windows, where density and pressure were homogeneous. The gas density in the vicinity of the hot sample surface decreased instead due to the high temperature, according to the ideal gas state equation:

$$P = \rho^* k_B T, \tag{4.22}$$

where k_B = Boltzmann constant and ρ^* = number of atoms per unit volume.

Since pressure remained unchanged due to the large total volume of the gas in the vessel and in the connected pipes, according to Eq. (4.22) the density ρ^* had to decrease as the temperature increased in this zone.

In such situation the path of the light beam from the sample surface through the high-pressure vessel could be schematised as follows:

LOW DENSITY GAS (≈ AIR) | SAPPHIRE | HIGH DENSITY GAS | SAPPHIRE | AIR

In order to reproduce such a sequence experimentally in a way suitable for transmittance measurements, it was assumed that, as far as optical effects were concerned, the first layer of low-density gas was equivalent to a layer of air at room pressure, and that the main transmittance loss was due to reflections at the interfaces. Thus an experiment was prepared as shown in Fig. 4.21: the radiation originating from an integrating sphere reached the OSC objective through a high-pressure vessel filled with the gas under investigation and closed at the extremities by two sapphire windows. The number and the nature of the interfaces crossed by the light beam were thus just the same as in the sequence above.

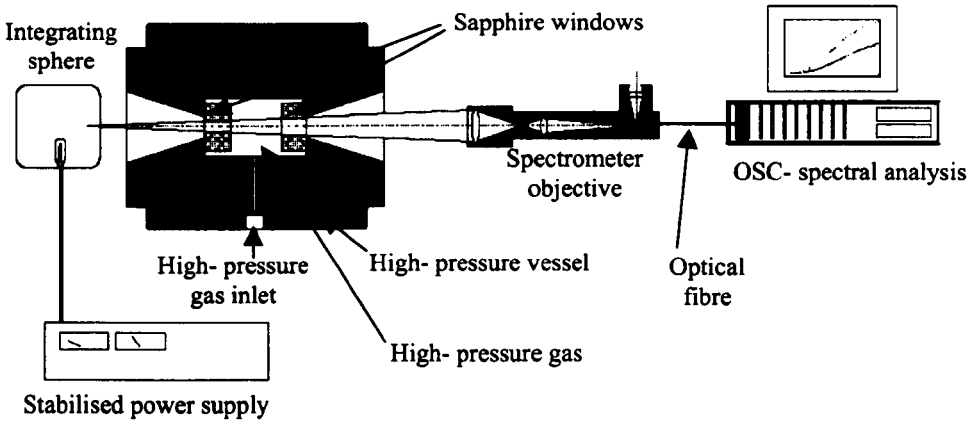

Fig. 4.21: Schematic of the experimental setup implemented for the measurement of the high pressure system transmittance changes depending on the buffer gas pressure.

An integrating sphere irradiated by a halogen lamp was chosen as light source in order to cancel the effect of possible shifts of the objective focus due to the changes in the gas

pressure. A steel shield was placed between the integrating sphere and the high-pressure vessel in order to avoid heating the autoclave. Spectra of the transmitted "probe" light beam were recorded successively for different pressures of the gas in the vessel. The spectrum measured at each pressure was divided by the reference spectrum recorded with the gas in the vessel at atmospheric pressure.

The resulting graph plotted in Fig. 4.22 shows the relative transmitted light intensity change due to the buffer gas pressure. The same graph shows that the observed transmittance dependence on the wavelength was negligible, at least within the uncertainty due to the background noise. The transmittance factor τ_{gas} (P_{gas}) in Eq. (4.21) was then taken as the ratio, averaged over the whole spectrum, between the intensity detected at pressure P and the intensity detected at room pressure. An increase of τ_{gas} was observed with increasing gas pressure. Such an effect was due to the optical behaviour at the interfaces.

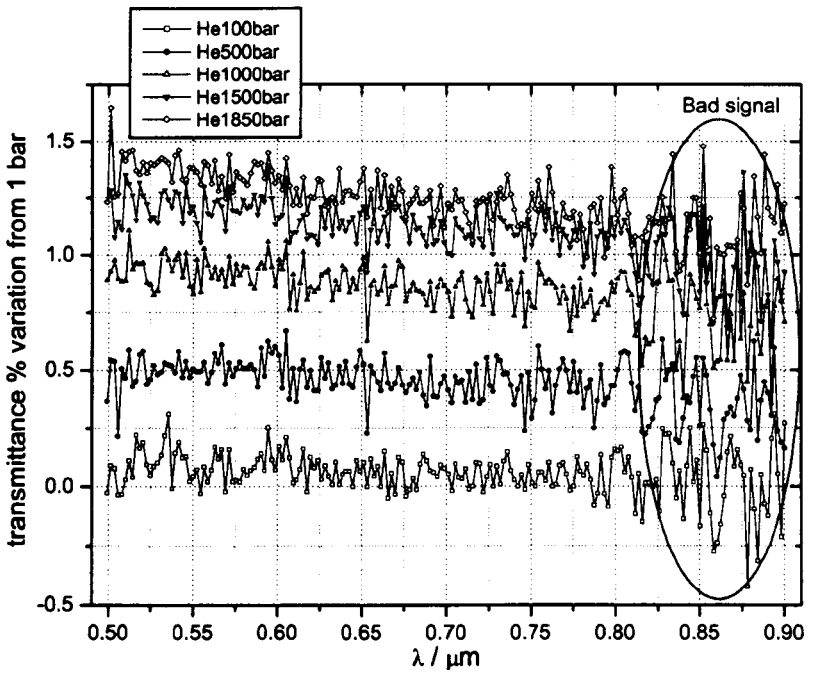

Fig. 4.22: Spectral transmittance dependence on the buffer gas pressure for the high- pressure system filled with He, referred to the transmittance at room pressure. Transmittance variation slightly decreases with λ, but this dependence could be reasonably neglected for sake of simplicity.

To explain this, one should consider that for an electromagnetic wave impinging perpendicularly to the interface between gas (refractive index n_g) and sapphire (refractive index n_s), the following relation holds for the energy reflected E_R (see, for instance, [15]):

$$E_R \propto \left(\frac{n_s - n_g}{n_s + n_g} \right)^2 . \tag{4.23}$$

The relation between refractive index, n_g, and pressure in an ideal gas stems from the equation:

$$n_g^{\,2} = 1 + \frac{\rho^* \alpha}{\varepsilon_0} . \tag{4.24}$$

In Eq.(4.24), ρ^* indicates the number of atoms in a unit volume, as in Eq. (4.22), α the atomic polarizability of the investigated gas, and ε_0 the dielectric constant in vacuum. Combining the ideal gas state equation (4.22) with Eq. (4.24), one obtains

$$n_g = \sqrt{1 + \frac{P\alpha}{k_B T \varepsilon_0}} , \tag{4.25}$$

P being the gas pressure.

Therefore, as the gas refractive index increased with pressure according to formula (4.25), the difference (n_s - n_g), and hence the energy reflected in (4.23) were reduced. Thus more radiative energy was passing through the optical system at pressures higher than the atmospheric one due the lower reflection at the interfaces, yielding an apparent $\tau_{gas}(P) > 1$.

The measurement was repeated using helium and neon as they were the buffer gases employed for the high-pressure melting experiment; and with argon for comparison. Results are displayed in Fig. 4.23. The observed τ_{gas} clearly increased with the atomic number of the gas.

The transmittance dependence on pressure interpolated by a polynomial fitting was then put in Eq. (4.21) as the best approximation of factor $\tau_{gas}(\lambda, P_{gas})$.

The total uncertainty affecting the factor $\tau(\lambda, P_{gas})$ in Eq. (4.4) was conservatively estimated as $\approx \pm 2.5$ %, accounting for a $\pm$ 0.25% approximately in the true temperature uncertainty.

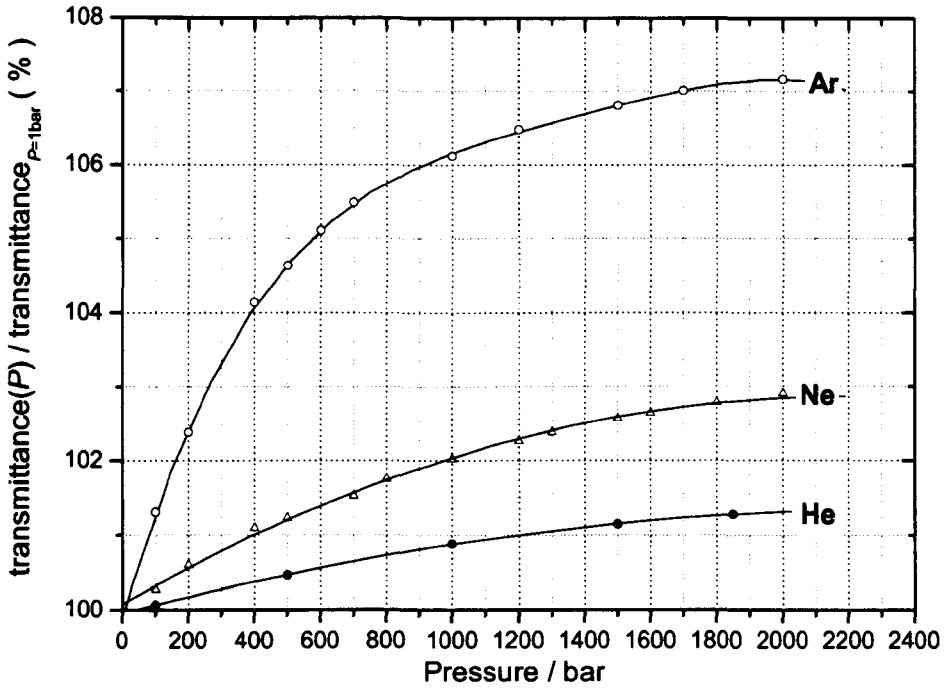

Fig. 4.23: High- pressure system total transmittance dependence on pressure using He, Ne and Ar.

True temperature determination

Finally, the true temperature of the sample surface for both pyrometer channels was obtained from Eq. (4.4). Fig. 4.24 shows the output graphs of a typical melting point measurement on stoichiometric uranium dioxide. A clear thermal arrest is visible at the solidification temperature on the thermograms recorded by the two pyrometers. The OSC multichannel pyrometer was mainly used for emissivity measurements of the liquid sample. However, due to the low time resolution, defined by the integration time τ_i, data points measured by this latter device during the fast cooling stage and the freezing arrest were affected by numerical instability in the calculation procedure described in § 4.2.4. Therefore, the specimen freezing temperature and the solid surface emissivity measured by the OSC were only partly reliable.

Freezing temperature obtained by the fitting procedure over 185 channels was only checked to be in reasonable agreement with the results provided by the two-channel IVTAN pyrometer.

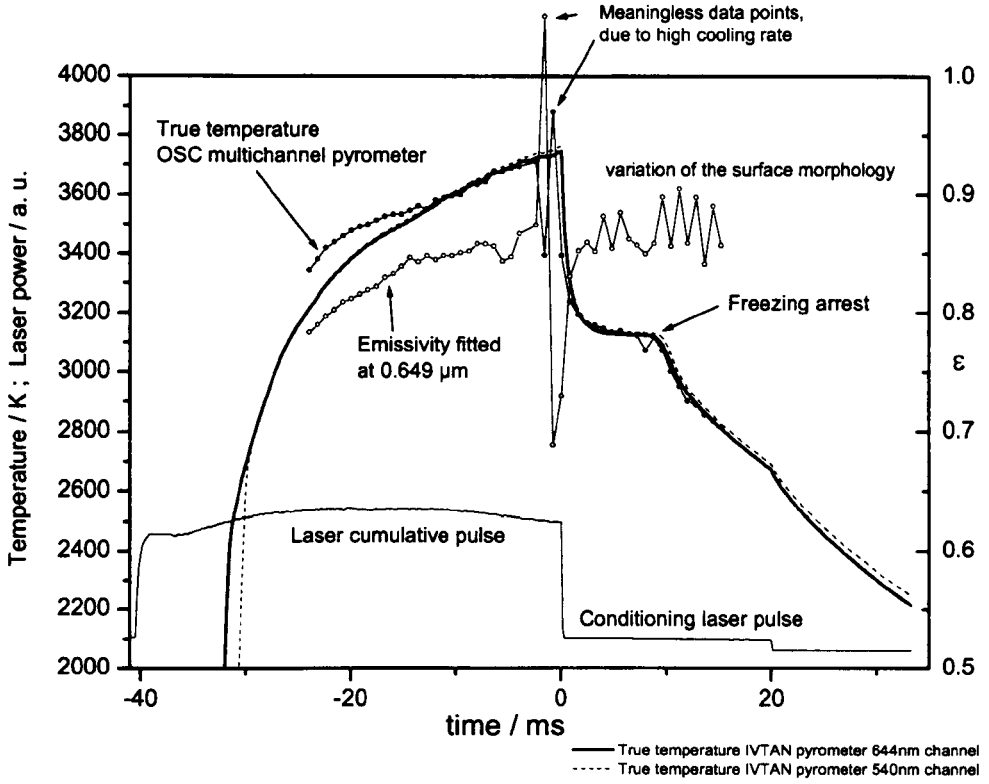

Fig. 4.24: Results of a measurement on a stoichiometric UO_2 sample. Emissivity is shown at one wavelength only (0.649 µm), as the sample could be considered as a grey body.

As expected, no reproducible thermal arrest upon melting was noticed in the ascending flank of the thermogram because during the heating stage the power laser beam heated the sample surface *locally*, so that equilibrium conditions could never be realised. In fact, the heat delivered onto a spot on the surface could diffuse into the rest of the sample and, since only a small portion of the specimen was attained by the melting front, the process never reached the equilibrium. Moreover, the speed of diffusion depended on the thermal conductivity of the investigated material and, since thermal conductivity is approximately the same both in solid and liquid uranium dioxide (§ 2.3.2), heat transport dynamics were practically

unaltered during the heating stage both before and after the formation of liquid inside the sample. For this reason, not even an inflection could be observed at the melting temperature in the ascending flank of the thermogram.

The situation was different during the cooling stage, when the liquid mass was allowed to cool naturally and equilibrium conditions were attained upon freezing in the solidifying mass; then a clear thermal arrest could be observed.

On the other hand, a slight but reproducible slope decrease was always observed in the ascending flank of the thermogram possibly due to evaporation well above the melting point, and to damping of the laser power intensity over the pulse.

In general, the temperature measured by the 0.644-μm channel was used as a reference, as this channel was directly calibrated against a standard lamp. Initially, the 0.540-μm channel temperature was used as confirmation only. The disagreement between the two never exceeded the 1% uncertainty affecting the temperature scale as defined by the pyrometer calibration in Eq. (4.7). The IVTAN pyrometer λ_2 channel was finally not used to measure the specimen temperature, but rather employed in the "reflected coherent light" method described in the next section.

Accuracy of the temperature measurements

Test measurements on standard materials of known optical properties and melting point were not feasible under the conditions of interest for this work. The experimental apparatus was tested on other high- melting materials such as graphite and tungsten, and results in good agreement with those reported in literature obtained. However, none of the investigated systems could be regarded as a reliable standard because none of the high- temperature thermophysical and thermodynamic properties of those refractory materials could be considered to be well assessed. Moreover, in all cases experimental conditions were quite different from those produced during melting point measurements on uranium dioxide, in

which high non-congruent evaporation rates and fast oxygen diffusion in the condensed material took place. Therefore, accuracy limits of the temperature measurements could not be defined in terms of systematic errors. Such limits were determined as an uncertainty band. This accuracy limit band was obtained by combining, according to the law of propagation of errors, calibration and emissivity/ transmittance uncertainties, assuming a uniform statistical distribution over the uncertainty bands.

The uncertainties to be taken into account were the following: uncertainty $\delta T_{calibration}$ with which the used temperature scale was defined by the pyrometer calibration procedure (§ 4.2.3), uncertainty δT_{ε} stemming from the emissivity $\varepsilon(\lambda, T)$ of the sample surface, uncertainty δT_{τ} due to the effective transmittance $\tau(\lambda)$ of the optical elements crossed by the thermal radiation emitted by the hot sample and uncertainty $\delta T_{\tau gas}$ of the high- pressure buffer gas layer transmittance. The cumulative uncertainty was

$$\delta T = (\delta T^2_{calibration} + \delta T^2_{\varepsilon} + \delta T^2_{\tau} + \delta T^2_{\tau gas})^{1/2} . \qquad (4.26)$$

Substituting the experimental values obtained for the terms in the right-hand side of Eq. (4.26), we have

$$\delta T\% = (0.5^2 + 0.25^2 + 0.25^2 + 0.25^2)^{1/2} = 0.66\ \%$$

Thus a total accuracy of ± 0.7 % on the measured temperature was taken as conservative in the measurement of the melting point of stoichiometric uranium dioxide samples. The uncertainty affecting the measured melting point was larger in hyperstoichiometric specimens, due to the additional uncertainty in the sample composition, to the higher complexity of the solidification process and the resulting difficulty in the interpretation of thermograms. In the worst cases, for highly hyperstoichiometric samples (O/U > 2.10), data dispersion could be larger than ± 2% of the average measured melting point.

4.2.6 The method of coherent reflected light

In addition to the thermal arrest observation, an independent effect was produced and analysed in order to provide a further means of detecting the onset of melting and solidification on the sample surface.

A probe laser beam was directed onto and reflected by the sample surface. Observation of the reflected light intensity permitted the detection of the exact instants at which melting and freezing occurred.

To realise such a procedure, an additional low power (≈ 700 mW) CW Ar laser (λ = 514 nm) was focused onto the sample surface in the centre of the zone concerned with the melting-freezing process. The λ_2 channel of the IVTAN pyrometer was tuned at the same wavelength in order to detect the Ar laser radiation reflected by the specimen. The method is graphically shown in Fig. 4.25. The fraction of the 514 nm coherent light reflected by the surface and detected by the pyrometer depended on the angular reflectivity of the sample. During the heating stage of an experiment, the first appearance of liquid on the surface caused a sudden change in the angular reflectivity leading to a well-defined variation in the light signal. Vibrations of the liquid mass resulted in oscillations of the reflected light intensity, and both disappeared when the freezing point was reached on cooling.

The advantage of such a method consisted of the possibility to locate the temperature of appearance/ disappearance of the liquid with great reliability (with practically no sources of error). Both *solidus* and *liquidus* points could be accurately determined from the reflected light signal analysis, independent of complex phenomena, connected to the fast diffusion from the solid into the liquid phase in the presence of high temperature and concentration gradients, which had hindered the readability of thermograms in the thermal arrest method.

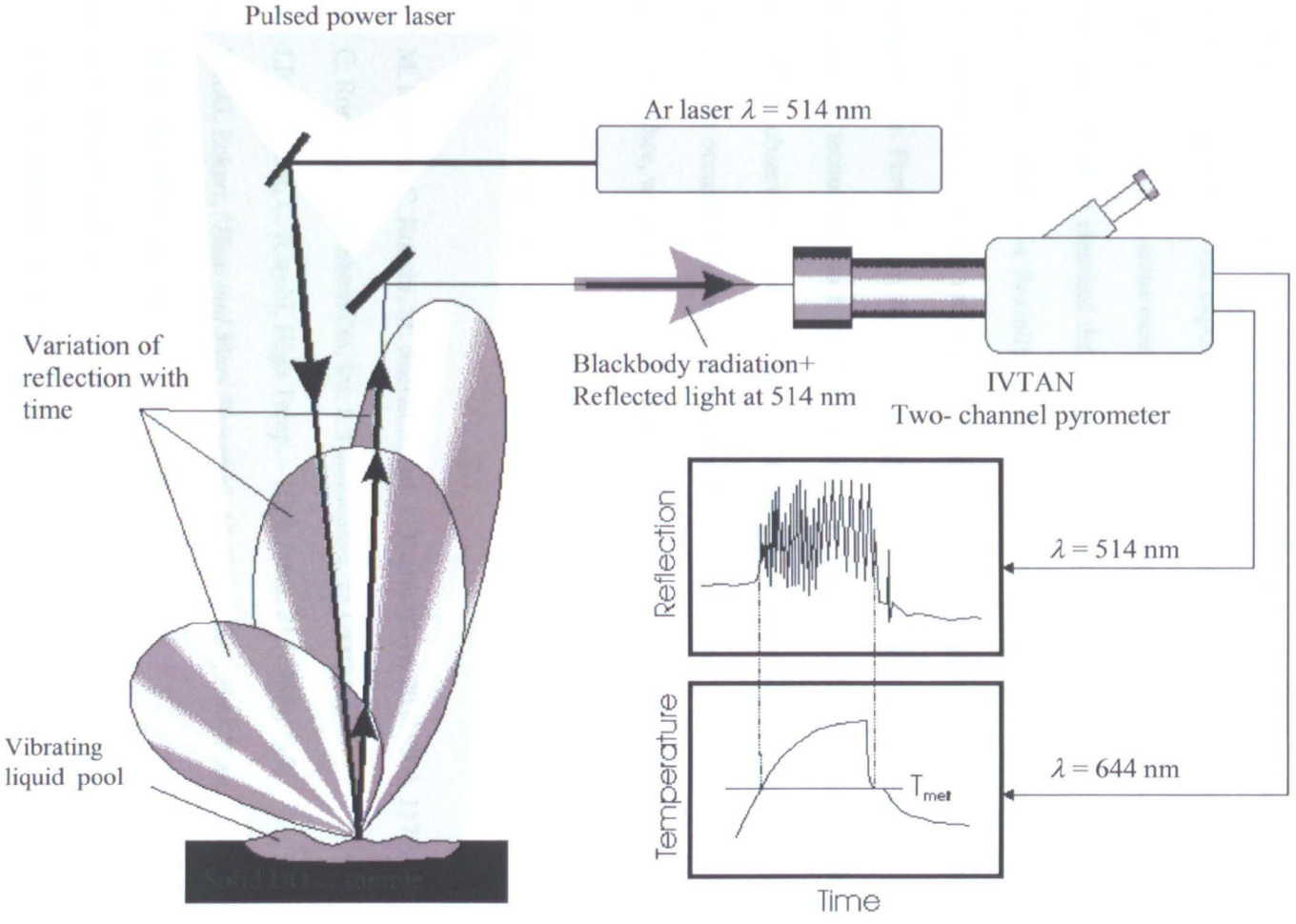

Fig. 4.25: The coherent reflected light method.

4.3 Conclusions

A novel method was developed to investigate the melting behaviour of refractory substances characterised by chemical instability at high temperature. This experimental approach tackles in an original manner the experimental difficulties encountered by other researchers that in the past attempted the same measurements with more traditional methods.

Besides allowing a classical thermal analysis based on thermograms recorded by means of optical pyrometers, the flexibility yielded by the use of pulse laser heating made possible direct observation of the melting onset by heating the sample surface just above the fusion temperature. Furthermore, the current experimental investigation was based on a combined alternative technique, such as the method of coherent reflected light. This technique permitted observation of the phase transition points independently of the complex phenomena occurring during melting/freezing of a thin layer of material very close to the sample surface, where significant temperature and concentration gradients were produced.

References Chapter 4

1. M. Musella, C. Ronchi, M. Sheindlin, Int. J. Thermophys. **20** (1999), 1177.
2. C. Ronchi and M. Sheindlin, Int. J. Thermophys. **23** (2002), 293.
3. J.P. Hiernaut, C. Ronchi, High Temp. – High Press. **21** (1989), 119.
4. E.R.G. Eckert, "*Heat and Mass Transfer*", McGraw- Hill, New York, 1959.
5. M.A. Sheindlin, Sov. Rev. B. Therm. Phys. **4** (1992), 1.
6. D.P. Dewitt and Gene D. Nutter, "*Theory and Practice of Radiation Thermometry*", J. Wiley and Sons, New York, 1988.
7. M. A. Sheindlin and V. N. Senchenko, Proc. Int. Symp. on Major Problems of Present-Day Radiation Pyrometry, Moscow 1987, 220.
8. M.A. Sheindlin, Sov. Rev. B. Therm. Phys. **4** (1992), 1.

9. W. Heinz, D. Manara, C. Ronchi, M. Sheindlin, "*Multichannel Pyrometry Applications in High Temperature Thermophysics*" presented at the 6th International Workshop on Subsecond Thermophysics, September 26-28 2001, Leoben, Austria.
10. Latiev, Petrov *et al.*, "*Radiation properties of solids*", Energia, Moscow, 1974.
11. M. Bober, J. Singer, K. Wagner, J. Nucl. Mater. **124** (1984), 120.
12. M. Bober, H.U. Karow and K. Muller, High Temp. – High Press. **12** (1980), 161.
13. J.K. Fink, J. Nucl. Mater. **279** (2000), 1.
14. *"The Book of Photon Tools"*, Oriel Instruments Catalogue, 12-10.
15. R.P. Feynman, R.B. Leighton and M. Sands: "*The Feynman Lectures on Physics*" Addison–Wesley Publishing Company, Reading, Massachusetts, 1964, Vol. II, Chapters 32- 33.

Chapter 5

Material preparation and characterisation

5.1 Sample preparation

5.1.1 Method used for the preparation of UO_{2+x}

The preparation of samples used in this melting-transition study was of the foremost importance to ensure good reliability of the final results. As mentioned in the previous chapter, the chosen experimental technique for thermal analysis used a fusion zone on the specimen surface, where equilibrium conditions could only be attained locally. A good reproducibility of experimental results could be obtained only from samples that were sufficiently homogeneous and reproducible from one to another.

The starting material for most of the investigated samples consisted of commercial nuclear grade UO_2 pellets, fabricated by Advanced Nuclear Materials Co., for which industrial standard manufacturing ensured good homogeneity and reproducibility of physical properties from one sample to another[1].

Table 5.1 shows the impurities contained in the Advanced Nuclear Materials Co. stoichiometric UO_2 samples.

[1] *Alternatively, UO_{2+x} samples were prepared at the ITU- Karlsruhe by blending and pressing UO_2 and U_3O_8 powders in the proportions needed to yield the desired total composition. Some of these specimens were analysed as "green pellets", i.e. without any sintering procedure, others were sintered under a suitable gas flow, in order to increase density and morphological homogeneity. However, in both cases these specimens were inhomogeneous, both in composition and in physical properties, possibly due to the rapid and irregular oxidation that affected the pressed powders even before the sintering procedure. This was mainly evidenced by the poor reproducibility of the melting point measured in different parts of the same sample, and in different samples. (Continues)*

Table 5.1: Impurity analysis of the Advanced Nuclear Materials Co. stoichiometric UO_2 samples as fabricated.

Element	Concentration (*ppm* in weight)
Li	<1
B	<1
C	56
N	11.7
F	6.8
Na	6.1
Al	208
Si	4.8
P	1.0
S	40
Cl	44
Ti	1.0
V	<1
Cr	1.3
Fe	11.3
Ni	1.7
Cu	1.8
Y	<1
Zr	2.3
Mo	<1
Ba	3.0
Ce	<1
Pb	1.0

These pellets were cylinders of diameter 8.3 mm and height 12 mm (Fig. 5.1). Each pellet was cut into three parts of approximately 4 mm height to fit into the sample holder of the high- pressure vessel. The cutting process was performed with a Buehler Isomet low- speed saw using a diamond- coated steel blade cooled and lubricated in ISOCUT® oil. Urania slices obtained were successively washed in ethanol and acetone. Samples were then annealed in an alumina oven for two hours at 673 K under an Ar 94% + H_2 6% flow in order remove oil or ethanol possibly left following the cutting process. Such a slightly reducing argon- hydrogen mixture was employed to remove possible excess of oxygen over the stoichiometric composition.

(Continued from page 116) Hence, all the results reported in this work were obtained on samples obtained starting from Advanced Nuclear Materials industrial samples only.

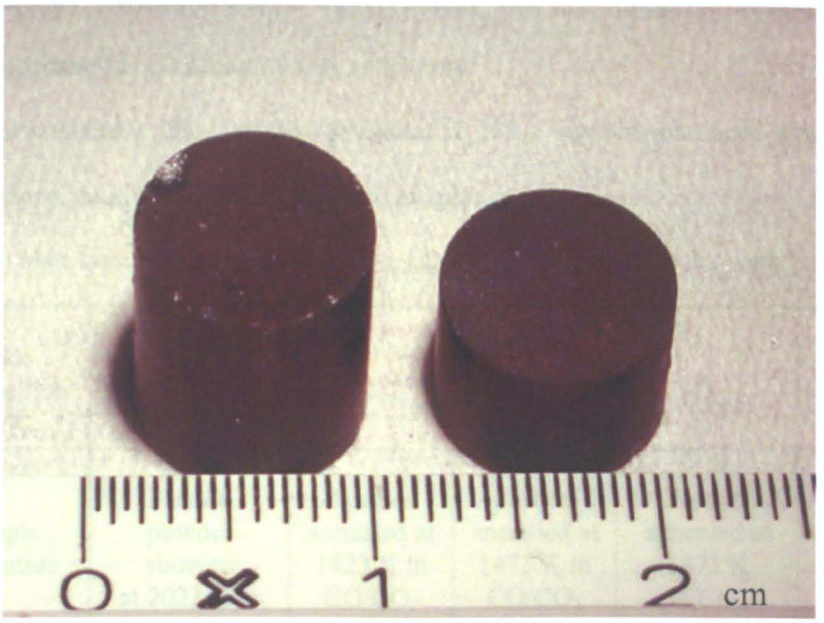

Fig. 5.1: Advanced Nuclear Materials Co. uranium dioxide pellets used as samples in the melting point measurements performed in this work.

Some samples were processed with a further annealing in a flux of Ar + 6% H_2 mixture at 1273 K to ensure that the composition was stoichiometric.

The pellet composition was determined by thermogravimetric measurements (see § 5.2 for a description of all the characterisation techniques used): after annealing, the O/U ratio was determined to be 2.000 ± 0.005.

Sample density was about 10.5 g cm^{-3}, i.e. 95% of the theoretical value.

To obtain hyperstoichiometric samples, the original pellets were treated in an alumina tube furnace at different temperatures under a CO/CO_2 oxidising gas flow of suitable composition, according to the UO_{2+x} Ellingham diagram briefly discussed in the next section. The final composition was estimated by the difference in the sample weight before and after the treatment. To ensure that such a weight difference was due to oxidation only, some samples were reduced again to stoichiometric UO_2 in an Ar + 6% H_2 flux, and the weight

difference between oxidised and stoichiometric state was checked to be the same as that measured after the oxidation treatment.

More accurate thermogravimetric measurements then confirmed the composition of the hyperstoichiometric samples prepared in this way.

Table 5.2 contains a list of some representative UO_{2+x} samples produced along with their compositions, densities and heat treatment program.

Table 5.2: Main features of some representative UO_{2+x} samples analysed in this work.

Oxide composition	$UO_{2.00}$	$UO_{2.03}$	$UO_{2.08}$	$UO_{2.11}$	$UO_{2.2}$
Sample fabrication	Pressed powder sintered at 2023 K in $Ar:H_2$	Further annealed at 1423 K in CO/CO_2 1:100	Further annealed at 1473 K in CO/CO_2 1:100	Further annealed at 1473 K in CO_2	Further annealed at 1573 K in CO_2
Grain size	10 μm	10 μm	10 μm	5 μm	5 μm
Density	$1.05\ 10^4$ kg m^{-3} (95% th.d.)	$1.05\ 10^4$ kg m^{-3} (95% th.d.)	$1.06\ 10^4$ kg m^{-3} (96% th.d.)	$1.07\ 10^4$ kg m^{-3} (97% th.d.)	$1.08\ 10^4$ kg m^{-3} (97% th.d.)

The following procedure was implemented in order to make sure that the samples produced were homogeneously oxidised from the surface inward. A set of three or four specimens was annealed under oxidising gas flow for a certain time. After that, the new composition of each specimen was determined from the weight difference. The annealing was repeated on fresh samples modifying the position of the specimens in the furnace to ensure that the same composition (within a 1% tolerance) was obtained in all the samples of one set (normally this could be obtained after the first run). Oxidised specimens were then subjected to the same heat treatment a second time. If upon repetition of the procedure the sample composition did not change, then the parameters of the heat treatment were certainly those required in order

to obtain homogeneous composition under equilibrium conditions. Homogeneity of the samples was finally confirmed by means of optical ceramography and SIMS (§ 5.2.5-6).

5.1.2 UO_{2+x} Ellingham diagrams

Ellingham diagrams [1] plot the free energy of the oxidation reaction of different materials as a function of temperature (Fig. 5.2). These diagrams are useful in order to determine the thermodynamical stability of metals and oxides toward oxidation. The values of ΔG^0 on an Ellingham diagram are expressed in kJ per mole O_2 in order to facilitate a direct comparison of the stability of different oxides, i.e. the lower the position of the line on the diagram the more stable is the oxide.

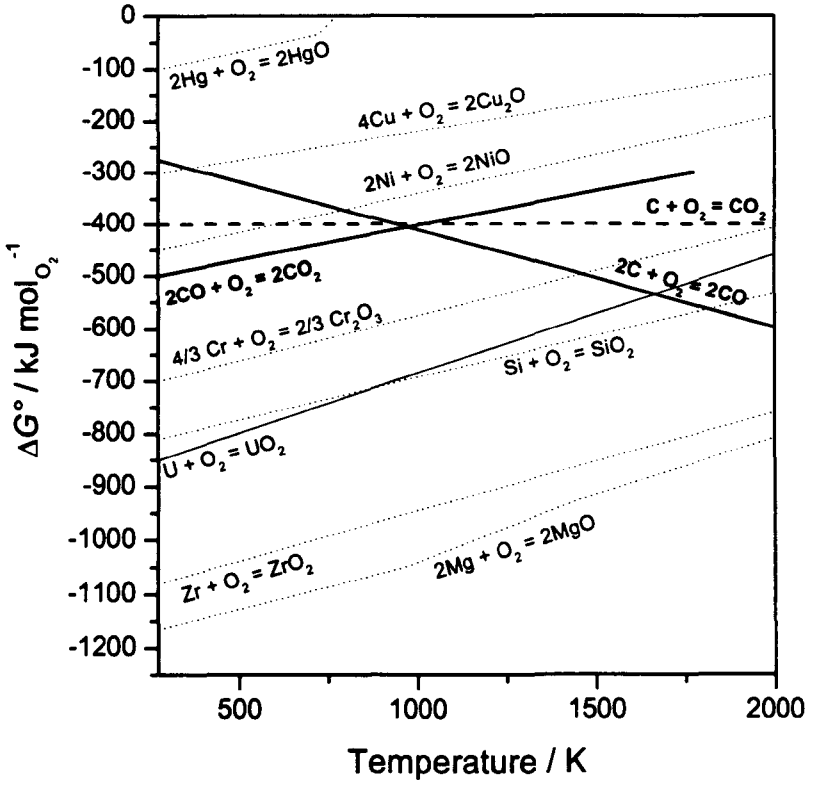

Fig. 5.2: Ellingham diagrams for the free energy of formation of some metallic oxides.

For a given reaction

$$M + O_2 \leftrightarrow MO_2 , \tag{5.a}$$

and taking the activities of M and MO_2 as unity, the following equations can be used to express the oxygen partial pressure at which metal and oxide coexist, i.e. the dissociation pressure of the oxide:

$$RT \ln p_{O_2}^{M/MO_2} = \Delta G_{O_2} , \tag{5.1}$$

In general, Ellingham diagrams are used to plan oxidation and reduction processes in a chemical buffer gas. If CO is employed in a mixture with CO_2, the combined red ox reaction occurring in the gas is:

$$2CO + O_2 \leftrightarrow 2CO_2, \tag{5.b}$$

that yields an oxygen free energy ($\Delta G_{O2} = RT \ln p_{O2}$)

$$\Delta G_{O_2} = \Delta G^0 + 2RT \ln \frac{p_{CO_2}}{p_{CO}} , \tag{5.2}$$

where ΔG^0, the free energy of reaction (5.a) under standard conditions, is, according to [2],

$$\Delta G_0 = -566 + 0.17506\ T \ (\text{in kJ mol}^{-1}). \tag{5.3}$$

Combining Eqs. (5.2) and (5.3) with Eq. (5.1), one can obtain the temperature at which a material is oxidised by the gas mixture CO/CO_2 with given ratio p_{CO2} / p_{CO} . Such a temperature and the corresponding oxygen potential give the intersection point between the line representing the free energy of the oxidising gas and the line representing the free energy of oxidation of the material (Fig.5.2).

Since the slope of the oxidising gas free energy vs. temperature plot depends on the composition of the gas itself, oxidation processes can be planned by selecting different gas compositions and correspondingly different annealing temperatures.

In this work, CO/CO_2 mixtures were employed with different compositions depending on the degree of hyperstoichiometry required for the different urania samples.

The general oxidation reaction of uranium dioxide is:

$$2UO_2 + xO_2 \leftrightarrow 2UO_{2+x} . \qquad (5.c)$$

The oxygen potential governing reaction (5.c) depends on temperature and on the degree of oxidation in a complex way. Equations for $\Delta G_{O2}^{(c)}$ in various x and T ranges were obtained in [3] by fitting the numerous experimental data available, using chemical models for the oxidation reactions. Fig. 5.3 displays the family of curves obtained in [3] to plot the dependence of oxygen potential on temperature for reaction (c), at various values of x, together with the same curves for reaction (b) at various values of the ratio p_{CO2}/p_{CO}.

The intersection points between curves belonging to different families give the temperature T and the CO/CO_2 gas composition at which the oxidative annealing treatment has to be performed in order to obtain a certain composition UO_{2+x}.

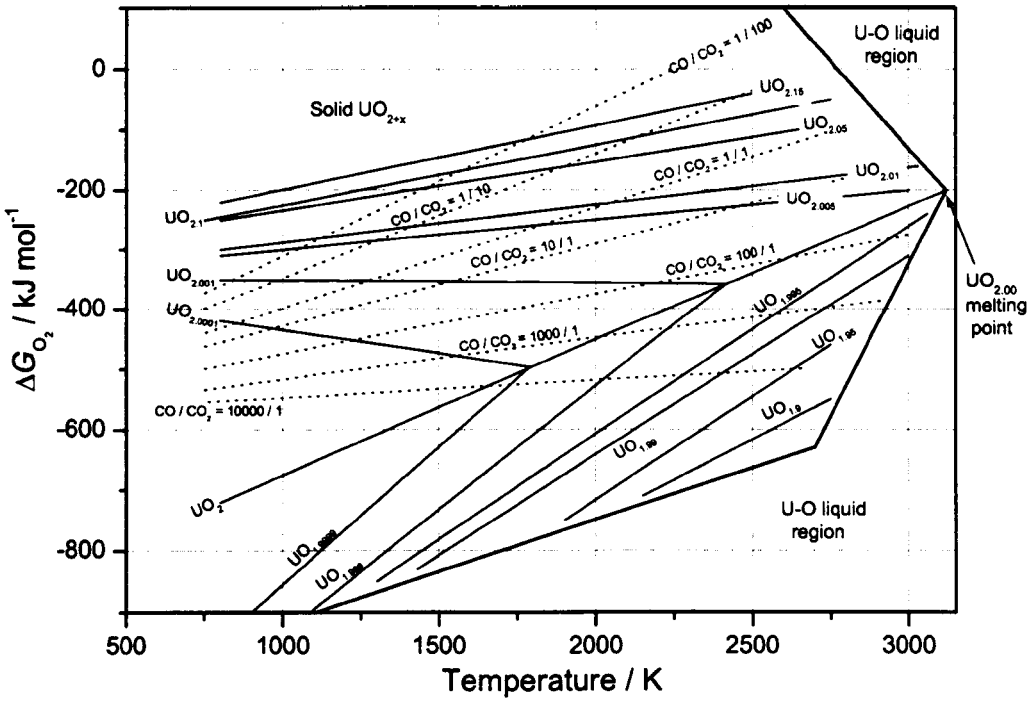

Fig. 5.3: Families of curves plotting the oxygen potential dependence on temperature for the reaction $2UO_2 + xO_2 \leftrightarrow 2UO_{2+x}$ at various values of x and for the reaction $2CO + O_2 \leftrightarrow 2CO_2$ at various values of the ratio p_{CO2}/p_{CO}. Calculations were performed according to [3].

5.1.3 Sample characterisation before and after the melting experiments

The uncertainty affecting the composition and homogeneity of a specimen was translated into the final uncertainty with which the melting transition points were established. Sample composition before the melting point measurements was determined essentially by observation of the weight change following oxidative annealing and by thermogravimetry. EMF measurements were also performed. However, due to the difficulties brought about by the calibration of this latter method, results obtained were only qualitative. A similar obstacle was met in Raman measurements. X-ray diffraction was used in order to detect the presence of different phases in the samples *at room temperature*. Both optical and SEM ceramography were used in order to observe the morphology of the specimens. Optical ceramography and SIMS were used to ascertain the homogeneity of the samples from the surface inward.

Sample characterisation *after* the melting measurements was considered to be unreliable for most of the listed techniques because of the very small size of the molten zone, and the very small volume of material available for analysis. Moreover, due to the impossibility to quench the frozen material to ambient conditions without changing its properties, the results of the post- melting characterisation were possibly not representative of the state of the sample at high temperature. Therefore, post-melting sample characterisation was used as a second-check only. Reliability of the measured fusion points was confirmed by repeating melting experiments under different conditions and checking for the invariance of the observed melting behaviour.

Analytical techniques used in this work are briefly described in the next section 5.2. In the same section results of the sample characterisation before melting experiments are also shown. Post- melting specimen analysis is presented in section 5.3.

5.2 Analytical techniques and sample characterisation before the melting measurements

5.2.1 Determination of sample composition by weight change after oxidising annealing

The change in the sample weight after annealing in CO / CO_2 was considered to be due to oxidation only. Let us indicate with W_{in} and W_{fin} respectively the initial and final weight of the sample, and with x_{in} and x_{fin} the initial and final values of x ($x = |O/U - 2|$). As mentioned in the previous section, the oxidation reaction occurring in a generic uranium dioxide starting samples is

$$2UO_{2+xin} + (x_{fin} - x_{in})\, O_2 \leftrightarrow 2UO_{2+xfin}. \tag{5.d}$$

The number of uranium moles contained in the sample is given by

$$moles_U = \frac{W_{in}}{238.0289 + (2 + x_{in})\, 15.9994}. \tag{5.4a}$$

The number of oxygen moles added to the sample by the oxidative annealing is

$$moles_{oxidation} = \frac{W_{fin} - W_{in}}{15.9994}. \tag{5.4b}$$

Thus, the total number of oxygen moles contained in the sample after annealing is given by

$$moles_O = (2 + x_{in})\, moles_U + moles_{oxidation}. \tag{5.4c}$$

The final O/U ratio is then

$$\left(\frac{O}{U}\right)_{fin} = 2 + x_{fin} = \frac{moles_O}{moles_U}. \tag{5.4d}$$

This scheme was used to calculate the final composition of UO_{2+x} samples starting from any initial composition and after any heat treatment having as sole chemical effect the change of oxygen content in the specimen.

The uncertainty in the final composition obtained with this method was mainly due to the precision of the balance employed ($\pm 10^{-6}$ g). However, large errors could occur if samples

were damaged, or contaminated during the annealing process, so that their weight could change for any reason other than oxidation. Therefore, this relatively simple method was reliable only for a first-approximation determination of the composition, which was determined with better precision by thermogravimetry measurements, described in the next section.

5.2.2 Thermogravimetry

A thermogravimetry (TG) analysis consists in keeping a sample under oxidising heat treatment and simultaneously measure its weight. Thermogravimetric measurements were performed on uranium dioxide samples by using a NETZSCH Simultaneous Thermal Analysis Apparatus STA 409.

A part of a pellet, of approximately 0.5 g, was powdered and put in the thermobalance alumina crucible. The crucible was contained in an oven where the powder was oxidised to pure U_3O_8 under a 50 cm^3s^{-1} air flow with temperature increasing by 5 K min^{-1} up to 1500 K. The crucible was fixed to a high- sensitivity analytical balance that allowed *in situ* weighing of the powder during the oxidation process. The sample oxidation reaction was:

$$6UO_{2+x} + (2-3x)\,O_2 \leftrightarrow 6UO_{2.666}\,. \qquad (5.e)$$

From the weight difference between initial and final powder one could calculate the initial composition through the following formula, where it was assumed that all the weight change was due to oxidation only, i.e. to reaction (5.e):

$$\frac{\Delta W}{W_i} = \frac{W_f - W_i}{W_i} = \frac{MW_{UO_{2.666}} - MW_{UO_{2+x}}}{MW_{UO_{2+x}}}\,, \qquad (5.5)$$

where W_i and W_f are the initial and final weights, and MW stands for „molar weight".

From (5.5) one can get the formula that leads to x from the measured $\Delta W / W$:

$$x = \frac{10.6556 - \left(\frac{\Delta W}{W}\right) \cdot 270.0277}{15.9994 \cdot \left(\frac{\Delta W}{W}\right) + 15.9994}. \tag{5.6}$$

Fig. 5.4 shows a graph illustrating TG measurements on samples with different O/U ratio.

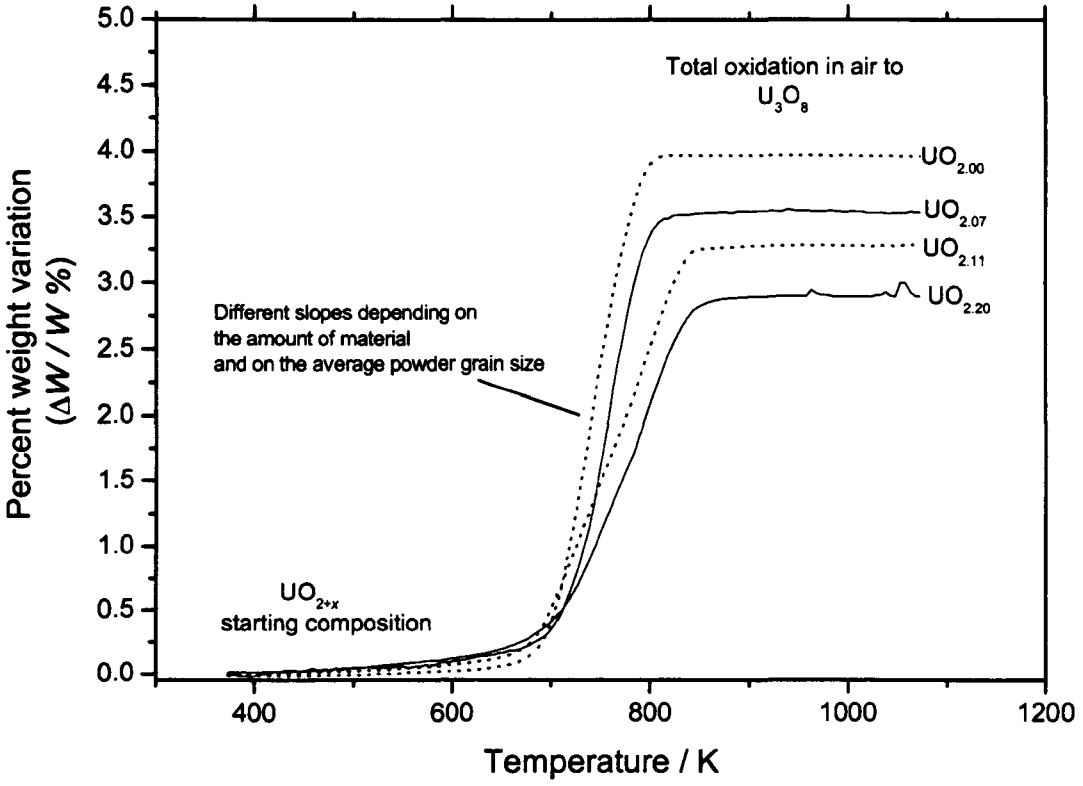

Fig. 5.4: TG measurements on uranium dioxide samples with different O/U.

The sample composition measured by thermogravimetry was taken as the reference for the definition of the *solidus* and *liquidus* lines of UO_{2+x}. Therefore it was of the primary importance to establish the error affecting such composition measurements.

Uncertainty in the weight measured by the balance (δw) and uncertainty due to imprecision in the buoyancy correction (δb) constituted the main error sources affecting the measurement of $\Delta W / W_i$.

The error δw was measured as $\approx \pm 0.005$ mg by checking the stability and the reproducibility of the balance reading on the weight of standard samples.[2] The buoyancy error consisted of the apparent variation of weight of an empty-crucible heated from ambient temperature to 1500 K. Such an apparent weight difference was basically caused by the non- prefect equilibration of the gas fluxes in the balance and in the crucible chamber when the temperature of the crucible was changed. For this reason, heating of the empty crucible from 300 to 1500 K was performed prior to any TG measurement. The apparent weight difference observed was then used to correct the measurement for buoyancy on a real sample. Nonetheless, this buoyancy effect was not perfectly reproducible from time to time. By repeating several heating cycles on both empty crucibles and standard samples, it was established that the residual error in the measured weight difference of a real sample after buoyancy correction was $\delta b \approx \pm 0.025$ mg, for heating cycles between 300 and 1500 K.

To obtain the error in the composition x, one should use the relation between x and $\Delta W / W_i$ given by Eq. (5.6), and consider that

$$\delta x = \frac{dx}{dY}\delta Y \ . \tag{5.7}$$

$Y = \dfrac{\Delta W}{W_i}$ in our case.

To obtain the uncertainty $\delta(\Delta W/W_i)$, one has to combine the independent effects of δw and δb according to the error propagation law. In order to do that, one can consider the relative weight variation $\Delta W/W_i$ as a function of the independent variables W_f and W_i, as in Eq. (5.5). The uncertainty affecting W_i is simply

$$\delta W_i = \delta w. \tag{5.8}$$

However, in determining the uncertainty affecting W_f the buoyancy error should also be taken into account, so that

[2] *The determination of the balance absolute accuracy was not relevant in this work, as weight differences only were to be measured.*

$$\delta W_f = \sqrt{\delta w^2 + \delta b^2}\,. \tag{5.9}$$

Similarly, for the uncertainty affecting $\Delta W / W_i$ we have

$$\delta\left(\frac{\Delta W}{W_i}\right) = \sqrt{A^2 \delta W_i^2 + B^2 \delta W_f^2}\,. \tag{5.10}$$

The factors A and B are the partial derivatives of $\Delta W / W_i$ with respect to W_i and W_f:

$$A = \frac{\partial}{\partial W_i}\left(\frac{W_f - W_i}{W_i}\right) = -\frac{1}{W_i} - \frac{\Delta W}{W_i^2} \tag{5.11}$$

$$B = \frac{\partial}{\partial W_f}\left(\frac{W_f - W_i}{W_i}\right) = \frac{1}{W_i}\,. \tag{5.12}$$

Substituting Eqs. (5.8, 5.9, 5.11 and 5.12) in Eq. (5.10) we have:

$$\delta\left(\frac{\Delta W}{W_i}\right) = \frac{1}{W_i}\sqrt{\left(2 + 2\frac{\Delta W}{W_i} + \left(\frac{\Delta W}{W_i}\right)^2\right)\delta w^2 + \delta b^2}\,. \tag{5.13}$$

Eq. (5.13) was employed in the calculation as it expresses the uncertainty connected to each TG measurement in terms of $\Delta W / W_i$ and W_i, which were the parameters directly outputted. Finally, substituting in Eq. (5.7) the expression obtained for $\delta(\Delta W / W_i)$, and differentiating x with respect to $\Delta W / W_i$ in Eq. (5.6), one obtains

$$\delta x = \frac{17.5433}{\left(\frac{\Delta W}{W_i} + 1\right)^2}\frac{1}{W_i}\sqrt{\left(2 + 2\frac{\Delta W}{W_i} + \left(\frac{\Delta W}{W_i}\right)^2\right)\delta w^2 + \delta b^2}\,. \tag{5.14}$$

Eq. (5.14) signifies that the error affecting the value of x obtained through TG measurements is smaller, the higher the initial weight of the sample. The effect of the weight change ΔW on the total uncertainty is, instead, with good approximation, negligible. Substituting the measured values for δw and δb, and considering that in most of the measurements performed the value of $\Delta W / W_i$ was around 3.5%, we obtain $\delta x \approx \pm 0.0045$ if $W \approx 100$ mg, whilst $\delta x \approx \pm 0.07$ if $W \approx 10$ mg (Fig. 5.5). In the specimens investigated in this work x ranged

between 0 and 0.2. Thus one can see that for samples weighing about 100 mg or more, as in the TG measurements performed on fresh samples before the melting experiments, the error was acceptable. However, the molten-refrozen material on the sample surface following a melting experiment weighed about 15- 20 mg, therefore the TG measurements performed on specimens of this kind, presented in § 5.3, lacked precision.

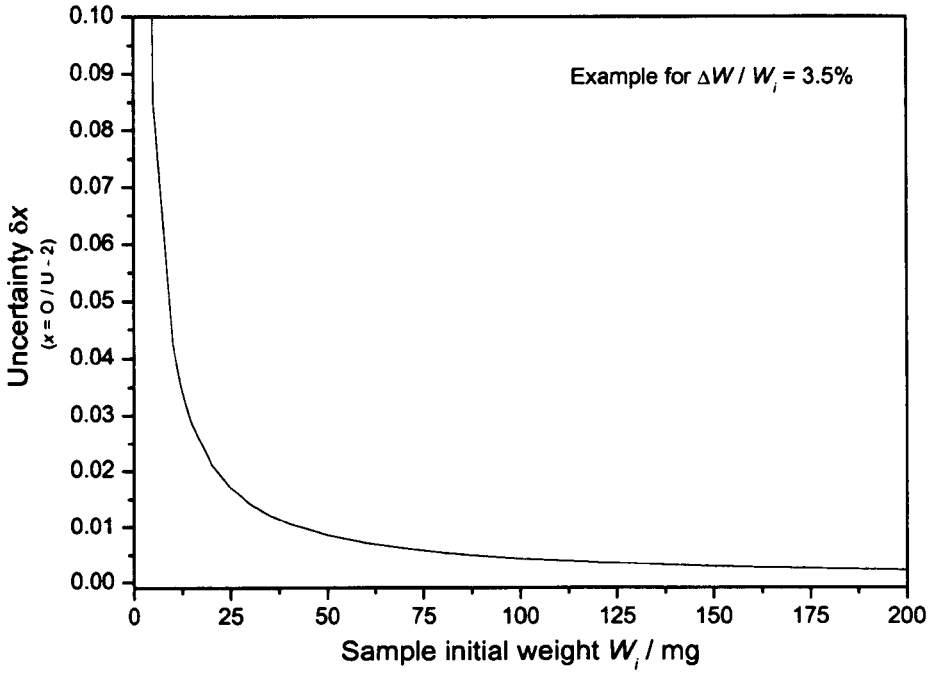

Fig. 5.5: Uncertainty yielded in the thermogravimetric determination of x (x = O/U – 2) as a function of the initial weight of the sample, with an example value of $\Delta W / W_i$ = 3.5 %.

5.2.3 Density measurements

Density of the samples was measured prior to the melting experiments by means of a Sartorius® hydrostatic balance. With such a balance it was possible to weigh a solid in air as well as in a liquid (ethanol in this case). According to Archimedes' principle, a solid immersed in a liquid is subjected to a buoyancy force that equals the specific weight of the

liquid multiplied by the volume of the solid specimen. Therefore, after measuring the weight of a sample in air (W_a) and in ethanol (W_{fl}), the density ρ of the solid sample was obtained as

$$\rho = \frac{W_a \rho_{fl}}{W_a - W_{fl}} \cdot \tag{5.15}$$

In (5.15), ρ_{fl} is the density of the fluid. In practical measurements, formula (5.15) was slightly corrected with empirical factors accounting for the accuracy limits of the balance.

The densities of some representative stoichiometric and hyperstoichiometric samples are reported in Table 5.2. Density increased monotonically with oxidation of the sample, as expected. In fact, oxidative annealing basically resulted in a weight increase, due to the inclusion of excess oxygen, at approximately constant volume (possible volume variations induced by the annealing process were neglected).

5.2.4 Electro- Motive Force (EMF)

EMF measurements were performed at ITU on UO_2 stoichiometric samples by means of an automated solid state galvanic cell. The use of high temperature cells of this kind was demonstrated to be a very useful method for the determination of the oxygen potential in a sample [5, 6]. The method was based on the determination of the EMF generated across an electrochemical chain at high temperature. The electrochemical chain consisted of two half-cells: the reference electrode, whose oxygen potential is known and the measuring (sample) electrode. The two half-cells were connected through a solid state electrolyte in which electrical conductivity is exclusively due to migration of oxygen ions. Externally platinum jumpers completed the circuit.

The process occurring in an EMF cell is well described in [7].

The electrochemical chain produced is

$$(-)\ M_1, M_1O \mid \text{electrolyte} \mid M_2O, M_2\ (+)$$

M_1O and M_2O are the metal saturated phases of the two oxides, of which one constitutes the reference electrode, one the sample. The overall red ox reaction in a cationic model, where the cell is seen as a galvanic chain, is

$$M_1 + M_2O \rightarrow M_1O + M_2 . \tag{5.f}$$

In this case, the cell potential is given by the Nernst equation

$$\Delta E_{(f)} = -\frac{\Delta G^0_{f,M_1O} - \Delta G^0_{f,M_2O}}{2F} , \tag{5.16}$$

where ΔG^0_f indicates the standard free energy of formation of the oxides, and F is the Faraday constant, 96490 Coulomb if ΔE is expressed in V.

In an anionic model, the system can be regarded as an oxygen concentration cell, with oxygen migrating from the anode to the cathode.

In this case, the overall reaction is

$$½\ O_2\ (p''_{O_2}) \rightarrow ½\ O_2\ (p'_{O_2}) , \tag{5.g}$$

where p'_{O2} and p''_{O2} are the oxygen partial pressures over the oxide M_1O and M_2O respectively. The cell potential for reaction (5.g) is given by

$$\Delta E_{(g)} = -\frac{RT}{2F}\ln\left(\frac{p'_{O_2}}{p''_{O_2}}\right)^{\frac{1}{2}} , \tag{5.17}$$

where R = gas constant, 8.314 $JK^{-1}mol^{-1}$, T = absolute temperature.

In the case in which the oxygen pressures over the oxide phases correspond to the true equilibrium pressures, $\Delta E_{(e)}$ and $\Delta E_{(f)}$ represent the same cell potential

$$\Delta E = \Delta E_{(f)} = \Delta E_{(g)} . \tag{5.18}$$

Eq. (5.18) can be obtained also by considering that, at thermal and chemical equilibrium, the following relation holds

$$\Delta G^0_{f,MO} = -RT \ln (p_{O2})^{1/2} . \tag{5.19}$$

Thus the standard free energy of formation of the sample oxide can be measured in the EMF cell if the free energy of formation is known for the reference electrode.

The system used in this work offered the possibility to perform measurements on very small specimens, as the sample half-cell was realised in a cylindrical hole 2 mm in diameter and 5mm in height. The specimen was either a small amount of powder or a small splinter extracted from a pellet. This feature allowed measurement of the *local* oxygen potential, extracting small pieces from a selected zone of a larger sample. In this case the galvanic cell was placed in an alumina furnace maintained under high vacuum (10^{-9} bar) during the measurements. Temperatures up to 1400 K could be reached. A Fe/FeO reference electrode was employed, with a Y_2O_3/ThO_2 solid electrolyte. At thermal and chemical equilibrium, the reversible EMF is given by Eq. (5.17):

$$\Delta E_{(g)} = -\frac{RT}{2F}\ln\left(\frac{p_{O_2}^{sample}}{p_{O_2}^{Fe/FeO}}\right)^{\frac{1}{2}}. \qquad (5.17')$$

In Eq. (5.17'), the following expression was taken for the oxygen potential of the reference electrode:

$$\Delta G_{O2Fe/FeO} = RT \ln p_{O2\,Fe/FeO} = -529778+130.583\ T\ (\mathrm{Jmol^{-1}}). \qquad (5.20)$$

The sample oxygen potential $\Delta G_{O2sample} = RT \ln p_{O2sample}$ was thus measured as a function of T. The use of EMF measurements consisted of the determination (at least qualitative) of the oxygen content in the samples. In principle, the oxygen potential may be translated into oxygen- to- metal ratio using empirical data relating these two properties.

Fig. 5.6 displays some measurements performed on stoichiometric and hyperstoichiometric urania samples along with the Ellingham diagram of the system UO_{2+x} according to [3]. The "stoichiometry zone" was established on the basis of several measurements carried out at the ITU. Its imprecision is due to the extreme sensitivity of the oxygen partial pressure to x in close vicinity to stoichiometry (see, for instance, [8]). In fact, over this range p_{O2} can vary by several orders of magnitude for variations of x much smaller than the detection limits of any instrument available to measure it[3].

[3] *By weight difference and TG, x could be measured with an uncertainty not better than 0.005 units O/U.*

Therefore, this method is more sensitive, the closer the compositions to the exact stoichiometry.

A proper calibration of the method was not feasible; therefore results obtained were used for a qualitative confirmation of the sample composition range only.

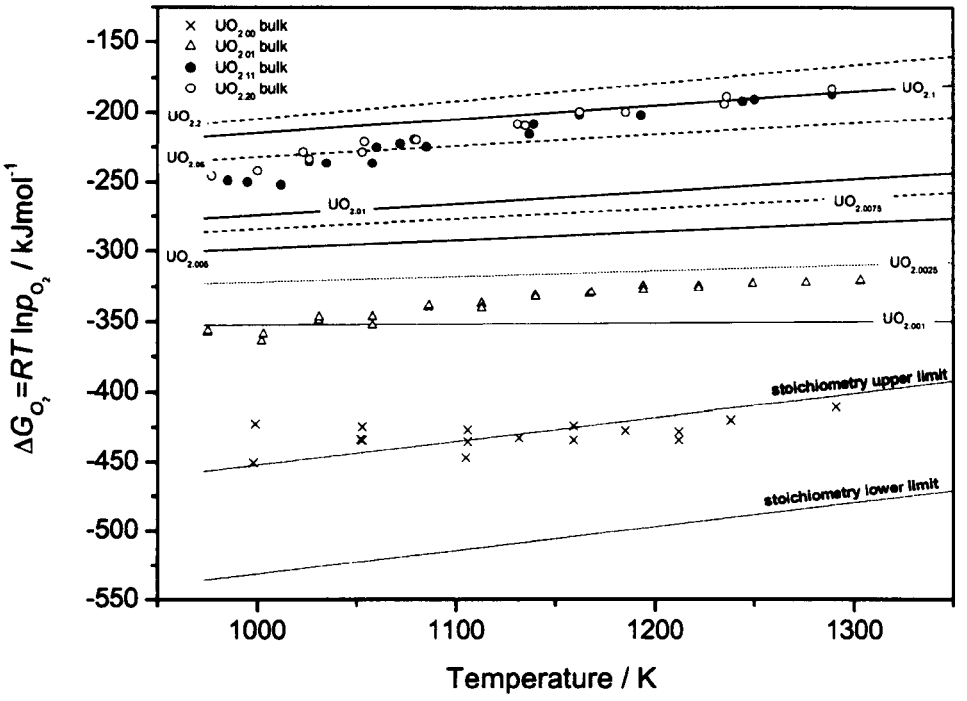

Fig. 5.6: EMF measurements on UO_{2+x} samples compared to oxygen potential curves recommended in [3].

5.2.5 Optical and SEM ceramography

Optical ceramography was performed by means of a Leitz MM6 Widefield Metallographic Microscope. Samples were etched in a H_2O: HNO_3: H_2O_2 2:6:1 solution for 5 minutes at room temperature. Uranium dioxide pellets were observed prior to melting point determination in order to check for homogeneity of the samples (Fig. 5.7a, b). Grain size (≈10 μm) and porosity were approximately the same from the surface inward.

The same kind of study was performed on samples subjected to laser melting in order to investigate the morphology of the refrozen material.

Scanning electron microscopy (SEM) micrographs of molten/refrozen samples were also realised with a SEM Philips 515. SEM micrographs clearly showed how different the material looked in different zones, moving from the surface towards the bulk. The morphology also appeared different in hyperstoichiometric samples with respect to the stoichiometric ones. Images of samples following laser melting will be shown in section 5.3 and in Chapter 8.

5.2.6 Secondary Ions Mass Spectrometry (SIMS)

The SIMS technique permits elemental and isotopic analyses on small volumes close to the surface of a specimen bombarded by a beam of "primary" ions. Under the impact of primary ions, several particles are emitted from the sample surface.

Some of these particles are ionised atoms or molecules coming from the near- surface layers of the specimen. Thus, every point on the sample surface behaves as a source of "secondary" ions characteristic of the elements present. Emitted secondary ions are then detected by a suitable mass spectrometer, which provides a local distribution profile of the different species contained in the vicinity of the sample surface. The analysis can be extended to a depth of approximately 50μm if the primary ions beam, with increased sputtering time, produces a suitable crater on the sample surface.

SIMS characterisation of UO_{2+x} specimens is in progress in the Nuclear Chemistry Unit of the ITU Karlsruhe. Measurements are performed by means of a Cameca® IMS 6F ionic microanalyser [9]. Such characterisation is meant to determine the oxygen content and its homogeneity over the depth of a specimen from the surface inward. Analyses could be performed on $UO_{2.00}$, $UO_{2.09}$ and $UO_{2.21}$ samples only.

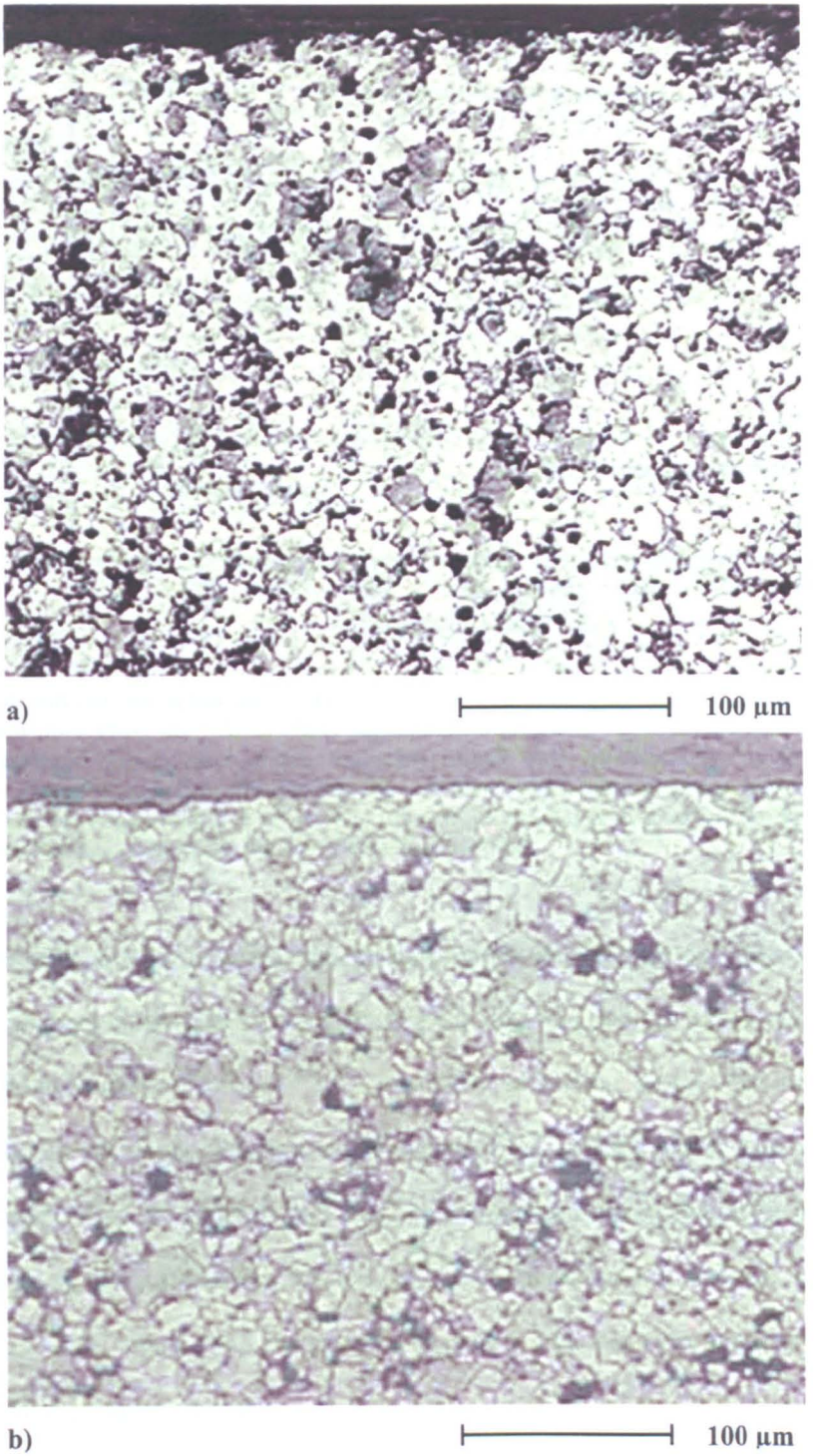

Fig. 5.7: a) Optical ceramography of a $UO_{2.17}$ sample in a region close to the surface. This sample was prepared by annealing a stoichiometric UO_2 pellet in CO : CO_2 1:1000 for 15h at 1573 K. b) Same, for a $UO_{2.07}$ sample obtained by annealing a UO_2 pellet in CO : CO_2 1:100 for 15h at 1623 K.

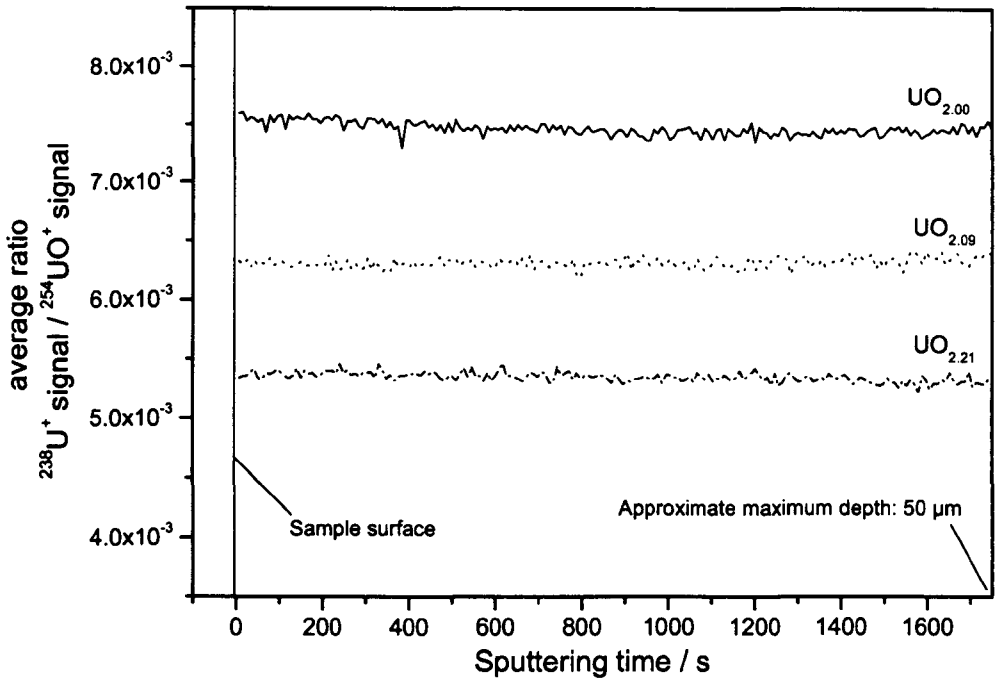

Fig. 5.8: Results of the SIMS measurements performed on $UO_{2.00}$, $UO_{2.09}$ and $UO_{2.21}$ samples. The plotted lines show the $^{238}U^+$ / $^{254}UO^+$ signals ratio for the three compositions as a function of the sputtered depth. Such depth was determined only qualitatively, as the sputtering sensitivity factor of uranium dioxide for the employed experimental setup was not available. Displayed ratios are averaged over several measurements. Oxygen distribution appears in the three cases homogeneous from the sample surface inward.

Since pure oxygen ions were too light to be properly detected by the mass spectrometer employed, oxygen concentration was determined in different samples by measuring the ratio between the numbers of $^{238}U^+$ and $^{254}UO^+$ ions detected in a fixed time. The method should be calibrated by accurately determining the average $^{238}U^+$ / $^{254}UO^+$ signal ratio characteristic of each composition for the system UO_{2+x}. Since this calibration is still in progress, the results obtained, presented in Fig. 5.8, are only qualitative. However, it is already clear that the $^{238}U^+$ / $^{254}UO^+$ signal ratio increases as expected with the O/U nominal ratio of the sample, and this ensures that the method is self- consistent. Moreover, it is clear from the depth profile of the measured ratio that the oxygen concentration is quite homogeneous from the sample surface inward in all the investigated specimens. This latter result is the most relevant to the objectives of this work.

5.2.7 Raman spectroscopy

Elementary Raman scattering (see, for instance, [10]) involves two photons, one impinging on the sample surface with frequency Ω, one being ejected from the specimen following the interaction of the incident electromagnetic radiation with the matter. For frequencies in the visible to infrared range, this interaction consists of the excitation/ annihilation of a vibration in the target material. Vibrations involved can be either phonons (vibration modes of the atoms in the lattice) or magnons (vibration modes of the spins), in the latter electronic states of higher energy than the ground level are excited.

Interaction of the impinging photon with phonons is more favoured the higher the temperature. The temperature effect is the opposite in the case of electronic interaction.

In a second-order Raman effect, two vibrations are involved in the inelastic scattering of the impinging photon.

If a vibration is excited or annihilated during the interaction of the impinging radiation with matter, the sample material will respectively either absorb or release energy and, correspondingly, the photon emitted will have lower or higher energy than the original photon. The energy difference will be

$$\Delta\varepsilon = \frac{h\omega}{2\pi}\,, \tag{5.21}$$

where ω is the frequency of the excited vibration and h the Planck constant. Therefore the energy content and the frequency of the photon out will be

$$\varepsilon_{Ph_{out}} = \frac{h(\Omega \pm \omega)}{2\pi} \tag{5.22}$$

$$\nu_{Ph_{out}} = \frac{(\Omega \pm \omega)}{2\pi} \tag{5.22'}$$

A Raman spectrometer is a device to measure the frequencies of the emitted photons, and

hence to give the values of the frequencies ω of vibration of the phonons involved in scattering of the incident electromagnetic radiation of known frequency Ω.

Such information is fundamental for the definition of the symmetry properties of a crystal. In spectroscopy the energy of the outcoming photons is normally expressed in terms of wavenumber $k = \omega / 2\pi c$ (in cm^{-1}).

Raman spectra were measured at the Forschungszentrum Karlsruhe (FZK)- Institut für Festkorper Physik (IFP) on six standard urania samples with O/U ranging from 2.00 to 2.20. The measurements were performed using a Dilor XY Raman microspectrometer with attached microscope. The excitation source was a 514 nm Argon laser. Spectra were recorded with a liquid N_2 cooled silicon detector (512 x 1024 pixels). The specimen presented low thermal sensitivity. Additionally, the laser beam was adjusted (in power and focal spot diameter) in order to avoid any oxidation of the sample surface during the measurements. The total wavenumber range from ≈ 200 to ≈ 1250 cm^{-1} was covered by three overlapping measurements, each being an average of three 90 s scans. Measurements were repeated several times on the same sample to make sure that no oxidation occurred, and on different samples to check the reproducibility of the results. The characterisation was also repeated at different points on the same sample, in order to check the homogeneity of the investigated surface. Samples that appeared inhomogeneous were rejected.

Fig. 5.9 shows the spectra recorded. The graph shows that it was possible to distinguish samples more or less oxidised through some typical peaks, as the spectra changed gradually as the oxygen content increased.

Three typical lines were detected at about 232, 445 and 1150 cm^{-1} in specimens with bulk composition close to stoichiometry (bulk O/U < 2.09). The vibration at 445 cm^{-1} is typical of the fluorite- structured UO_{2+x} close to stoichiometry, corresponding to the T_{2g} triply degenerate Raman active vibration [11, 12], whilst the mode at 232 cm^{-1} is of uncertain origin.

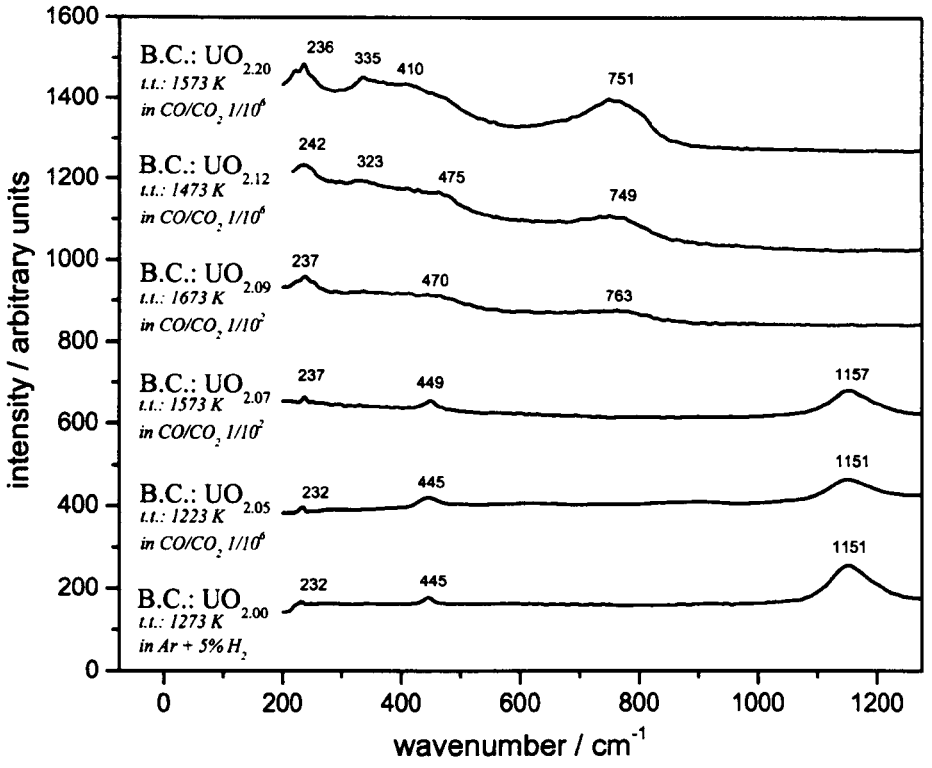

Fig. 5.9: Raman spectra measured on oxidised UO_{2+x} samples of several oxidation levels (see [14]). Beside each spectrum is indicated the bulk composition (B.C.) of the corresponding specimen and the thermal treatment (t.t.) to which the specimen was subjected. Bulk composition corresponds to surface composition in slightly oxidised samples (O/U ≤ 2.07). Superficial composition of more oxidised samples is uncertain, due to the precipitation of higher oxides on the surface in contact with air.

The peak at 1151 cm^{-1} completely disappeared at higher oxidation levels, where the superficial precipitation of higher oxides was likely to cover the uranium dioxide cubic structure. Therefore, this line could also be regarded as a fingerprint of the quasi-perfect fluorite structure. Raman spectra on stoichiometric $UO_{2.00}$ were measured at low temperature, down to 5 K, in order to better establish the nature of the 1151 cm^{-1} mode (Fig. 5.10). The intensity of this peak was higher at low temperature, indicating that the line does not stem from lattice vibrations, but is rather of electronic origin. The 1151 cm^{-1} line was still easily visible in hyperstoichiometric specimens with O/U ≤ 2.07. Since these specimens contained the two phases UO_{2+x} and U_4O_{9-y} (see Chapter 1 and next section), the presence of the peak indicated that the crystal electric field (CEF) levels scheme should be maintained when the second phase precipitates.

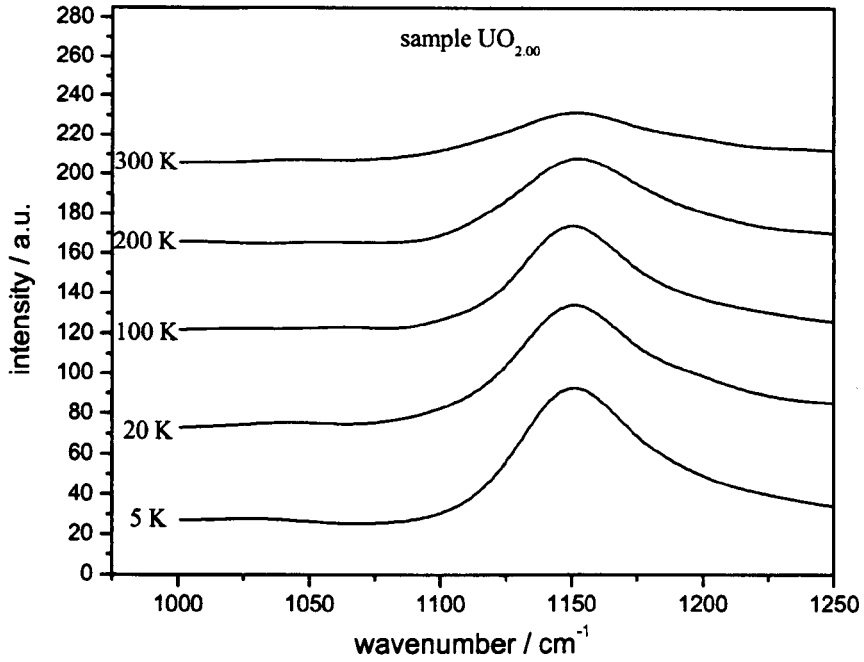

Fig. 5.10: Low temperature Raman spectra of stoichiometric UO_2 around 1000 cm^{-1}.
The sample was cooled under a stream of He in a continuous flow cryostat Optistat-CF manufactured by Oxford Instruments.
The intensity of the peak at 300 K is lower than the one reported in Fig. 5.9 because the scattered light was significantly attenuated by the cryostat.

A broad peak of low intensity appeared at 763 cm^{-1} for the $UO_{2.09}$ composition, and was visible with increased intensity, at about 750 cm^{-1}, in more oxidised samples. Lines in these samples could be identified at about 240 cm^{-1} and, for bulk O/U ≥ 2.12, about 330 cm^{-1}. A barely visible line at 470- 475cm^{-1} for $UO_{2.09}$ and $UO_{2.12}$ was probably overlapped with other modes in $UO_{2.20}$. All these lines were attributable to lattice vibrations of the higher oxide U_3O_8 [13], which was likely to be formed on the surface of hyperstoichiometric samples in contact with air.

Lines were in general barely distinguishable at wavelength < 500 cm^{-1} in samples with bulk O/U > 2.09. Such behaviour was likely due to the fact that the spectra of hyperstoichiometric samples tended to be composites of the single spectra of different species, such as UO_2, U_3O_7 and U_3O_8, as higher oxides were likely to precipitate in traces on the surface. If this happened, several peaks could overlap, covering each other. A more detailed discussion of the Raman spectra shown in Fig. 5.9 can be found in [14].

According to the Raman measurements presented, one should conclude that the exact composition of the samples surface was unknown, at least in samples with O/U > 2.09, due to the precipitation of higher oxides, that occurred as the specimens were kept in contact with air. Moreover, even in the absence of precipitates (for composition O/U < 2.09), since hyperstoichiometric uranium dioxide exists at room temperature as a mixture of two phases (UO_{2+x} and U_4O_{9-y}), the results obtained were not fully indicative of the evolution of the solid solution phase at increasing oxidation state. Nonetheless, spectra measured in this work changed progressively with oxygen content of the bulk, which was well known, and the trend shown was certainly useful in identifying different oxidation levels in hyperstoichiometric uranium dioxide samples *in contact with air*.

The precipitation of higher oxides on the sample surface could be thought to affect the melting point measurements, which were performed by producing surface melting. However, one should not forget that Raman investigation extends to a very thin superficial layer only (few nm), whilst the melting process occurred to a depth of several tens of μm. The analysis of the thermograms obtained in the melting/freezing experiments, as well as the sample characterisation by other techniques (TG, EMF, SIMS, SEM and optical ceramography in particular), ensured that no precipitation of higher oxides affected the melting point determination at such a depth.

Spectra of the molten-refrozen zones in stoichiometric samples were also measured. All those spectra showed the features typical of the stoichiometric standard, suggesting that samples did not become oxidised during the melting experiments, even in the presence of high p_{O2}. Raman measurements on hyperstoichiometric urania samples after melting are presented in §5.3.

5.2.8 X - Ray Diffraction (XRD)

Fig. 5.11 shows XRD spectra measured on three different powdered pellets of composition respectively $UO_{2.00}$, $UO_{2.09}$ and $UO_{2.11}$. These spectra were measured in the Hot Cells Unit of the ITU Karlsruhe making use of a Seifert 3000 powder x-ray diffractometer (XRD) with Ni-filtered Cu Kα radiation at different temperatures. Measurements were carried out in step-scanning mode. A scanning step of 0.015° for 2 s was used.

The main effect of oxidation on the XRD spectra at *room temperature*, appeared to be the broadening of several characteristic peaks. Such broadening was a consequence of two distinct overlapping peaks, due to the coexistence of two separated phases, belonging to the same symmetry group, in samples with O/U > 2.09.

The presence of a solid- state solubility gap in the system U-O is well established between the phases UO_{2+x} and β-U_4O_{9-y} at room pressure and for temperatures ranging from room temperature to about 1500 K (see Chapter 2). The lower-x phase boundary is at O/U ≈ 2.00 at room temperature and moves towards higher oxygen contents up to 1500 K, where it is recognised to be at O/U ≈ 2.25. At temperatures higher than 1500 K, U_4O_9 disappears, quickly merging into one single UO_{2+x} phase that exists up to the melting point. Therefore, the melting experiments should not be influenced by the actual coexistence, in the starting material at room pressure, of two phases. XRD spectra could not be measured on the molten and refrozen parts of our samples due to the very small volume of material available.

5.2.9 Knudsen Effusion Measurements

A Knudsen cell consists of a small chamber with a volume of the order of 1 cm^3 and a small hole on the top, whose diameter is about 1 mm. This chamber contains a sample under high-vacuum.

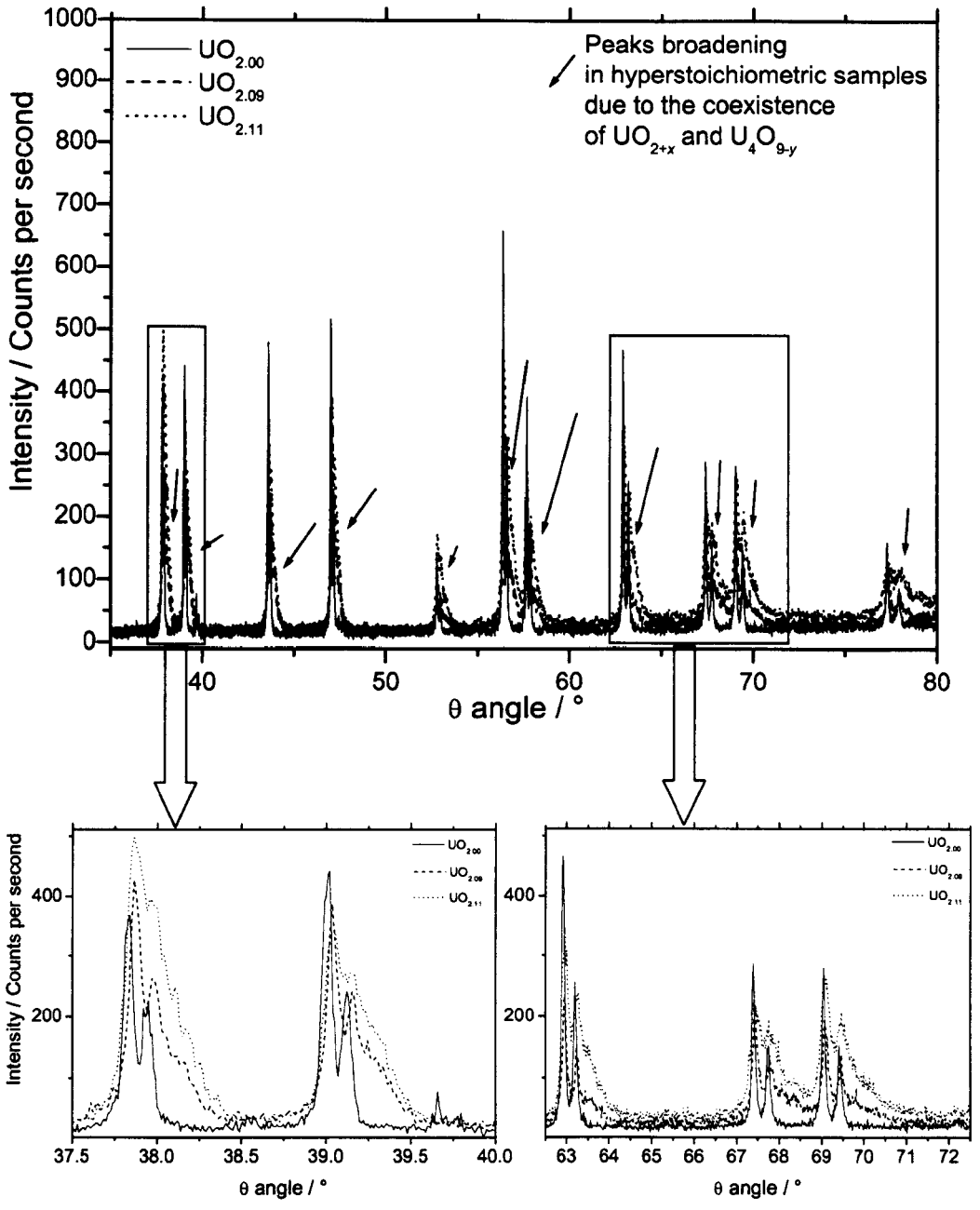

Fig. 5.11: X-ray diffraction spectra measured on $UO_{2.00}$, $UO_{2.09}$ and $UO_{2.11}$ powdered samples. The insets show the enlargement of two example regions of the spectrum, where the broadening of several characteristic peaks is visible.

The cell is heated to a desired temperature and, with the help of a suitable mass spectrometer, the effusion beam is used to investigate the release of gas from the specimen under nearly- ideal conditions [15]. A detailed description of the used assembly is given in [16]. In this work such measurements were aimed at the determination of the helium content inside the uranium oxide specimen following the high-pressure melting experiments.

Fig. 5.12 shows the most significant output curves of one of such experiments. The mass spectrometer signal, proportional to the amount of helium released, is displayed as a function of time. The Knudsen cell temperature was varied in steps, as indicated by the corresponding thermogram plotted in Fig. 5.12, in order to facilitate the kinetic development of the helium release process. One can argue from Fig. 5.12 that helium was present inside the sample, with a concentration of the order of 100 ppm, both in the form of bubbles and in solid solution. The gas was released in the temperature range $800 \leq T \leq 2500$ approximately. In this range the spectrum obtained shows several low and narrow spikes, corresponding to the release of bubbles, superimposed on a more regular peak relative to the release of gas in solution in the solid matrix.

It is quite unlikely that the presence of about 100 ppm helium in the matrix may have affected the melting measurements, as this gas was supposedly not present in the condensed material at temperatures close to melting. On the other hand, due to the small size of its atoms and to the high pressure, helium was likely to rapidly fill all the pores in the proximity of the urania sample surface, even at room pressure. This latter effect could be regarded as advantageous, as in this way helium further contributed to a reduction in the kinetics of evaporation of oxygen from the specimen surface, and also inhibited the reaction of some oxygen, possibly contained in the high-pressure cell, with the sample surface itself. The Knudsen method was used, on the same urania samples employed in this work, to study the solubility of helium in uranium dioxide [17].

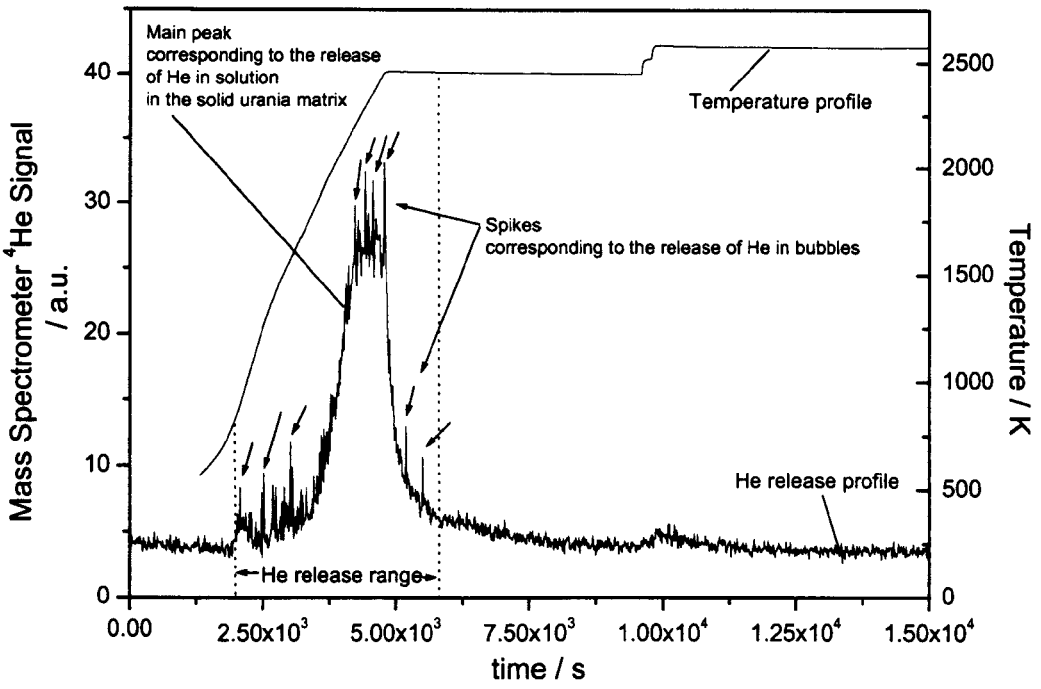

Fig. 5.12: Knudsen effusion measurement performed on a $UO_{2.00}$ sample subjected to one melting/freezing experiment under helium at 0.1 GPa.

5.3 Analysis of samples after the melting point measurements

As already pointed out in the previous section, characterisation of samples after the melting/freezing experiments was hardly feasible, due to the very small amount of material available. Moreover, it was stated that any characterisation of the UO_{2+x} specimens conducted at room pressure and temperature could reveal features of the specimen (morphology, number of phases, local composition etc.) significantly different from those present at temperature close to the melting point, and under relatively high pressure. Finally, it was believed that the best verification of the specimen homogeneity would be obtained by repeating several melting experiments on similar samples, as well as on different sections of the same sample, and ensuring the good reproducibility of the resulting melting points. However, TG (§ 5.2.2), EMF (§ 5.2.4) and Raman (§ 5.2.5) measurements were performed on samples previously subjected to melting experiments, confirming that the original

composition remained approximately invariant in the molten/refrozen part of the specimen surface. The molten/refrozen zones were manually detached from the original pellet and powdered. The results of thermogravimetric measurements are presented in Fig. 5.13. The original composition was approximately unaltered in the molten/refrozen specimens, at least within the uncertainty limits affecting the TG measurements carried out on the small amount of material available. Only in the most oxidised samples, like the $UO_{2.20}$ specimen of Fig. 5.13, did the molten-refrozen zone appear somewhat richer in oxygen. Even in this case, however, the observed post-melting deviation from the original composition was well within the uncertainty limits of the TG measurements. A post-melting enrichment of oxygen in samples with O/U > 2.10 would confirm the results of the one- dimensional simulation of Chapter 8.

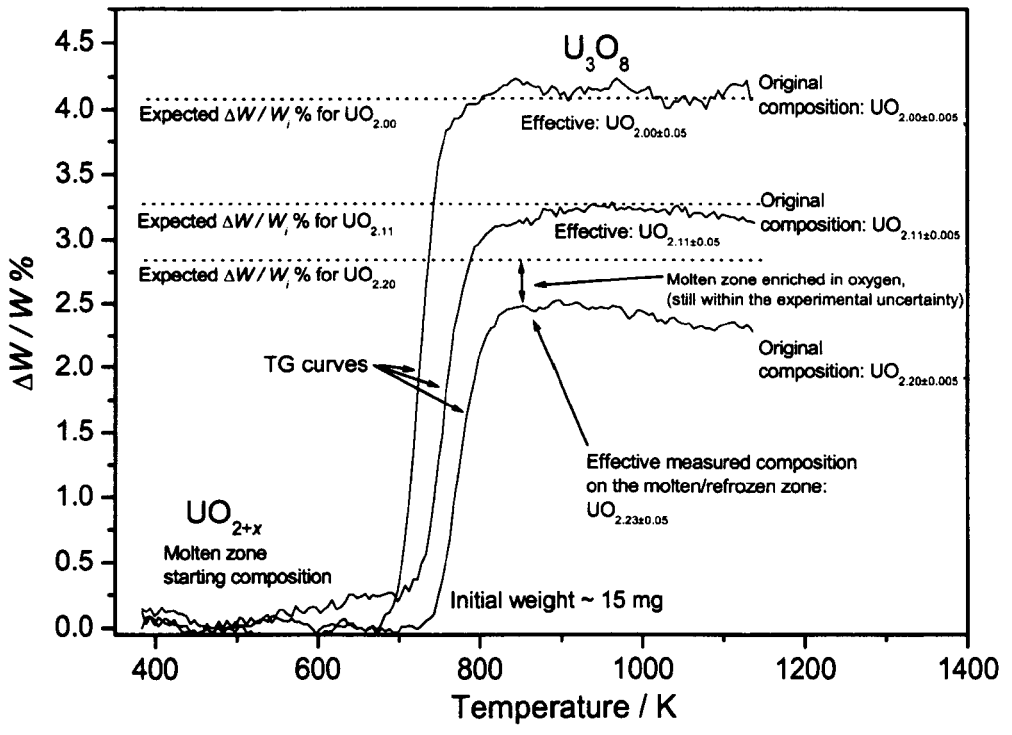

Fig. 5.13: Thermogravimetric (TG) measurements performed on the molten/refrozen zones of $UO_{2.00}$, $UO_{2.11}$ and $UO_{2.19}$ samples. The measurements were affected by large uncertainty (± 0.05 on the value of O/U) due to the very small amount of material available. Horizontal dotted lines indicate the relative weight change ($\Delta W/W$ %) expected in samples with composition perfectly unaltered by the melting/freezing process.

Figs. 5.14 and 5.15 show the outputs of EMF and Raman measurements on molten and refrozen specimens, compared with results from fresh samples having the same composition. These latter characterisation techniques also seem to confirm the results of the TG measurements. However, both EMF and Raman results were of questionable reliability in this case; EMF results were not very significant due to the low sensitivity of the method in oxidised samples, and Raman measurements were hindered by the irregular morphology of the refrozen sample surface, which produced low intensity in the scattered light, resulting in a bad definition of the detected Raman peaks.

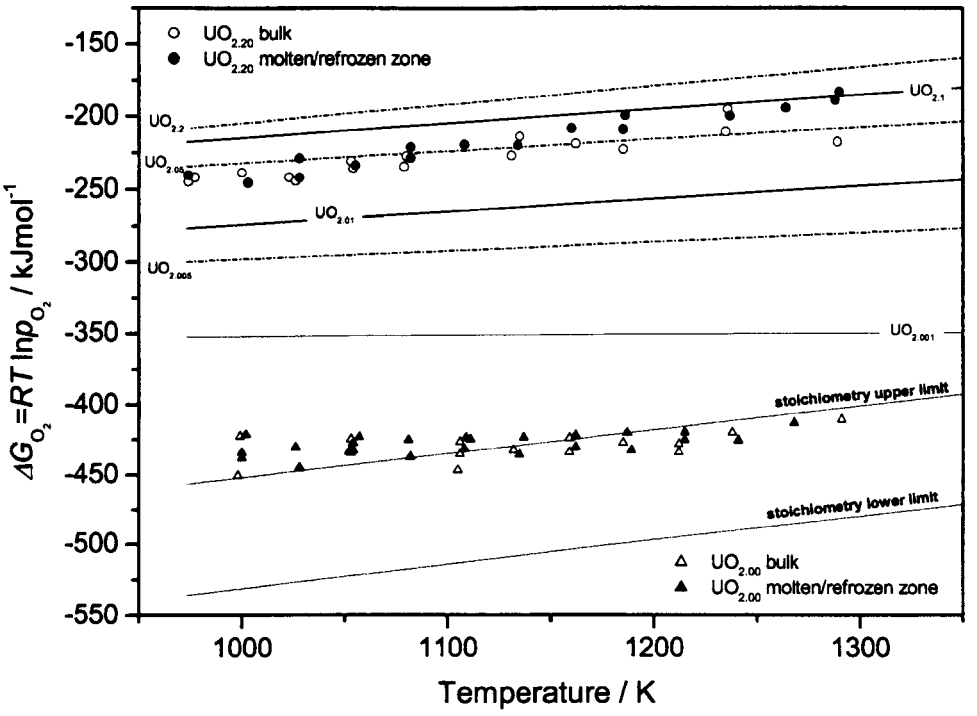

Fig. 5.14: EMF measurements on splinter extracted from the molten / refrozen zones of $UO_{2.00}$ and $UO_{2.20}$ samples. Results are compared with those obtained on specimens extracted from the bulk of the same pellets *prior* to the melting / freezing experiments.

Fig. 5.15 shows Raman spectra measured on a $UO_{2.07}$ sample before and after melting point measurements. This composition was of particular interest, because it was proved to be the threshold composition for the formation of higher uranium oxides (mainly U_3O_8) on the surface of samples in contact with air.

In particular, in samples with O/U > 2.07 a clear Raman peak typical of the U_3O_8 orthorhombic structure was observed around 750 cm^{-1} (see Fig. 5.4). Since such peak, like any other peak typical of higher uranium oxides, was not visible in the spectrum recorded on the $UO_{2.07}$ specimen after melting, one could conclude that this sample was not oxidised by the melting/freezing process. It should be noted that, due to the poor quality of the "after-melting" spectra, even some of the peaks typical of the UO_{2+x} structure were not visible. In particular, the peak at 1151 cm^{-1}, being due to a CEF transition, required a particularly good sensitivity of the measurement to be detected.

Finally, the limited information obtained from the TG, EMF and Raman characterisation of samples after melting experiments confirmed that no significant deviation from the initial composition remained in the molten zone after complete freezing.

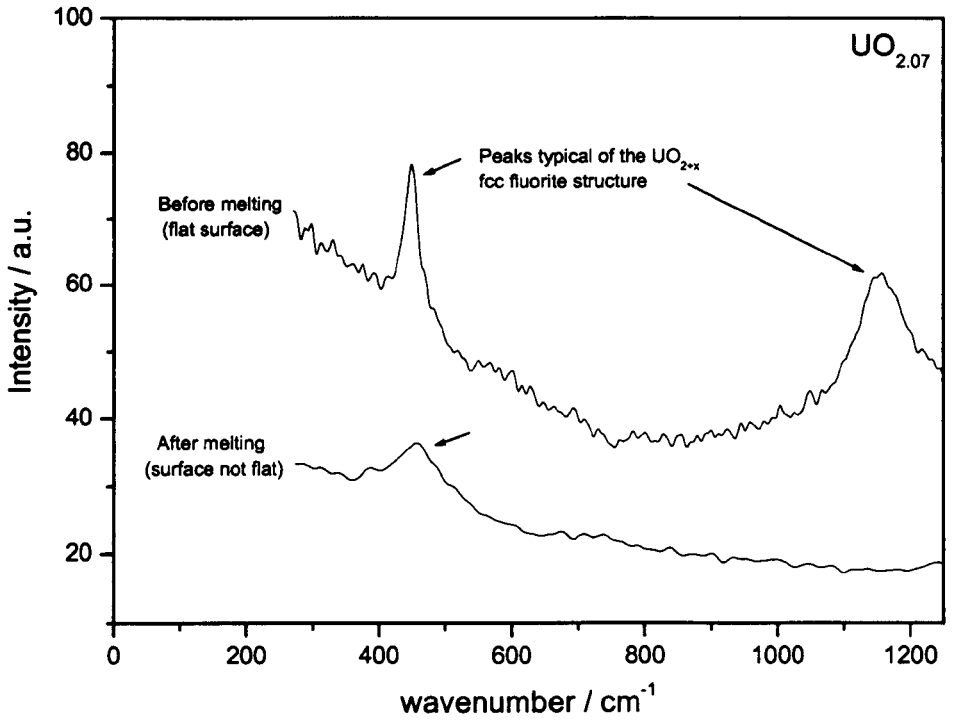

Fig. 5.15: Raman spectra measured on a $UO_{2.07}$ sample before and after a melting / freezing experiment.

SEM micrographs of molten/re-frozen uranium dioxide samples revealed interesting differences between stoichiometric and hyperstoichiometric specimens. Fig. 5.16 shows SEM micrographs for a stoichiometric UO_2 sample (Figs. 5.16a and 5.16b), and for a hyperstoichiometric $UO_{2.08}$ sample (Figs. 5.16c and 5.16d).

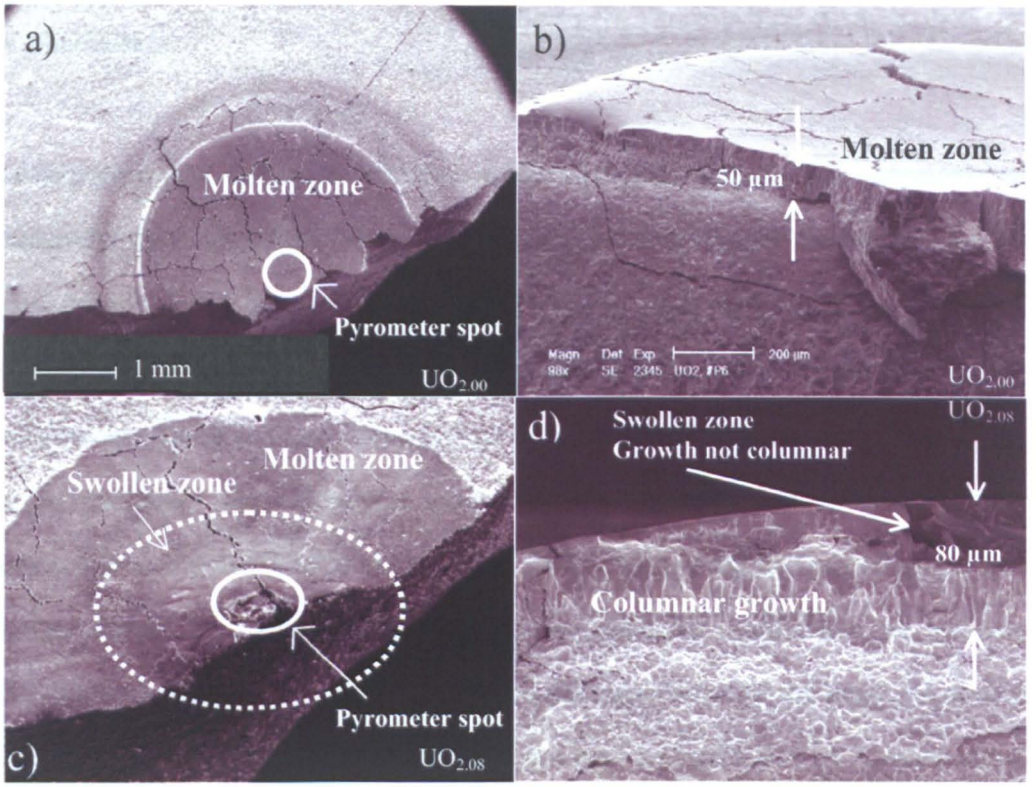

Fig. 5.16: SEM micrographs of samples subjected to laser induced melting/freezing experiments. a) and b): stoichiometric sample ($UO_{2.00}$). c) and d): hyperstoichiometric sample ($UO_{2.08}$).

In the stoichiometric sample the regular network of cracks and the practically flat surface of the re-frozen zone (Fig. 5.16a) are signs of a homogeneous freezing process that could be considered one-dimensional throughout the melting-freezing process. Furthermore, the columnar crystal formation (Fig. 5.16b) confirmed that the process was mostly axial. In hyperstoichiometric samples, instead, a "swollen" zone was visible in the centre of the molten surface, where the crystal growth was not columnar (Fig. 5.16c and d). A similar swelling appeared in the centre of the re-frozen zone in *all* the samples with O/U > 2.03, without any exception, if a sufficient amount of liquid was produced. This "swelling" was

probably a consequence of a displacement of the liquid mass in the radial direction during the solidification process, and the presence of large concentration gradients in highly oxidised samples was possibly at the origin of this effect. This point will be discussed in better detail in Chapter 8.

5.4 Conclusions

Stoichiometric and hyperstoichiometric uranium dioxide pellets were prepared and extensively characterised before being subjected to melting point measurements. The composition of each sample was determined with known precision by thermogravimetry and by observing the weight difference induced by the oxidative heat treatment in originally stoichiometric samples. Composition proved to be satisfactorily homogeneous throughout the sample. Other characterisation techniques such as EMF and Knudsen Effusion measurements, optical and SEM ceramography, SIMS, Raman and XRD spectroscopy were also employed. By means of these techniques, additional information on structure, morphology, presence of impurities and superficial composition of the produced samples could be obtained. TG, EMF and Raman spectroscopy measurements on samples already subjected to the melting experiments were rather difficult due to the small volume of material available. SEM micrographs revealed that the morphology of molten /re-frozen samples presents interesting features, that will be discussed extensively in chapter 8.

References Chapter 5

1. N.N. Greenwood and A. Earnshaw, "*Chemistry of Elements*", Pergamon Press, Cambridge, UK, 1984, 327.
2. A. Caneiro, J. Fouletier and M. Kleitz, J. Chem. Thermodynamics **13** (1981), 823.
3. B. Lindemer and T. Besman, J. Nucl. Mater. **130** (1985), 473.

4. J. Spino (JRC, ITU, Karlsruhe), private communication.
5. C.M. Mari, S. Pizzini, L. Manes and F. Toci, J. of Electrochem. Soc. **124** (1977), 1831.
6. F.T. Ewart, L. Manes, Hj. Matzke, C.M. Mari, F. Toci and R. Schreiber, J. Nucl. Mater. **81** (1979), 185.
7. G.G. Charette and S. N. Flengas, J. Electrochem. Soc.: Electrochemical Science, **115** (1968), 796.
8. P.E. Blackburn, J. Nucl. Mater. **46** (1973), 244.
9. G. Tamborini, *"Développement de la Technique SIMS pour l'Analyse de Particules Radioactives et ses Applications à Différents Échantillons"*, PhD Thesis, Université de Paris- Sud, U.F.R. Scientifique d'Orsay.
10. C. Kittel, "*Introduction to Solid State Physics*", J. Wiley and Sons, New York 1996 (7^{th} Edition), Chapter 4.
11. V.G. Keramidas, W.B. White, J. Chem. Phys. **59** (1973), 1561.
12. G.C. Allen, I. S. Butler, N.A. Tuan, J. Nucl. Mater. **144** (1987), 17.
13. I.S. Butler, G.C. Allen, N.A. Tuan, Appl. Spectrosc. **42** (1988), 901.
14. D. Manara, B. Renker, J. Nucl. Mater. **321** (2003), 233.
15. T. H. Swan and E. J. Mack Jr., J. Am. Chem. Soc. **47** (1925), 2112.
16. R. Fromknecht, J.-P. Hiernaut, Hj. Matzke and T. Wiss *Nucl. Instr. and Meth. B* **166/167** (2000), 263.
17. C. Ronchi and J. P. Hiernaut, in press on J. Nucl. Mater.

Chapter 6

Measurement of melting point and melting line of stoichiometric uranium dioxide

The melting point of stoichiometric uranium dioxide was determined by detecting with good accuracy the exact temperature at which a thermal arrest- plateau on the recorded thermograms revealed freezing of the molten material. Experimental facilities employed to realise such measurements were extensively described in Chapter 4. The coherent reflected light method (§ 4.3.7) was also used for the determination of the melting point in stoichiometric samples. However, in this special case of congruently melting material, thermal analysis provided more precise results. The melting behaviour of stoichiometric uranium dioxide was investigated over a wide range of pressures, leading to the experimental determination of the UO_2 melting line. This study constituted the first necessary step in the investigation of the melting behaviour of uranium dioxide at high pressure. Moreover, the measurement of the melting line was an important test for the new experimental method. Therefore, the whole experimental study on melting point and melting line of stoichiometric UO_2 is extensively described in this chapter, including statistical analysis of data and discussion of the results. The determination of the *liquidus* and *solidus* lines of UO_{2+x} is described in the next Chapter.

6.1 Melting point of stoichiometric uranium oxide

Stoichiometric uranium dioxide is known to melt congruently, at least within the uncertainty limits of the experimental determination of the material composition. Since liquid and solid coexist with the same composition during the phase transition, according to Gibbs' phase rule (see Chapter 2) the transition itself has to occur at a constant temperature.

In this case, the analysis of experimental thermograms was quite simple and could be successfully used to determine the $UO_{2.00}$ melting behaviour with considerable precision.

6.1.1 Description of the empirical thermograms

Figure 4.1 shows the results of a melting point measurement on stoichiometric uranium dioxide. The thermogram $T = T(t)$ recorded by the 644-nm IVTAN pyrometer channel constituted the temperature reference. The power *vs.* time profile of the laser beam impinging on the sample surface is also plotted. The arbitrary units here just signify the average power delivered per square centimetre on the focal spot. As explained in § 4.2.2, the radial distribution of the laser power over the focal spot could be considered constant with quite good approximation, as a result of the mixing of the laser modes within the fibre optics pathways of the beam. Unlike the case reported in Fig. 4.23, in this example the pyrometer second channel was employed for the analysis of the coherent reflected light signal (RLS). As expected (see § 4.3.6), no inflection upon melting could be noticed during the heating stage, since thermal equilibrium conditions were never achieved in this part of the measurement. A slight decrease in gradient of $T(t)$ was always detected at temperatures significantly above the melting point, due to evaporation from the molten surface, and, in addition, to the instability of the laser pulse power after some tens of milliseconds. After the end of the higher power pulse, the surface cooled down, and a clear thermal arrest was visible (Fig. 4.1) corresponding to the freezing point.

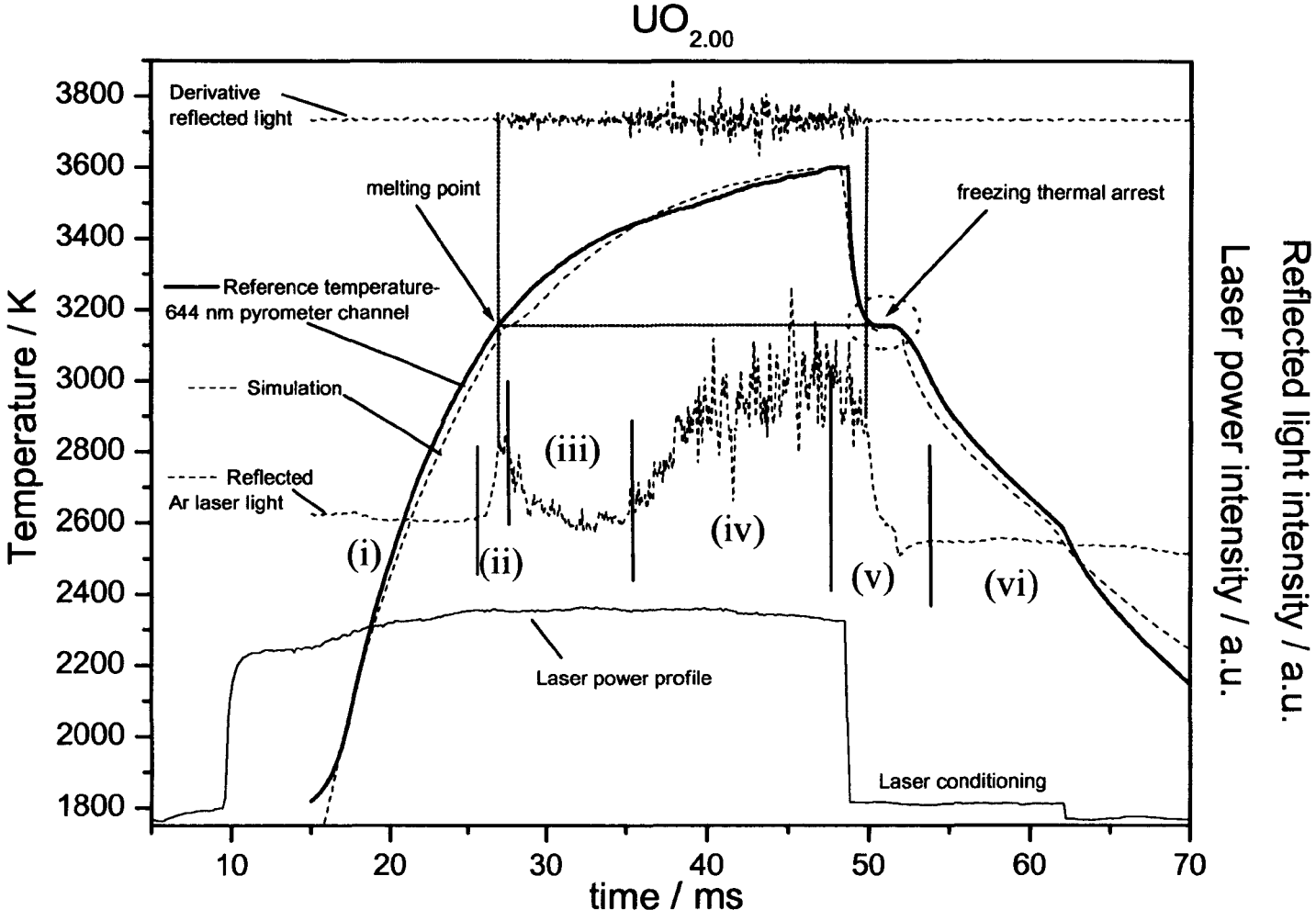

Figure 6.1: Melting point measurement on stoichiometric uranium dioxide. Vertical lines across the RLS graph mark the beginning and the end of each of the six stages.

Empirical curves were compared with the theoretical calculations made by means of the one-dimensional model described in Chapter 8. Unlike the experimental curve, the calculated thermogram in Fig. 6.1 shows a slight thermal arrest on the ascending flank corresponding to the melting point. This is due to the fact that the presence in the real experiment of any thermal flux in the radial direction, not represented in the one-dimensional model, smoothes any inflection on the thermogram. This point could also explain the shape of the edge observed on the experimental thermogram at the end of the freezing plateau, rounder than the corresponding inflection in the calculated curve. The shape of the simulated curve was also somewhat irregular on the cooling stage corresponding to the beginning of freezing, where the phase transition onset caused some numerical instability. Nonetheless, the overall agreement between experimental and simulated curves was satisfactory, proving that the one-dimensional approximation, assuming homogeneous power density across the laser spot, was adequate.

The analysis of the 514 nm reflected light signal (RLS) constituted another significant means of investigation. The RLS curve, dashed in Fig. 6.1, identified six different stages of the experiment, indicated with roman numbers in the graph: i) The sample surface was not yet molten, and the RLS showed an approximately constant intensity. ii) A sudden increase in the RLS was observed when the sample surface reached the melting temperature. An extremely thin, motionless molten layer was formed, acting like a mirror and reflecting a greater part of the Ar laser beam into the pyrometer detector. The RLS revealed the gradual onset of vibrations on the liquid surface. iii) The amount of liquid produced increased to a point where the molten mass started vibrating under capillarity forces, and correspondingly it scattered the incident laser beam. This scattering phenomenon caused, at first, a decrease of the RLS detected intensity. iv) The 514 nm signal intensity increased due to the contribution of thermal radiation self-emitted by the hot surface. v) The more powerful part of the Nd: YAG laser pulse was turned off and the temperature decreased very rapidly (at $\approx 10^6$ K s^{-1}). As the solidification front advanced, light scattering due to irregular motion of the liquid

mass became important. Such an irregular motion was cut off when the surface reached the freezing temperature and the first solid seed was formed (revealed by a slight spike in the RLS). Correspondingly, the freezing plateau started on the 644 nm channel thermogram. Superficial vibrations revealed by the RLS faded during the freezing process, and finally disappeared when all the molten material was solidified, in correspondence with the end of the freezing plateau. vi) After complete freezing the RLS stabilised around a certain constant level depending on the (new) angular distribution of the reflectivity.

The time first derivative of the RLS could be used to more clearly observe the vibrations of the superficial liquid layer. Finally, *both* melting and freezing points could be observed in the experiment based on the RLS analysis.

In summary, the melting point of stoichiometric uranium dioxide was well established from two independent physical effects within the same experiment.

6.1.2 Characteristic parameters of the thermal arrest as a function of experimental conditions for stoichiometric uranium dioxide

Definition of the freezing plateau

Good definition of the freezing plateau determined the precision with which the melting/freezing temperature was established. Undercooling of the liquid phase below the equilibrium freezing point was to be avoided, and for this purpose a double laser pulse was used as heating agent, as discussed in § 4.2.1. Both duration and intensity of the two laser pulses were adjusted to define the time interval for which the surface was maintained above the melting point and the maximum temperature reached. These parameters, along with the buffer-gas pressure, controlled the amount of mass melted and the cooling rate, and hence the shape and extent of the freezing plateau. When the sample surface was allowed to cool to

the thermal arrest of freezing the second Nd: YAG laser pulse, less powerful but of longer duration, controlled the cooling rate.

The freezing plateau was not well detectable in the case of two different, undesirable, experimental conditions:

- When the cooling rate was too rapid, the liquid was initially cooled below the freezing point (undercooling). As freezing occurred the latent heat released by the surface resulted in a "temperature recovery", leading to a thermal arrest having the shape shown in Fig. 6.2-a. It was difficult to ensure that the effective phase transition temperature was recovered up to the true freezing point. Nonetheless, when the undercooling was only one or two degrees Kelvin, and therefore within the uncertainty of the pyrometer itself, the measured freezing temperature could be considered reliable.

- An inflection was visible instead of a plateau around the melting temperature (Fig.6.2-b). This could be caused by one or more of the following three reasons:

1. The conditioning pulse power was too high. In this case the heat provided by the laser beam would balance the thermal losses and cause a thermal arrest to start on the cooling stage above the freezing point.
2. The sample surface was somehow damaged and no longer homogeneous, or even broken. This would randomly affect the apparent surface emissivity at the thermal arrest.
3. The sample was not perfectly stoichiometric. Two separate changes of the thermogram slope would in this case appear corresponding to *liquidus* and *solidus* instead of a single flat plateau signifying a congruent freezing process.

In these cases thermograms were in general not easily interpretable and therefore left out of the analysis, unless the uncertainty in defining the freezing point was considerably smaller than the uncertainty of the pyrometer temperature scale.

Thermograms presenting well-defined melting plateau could be further analysed, in order to deduce the effect of some experimental parameters on the final shape of the curve.

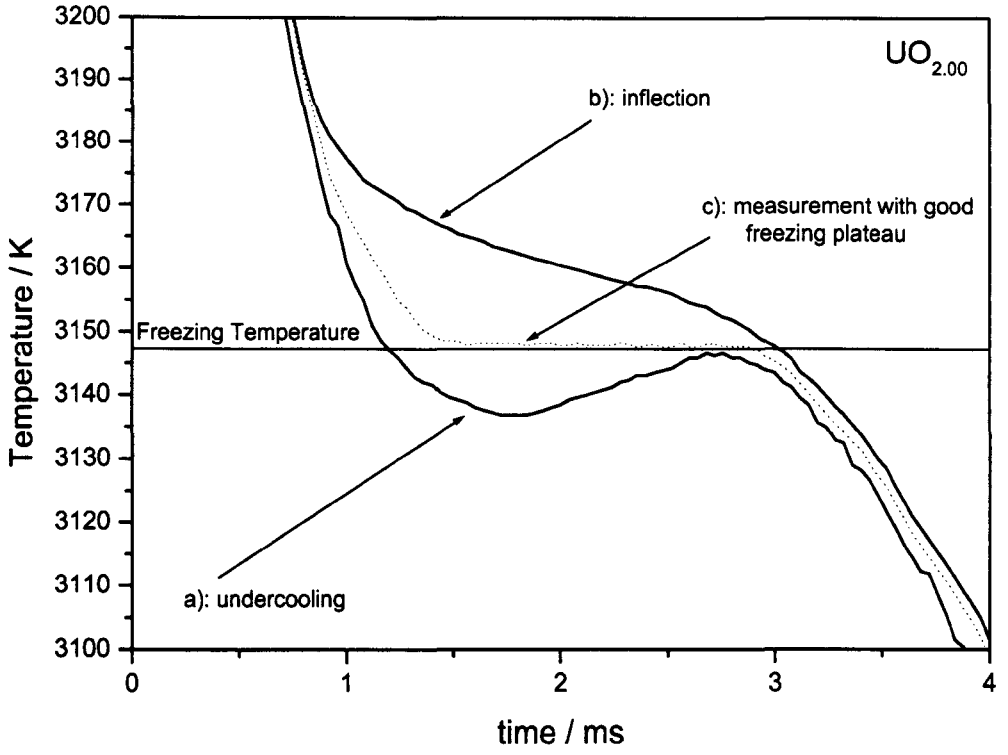

Fig. 6.2: Possible shapes of the freezing arrest observed in thermogram recorded on stoichiometric $UO_{2.00}$ samples : a) undercooling; b)inflection; c) good definition of the freezing plateau.

Effect of the buffer gas pressure

The purely thermodynamic effect of the buffer gas pressure on the measured melting points is described by the Clausius- Clapeyron equation discussed in the next section. In addition, the effect of pressure on the melting behaviour of uranium dioxide specimens was essentially of a thermal nature. Thermal losses Q_L at the interface between condensed sample and high pressure buffer gas are given by: $Q_L = -Q_{RADIATIVE} - Q_{CONDUCTIVE} - Q_{CONVECTIVE} - Q_{EVAPORATIVE}$ components, i.e.:

$$Q_L = -\varepsilon\sigma T_{surf}^{\ 4} - \xi(T_{surf} - T_{gas}) - h(T_{surf} - T_{gas}) - \Delta H_{vap}\varphi_{vap}, \qquad (6.1)$$

where ε = surface total emissivity, σ=Stefan- Boltzmann constant, ξ = wall conductive heat transfer coefficient, h = wall convective heat transfer coefficient; ΔH_{vap} = latent heat of

evaporation, φ_{vap} = net evaporation rate, T_{surf} = sample surface temperature, T_{gas} = buffer gas temperature.

Radiative heat losses are pressure-independent. However, the higher the pressure, the higher are the thermal losses due to convective and conductive heat flux (both ξ and h are proportional to the square root of the buffer gas pressure, $\xi, h \propto P_{gas}^{1/2}$). On the other hand, high pressure would inhibit evaporation from the sample surface ($\varphi_{vap} \propto P_{gas}^{-1/2}$), and evaporative cooling along with it. However, the three factors ξ, h and φ_{vap} depend on the experimental conditions and on the "heating history" of the sample surface in a rather complex way, fully described my means of semiempirical parameters. Therefore, the overall thermal effect of P_{gas}, a combination of conductive, convective and evaporative heat losses, was determined empirically by analysing the results of experiments carried out at different pressures. An appropriate reference parameter had to be chosen in order to perform such analysis. A possible candidate parameter was the conditioning laser pulse power necessary to balance thermal losses and obtain a flat freezing plateau at different pressures. Unfortunately, the Nd: YAG laser power was not controllable with precision during the experiment (even the profile measured by the power detector set at the exit of the fibre optics was qualitative only), thus a fine analysis based on such parameter had to be discarded. The only (approximately) invariant reference over experiments carried out at different pressures was the freezing point. Therefore the analysis was performed taking as a reference parameter the time duration of the freezing plateau for samples heated up to the (approximately) same maximum temperature under different buffer gas pressures. Supposing that any convective motion in the gas was ruled out by the insertion of a sapphire window just above the sample surface (§ 4.2.1), the third term in Eq. (6.1) could be left out. Under this assumption, the power balance equation at the freezing arrest was

$$q(t) = \Delta H_m \varphi_m(t) + A_l Q_l(t) - \varepsilon\sigma T_m^4 - \xi(t)(T_m - T_{gas}) - \Delta H_{vap}\varphi_{vap}(t), \qquad (6.2)$$

being q ($q = -\lambda \frac{\partial T}{\partial z}$, λ = thermal conductivity of the sample, z = depth in the sample) the conductive heat flux in the sample (considered in the axial direction only), ΔH_m the latent heat of melting, φ_m the solidification rate, ($\varphi_m = \frac{dmol_f}{dt}$, with mol_f = moles refrozen), Q_l the "conditioning" laser power and A_l the optical absorptivity of the surface at the laser wavelength.

The duration of the freezing plateau was

$$\Delta t_{plateau} = \int_0^{Mm} \varphi_m^{-1} dmol_f , \tag{6.3}$$

with M_m = total number of moles molten. Thus $\Delta t_{plateau}$ was the larger the smaller was φ_m.

The heating laser pulses were set so that maximum temperature, cooling rate and the amount of molten material were practically the same at each pressure. The heat flux q (t) could be considered to be approximately zero over the freezing layer close to the surface, where the temperature was practically constant during the solidification process. Therefore the solidification rate φ_m, and hence the plateau length, was determined by the conditioning laser power and by the last two terms in Eq. (6.2). As shown in Fig. 6.3, in general the freezing plateau tended to last longer at high pressure, where convective thermal losses were larger and evaporative losses minimised. This indicated that evaporative losses at low pressures, namely below 100 MPa, were more important than conductive losses at higher pressure were. Such a result could signify that non-congruent evaporation from the sample surface was not reduced to a negligible level at pressures below 100 MPa circa. This conclusion was confirmed by the analysis of the uranium dioxide melting line presented in the next section. Melting experiments were not feasible at pressures lower than 10 MPa, due to the occurrence of massive evaporation.

Experiments were conducted in a similar way using neon as a buffer gas instead of helium. Due to the higher molecular weight of neon, melting point measurements were feasible at

pressures lower than 0.15 GPa only. In fact in this case turbulence and convection in the gas did occur at higher pressures, despite the presence of the protective window just above the sample surface. This caused significant thermal losses and, additionally, affected uncontrollably the optical transmittance of the high- pressure gas layer.

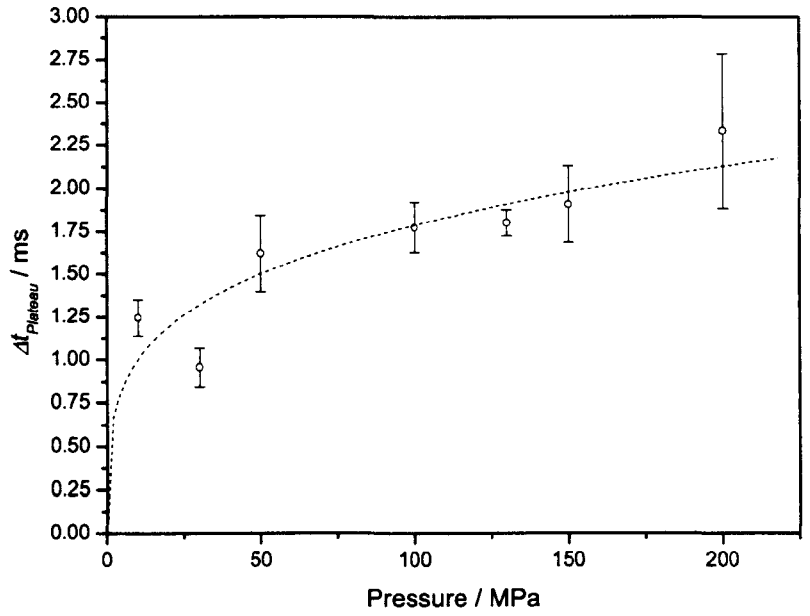

Figure 6.3: Freezing plateau duration as a function of the buffer gas pressure during the experiment. The dotted line is the result of a non-linear fitting procedure, of the type $y = A\sqrt[B]{P}$. In this case, $A = 0.56$, $B = 4$.

Effect of the experiment duration

The duration of the heating laser pulses, and therefore of the whole experiment, could be changed with a certain freedom. The maximum nominal pulse duration obtainable for the high power Nd: YAG laser was 100 ms. However, high power pulses longer than 40 ms were never used, as evaporation from the sample surface and convection phenomena in the gas occurred under any pressure of the buffer gas, if the specimen was kept for too long at several hundreds degrees K above the melting point. Another reason to avoid too lengthy high-power pulses was that the transient decrease of the laser power, due to the discharge of the pumping system capacitors, would make the power profile completely uncontrollable.

Most of the experiments were performed with a power laser pulse duration of about 35ms, with the sample surface being kept over the melting point for about 25 ms. In this way, the freezing plateau lasted some milliseconds, and was perfectly distinguishable as in Fig. 6.1. Interesting trials were performed with power laser pulses of less than 10 milliseconds. In this case, the power needed in order to melt a visible volume of material was much higher, and the Nd: YAG laser pumping system had to be charged with double energy (capacitor voltage at 700 V instead of 350 V, see § 4.2.2). Under these conditions, the sample surface remained above the melting point for some milliseconds, and the freezing plateau would last some tenths of millisecond. The freezing temperature measured in this latter case was invariant (Fig. 6.4) with respect to that measured in experiments of longer duration.

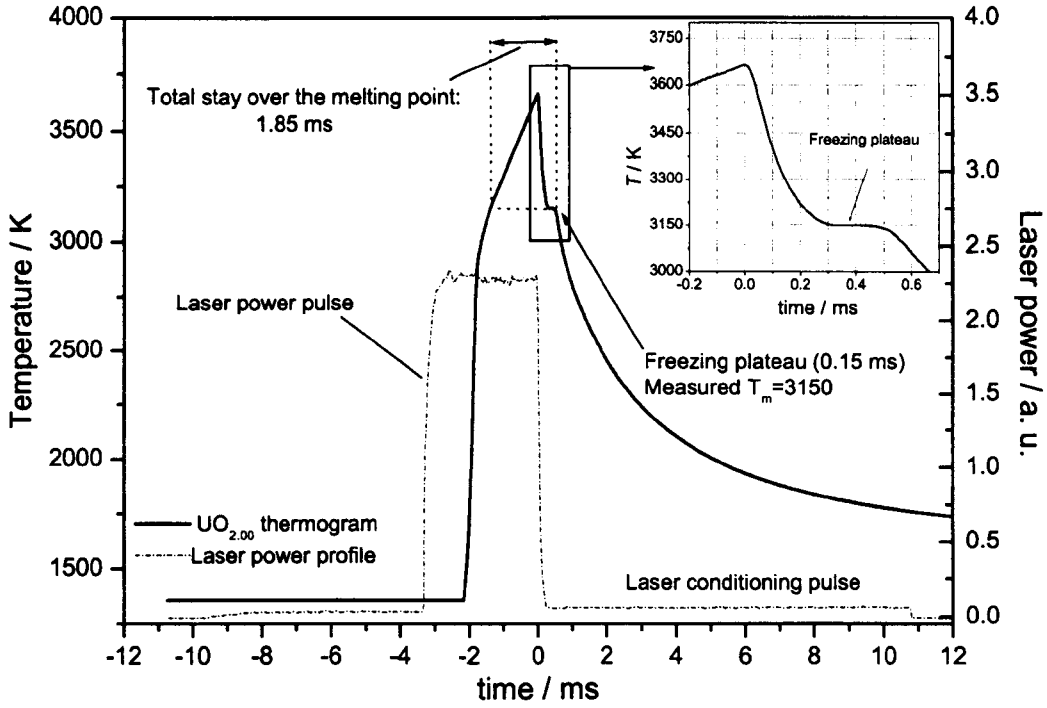

Fig. 6.4: Fast melting /freezing experiment performed on a stoichiometric UO_2 sample. The inset shows an enlargement of the freezing- range.

This result was of great importance. It confirmed that, independently of the whole duration of the experiment (provided that the sample was kept over the fusion temperature for not

more than some tens of milliseconds), no significant diffusion or non-congruent evaporation phenomena possibly affecting the measured melting point occurred in the liquid phase.

Effect of repeated shots

In general, no systematic variation in the measured melting point was observed if melting/freezing experiments were repeated on the same stoichiometric uranium dioxide specimen. This result also confirmed that neither non-congruent evaporation, nor segregation phenomena occurred upon freezing. However, at P_{gas} < 100 MPa a slight but detectable decrease in the melting point measured over successive shots was observed, once more indicating the possible occurrence of non-congruent evaporation during the stay of the sample at temperature over the melting point. Non-congruent evaporation would lead to a change in the surface oxygen content, hence to a decrease of the melting temperature, according to the U-O phase diagram (Chapter 1).

Finally, the results presented include "first shots" only, measured on fresh samples. Successive shots were performed on previously molten surfaces in order to confirm the results, not to assess any statistical significance to the data.

6.2 Uranium dioxide melting line $T_m = T_m(P)$. Consistency of the melting measurements with the Clausius- Clapeyron equation.

6.2.1 Measurement of the uranium dioxide melting line

The melting point of uranium dioxide was determined in a successful measurement with precision of ± 1.5 K. Such a precision was sufficient to distinguish the melting temperature changes due to the thermodynamic effect of the buffer gas pressure on the system.

Fig. 6.5 shows the freezing plateaux measured on $UO_{2.00}$ samples at four different external pressures.

The trend of the melting point of a substance with pressure is expressed by the *melting line.*

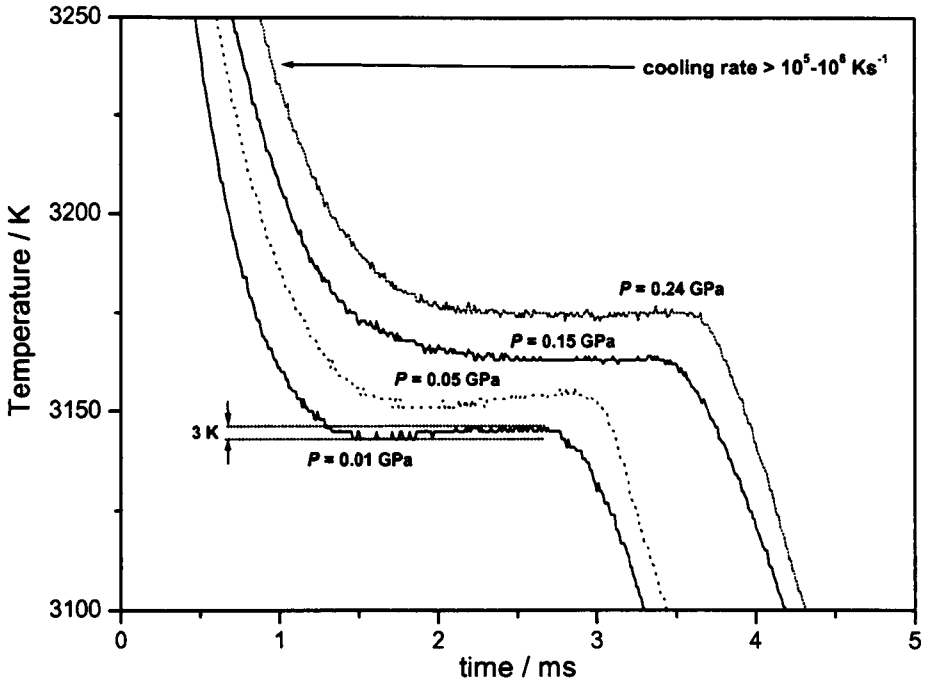

Fig. 6.5: Freezing stage of thermograms measured on UO_2 samples at different pressures.

The knowledge of the melting line may be used for the determination of some thermodynamic parameters, such as the density variation upon melting or the latent heat, or to verify if melting occurs without molecular change. The latter question is of particular interest for the study of UO_{2+x}. In the present work, moreover, the determination of the melting line of UO_2 necessarily constituted the first step in the study of the high-pressure melting behaviour of UO_{2+x}.

Over one hundred melting point measurements were performed at pressures from 10 MPa to 0.25 GPa. The samples were submitted to measurements cycling over the whole pressure range, with oxygen partial pressures varying from 10^{-5} to 0.05 MPa, with good

reproducibility of the melting points measured at the same pressure. Fitting was made on distinct sets of experiments performed at eleven different pressures.

The regression line plotting the freezing point variation with pressure is shown in Fig. 6.6. The slope of the melting line was not fully reproducible if calculated over different subsets of experimental points. Low-pressure (< 0.05 GPa) data were slightly below the linear trend represented by the melting line, probably due to vaporisation effects leading to changes in the O/U ratio and to cracking of the samples. Alternatively, at the highest pressures, optical effects could occur, which were difficult to control. In order to identify the influence of these different pressure-dependent effects on the resulting melting line, linear regression was performed over different subsets of points over pressure intervals of 0.15 GPa (1500 bar), starting from increasingly high pressures (0-0.15 GPa; 0.02-0.17 GPa; 0.03-0.18 GPa and so on). The procedure is illustrated in Fig. 6.7. Regressions performed on pressure intervals starting from 0 up to 0.02 GPa yielded melting line parameters (gradient and intercept) significantly different from the average of the others, and were therefore left out. Gradients and intercepts obtained on the remaining subsets of points were averaged up. In this way diverse effects of different experimental conditions at different pressures were averaged in the final determination of the melting line.

The resulting melting line equation was

$$T_m\,(\mathrm{K}) = 3147 + 92.9\,P\,(\mathrm{GPa}), \tag{6.4}$$

where T_m is the melting temperature (in K) and P the buffer gas pressure expressed in GPa. The same melting line was measured for comparison using Ne instead of He as buffer gas, up to 0.15 GPa. Results were in good agreement, but the statistical robustness was poorer in the sets of data obtained with Ne due to the smaller number of experimental points and to the limited pressure range investigated. For this reason only measurements made under He were taken into account in order to assess the presented melting line.

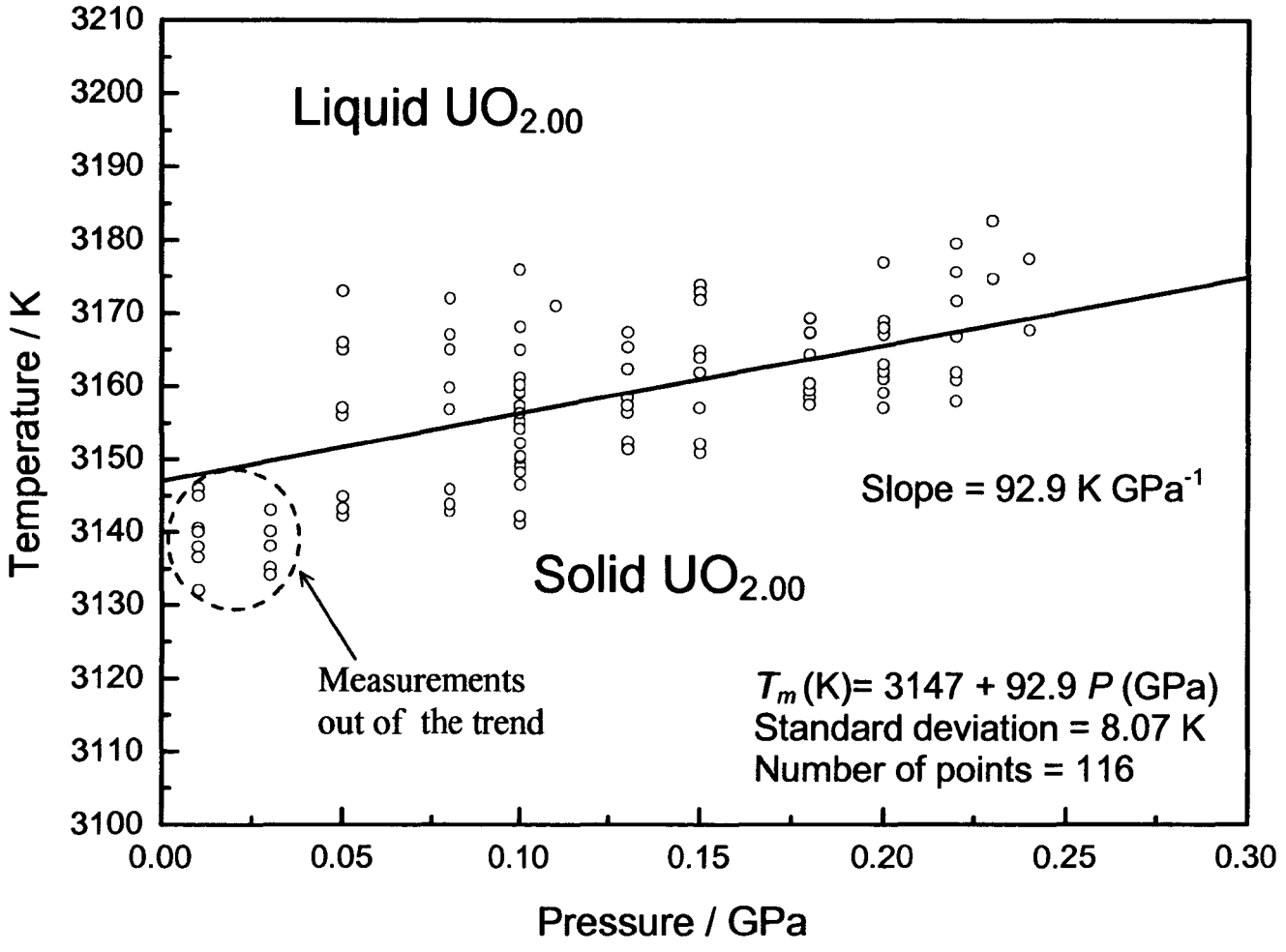

Fig. 6.6. Measured melting line of stoichiometric UO_2.

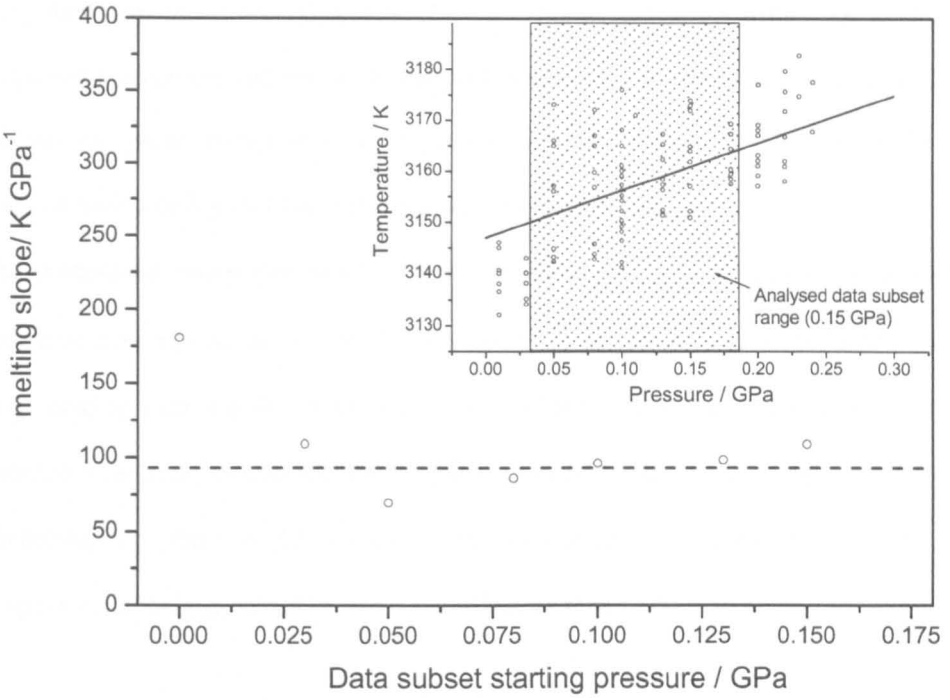

Fig. 6.7: Procedure employed to obtain an average melting slope for stoichiometric uranium dioxide. A linear regression was performed over different subsets of points ranging pressure intervals of 0.15 GPa (1500 bar), starting from increasingly high pressures (0-0.15 GPa; 0.02-0.17 GPa; 0.03-0.18 GPa and so on), as shown in the inset.

6.2.2 The uranium dioxide melting point at room pressure

In Eq. (6.4), the intercept at 3147 ± 5 K represents the extrapolated melting point of uranium dioxide at zero- pressure. This value can be taken as the melting temperature at room pressure too, the atmospheric pressure effect being negligible ($P_{atm} \approx 1 \cdot 10^{-4}$ GPa, corresponding to about $9 \cdot 10^{-3}$ K difference in the melting point according to Eq. (6.4)). The value 3147 K is higher than the one recommended in literature (3120 ± 30 K [1]), although still within the uncertainty range. This can be explained, considering that variations in the sample oxygen content lead to a lower melting point, according to the UO_{2+x} state diagram (§ 2.1.3). Possibly, all the previous melting point measurements on uranium dioxide were affected by oxygen content changes due to non- congruent evaporation in the sample during the experiments. On the other hand, any variation in the sample composition due to non-

congruent evaporation was ruled out in the experiments carried out within this work, because evaporation itself was suppressed by the presence of the high-pressure buffer gas. Therefore the melting point extrapolated at atmospheric pressure from the results of the current research had to be higher than that previously recommended.

The extrapolated value was obtained with a precision of ± 5K. However, the accuracy was not better than ±20 K, due to the uncertainty in the temperature scale definition by the gas lamp used to calibrate the pyrometer (§ 4.2.5), and to the uncertainties in the measured transmittances and reflectivities of the optical elements included in the high-pressure system. Therefore, according to the results of the current research, the room pressure melting temperature of $UO_{2.00}$ should be 3147 ± 20 K rather than 3120 ± 30 K.

6.2.3 Gradient of the uranium dioxide melting line

The gradient of the melting line is called the melting slope (S_m). The measured S_m was

$$S_m = (dT_m / dP)_{\text{experimental}} = 92.9 \pm 17.0 \text{ K GPa}^{-1}, \tag{6.5}$$

The melting slope is a parameter connected with variations of the measured melting point, and not with its absolute value, so it is only bound to the precision, and not to the accuracy of the measured temperature. Therefore the uncertainty reported in formula (6.5) takes into account all the possible sources of error (except the, negligible, uncertainty in the exact value of the pressure inside the vessel).

The experimental value of the melting slope S_m should be compared to the one predicted by the Clausius- Clapeyron equation

$$\left(\frac{dT_m}{dP}\right) = \frac{T_m \Delta v_m}{\Delta H_m}, \tag{6.6}$$

where T_m is the melting point, Δv_m the specific volume change on melting and ΔH_m the latent heat of melting. The Clausius- Clapeyron equation (6.6) describes the line of coexistence, at

thermodynamic equilibrium, of two phases having the same composition, and is obtained by equating the free energies of the two phases. T_m in the left- hand side can be considered constant and equal to its value at atmospheric pressure with good approximation. Values for T_m, Δv_m, and ΔH_m were chosen among those reported in the literature (see Chapter 1). For Δv_m the value (8.26 ± 3.3) 10^{-6} m^3kg^{-1} was calculated from the density values recommended in [2, 3]. For ΔH_m, the value of 277.1 ± 3.7 kJ kg^{-1} quoted in [4] was chosen as based on enthalpy data near the melting point, rather than being extrapolated from the fitting of several enthalpy and thermal capacity databases over a wider temperature range reported in literature. For the standard melting point of stoichiometric $UO_{2.00}$ the value obtained in this research could be used: T_m = 3147 ± 20 K. The errors reported represent the 66.7 % confidence limits ($\pm\sigma$).

By substituting the chosen values in the right hand side of Eq. (6.6), one calculates the theoretical melting line slope S_m^*

$$S_m^* = (dT_m / \mathrm{dP})_{\mathrm{calculated}} = 93.8 \pm 37.5 \text{ K GPa}^{-1} \tag{6.7}$$

The error δS_m^* = 37.5 K GPa^{-1} was calculated by differentiating equation (6.6) and by applying the law of errors propagation:

$$\delta S_m^* = \sqrt{\left|\frac{\partial S_m}{\partial T_m}\delta T_m\right|^2 + \left|\frac{\partial S_m}{\partial \Delta v_m}\delta \Delta v_m\right|^2 + \left|\frac{\partial S_m}{\partial \Delta H_m}\delta \Delta H_m\right|^2}, \tag{6.8}$$

where δT_m , $\delta \Delta v_m$, and $\delta \Delta H_m$ indicate the known uncertainties on the three parameters.

The agreement with the experimental average melting slope S_m is excellent. This result was of the foremost importance. It actually constituted the "experimental" proof ensuring that the laser-induced melting / freezing process realised with the method presented in this work occurred under *thermodynamic equilibrium conditions* despite the high heating and cooling rates involved[1]. Inversely, this result can be considered as the experimental proof of the

[1] *Thermodynamic equilibrium was realised locally, in the molten part of the sample surface, far enough from the moving interface solid/liquid.*

validity of the Clausius- Clapeyron equation for stoichiometric uranium dioxide, confirming that this compound melts congruently without any detectable chemical change.

One can notice that the error affecting S_m^* calculated with the literature data is more than twice larger than the experimental S_m obtained in the current research. This result was used to inversely calculate the value of Δv_m, which was the parameter affected by the largest uncertainty in formula (6.6).

We have:

$$\Delta v_m = \frac{S_m \, \Delta H_m}{T_m}, \tag{6.9}$$

Differentiating equation (6.9) in order to calculate the uncertainty, and considering that the error on the experimental melting slope was 17.0 K GPa^{-1}, we obtained:

Δv_m=(8.18 ± 1.50) 10^{-6} m^3 kg^{-1} . (6.10)

The value, though obtained with an indirect calculation, confirmed the one reported in [5], with a smaller error.

6.3 Conclusions

The determination of the melting point of uranium dioxide at different hydrostatic pressures, and, consequently, of the melting line of this material, constituted a first important result and also a successful test of the new experimental method presented in this work.

The agreement between the melting slope obtained experimentally and that predicted by the Clausius- Clapeyron equation, in addition, confirmed that an unstable oxide such as uranium dioxide melts without any chemical change.

These points constituted the necessary premises to proceed in the investigation of the melting behaviour of uranium dioxide presented in the next chapters.

References Chapter 6

1. J.K.Fink, M.C. Petri, Thermophysical Properties of Uranium Dioxide, Argonne National Laboratory Report ANL/RE-97/2, 1997.
2. J.K.Fink, J. Nucl. Mater. **279** (2000), 1.
3. J. H. Harding, D.J. Martin, P.E. Potter, *Thermophysical and Thermochemical Properties of Fast Reactor Materials*, Harwell Laboratory UKAEA Report EUR 12402, 1989.
4. M. Musella, C. Ronchi and M. A. Sheindlin, Int. J. Thermophys. **20** (1999), 1177.
5. W.D. Drotning, in: *Proceedings of the Eighth Symposium on Thermophysical Properties,* Gaithersburg, MD, National Bureau of Standards 1981, 15- 18 June 1981.

Chapter 7

Liquidus and *solidus* determination in hyperstoichiometric uranium dioxide

The measurements of stoichiometric uranium dioxide melting point under different buffer gas pressures, presented in the previous chapter, suggested that the ideal pressure range of operation for the method should be between 0.1 and 0.15 GPa. Measurements would be influenced by evaporation from the sample surface at lower P_{gas} and by convection and turbulence phenomena in the gas at higher P_{gas}. Thus most of the melting point measurements on *hyperstoichiometric* uranium dioxide samples were performed under a buffer gas pressure of 0.1 GPa. The melting point shift due to the high pressure was assumed, in the case of hyperstoichiometric samples, to be considerably smaller than the precision of the measurements. This was experimentally confirmed by some melting measurements made on $UO_{2.07}$, $UO_{2.11}$, $UO_{2.17}$ and $UO_{2.2}$ at 0.05, 0.1, 0.15 and 0.2 GPa. Melting point measurements on hyperstoichiometric uranium dioxide could not be conducted at pressures lower than 0.05 GPa due to the high non-congruent evaporation rate, which would lead, under the produced experimental conditions, to decomposition of the sample.

The determination of the *liquidus* of hyperstoichiometric uranium dioxide, described in the first part of this chapter, involved the same experimental aspects as the study of the melting point and melting line of stoichiometric urania. The thermal arrest technique and the coherent reflected light method were used in order to determine the point of first appearance of the solid phase within the cooled liquid in UO_{2+x} samples.

The *solidus* of hyperstoichiometric uranium dioxide was obtained with different methods that are separately reported in the second part of this chapter. Exhaustive discussion of the

results obtained on the *solidus* and *liquidus* lines of hyperstoichiometric uranium dioxide will then be presented in Chapters 8 and 9 along with an analysis of possible error sources.

7.1 *Liquidus* determination

Melting experiments were performed on hyperstoichiometric UO_{2+x} samples, with $0 \leq x \leq 0.21$. The experimental procedure was the same as the one presented in the previous section and in Chapter 2 for stoichiometric samples.

7.1.1 Thermal arrest method

Typical thermograms measured in samples having six different oxygen contents are plotted in Fig. 7.1. As in the case of stoichiometric samples, no inflection was observable on the heating stage corresponding to the melting transition. As the O/U ratio slightly increased (see $UO_{2.00}$, $UO_{2.01}$ and $UO_{2.03}$ curves in Fig.7.1), the freezing arrest plateau was gradually replaced by two inflection points on the cooling flank of the thermogram. The first one was attributed to the appearance of the solid phase inside the molten pool (*liquidus* transition). The cooling rate decreased at this point due to the onset of latent heat release. The second one corresponded to the temperature of total solidification - *solidus* transition. After this transition, the cooling rate increased again, indicating that freezing was completed (Fig. 7.2). The shape of thermograms recorded on specimens with an O/U ratio higher than 2.03 was more complicated. In the cooling stage of these thermograms, after a first knee point (sometimes followed by a very short thermal arrest) corresponding to the *liquidus* transition, a second *thermal arrest* occurred, more difficult to explain. Sometimes even a slight thermal recalescence was observed at this point (see, for instance, the $UO_{2.20}$ thermogram in Fig. 7.1). Therefore, the second inflection point did not show the features expected for a simple freezing transition, but was possibly produced by the combination of some more complex

phenomena. Since the *solidus* transition could not be directly correlated to the described second thermal arrest, alternative methods had to be devised for its investigation, separately described in the second part of this chapter.

The determination of *liquidus* by means of the thermal arrest technique was not always straightforward. The "first knee point" on the cooling flank of thermograms was sometimes difficult to detect. Moreover, considerable statistical dispersion affected the set of experimental temperatures at which this "first knee point" was observed over several measurements repeated on specimens of the same composition. This was due to the complexity of the laser-induced melting/freezing process in non-congruently melting samples, where fast oxygen diffusion could occur from the solid into the liquid phase, and oxygen concentration gradients could be produced in addition to temperature gradients.

In this case, a generalisation of Eq. (6.2) describing the heat balance on the sample surface in presence of oxygen diffusion in the molten zone during the freezing process is

$$\begin{aligned} q = {} & \Delta H_m(C)\varphi_m(t,C) + A_l Q_l(t) + \\ & -\varepsilon\sigma T_m^4 - \xi(t)(T_m - T_{gas}) - \Delta H_{vap}(C)\varphi_{vap}(t,C) - \rho(t,C)D(t,C)\theta(t,C)\nabla^2(C) \end{aligned} \quad (7.1)$$

Here $\rho(t, C)$ is the material density, $D(t, C)$ the local diffusion coefficient and C the excess-oxygen concentration, scalar function of the spatial co-ordinates x, y, z as well as of time t. ∇^2 is the laplacian operator. θ (t, C) is the enthalpy change caused by a unit variation of concentration,

$$\theta = \frac{dh}{dC}.$$

All the remaining symbols in Eq. (7.1) were defined in § 6.1.1.

In Eq. (7.1), the dependence of ρ, D and θ on time is indirect, being defined through the dependence of these parameters on temperature $T(t)$. Eq. (7.1) represents a simplified situation where only concentration and no temperature gradients exist in the radial direction.

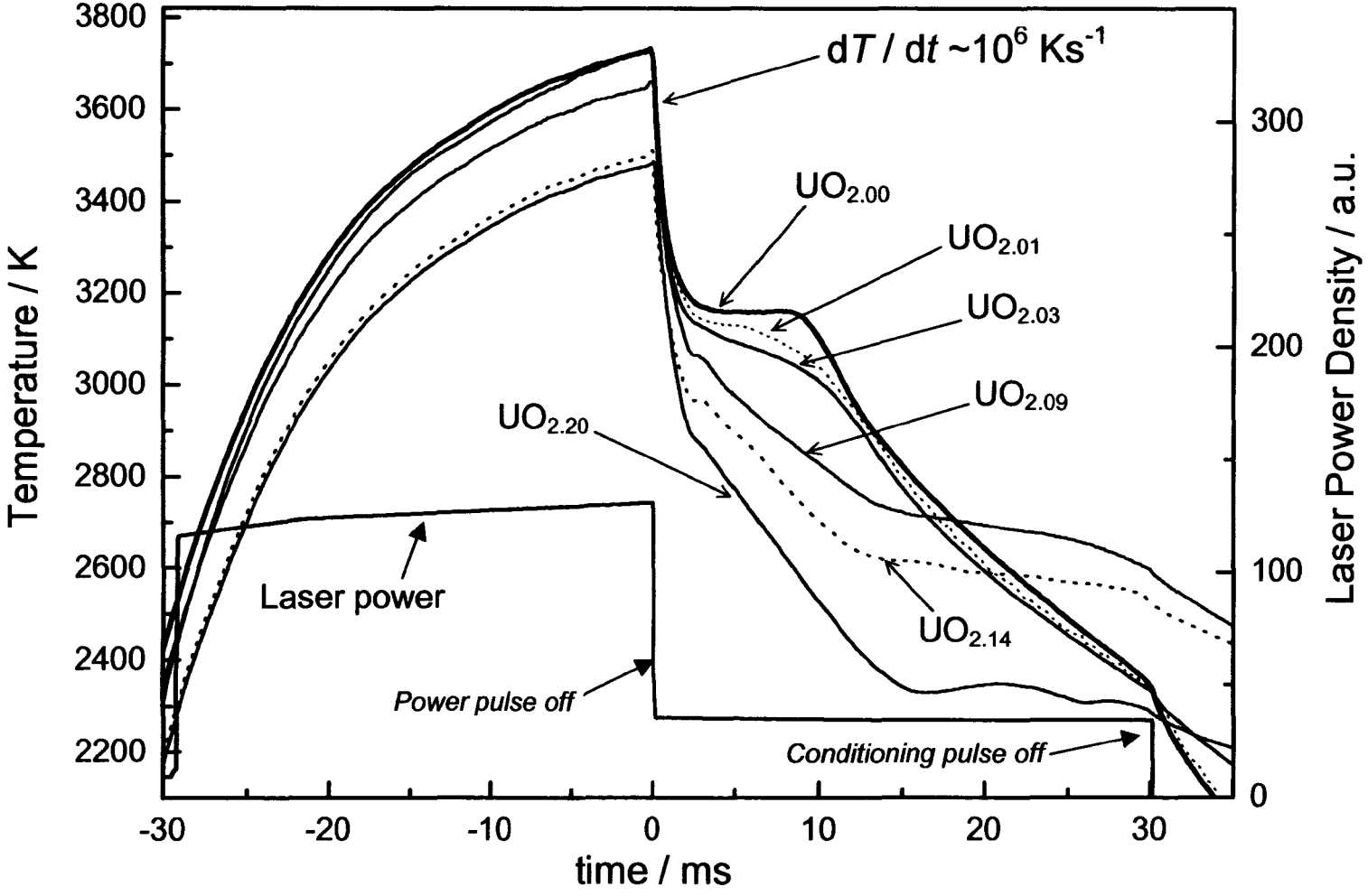

Figure 7.1: Thermograms measured on stoichiometric and hyperstoichiometric uranium dioxide samples. The conditioning part of the heating laser pulse was not used in all the cases.

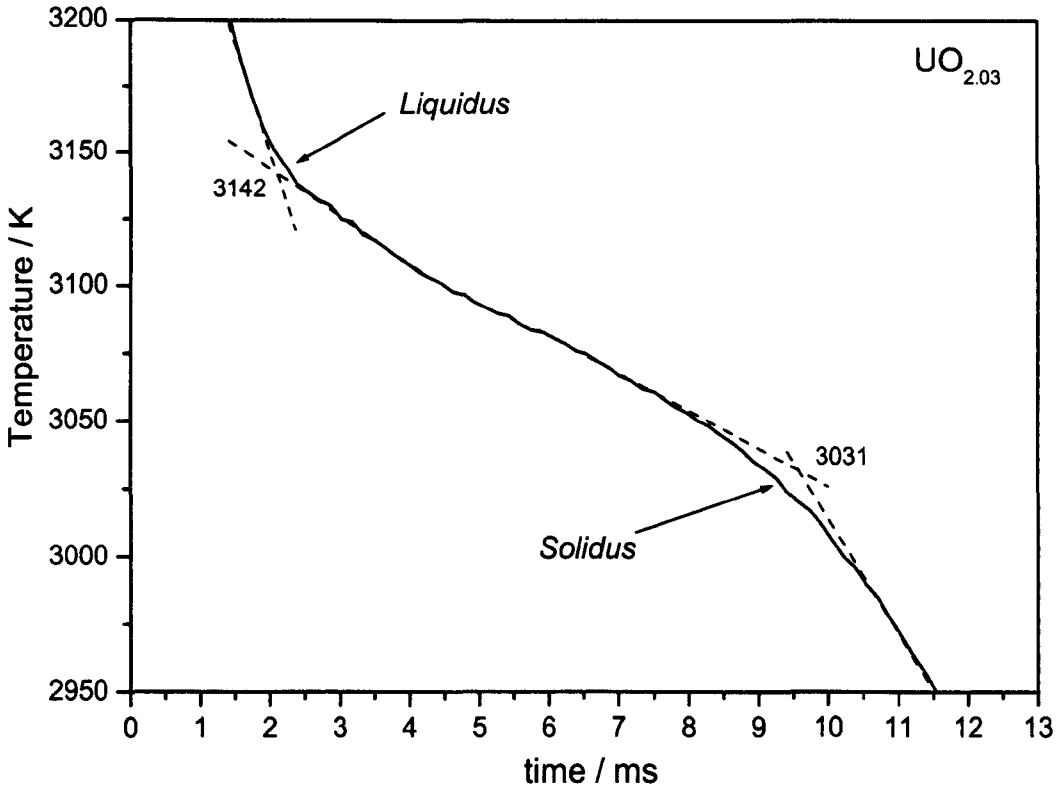

Fig. 7.2. *Liquidus* and *solidus* inflections on a thermogram measured on a $UO_{2.03}$ sample.

The formation of large oxygen gradients in the liquid and in the re-frozen solid is an important issue. Such problem will be extensively discussed in Chapter 8, with the help of a computer simulation of the melting-freezing experiments.

As a consequence of the oxygen redistribution in the liquid, the composition of the sample surface at the onset of freezing could significantly differ from the initial one. In this case, the *liquidus* temperature would be measured on an *a-priori* unknown composition.

The determination of the *liquidus* through the thermal arrest method could become even more complicated if segregation occurred in the solidification process. In fact, the release of an amount of latent heat sufficient to produce a detectable knee point on the thermogram requires the formation of a certain quantity of solid in the liquid pool. Although small, this solid mass cannot be considered as infinitesimal, like the very first solid seeds, and can therefore be

affected by segregation of the oxygen concentration, if oxygen diffusion from the solid into the liquid occurs rapidly enough.

Simulation results presented in Chapter 8 show that the formation of large composition gradients constituted a problem in highly oxidised samples (initial composition O/U > 2.10).

Despite all the mentioned issues, the observation of the first knee point led to an estimate of the *liquidus* temperature that was proved to be reliable in most of the cases. In fact, both undercooling and composition gradients depended on the experiment duration, in particular on the time interval during which the sample surface was kept above the melting point. This time interval was reduced by nearly one order of magnitude in experiments carried out with shorter heating pulses. *Liquidus* temperatures obtained in short and long experiments were finally in quite good agreement (see also discussion in Chapter 8), ensuring that the total error due to possible undercooling and segregation was not large enough to discredit the measured data.

7.1.2 Coherent reflected light method

The employment of an additional independent method for the experimental determination of the *liquidus* gave further reliability to the empirical data obtained with the thermal arrest technique. Thus the coherent reflected light method (§ 2.3.7) was also in this case very useful. The procedure and the information obtained were the same as in the investigation of the stoichiometric uranium dioxide melting point (§ 4.1.1). A complete thermogram and reflected light signal (RLS) diagram obtained on a hyperstoichiometric uranium dioxide sample will be shown and described in detail in the next section. Here only the part of a thermogram around the *liquidus* point is considered. Fig. 7.3 shows the *liquidus* range of the thermogram and the RLS graph recorded during a melting point measurement on a $UO_{2.09}$ specimen. An accurate description of the cooling process occurring in the molten zone during this stage of the experiment was obtained with the help of the simulation code and the post-melting sample characterisation, both presented in Chapter 8. The thermogram of a $UO_{2.09}$ sample was

simulated with the same starting conditions as those of the true experiment, and is also plotted in Fig. 7.3. Simulation and experiment were in fair agreement. This suggested that the succession of events occurring on the sample surface according to the simulation should be not far from the reality.

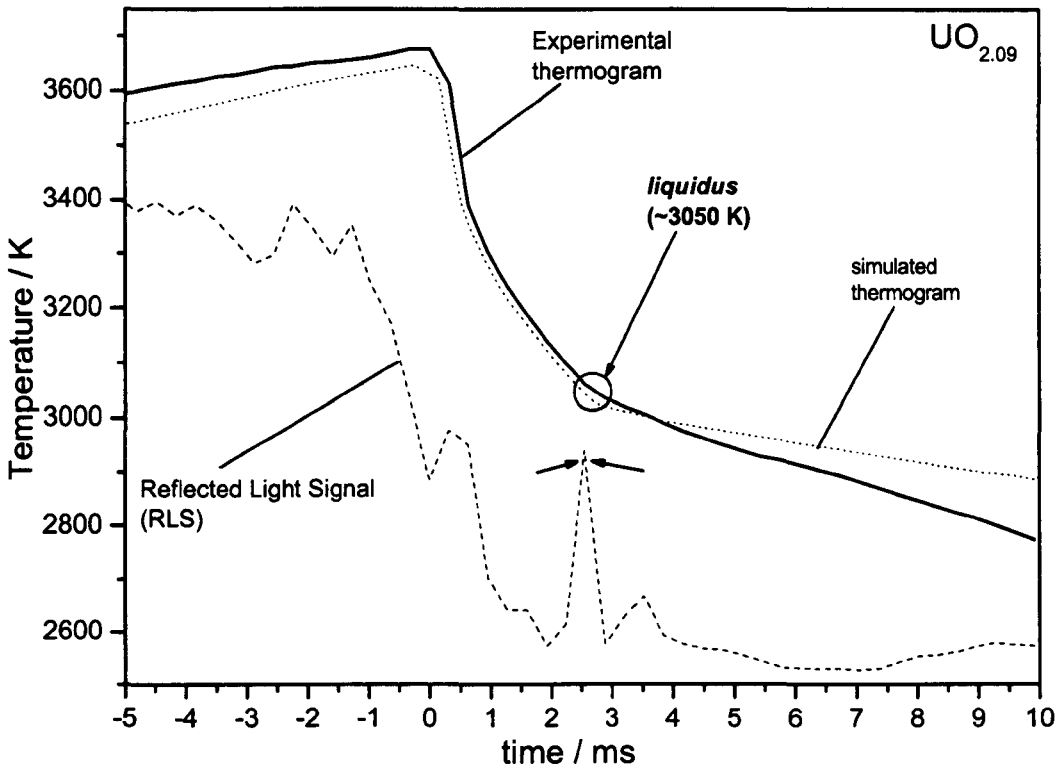

Fig. 7.3: Experimental determination of *liquidus* on a $UO_{2.09}$ sample. Techniques employed: thermal analysis and reflected light signal (RLS) analysis.

The sample surface temperature reached its maximum when the power laser pulse had come to its end. Then the temperature decreased very rapidly up to the slight inflection point indicating the first appearance of the solid phase. In this case, a *liquidus* knee point was difficult to identify with precision. The transition was however clearly revealed by the analysis of the RLS. This latter signal was the composition of 514-nm reflected light and thermal radiation emitted by the sample surface. As the temperature decreased, the RLS intensity also decreased

rapidly with the thermal-radiation component. An instant after the onset of cooling, the molten pool bottom started to freeze over. The freezing front advancing towards the surface generated then vibrations in the liquid. These vibrations scattered the 514-nm Ar probe- laser light, and, therefore, decreased the intensity of the RLS reflected light component. After a few milliseconds, a solid seed appeared on the surface of the molten pool starting a new freezing front moving from the surface inward. As soon as this happened, the surface would reflect the Ar probe laser beam like a mirror, generating a sudden spike in the RLS intensity detected by the pyrometer. Such a spike is clearly visible in Fig. 7.3. According to the described process, the spike corresponded to the exact instant at which the surface of the molten pool reached the *liquidus* temperature. After that, the RLS intensity decreased again due to the roughness of the newly formed solid surface and to the temperature decrease.

Fig. 7.3 shows an experiment where the *liquidus* point given by the thermal arrest is in almost perfect agreement with the one obtained to RLS analysis. Unfortunately, such an agreement was obtained seldom. The thermal arrest technique measured a *liquidus* temperature normally lower than that measured by the RLS technique. This behaviour was attributed to the effects of undercooling and heterogeneous composition on the *liquidus* measured by thermal arrest, as discussed in the previous subsection.

7.1.3 Conclusion

Fig. 7.4 shows the *liquidus* points measured for several UO_{2+x} compositions. Data measured by means of the thermal arrest technique are separated from those obtained with the RLS analysis. The difference between the two data sets increases with the oxygen content of the samples. This confirms that composition-dependent out-of-equilibrium phenomena, like the formation of oxygen concentration gradients, were the main causes of the discrepancy. Experimental data obtained with the thermal arrest analysis were discarded whenever this disagreement was beyond the uncertainty limits. Otherwise, they were included in the statistics

with a weight inversely proportional to their standard deviation. Fig. 7.5 shows the standard deviation of subsets of data obtained for different sample compositions. Also here the data sets for the thermal arrest technique and RLS method are plotted separately. In both cases, the data dispersion increased with the O/U ratio.

Despite the experimental difficulties listed in § 7.1.1, the *liquidus* point could be reliably measured in a number of UO_{2+x} samples with several different compositions. The precision of the measurements was in this case lower than the one yielded for stoichiometric UO_2. This was due to the non- perfect definition of the first knee point on the thermograms and to the sometimes uncertain location of the *liquidus* spike on the RLS. Nonetheless, the experimental results were proved to be well reproducible within the standard deviation. Finally, a *liquidus* line could be proposed for the system UO_{2+x} with $0< x < 0.21$. This line will be discussed in Chapter 9.

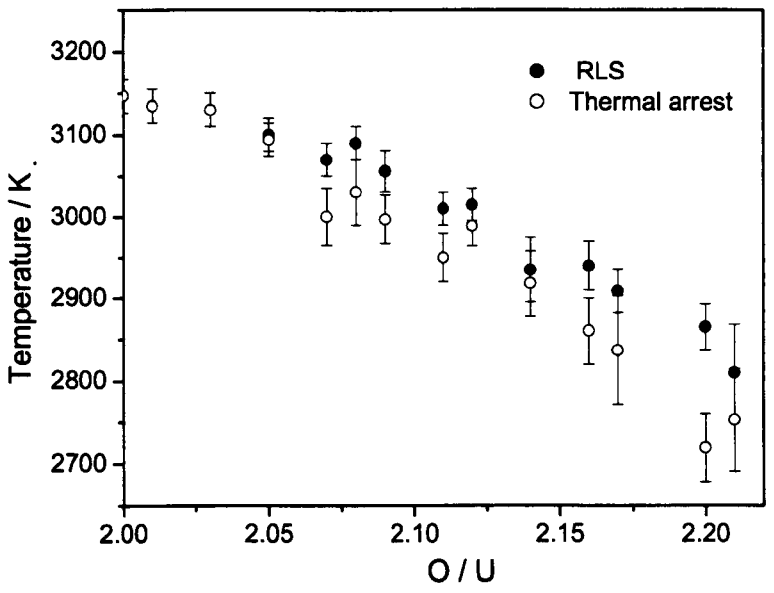

Fig. 7.4: Comparison between UO_{2+x} *liquidus* points measured at several O/U compositions by means of thermal arrest method and reflected light signal (RLS) analysis.

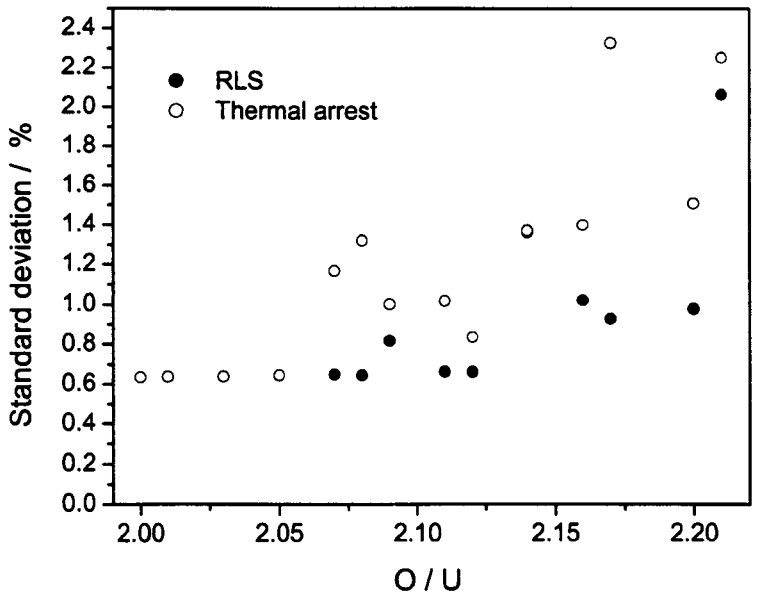

Fig. 7.5: Relative standard deviation on the *liquidus* temperature measured at several O/U compositions. Comparison between thermal arrest and RLS techniques.

7.2 *Solidus* determination

7.2.1 Limits of the thermal arrest method in determining the solidus

In § 7.1.1 it was pointed out that, for samples with composition sufficiently close to stoichiometry, both *liquidus* and *solidus* points could be deduced from the empirical thermograms with a classical thermal analysis. For samples with O/U > 2.03 approximately, the shape of thermograms during the cooling stage was more complex. Fig. 7.6 shows an example thermogram recorded on a $UO_{2.17}$ specimen, displaying all the features typical of thermograms recorded on samples with O/U > 2.03.

The heating flank of the curve does not present any significant difference with respect to the thermograms already discussed for stoichiometric UO_2 in § 6.1.1.

In correspondence to the *liquidus* knee point in the cooling stage, the cooling rate decreased from $\approx 10^6$ K s^{-1} to approximately $\approx 10^4$ K s^{-1}, due to the release of the latent heat of solidification.

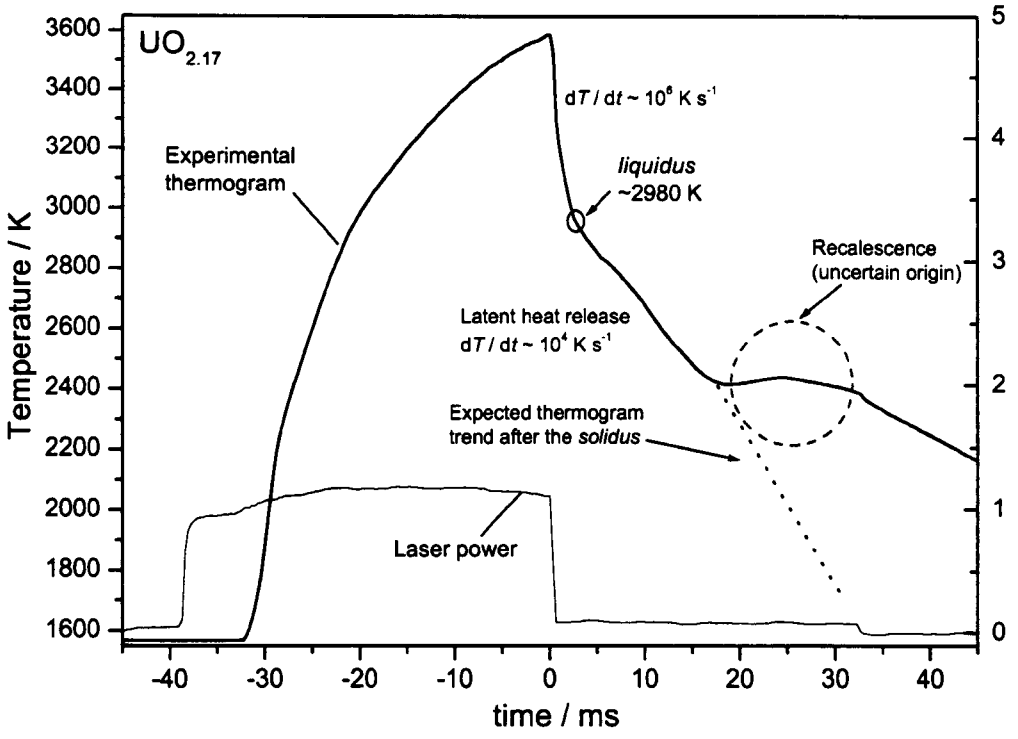

Fig. 7.6: Example experimental thermogram recorded on a $UO_{2.17}$ sample.

This phase of the measurement, unlike the case of stoichiometric $UO_{2.03}$ and slightly hyperstoichiometric UO_{2+x}, terminated with a second point of inflection followed by a stage with lower cooling rate. In the thermogram of Fig. 7.6, even a thermal recalescence was clearly observed at this point, which was detected in several other UO_{2+x} samples. Such a behavior could not correspond to a simple *solidus* transition. Had that been the case, a second knee point would have been observed, followed by a re-increase of the cooling rate, as the latent heat release would have been complete (the thermogram would have followed the dotted line in Fig. 7.6). The shape of the empirical thermogram could instead be typical of a *monotectic* transition, described in § 3.2.1 and Fig. 3.3b. However, the temperature of the observed second thermal arrest should have been the same (within the experimental uncertainty) for all sample compositions, if the thermogram shape had been generated by a monotectic transition. As shown in Fig. 7.1, instead, the lower the sample oxygen content, the higher was the temperature at which the second thermal arrest was observed.

The dispersion in the reproducibility of the temperature of the second thermal arrest is plotted in Fig. 7.7 as a function of the sample composition. The uncertainties yielded are in most of the cases too large to be associated with the measurement of a simple phase transition only. Evidently, further out-of-control phenomena were likely to be involved in the process, probably connected with the displacement of the remaining liquid mass during the freezing process, in the simultaneous presence of gradients of temperature, concentration and density. Some more clues about a possible interpretation of the shape of these thermograms will be discussed in the next chapter. As for the present discussion, the point of interest is that the reliability of the *solidus* temperature, determined by means of the thermal arrest method, needed to be confirmed, in samples with O/U > 2.03, by further, independent measurements.

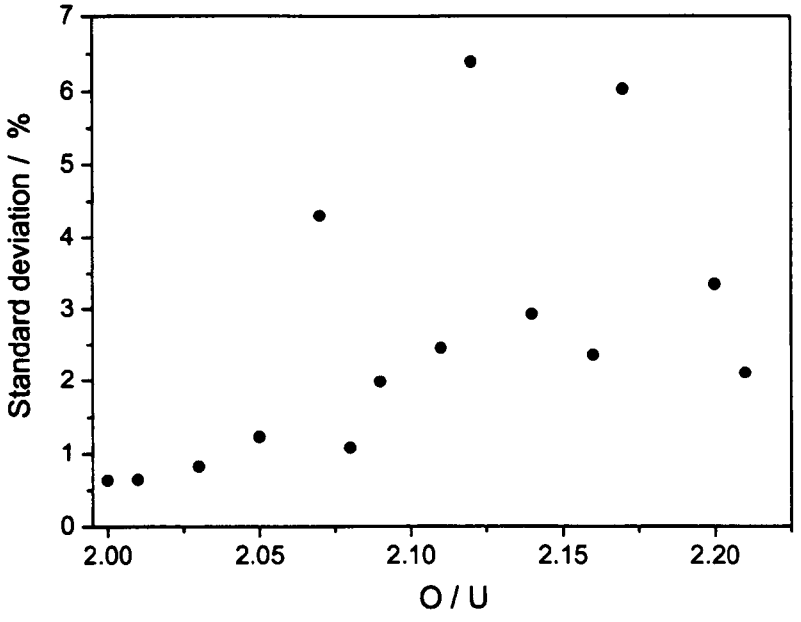

Fig. 7.7: Relative standard deviation on the second thermal arrest temperature at several O/U compositions. In the worst cases, a relative σ of ± 6.4 % signifies an absolute uncertainty of approximately ± 145 K.

7.2.2 Alternative ways for determination of the solidus

The coherent- reflected- light technique was developed within this project as an alternative method for establishing the *solidus* temperature on the heating flank of a thermogram.
Another simple but effective method for a reliable estimate of the UO_{2+x} *solidus* was the visual observation of the sample after experiments in which high- power laser pulses heated the surface up to an increasingly high maximum temperature.

Coherent reflected light method

The coherent- reflected- light technique was the most effective method for the determination of the UO_{2+x} *solidus*. Fig. 7.8 shows the thermogram of Fig. 7.6, recorded by the 644-nm pyrometer channel, along with the reflected light signal (RLS) recorded during the same experiment by the second pyrometer channel tuned at 514 nm.
The first time derivative of the RLS, also plotted in Fig. 7.8, could be used to observe the onset and disappearance of vibrations in the superficial liquid layer.
The RLS showed variations of the sample surface state, and, accordingly, six stages could be evidenced in Fig. 7.8, generally similar to the stages distinguished in Fig. 6.1 (§ 6.1.1): i) The RLS showed an approximately constant intensity before the onset of melting on the sample surface. ii) As the sample surface reached the *solidus* temperature, a sudden increase in the RLS was observed. At this point an extremely thin, motionless liquid layer was produced, acting like a mirror on the surface, and reflecting a greater part of the Ar laser beam into the pyrometer detector. The RLS revealed the gradual onset of vibrations in the liquid mass under capillarity forces. Such vibrations were translated into oscillations easily visible in the RLS first time derivative. iii) The liquid mass increased and the capillarity-force-induced vibrations were augmented leading to significant scattering of the probe laser beam. The resulting effect was the decrease of the reflected light component intensity of the signal detected by the 514-

nm pyrometer channel. On the other hand, at this stage the *total* 514-nm signal intensity increased due to the contribution of radiation self-emitted by the hot surface.

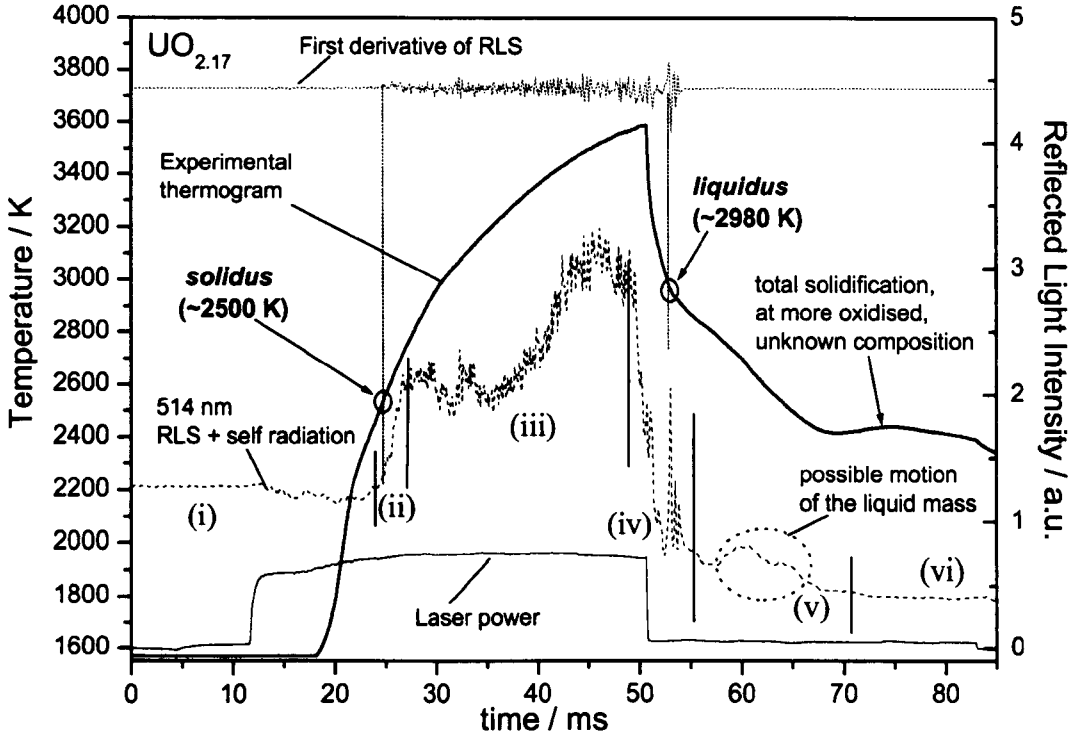

Fig. 7.8: Experimental thermogram recorded for a $UO_{2.17}$ sample. 514-nm reflected light signal and its derivative are also displayed, with the help of which six stages in the melting/ freezing process could be distinguished, and *solidus* and *liquidus* transitions determined.

iv) The end of the more powerful part of the *Nd: YAG* laser pulse initiated the rapid decrease of the specimen surface temperature. When the surface reached the freezing temperature and the first solid seed was formed, the *liquidus* point was revealed by a spike in the RLS, as already described in § 6.2.2. The RLS first derivative revealed that the liquid mass vibrations disappeared almost immediately after the first solid seed formation, as most of the surface froze over starting from the first solid nucleus. v) Inhomogeneous oxygen distribution over the molten mass was likely to cause different parts of the pool to solidify at different temperatures, probably leading to a radial displacement of the remaining liquid mass. This could be the origin of the slight, low- frequency oscillations of the RLS during freezing (between *liquidus*

and total solidification). vi) After complete freezing, vibrations disappeared, and the RLS stabilised around an approximately constant level depending on the (new) angular distribution of the reflection.

Finally, in spite of the complex effects occurring during the freezing process, the *solidus* point could be reliably determined during the heating stage of the experiment from the presented RLS analysis.

Post-melting visual examination

A good estimate of the *solidus* point could be independently obtained with an alternative, simple method. A "visual test" was performed on the samples with O/U > 2.03 in order to estimate if the liquid phase was really appearing around the *solidus* temperature measured by means of the RLS analysis.

The method is illustrated in Fig. 7.9 a-f, referring to samples with the same composition as the one investigated in the experiment of Fig. 7.8. In successive shots, the sample was heated by the pulsed Nd: YAG laser beam up to increasingly high maximum temperature. After each shot the specimen surface was observed with the optical microscope, and possible formation of liquid was checked from topographic changes. The *solidus* temperature should be situated above the maximum temperature reached in the previous shot in which liquid was not formed and below the maximum temperature reached in the successive shot leading to a change in the surface topography.

Fig. 7.10 shows this "post- melting" visual examination on a $UO_{2.12}$ sample surface where traces of liquid were formed by heating the sample just above its *solidus* point (≈ 2700 K).

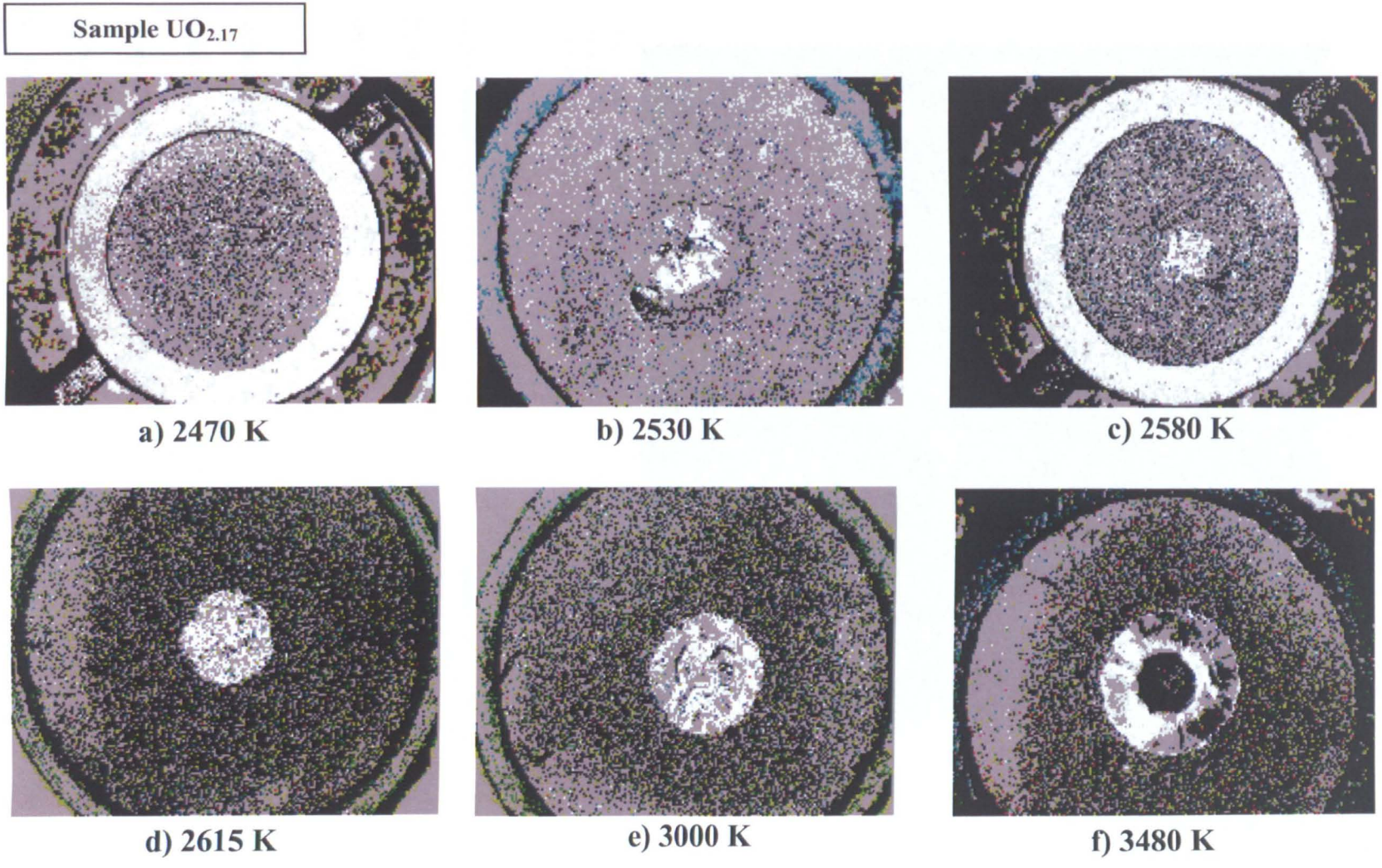

Fig. 7.9 a)- f): Post-melting visual examination to determine the *solidus*.

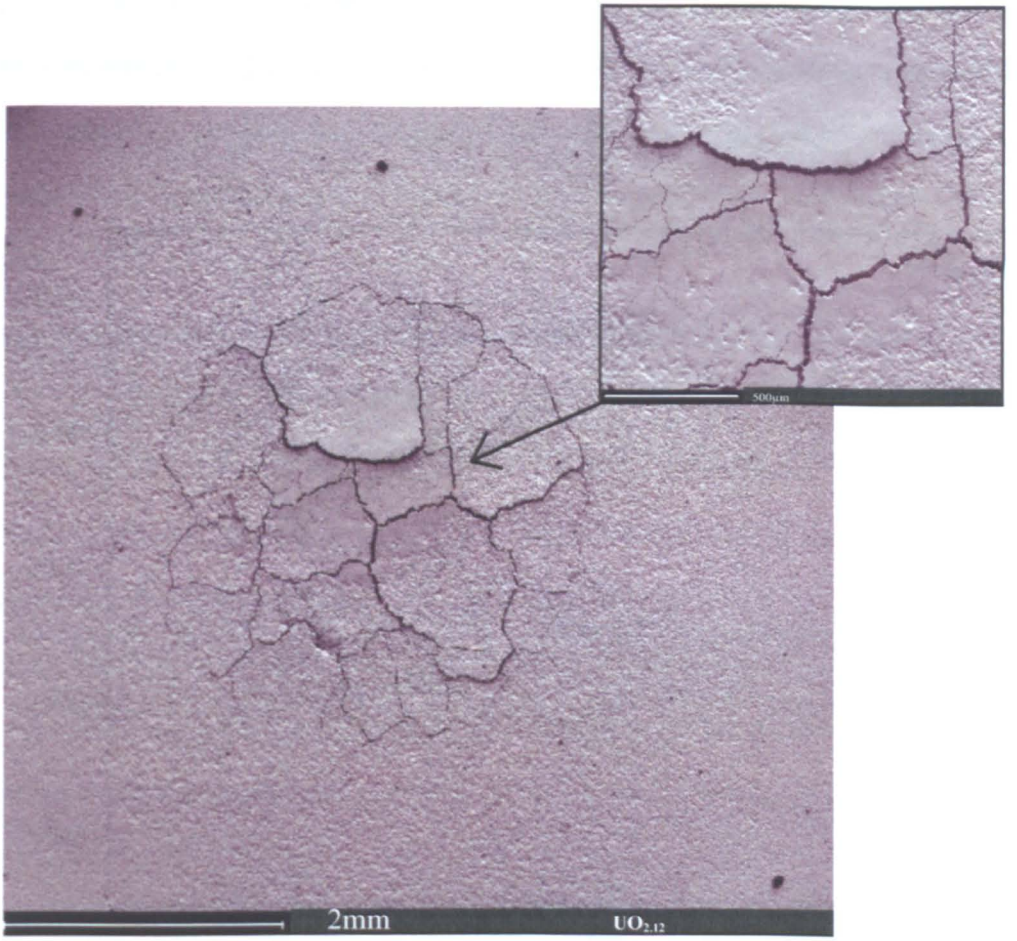

Fig. 7.10: Surface of a $UO_{2.12}$ sample where traces of liquid were formed by heating the sample few tens of degrees Kelvin above the *solidus* point (≈ 2700 K). The inset shows an enlargement of the zone where traces of liquid were formed.

In the example given in Fig. 7.9, the *solidus* point was estimated to be between 2470 and 2530 K, in perfect agreement with the result yielded by the RLS analysis.

Due to the limited controllability of the Nd: YAG laser power, the maximum temperature reached in each shot could not be planned with precision. On the other hand, the very simple technique provided a method that could reinforce the information obtained from other methods, practically without any uncontrollable source of error. Of particular interest is the series of optical microscope images after each shot (Fig. 7.9), compared with the thermogram recorded during some selected shots (Fig. 7.11). Thermograms did not show any inflection at all, unless the maximum temperature reached was well above the *liquidus* point, so that a sufficient amount of liquid was formed. In this latter case, the sample after the melting

experiment showed a peculiar morphology, which will be described in the next Chapter 8. The agreement between results of RLS analysis and post- melting visual examination methods was satisfactory.

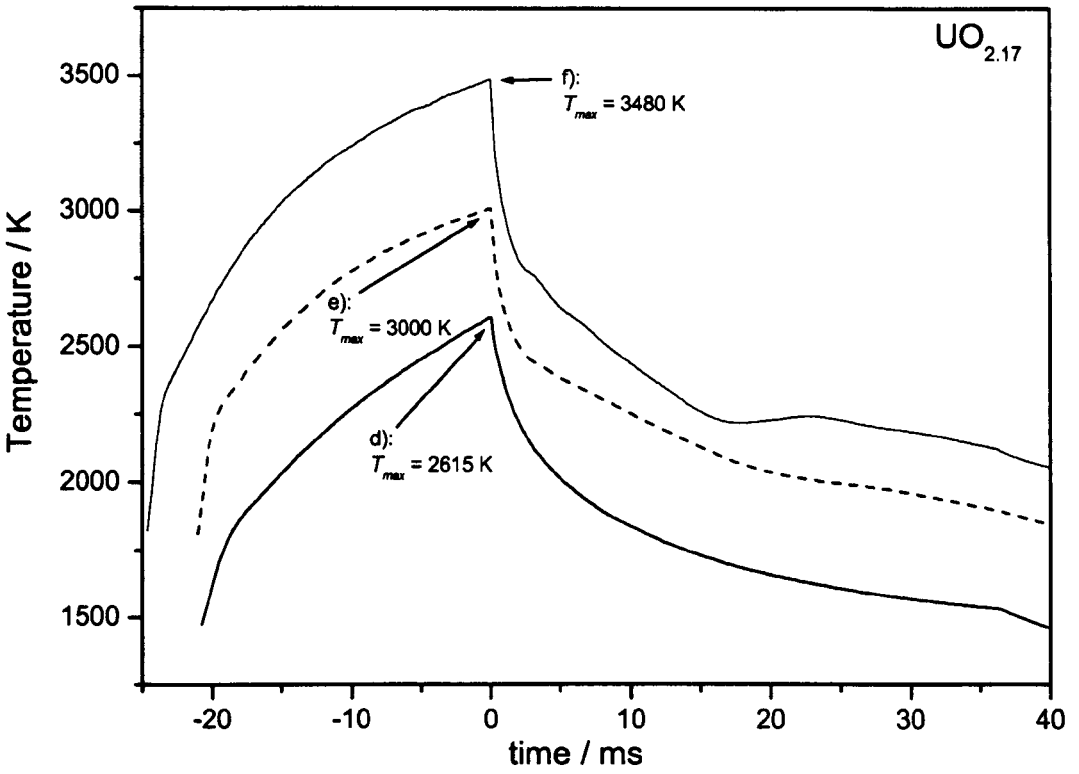

Fig. 7.11: Thermograms corresponding to samples d), e and f) of Fig. 7.9. Thermograms did not show any inflection at all, unless the maximum temperature reached was well above the *liquidus* point, so that a sufficient amount of liquid was formed.

7.2.3 Uncertainty in the measured solidus and conclusions

In the RLS- analysis technique, the uncertainty affecting the measured *solidus* temperatures was mainly due to two independent causes:

- the accuracy of the temperature measured by the 644-nm pyrometer channel at the point concerned;

- the precision with which the exact moment of melting onset could be detected through a sudden increase in the RLS intensity.

As for the latter point, the inflection initiating the sharp intensity increase on the RLS signal during the heating stage was chosen as indication of the melting onset. The RLS derivative could be used as a reference too, as the onset of melting had to occur immediately before the appearance of oscillations well visible in this derivative. Finally, the *solidus* could be obtained by means of the RLS analysis method with an approximate precision of ± 25 K. Uncertainty bands were obtained from the standard deviation of the results of several experiments.

As for the post- melting visual examination method, the uncertainty was due, apart from the pyrometer accuracy, to the precision with which the maximum temperature reached in a shot could be planned by changing the Nd: YAG laser pulse parameters. In this case ± 40 K was estimated a conservative precision for all compositions.

Finally, Fig. 7.12 displays the *solidus* points measured for several UO_{2+x} compositions by means of RLS analysis and post- melting visual examination, with the respective uncertainties. The agreement between the results yielded by the two independent techniques suggests that the measured *solidus* temperatures can be considered as sound and reliable data. Fig. 7.13 shows a comparison between the temperatures at which second thermal arrests were observed on the thermogram cooling flank and the *solidus* points measured by means of RLS analysis. As expected on the basis of the explanation of § 7.2.1, the second thermal arrest temperatures were, in average, systematically lower than the RLS- measured *solidus*. However, the difference between the two temperatures was mostly contained within the yielded uncertainty, suggesting that, in general, the complex phenomena occurring during the freezing process generated only relatively small deviations from the finally accepted *solidus*. The temperature at which a "second thermal arrest" was observed in the most oxidised samples investigated ($UO_{2.20}$, $UO_{2.21}$) is a further point of interest. In fact, such temperature (2300 ± 50 K) is the lowest point at which the existence of liquid UO_{2+x} has ever been observed. Therefore, this can be considered as an upper bound for the temperature at which the monotectic three- phase reaction solid UO_{2+xs} / liquid UO_{2+xl} / solid U_3O_8 (or gas UO_y), foreseen in several theoretical

investigations (see § 2.1), should take place. This latter point will be further developed in Chapter 9.

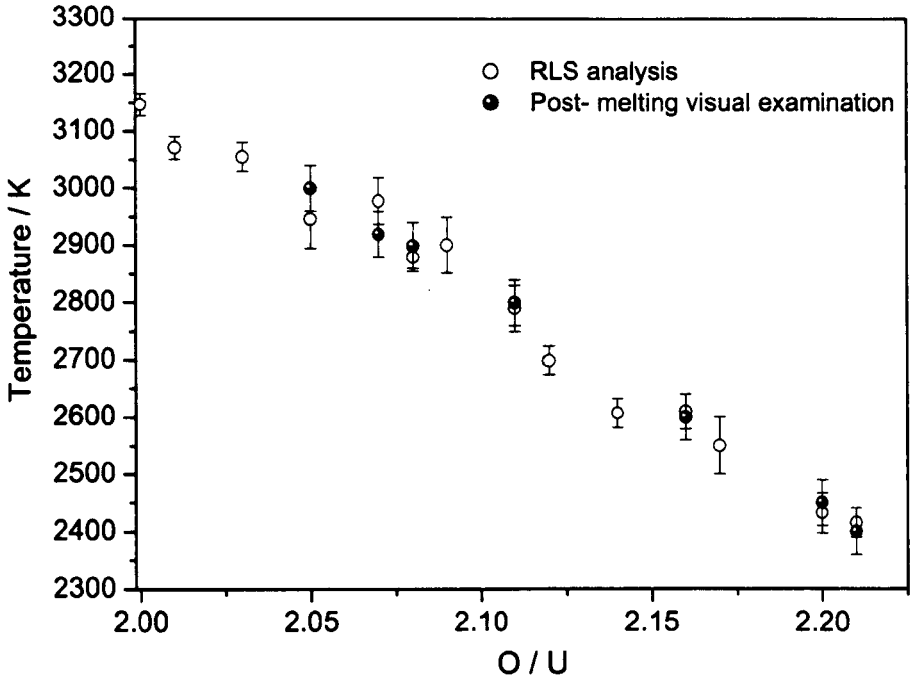

Fig. 7.12: *Solidus* points measured for several UO_{2+x} compositions by means of RLS analysis and post- melting visual examination, with the respective uncertainties. Post- melting visual examination of samples was performed for some compositions only.

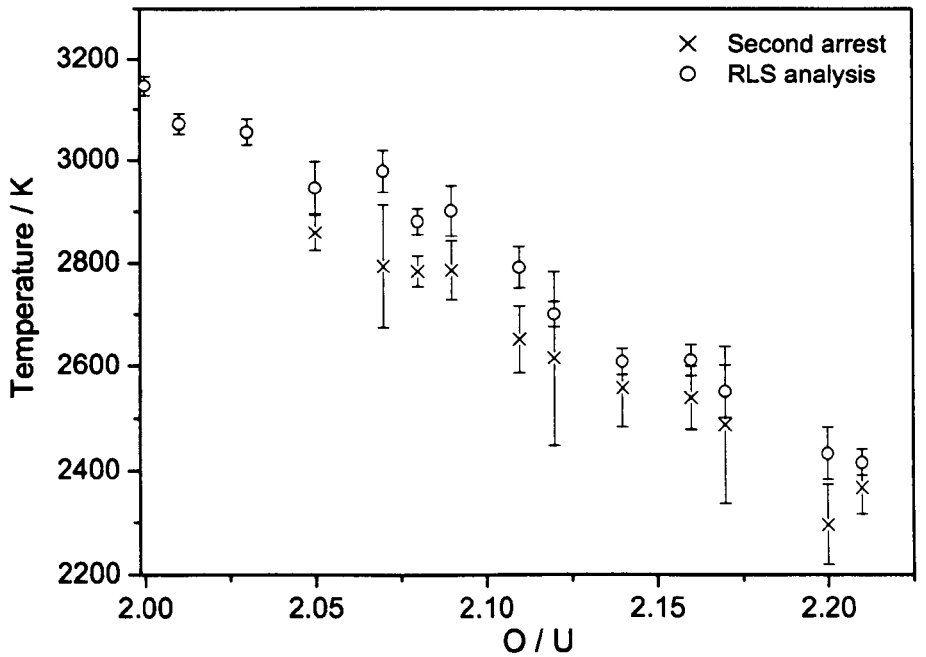

Fig. 7.13: Comparison between *solidus* points measured for several UO_{2+x} compositions by means of RLS analysis and temperature at which the second thermal arrest was observed on the cooling stage of thermograms.

Chapter 8

Simulation and discussion of the experimental curves

The experimental thermograms presented in the previous chapters signify the natural complexity of the melting – freezing behaviour of a system with *solidus- liquidus* transition, subjected to fast laser heating (i.e., to high temperature and oxygen concentration gradients). In this situation, the development of a suitable mathematical model was necessary to simulate the experiments, and to support a sound interpretation of the thermograms.

The one-dimensional model employed to simulate the experiments is presented in § 8.1 and some simulation results in § 8.2.

In the successive sections of this chapter, experimental data are discussed on the basis of results of both the one- dimensional simulation and the characterisation of specimens after the melting experiments.

8.1 One-dimensional model for the analysis of the empirical thermograms

A theoretical model was developed in collaboration with the Joint Institute for High Temperatures of RAS, Moscow (Russia) in order to perform a numerical simulation of the melting and freezing process in binary mixtures heated by a pulsed laser beam [1].

8.1.1 Task formulation

The model describes a two-component specimen heated from one side by a laser pulse with known time-dependent power profile, as illustrated in Fig. 8.1.

Within a one-dimensional approximation, it permits a calculation, by means of a numerical code, of temperature T and composition C in the sample as functions of depth z and time t during the whole experiment. Dynamics of the inter-phase boundary and depth of the molten zone are also calculated as functions of z and t.

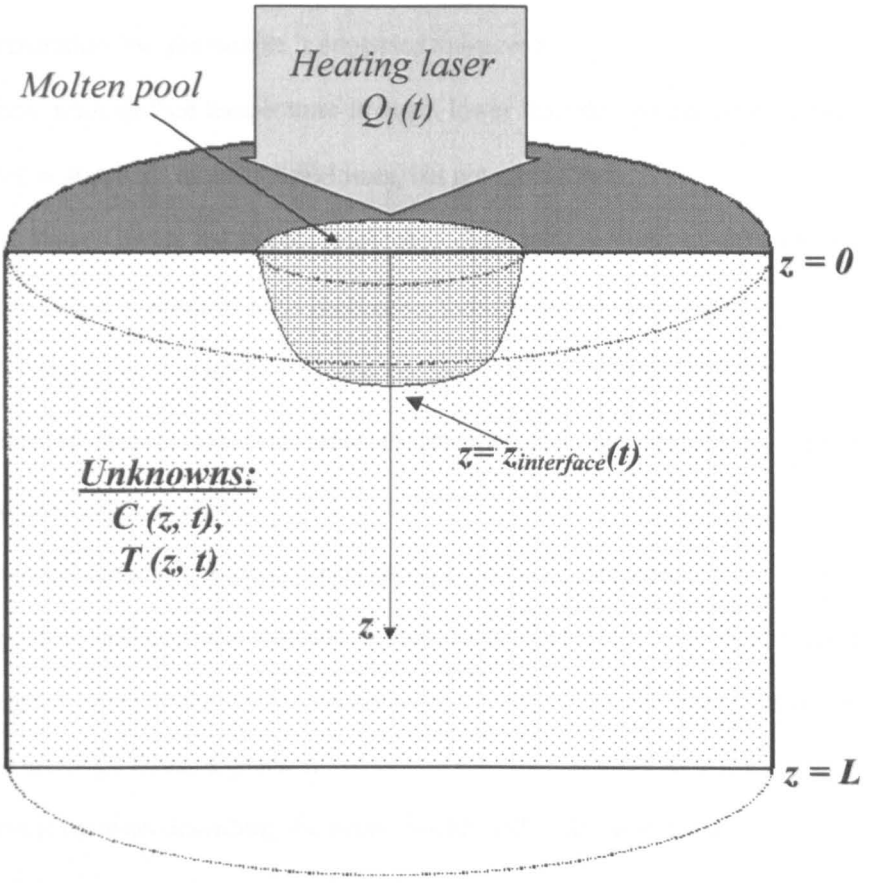

Fig. 8.1: Schematic view of the one-dimensional model developed to simulate the laser-induced melting- freezing experiments. Depth from the heated surface inward is the only spatial dimension considered in the simulation. C = concentration; T = temperature.

8.1.2 Main hypotheses, constitutive equations and boundary conditions

At the start, the composition over the whole sample is homogeneous. From one side a laser radiation pulse with a known time-dependent power profile is applied on the sample front surface at $z = 0$. The spatial distribution of the laser power intensity is assumed to be

constant on the surface. The material cooling is governed by radiative and convective heat exchange with the surrounding environment at both the front and the rear surfaces ($z = 0$ and $z = L$ respectively, in Fig. 8.1).

The following approximations are taken:

1) The deposited laser radiation is totally absorbed on the surface at $z = 0$ (the laser beam optical penetration into the sample is supposed to be zero).

2) The maximum surface temperature is much lower than the boiling point. Hence surface evaporation is supposed to entail heat losses, but not mass losses.

3) Heat exchange inside the molten pool takes place only by thermal diffusion and not by convection. Liquid is assumed to be motionless throughout the experiment.

4) On the sample rear surface ($z = L$) heat exchange occurs through radiation.

5) The material density ρ is temperature-independent and depends only on the state of the material (either solid or liquid).

6) The material remains two- component throughout the experiment.

A trial *liquidus- solidus* phase diagram is given as an input to the code. According to such a phase diagram, melting can lead to violation of the oxygen homogeneity inside the sample during the melting / freezing process.

The diffusion equation describing the mass transfer within the material is:

$$\rho \frac{\partial C_i}{\partial t} + \frac{\partial J_i}{\partial z} = 0 \quad (i=1,2), \tag{8.1}$$

where t= time; z = depth (z =0 on the heated surface); $\rho = \rho_1 + \rho_2$ = constant, total material density; $C_i = \rho_i / \rho$, mass fraction of the component i. The quantity

$$J_i = -\rho D \frac{\partial C_i}{\partial z} \tag{8.2}$$

is the mass flux; $D = D(C, T)$ is the temperature-dependent effective diffusion coefficient, to be given as an input.

By assuming that oxygen is the only mobile species, indices can be omitted, and C and J represent respectively concentration and diffusion of the excess oxygen in the stoichiometric UO_2 matrix. The energy equation of the heat transfer in the bulk is:

$$\rho\frac{\partial h}{\partial t}+\frac{\partial q}{\partial z}+\frac{\partial}{\partial z}\left(J\frac{\partial h}{\partial C}\right)=0, \tag{8.3}$$

where $h = h(C, T)$ is the specific enthalpy, given as input.

$$q=-\lambda\frac{\partial T}{\partial z} \tag{8.4}$$

is the conductive heat flux, and $\lambda = \lambda(C, T)$ is the input thermal conductivity of the material under investigation.

The last term in Eq. (8.3) represents the diffusion heat transfer.

Conditions 1), 2), 3) and 4) above define the boundary conditions for Eqs. (8.1) and (8.3).

The boundary condition for power transfer on the heated front surface ($z = 0$) is:

$$q_{z=0}(t)=A_l Q_l(t)-\varepsilon\sigma T_m^{\ 4}-\xi_0(t)(T-T_{gas})-\Delta H_{vap}\varphi_{vap}(t). \tag{8.5}$$

A_l is the material absorbivity at the laser wavelength; $Q_l(t)$ the laser radiation power-time profile on the sample front surface; $\xi(T, P_{gas}, t)$ is the wall heat transfer coefficient in $z = 0$, $\Delta H_{vap}(C, T)$ the specific evaporation heat and $\varphi_{vap}(C, T, P_{gas}, t)$ is the evaporation rate

$$\varphi_{vap}=\frac{dmol_{vap}(t)}{dt},$$

with mol_{vap} = moles of vapour formed at the time t.

Moreover, ε is the material total emissivity, σ the Stefan- Boltzmann constant, ξ the wall heat transfer coefficient, T the sample surface temperature and T_{gas} the temperature of the surrounding buffer gas; all these quantities should be inputted.

On the rear sample surface ($z = L$) we have:

$$q_{z=L}=-\varepsilon\sigma T_m^{\ 4}-\xi_L(T-T_{gas}). \tag{8.6}$$

The factors $\xi_{(0, L)}(T, P_{gas}, t)$ and $\varphi_{vap}(C, T, P_{gas}, t)$ in the last two terms of Eq. (8.4) and in the last term of Eq. (8.5) have to be calculated. This was done by using the solution of the one-

dimensional non-stationary problem for a half-infinite layer, obtained by the integral heat balance method [1- 3]. The wall heat transfer coefficient $\xi_{(0,L)}$ is obtained as

$$\xi_{0,L}(t) = \frac{q_{sgc}}{(T_s(t) - T_{gas}(t))}, \tag{8.7}$$

where T_s is the temperature of the front ($z = 0$) or rear ($z = L$) sample. The power q_{sgc} exchanged by conduction between the surface and the surrounding buffer gas depends on the gas pressure P_{gas} and on the heating history previous to the instant t according to the following equation:

$$q_{sgc} = K_q \frac{[P_{gas}\,\lambda_{gas}(T^*_{gas})]^{1/2}}{T_s^{1/6}(t)\,T^{*1/3}_{gas}} \frac{u^2(t)}{\left(\int_0^t u^2(\tau)d\tau\right)^{\frac{1}{2}}} \text{ kW m}^{-2}. \tag{8.8}$$

Here $u(t) = T_s(t) - T_s(0)$; P_{gas} = buffer gas pressure (in atm), T^*_{gas} = asymptotic gas temperature, far from the sample surface - λ_{gas} = inert gas heat conductivity (W m^{-1}K^{-1}) at the temperature T^*_{gas}. Surface temperature $T_s(t)$, initial temperature $T_s(0)$ and T^*_{gas} are expressed in kK. In constructing Eq. (8.8) the typical inert gas conductivity dependence on temperature was used: $\lambda_{gas} \propto T_{gas}^{2/3}$. K_q is a physical constant the value of which is 9 kg$^{1/2}$s$^{-1/2}$.

In the calculation of φ_{vap}, P_{gas} was supposed to be considerably higher than the saturated vapour pressure at the surface temperature (condition 2) above). Under this assumption, the vapour produced on the sample surface constitutes only a minor admixture to the inert gas. In this case the vapour transfer from the specimen surface into the gas occurs by diffusion. Since in gaseous mixtures mass and heat diffusion are formally analogous, it was possible to calculate the evaporation rate with the same method used above for the heat transfer. The resulting expression for the evaporation rate at the instant t (diffusion limited rate) was:

$$\varphi_{vap}(t) = K_\varphi \frac{M_{gas}P^{1/2}_{gas}}{T_s^{1/4}(t)} \left(\frac{M_v + M_g}{2M_vM_g}\right)^{1/4} \frac{C_v^2(t)}{\left(\int_0^t C_v^2(\tau)d\tau\right)^{\frac{1}{2}}} \text{ kg m}^{-2}\text{s}^{-1}. \tag{8.9}$$

Here $K_\varphi = 2\cdot10^{-4}$ K$^{1/4}$ m$^{-3/2}$ kg$^{-1/4}$, and

$$C_v(t) = \frac{M_v}{M_g}\frac{P_s(T_w(t))}{P_{gas}},\ (C_v << 1),$$

M_v, M_g = molecular weights of vapour and gas; P_s = saturated vapour pressure, depending on the surface temperature and condensed phase composition. In constructing the dependence $P_s = P_s(T, C)$ the vapour components were supposed to follow a law of the kind

$$\ln P_{si} = a_i - \frac{b_i}{T},$$

Producing a total equilibrium vapour pressure following the law:

$$\ln P_s = \sum a_i C_i - \sum b_i C_i / T.$$

The constants a_i and b_i were chosen from the data reported in [4].

For the calculation of Eq. (8.9), an expression for the diffusion coefficient of the vapour into the buffer gas was applied, obtained from the elementary kinetic theory: $D \propto T^{3/2}/P$.

Assumption 2) above is also translated into the following further boundary conditions:

$$\frac{\partial C}{\partial z} = 0 \text{ for } z = 0 \text{ and } z = L. \tag{8.10}$$

Mass and energy conservation laws define the conditions connecting the variables values ahead of and behind the melting front (indicated by indexes $^+$ and $^-$, respectively). If v_f is the velocity at which the melting/freezing front advances, such conditions are:

$$J^- - J^+ = \rho v_f (C^- - C^+), \tag{8.11}$$

$$q^- - q^+ + (J\frac{\partial h}{\partial C})^- - (J\frac{\partial h}{\partial C})^+ = \rho v_f (h^- - h^+). \tag{8.12}$$

Knowledge of the nature of the solid-liquid interface (discontinuity surface) is not a necessary condition for the solution of the formulated problem. Thus the mathematical formulation of the task is fully defined by equations (8.1) – (8.12), independently of the type of phase transformation occurring.

8.1.3 Numerical method

The calculation method chosen for the solution of the Stefan problem with a moving front represented by Eqs. (8.1 - 8.4) is presented and discussed in [1].

In order to avoid possible numerical instabilities stemming from the large gradients concentrating around the solid- liquid interface, the time step in the program was adapted automatically. This resulted in an optimal number of iterations, permitting to construct the solution on each successive time interval with a given precision. The spatial grid was also constructed automatically and was gradually corrected, depending on the interphase front location. The number of grid nodes was maintained constant over the sample, whereby their density was the highest around the phase front.

The integration of Eq. (8.1) in time t and space z within the limits of elementary cells $\Delta z_i = z_{i-1} - z_i$, $\Delta t^j = t^{j+1} - t^j$, and of Eq. (8.2) in z defined the following difference approximation of the diffusion equation:

$$\rho\Delta z_i(C_{i+1}^{j+1} + C_i^{j+1}) + \Delta t^j(J_{i+1}^{j+1} - J_i^{j+1}) = \rho\Delta z_i(C_{i+1}^{j} + C_i^{j}) - \Delta t^j(J_{i+1}^{j} - J_i^{j}), \tag{8.13}$$

$$\frac{\Delta z_i}{2}\left(\frac{J_{i+1}^{j+1}}{\rho D_{i+1}^{j+1}} + \frac{J_i^{j+1}}{\rho D_i^{j+1}}\right) + C_{i+1}^{j+1} - C_i^{j+1} = 0. \tag{8.14}$$

The unknowns here are the composition C_i^{j+1} and the diffusion flux J_i^{j+1}.

The system (8.13), (8.14) was solved with the boundary conditions given by (8.10),

$$J_1^{j+1} = J_N^{j+1} = 0 \quad \text{in } z_1 = 0 \text{ and } z_N = L. \tag{8.15}$$

The difference approximation for the energy equation (8.3) was constructed in a similar way. Numerical solutions could be obtained with two different methods: without interphase detection and with interphase detection. In the first case, the solid- liquid front was explicitly simulated with a non-isothermal layer of finite thickness, where all parameters varied continuously. In this case, a two-phase region existed, as a mixture of clusters of solid and liquid in thermodynamic equilibrium. Their concentrations were different and depended on x

within the two-phase region. The mean concentration remained, however, constant over any macroscopic volume.

In the solution with interphase detection, instead, calculations were performed admitting a discontinuity of the concentration on the phase front. In this case, temperature and velocity of the phase front on each time step were chosen in such a way that gaps of concentration and enthalpy on the front corresponded to the input phase diagram. In this second case, the difference approximation around the phase front had to be constructed in a slightly different way, to avoid instability due to the discontinuity of the solution on the interface. Finally, the solution with interphase detection was found to be more stable, and, therefore, was used in most of the simulations performed. In any case, no significant difference was observed between solutions obtained with the two methods.

8.1.4 Sample properties and experimental conditions

The material properties to be provided as input were:

-Physical properties: density ρ (g·cm^{-3}), sample thickness L (cm), composition C ($0 \leq C \leq 1$) and starting temperature $T(0)$ (kK);

-Thermophysical and thermodynamic properties: *solidus- liquidus* trial phase diagram; specific enthalpy $h(T, C)$ (kJ g^{-1}); heat conductivity $\lambda(T, C)$ (W m^{-1} K^{-1}); total surface emissivity $\varepsilon(T, C)$ and spectral absorbivity $A(T, C)$ at the heating laser wavelength l; sample saturated vapour pressure $P_s(T, C)$ (atm); latent heat of evaporation $\Delta H_{vap}(T, C)$ (kJ g^{-1}); vapour molecular mass M_v (assumed as temperature- and composition- independent); diffusion coefficient of the migrating species (oxygen in this case) in solid, $D(T, C)$ (cm^2 s^{-1}).

-Environmental properties: buffer gas molecular mass M_g, pressure P_{gas} (atm), asymptotic temperature T^*_{gas} (kK), atmospheric pressure gas heat conductivity $\lambda_{gas}(T^*_{gas})$ (W m^{-1} K^{-1}); laser power profile $Q(t)$ (kW cm^{-2}).

Physical and environmental properties

Data on the gas properties were taken from [5], whereas those relative to the UO_{2+x} sample and the experimental conditions were measured for each experiment to be simulated. The input laser power $Q_l(t)$ was set in order to obtain, in the simulation, the same maximum sample surface temperature as in the real experiment.

Thermophysical and thermodynamic properties

The input of thermophysical and thermodynamic data constituted a crucial point of the simulation, especially where the UO_{2+x} phase diagram and diffusion constants were concerned.

The code was first implemented and checked by simulating laser- induced melting experiments in the better known binary system UO_2 + ZrO_2. In applying the simulation to UO_{2+x} samples, the system UO_2 + 1/2 O_2 had to be represented, in the range of interest, as an ideal binary mixture of two uranium oxides. These two oxides were chosen as UO_2 and $UO_{2.55}$. The second composition was taken because it is close to the eutectic composition recommended by some authors [6], and in particular it corresponds to that calculated by Babelot *et al.* [7]. Actually, *liquidus* and *solidus* lines obtained by these latter authors on the basis of extrapolated free energy data are in rather good agreement with the same lines measured in this work in the range UO_2 - $UO_{2.21}$ (see Chapter 9). Therefore, in the range UO_2 - $UO_{2.55}$ the phase diagram calculated by Babelot *et al.* was taken as a first trial input for the calculation. This diagram was then slightly modified, by a trial-and-error procedure, in order to better fit the experimental results obtained in this work. The final *liquidus* - *solidus* diagram supplied as an input to the code is plotted in Fig. 8.2, with a normalised composition.

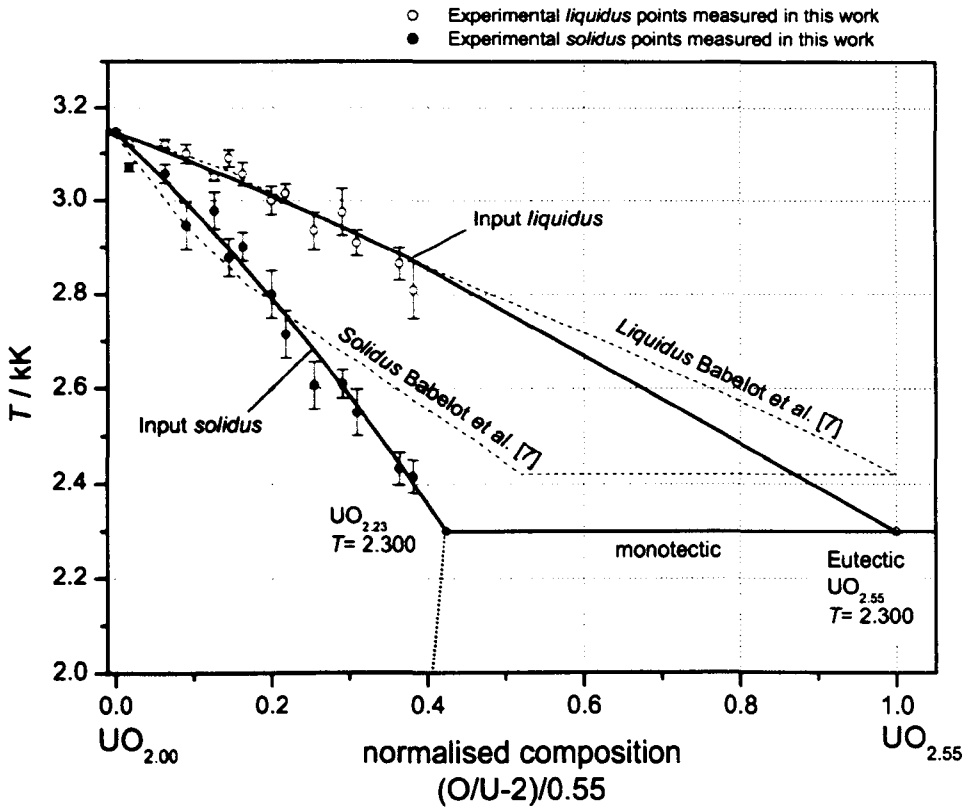

Fig. 8.2: UO_{2+x} *solidus – liquidus* phase diagram used as input for the simulation code.

The presence of a *monotectic* line, starting at a composition between $UO_{2.2}$ and $UO_{2.25}$ at a temperature between 2200 and 2500 K, was postulated in a number of theoretical publications, but never experimentally proved. The *monotectic* temperature was assumed to be 2300 K. This was the lowest average temperature at which the presence of liquid uranium dioxide was detected in our experiments. Of course this is to be taken as a tentative value only. Such a hypothetical monotectic line was then supposed to start at $UO_{2.23}$, extrapolating to 2300 K our measured *solidus*.

The values of enthalpy and heat conductivity were assumed to be composition- independent, and taken, in the range 300 - 6000 K, from Refs. [8] and [9] respectively. Optical properties of the sample surface were taken from Refs. [8,10]. Emissivity values were in agreement with those measured in this work by means of the multi-channel Optical Spectrometric Card presented in § 4.2.4. Saturated vapour pressure P_s and evaporation latent heat ΔH_{vap} were

taken for stoichiometric UO_2 from [8], where the numerous experimental data available were critically reviewed and fitted. Dependence of these latter parameters on the composition at high temperature was deduced by extrapolating the results reported in [11, 12]. The same references were used in order to estimate the value of the average vapour molecular mass M_v over solid UO_{2+x} at high temperature. Results proposed in theoretical and review work [6, 8] were used to estimate the values of P_s, ΔH_{vap} and M_v, in liquid UO_{2+x}.

The values of many thermophysical and thermodynamic parameters at high temperature and high degree of oxidation sometimes had to be estimated by difficult extrapolations. Therefore, several trial simulations were performed changing the values of these parameters. Input thermodynamic data significantly affecting the simulation results were the *solidus-liquidus* phase diagram, the enthalpy $h(T, C)$ and the diffusion coefficient $D(T, C)$; this latter is discussed in the next subsection. Under the conditions of the measurements performed in this work, the results of the simulation were negligibly dependent on small variation of the other input parameters.

Diffusion coefficients

Values for the diffusion coefficient $D(T, C)$ were taken, for solid UO_{2+x}, from [13]. The values of D for liquid UO_{2+x} were extrapolated from the results presented in [13] and compared with [14, 15]. Also in this case trial simulations were performed with different sets of values for $D(T, C)$. The final results of the simulation actually depended on whether the oxygen self- diffusion coefficient D_s or the oxygen chemical- diffusion coefficient D_c was chosen for D. The difference between D_s and D_c is discussed in [13] on the basis of early investigations conducted by Darken [16] and Lay [17]. D_s describes the random walk of oxygen ions in a UO_{2+x} lattice of given *uniform* composition and temperature, where no chemical potential gradients exist. D_c describes the movements of oxygen ions in the presence of chemical potential gradients, i.e., in the present case, in the presence of oxygen

concentration gradients. A relation linking D_c and D_s in uranium dioxide is proposed in [13] and derived in [17]:

$$D_c = D_s \frac{2+x}{2RT} \frac{d(\Delta G_{O_2})}{dx} = D_s F(x). \tag{8.16}$$

R = 8.314 J K^{-1} mol^{-1}; ΔG_{O2}= oxygen chemical potential; x = (O/U) - 2.

The thermodynamic factor $F(x)$ in Eq. (8.15) is higher at values of x close to 0, due to the very high sensitivity of the oxygen potential on the oxygen content in the vicinity of the exact stoichiometry (see § 2.2.1). For $x \approx 1 \cdot 10^{-4}$, $F(x) > 10^4$. However, even for $0.05 < x < 0.2$ (the range of interest for this work) $F(x)$ remains in the range $10 < F(x) < 100$. Thus one can see that the choice of D_c rather than D_s implied a significant difference in the modelling of diffusion phenomena. In the experiments performed in this work, the sample composition could be considered as uniform over the whole specimen before the onset of melting. However, in the presence of a molten zone on the sample surface large concentration gradients were certainly formed at the solid- liquid interface, according to the *solidus - liquidus* phase diagram. Thus the possible onset of chemical diffusion had to be taken into consideration at that stage. Unfortunately, dependence of D on local concentration *gradients* could not be set in the code input. Therefore, values of D (T, C) were inputted as fixed functions of temperature and concentration. For *solid* UO_{2+x}, the values for the oxygen self-diffusion coefficient recommended in literature were taken ($10^{-7} < D < 10^{-5}$ cm^2 s^{-1}), whereas at temperatures around the *solidus - liquidus* gap D had to be rather considered as a chemical- diffusion coefficient, and therefore given higher values according to Eq. (8.16) ($10^{-5} < D < 10^{-3}$ cm^2 s^{-1}). It was eventually discovered that changes in the final results of the simulation due to the input of chemical- rather than self- diffusion D coefficients were visible, but not essential (see next section).

8.2 Results of the simulation

Figs. 8.3-8.12 show the results of calculations performed in order to simulate the empirical thermograms presented as examples in Fig. 7.1 of Chapter 7. At each simulation, the code-calculated concentration $C(z, t)$, enthalpy $h(z, t)$ and temperature $T(z, t)$ profiles in the sample ($0 \leq z \leq L$) and for the whole experiment duration. Dynamics of the interphase boundary were also calculated (co-ordinate $z_f(t)$ and velocity $v_f(t)$ of the melting/ freezing front(s)), along with the laser power effectively absorbed, $A_l\ Q_l\ (t)$, and the different components of the thermal losses on the surface ($Q_{radiative}(t)$, $Q_{convective}(t)$ and $Q_{evaporation}(t)$). In practice, the trends in surface temperature $T(t)_{z=0}$ and composition $C(t)_{z=0}$ constituted the most interesting results for the comprehension of experiments. Therefore, in this section simulated $T(t)_{z=0}$ and $C(t)_{z=0}$ are presented and compared with the corresponding empirical thermograms for several specimens. The calculated concentration profile $C(z, t)$ is also presented for some representative samples, in order to better illustrate the development of the melting / freezing process from the surface into the bulk of the specimen. The simulation of the concentration trend on the sample surface was of the foremost importance, as it allowed a prediction of whether or not oxygen concentration gradients could affect the measured *solidus* and *liquidus* points. In particular, the main question to be answered in this respect was whether or not the superficial composition on the sample surface during the cooling stage at the onset of freezing (*liquidus*) was the same as the original starting composition. Fig. 8.3 reports the simulation of a pulse melting in a stoichiometric UO_2 sample. Here melting occurred congruently, and no composition gradients were formed. The real process could be considered with good approximation as one-dimensional, as confirmed by the satisfactory agreement between simulated and empirical thermograms.

The situation became more complicated if the investigated specimen composition was even slightly hyperstoichiometric. Figs. 8.4 and 8.5 show the results of a simulation carried out on a $UO_{2.01}$ sample.

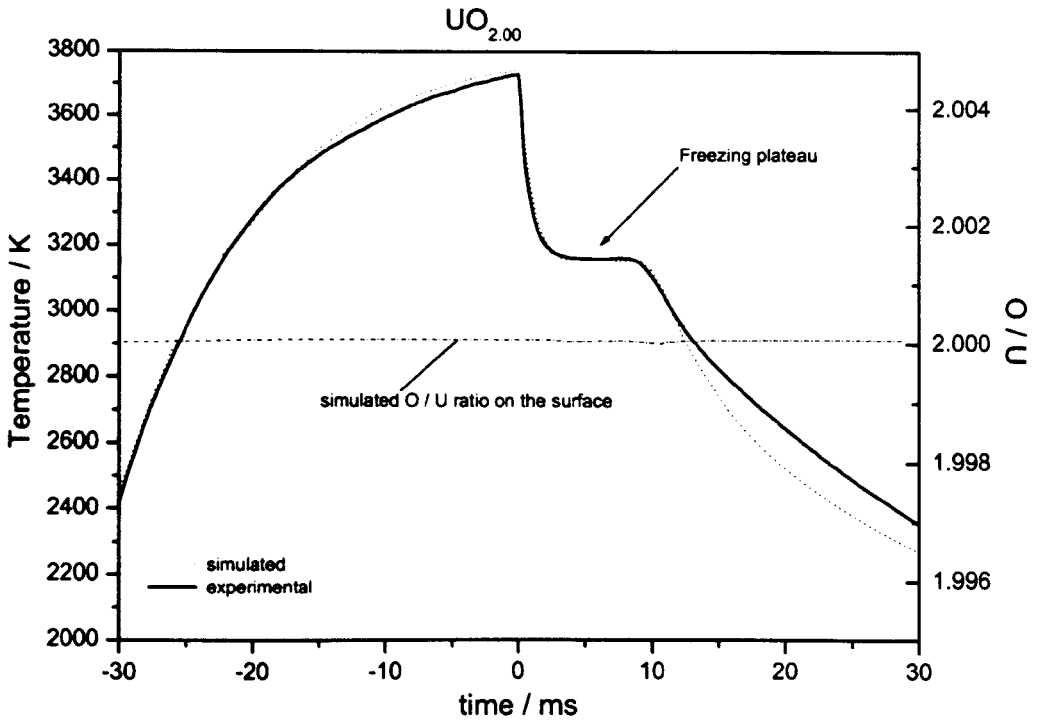

Fig. 8.3: Experimental and simulated thermograms for a stoichiometric UO_2 sample.

Fig 8.5 shows the concentration profile $C(z, t)$ calculated from the surface inward in the same experiment at eight successive time points. Here composition gradients were immediately formed as melting took place, because the resulting liquid phase had to be richer in oxygen with respect to the corresponding solid, according to the *liquidus- solidus* phase diagram. However, due to fast diffusion, the original composition in the liquid was soon nearly restored at a sufficient distance from the melting front. As a result, when, during the cooling stage, the input *liquidus* temperature was crossed on the sample surface, the oxygen content in the superficial layer was sufficiently close to the original value not to influence the actual temperature at which solidification began. Fig. 8.5 shows that, after the onset of solidification in the bulk and on the surface, freezing occurred on two fronts, one advancing from the bulk towards the surface, the other one in the opposite direction. Concentration gradients were naturally produced on both the freezing fronts, so that the very last liquid layer remaining before the total solidification was considerably enriched in oxygen.

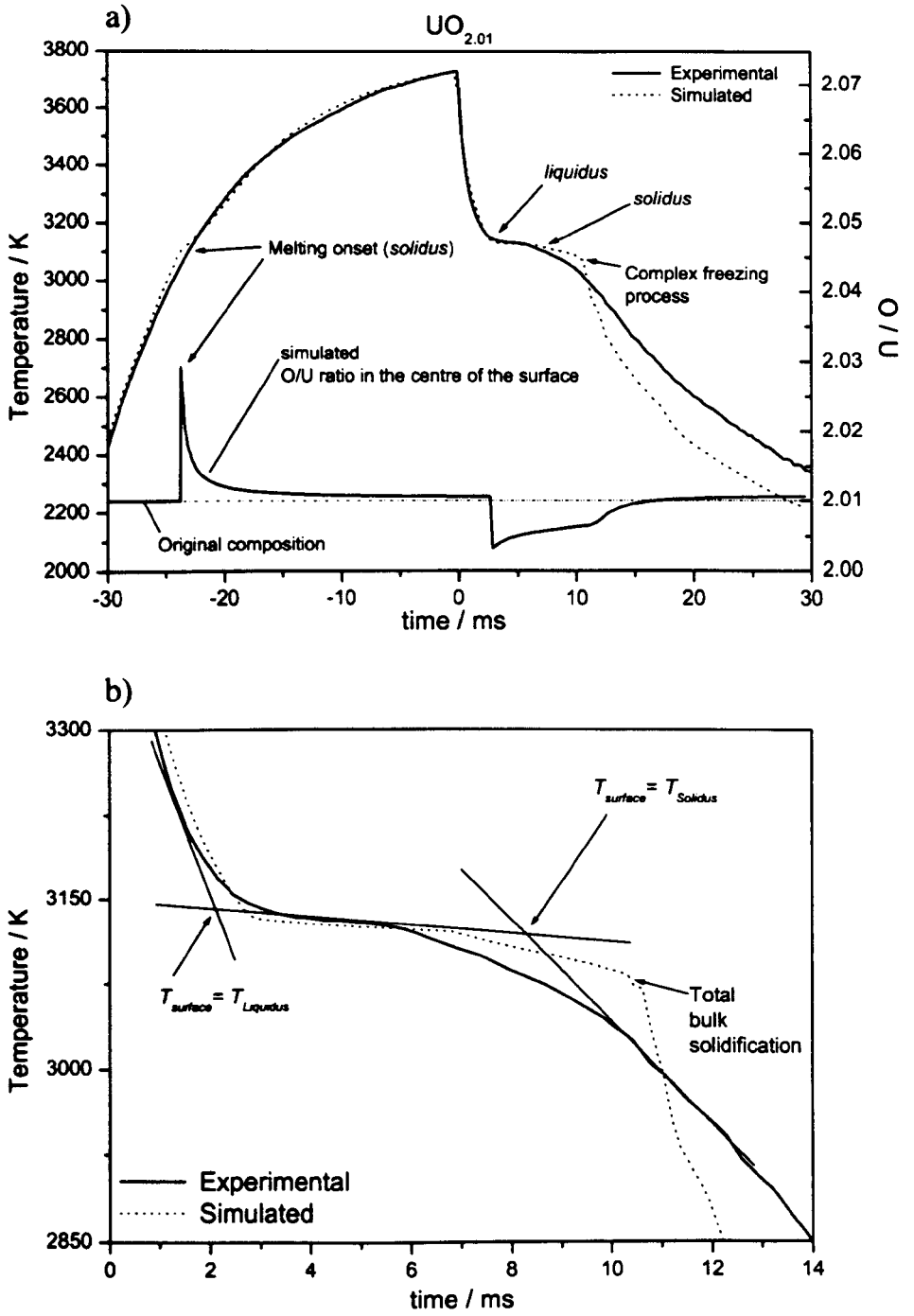

Fig. 8.4: a) One- dimensionally simulated and experimental thermograms for a $UO_{2.01}$ sample. The simulated trend of the oxygen concentration on the surface is also plotted. Slight concentration gradients occurred in the simulation in correspondence to the onset of melting and freezing. b) Enlargement of the thermograms around the freezing range. A classical thermal analysis (§ 3.2.1) was performed to obtain *solidus* and *liquidus* temperatures from the empirical thermogram.

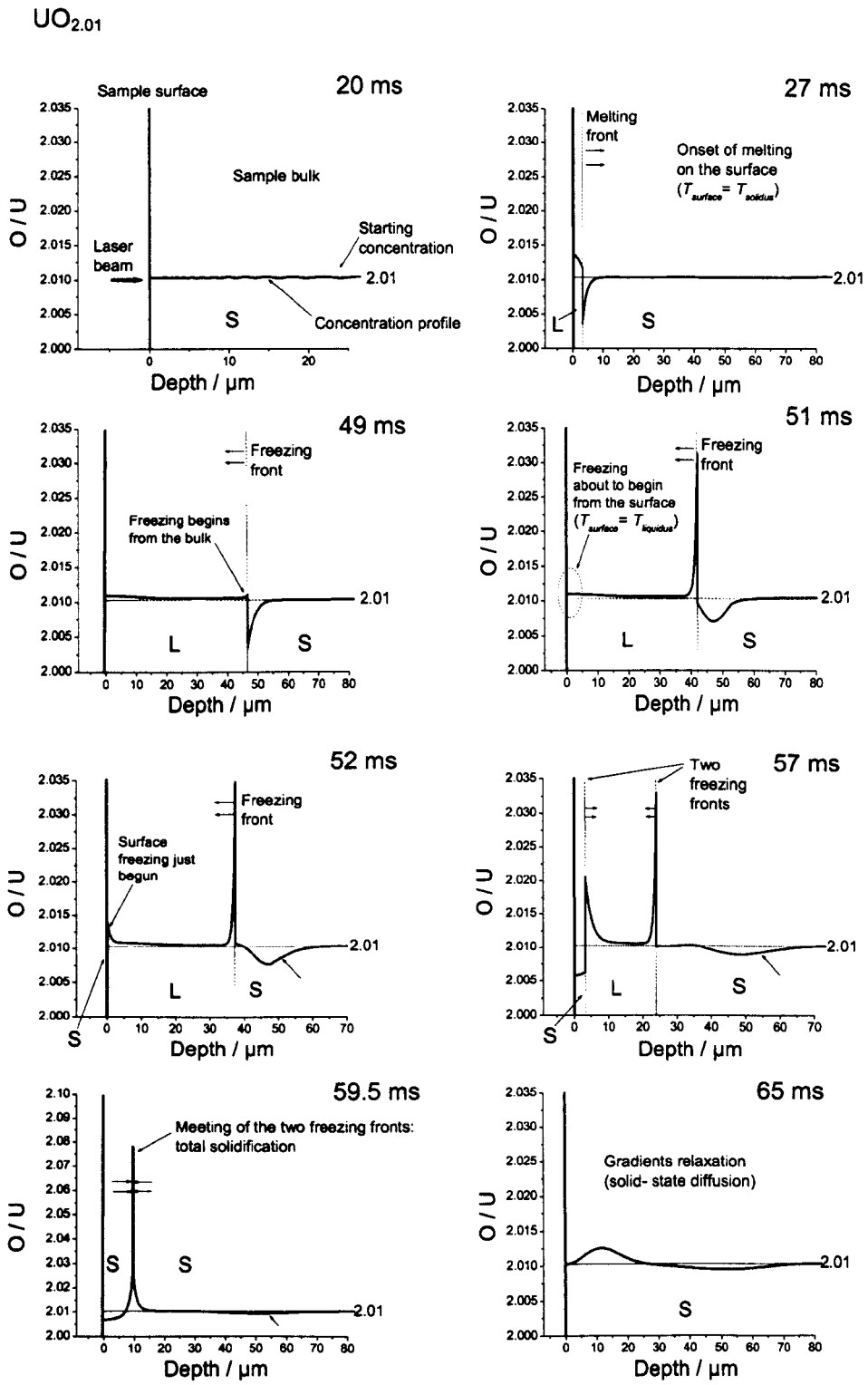

Fig 8.5: Concentration profile $C(z, t)$ calculated from the surface inward at eight successive time points during the melting- freezing experiment on $UO_{2.01}$ of Fig. 8.4.

This composition heterogeneity caused also an irregular release of latent heat resulting in a rather complex temperature profile, and, therefore, in the irregular shape of the simulated thermogram around the freezing transition (as in Fig. 8.4). In the real sample, concentration gradients were probably less pronounced, due to the fact that diffusion occurred in three dimensions rather than one. As a consequence, the empirical thermogram between *liquidus* and *solidus* was smoother than that calculated. In this example, composition gradients were in any case so small, that only oxygen-self diffusion was assumed to occur. Possible deviations caused on the *liquidus* and *solidus* points by variations in the surface composition were negligible compared to the uncertainty affecting the measurements. The situation was the same in the $UO_{2.03}$ specimen example reported in Fig. 8.6. Figs. 8.7 and 8.8 illustrate the results of a simulation concerning a $UO_{2.09}$ sample.

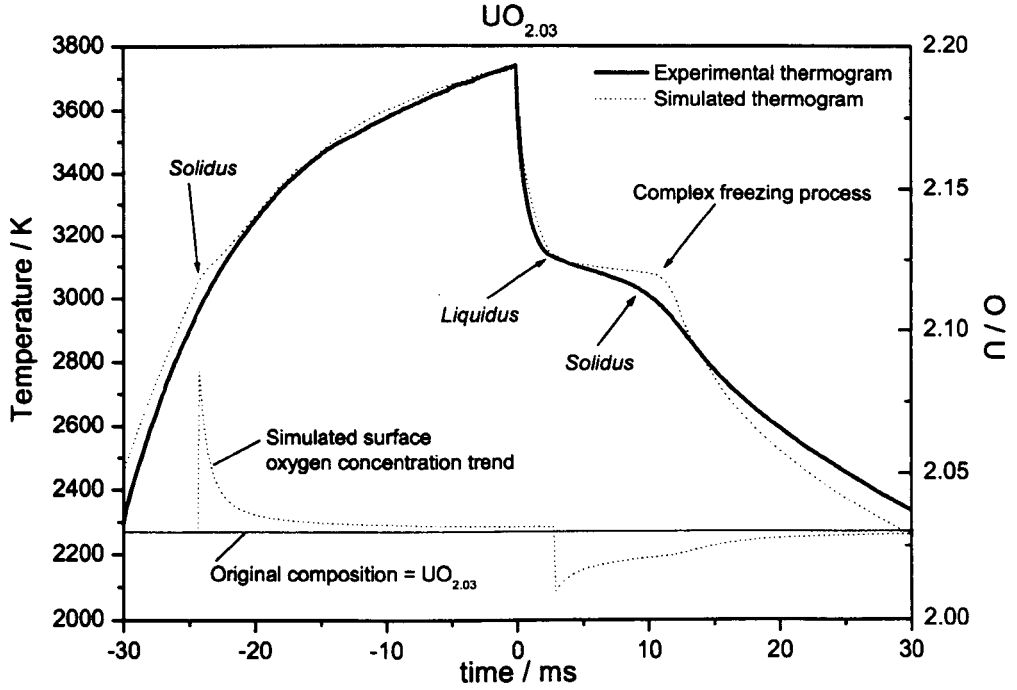

Fig. 8.6: Simulated and experimental thermograms for a $UO_{2.03}$ sample, plotted together with the simulated oxygen concentration profile on the surface during the experiment.

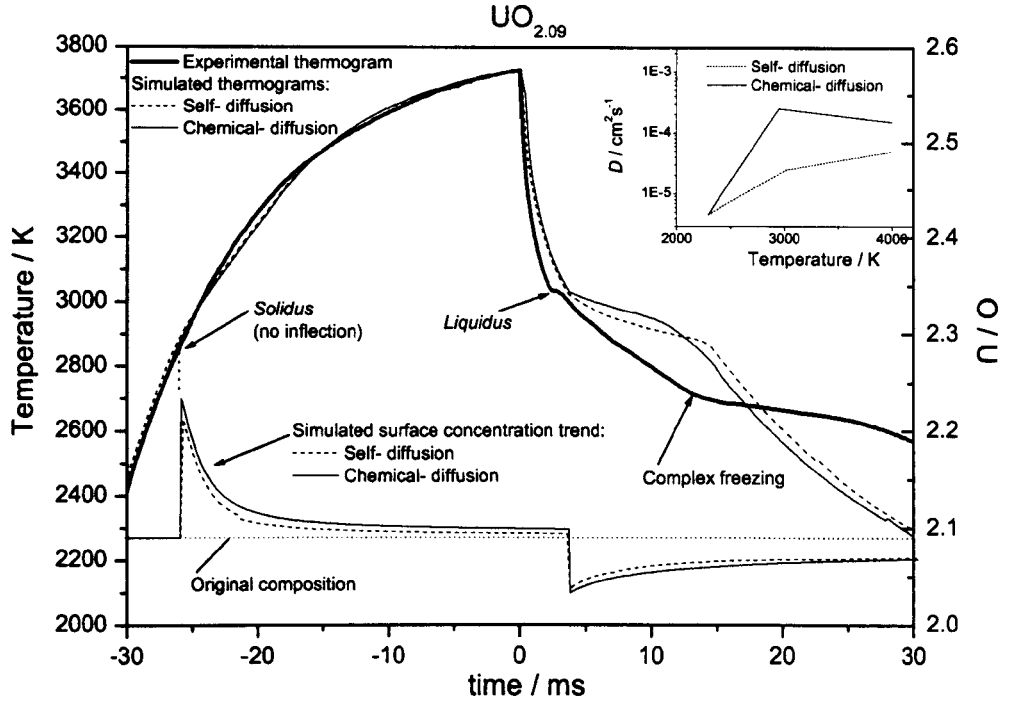

Fig. 8.7: Simulated and experimental thermograms and surface oxygen concentration trend for a $UO_{2.09}$ sample. In the inset, self- and chemical- diffusion coefficients are plotted *vs. T*.

Similar results were obtained on all samples with $2.03 \leq O/U \leq 2.10$.

The simulation results were similar to those obtained in the $UO_{2.01}$ sample, although larger gradients of composition were produced, due to the higher oxygen content. In this case, as well as in the following examples, simulations were performed under both oxygen self-diffusion and oxygen chemical diffusion conditions (see inset in Fig. 8.7). However, the final results did not differ significantly in the two cases, at least within the uncertainty limits obtained for the empirical melting points. The main difference with respect to the previous simulations consisted here of the larger disagreement between calculated and empirical thermograms *after* the *liquidus* point. By no means could the second thermal arrest observed in the experimental curves be reproduced in the calculation.

Empirical and simulated thermograms of more oxidised samples ($O/U > 2.10$) are presented in Figs. 8.9 - 8.11. Here the disagreement between experiment and simulation is more pronounced.

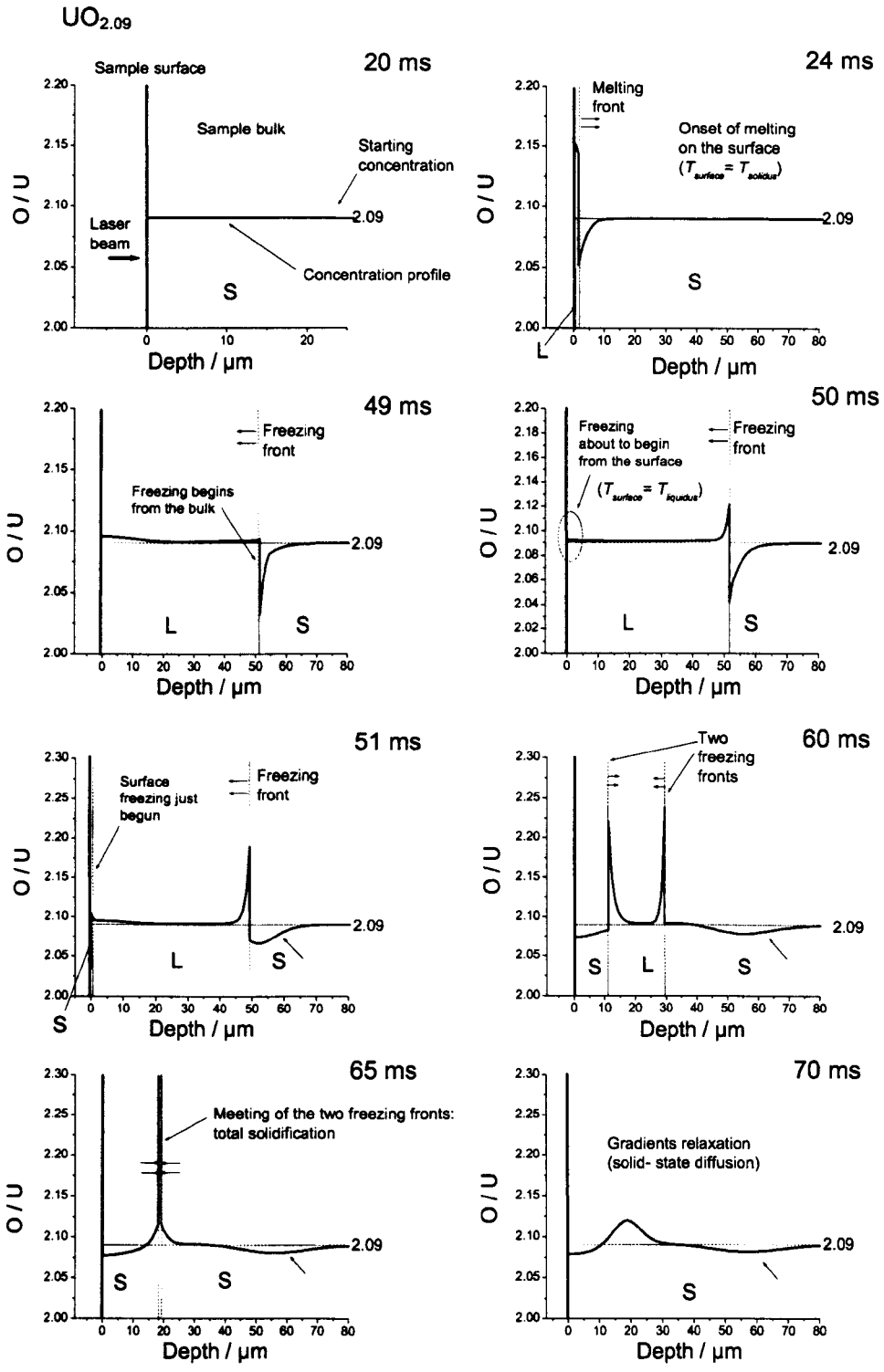

Fig 8.8: Concentration profile $C(z, t)$ calculated for the melting- freezing experiment on $UO_{2.09}$ of Fig. 8.7.

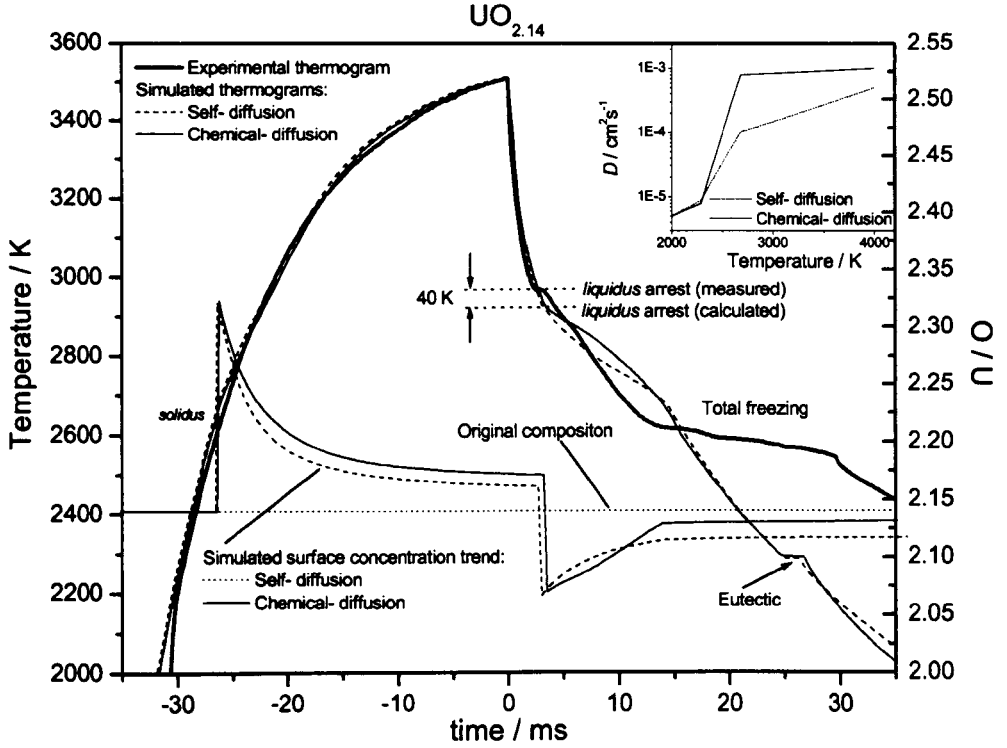

Fig. 8.9: Simulated and experimental thermograms for a $UO_{2.14}$ sample. According to the simulation, the large concentration gradients produced during the melting/freezing process caused a shift of the *liquidus* arrest comparable with the measurement uncertainty.

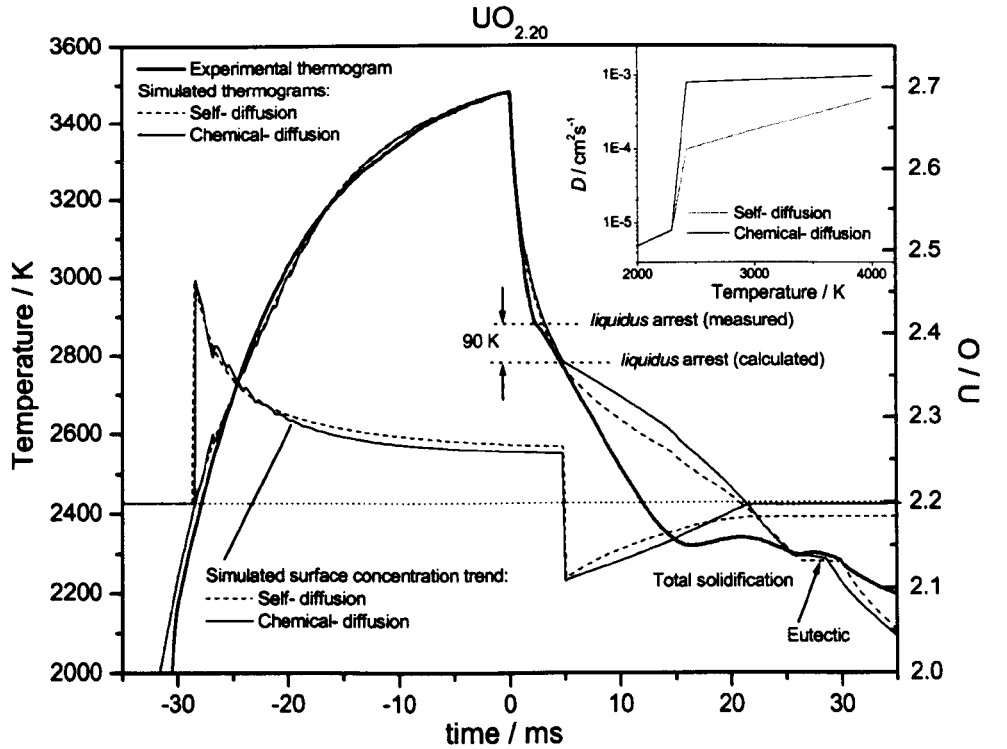

Fig. 8.10: Simulated (self-diffusion and chemical-diffusion assumptions) and experimental thermograms for a $UO_{2.20}$ sample.

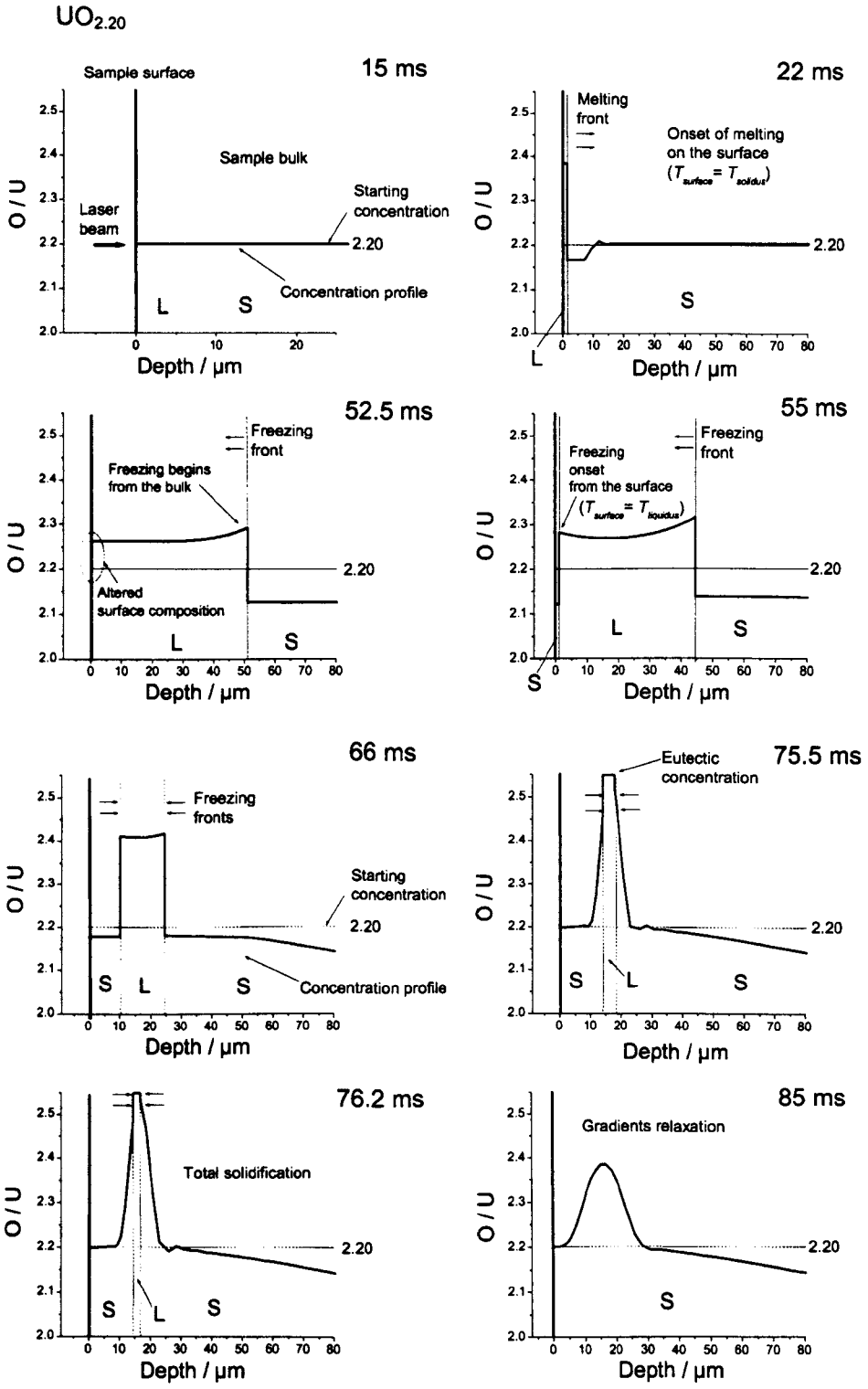

Fig 8.11: Concentration profile $C(z, t)$ calculated during the melting- freezing experiment on $UO_{2.20}$ of Fig. 8.10. Due to the high initial oxidation level, in the simulation the superficial composition of the liquid was far from the original one at the onset of freezing.

In the curves calculated for samples with O/U > 2.10, the position of the *liquidus* arrest was influenced by the variations of the oxygen distribution over the specimen during the melting-freezing process. Concentration gradients in these cases were considerably larger, and, according to the one-dimensional simulation, diffusion in the liquid was not sufficient to restore the original composition on the sample surface before the onset of freezing. Fig. 8.9 shows an example of $UO_{2.14}$ melting experiment, where the simulated oxygen content on the sample surface at the onset of freezing was still well above the starting level. This effect appeared even more dramatic for the $UO_{2.20}$ case of Figs. 8.10 and 8.11. In this latter example, the error in the *liquidus* due to the change in composition was definitely larger than the measurement uncertainty itself. These results suggested that the input *liquidus*, based on the experimental results obtained, was possibly wrong for samples with O/U > 2.10. On the other hand, one should consider that in all these cases characterised by large composition gradients a one-dimensional model of diffusion could provide too poor a description of the phenomena involved. A two- or three- dimensional diffusion simulation, closer to the real situation, would have yielded smaller gradients.

A clear second thermal arrest was actually observed in the simulation of this latter group of thermograms. However, this second thermal arrest occurred at 2300 K for all the compositions, because in all these cases the oxygen- enriched simulated liquid during the freezing process reached the input eutectic composition $UO_{2.55}$, freezing at just 2300 K.

The simulated behaviour did not reproduce the shape of empirical thermograms, in which the second thermal arrest systematically occurred at a temperature dependent on the starting composition.

Fig. 8.11 shows that when the eutectic composition is reached in the last liquid remaining during the freezing process, large gradients also remain in the solid formed.

Fig. 8.12 a shows the SEM picture of a $UO_{2.20}$ section after a melting point measurement. Though not very clear, the picture shows that there is a horizontal band, in the molten pool, where the re-frozen material seems to be slightly more porous (Fig. 8.12 b). This zone could

indicate the area where the two freezing fronts, advancing from the bulk and from the surface, met, and therefore where the solidification process was completed. Since the last liquid to freeze was significantly rich in oxygen, upon solidification oxygen bubbles were possibly produced, resulting in the higher porosity observed on the formed solid.

In summary, the agreement between simulated and empirical thermograms was good over the entire experiment for stoichiometric and slightly hyperstoichiometric (O/U $\leq$ 2.03) samples. Thermograms measured on specimens with 2.03 < O/U < 2.10 were well reproduced by the one-dimensional simulation only in the first part of the experiments, up to the *liquidus* point on the cooling stage. For more oxidised specimens, the empirical *liquidus* was not well reproduced in the simulation, due to the large oxygen concentration gradients formed in the liquid.

8.3 Discussion of experimental thermograms

8.3.1 Samples with 2 $\leq$ O/U $\leq$ 2.10

The agreement between empirical and one-dimensionally simulated thermograms was satisfactory, apart from some small discrepancies, for stoichiometric and slightly hyper-stoichiometric samples (O/U $\leq$ 2.03). This confirmed that the melting- freezing process could be considered one-dimensional in these cases, i.e. that thermal and concentration gradients were formed almost exclusively in the axial direction. In more oxidised specimens (2.03 < O/U $\leq$ 2.10) instead, empirical and calculated thermograms were in fair agreement up to the first (*liquidus*) thermal inflection on the cooling stage. This partial agreement still constituted an important result, because it confirmed that the measured *liquidus* was not influenced by heterogeneity in the oxygen distribution over the specimen. Simulations ensured, in fact, that fast diffusion in the liquid lead to almost complete recovery of the original composition on the sample surface before the onset of freezing.

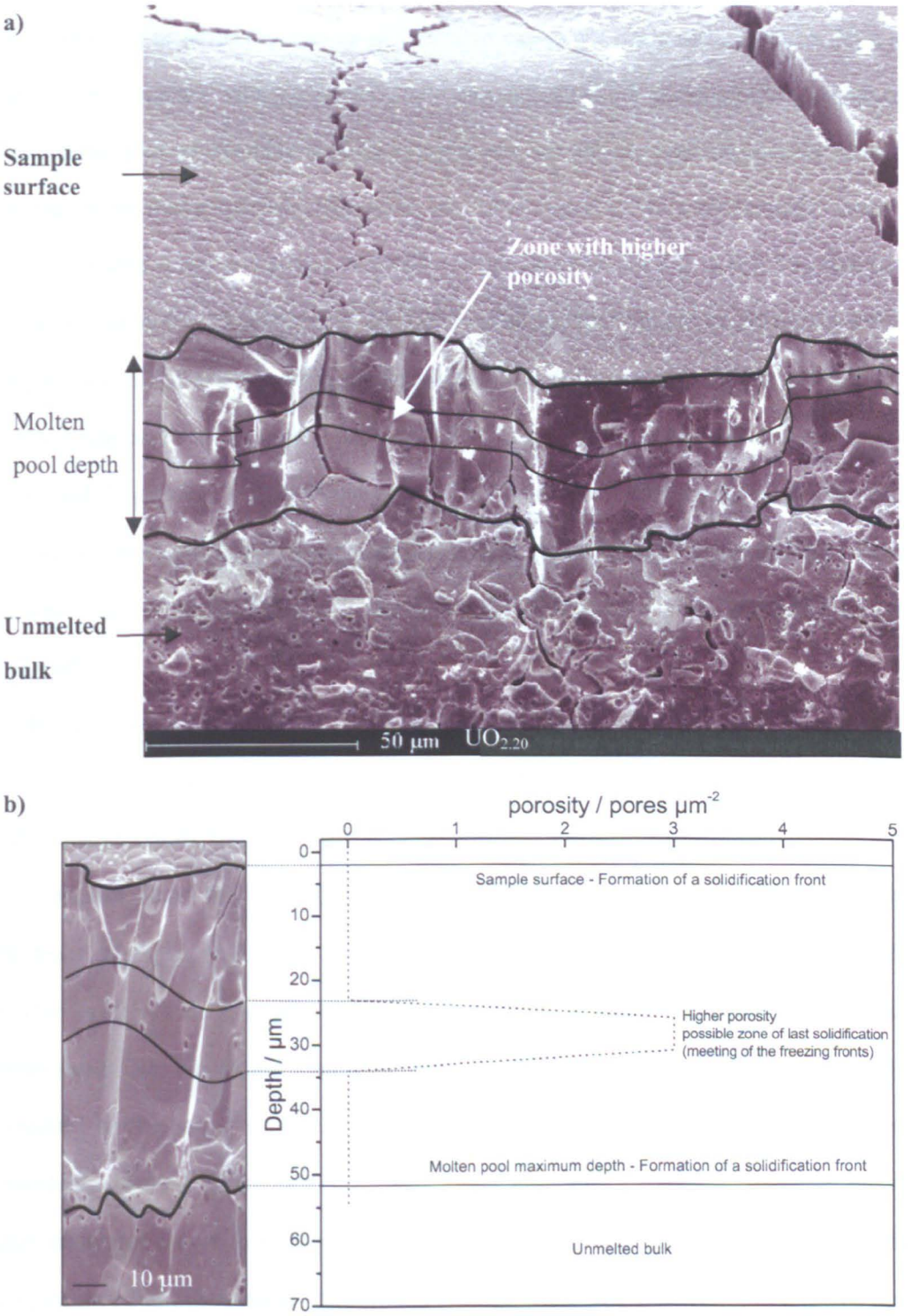

Fig. 8.12: a) SEM picture of a $UO_{2.20}$ section after a melting point measurement. The picture shows that there is a vertical band, in the molten pool, where the refrozen material seems to be slightly more porous (Fig. 8.12 b). This zone could indicate the area where the freezing fronts advancing from the bulk and from the surface met, and therefore where the solidification process was completed.

On the other hand, the typical shape exhibited by empirical thermograms after the *liquidus* transition could never be reproduced in simulated curves for compositions O/U > 2.03, no matter how much the input parameters were changed. This led to the conclusion that the solidification process in highly oxidised samples *was not* one-dimensional after the onset of freezing on the molten surface. This point was corroborated by the ceramographic analysis of samples after melting, reported in Chapter 5 (see in particular Fig. 5.16). The columnar crystal formation (Fig. 5.16b) confirmed that the melting / freezing process in stoichiometric samples was mostly axial. In *all* the samples with O/U > 2.03, instead, a "swollen" zone was visible in the centre of the molten surface, where the crystal growth was not columnar (Fig. 5.16 c and d), probably due to displacement of the liquid mass in the radial direction during the solidification process. The presence of density and concentration gradients, causing different points of the molten zone to freeze at different temperature, was possibly the origin of this effect.

Further melting/ freezing experiments *ad hoc* were of some help in the search for a possible explanation for the swollen part observed in the centre of the molten zone and for the shape of the final part of the thermograms.

Figs. 8.13a-b show SEM micrographs of a $UO_{2.09}$ specimen subjected to a very fast (existence of liquid ≈ 8 ms in total) melting – freezing experiment. An approximately circular swollen zone was observed around the centre of the molten part. However, the centre itself was flat in the middle of the swollen zone. Thus one could imagine this "circular" swollen zone simply as a wave of molten UO_{2+x} moving from the periphery towards the centre. In fact, in the real experiment the boundary (periphery) of the molten zone constituted the starting range of another freezing front. In a fast experiment such as the one performed in this example, the hypothetical molten urania wave would be frozen on a circular front before reaching the centre. In the general situation of longer experiments, instead, the moving liquid mass would converge and freeze into a single compact "swell" in the centre of the re-frozen zone, just in the pyrometer spot on the sample surface. A

significant amount of latent heat would be released as a consequence of the solidification of this mass, justifying the presence of the observed "second thermal arrest" in the empirical thermograms. If this were true, the absence of a "central swell" would correspond to the non-observation of any "second thermal arrest". Fig 8.14 shows the experimental thermogram recorded on the sample of Fig. 8.13.

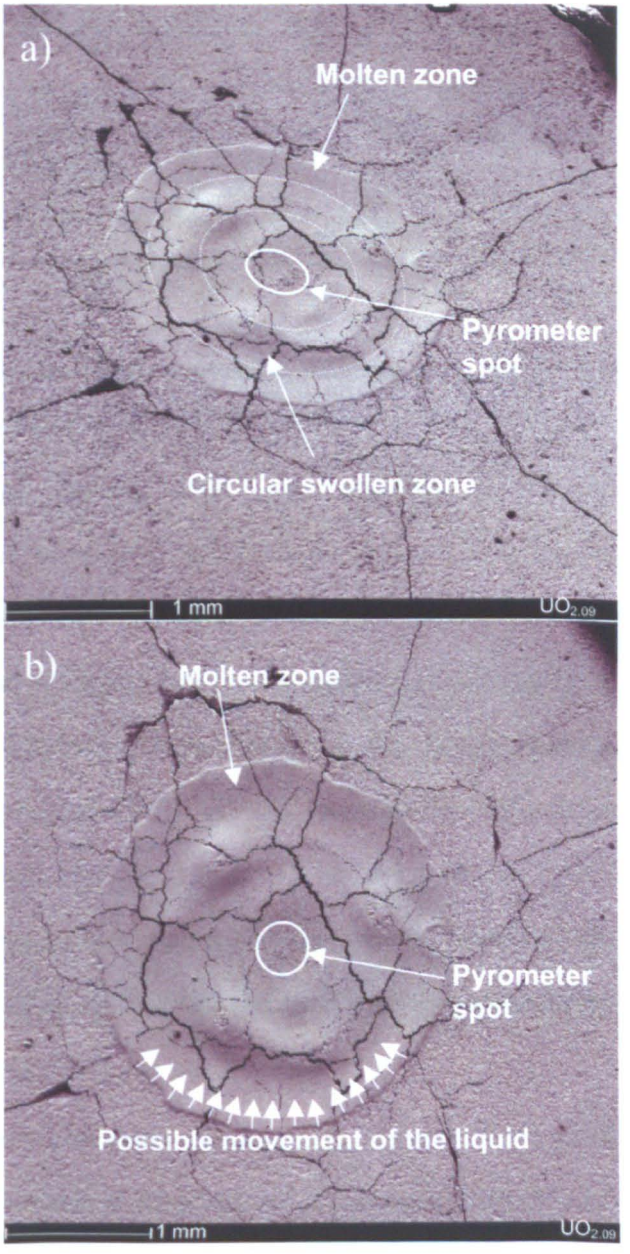

Fig. 8.13a-b: SEM micrographs of a $UO_{2.09}$ specimen subjected to very fast melting/freezing experiment (total duration of the experiment ≈ 20ms).

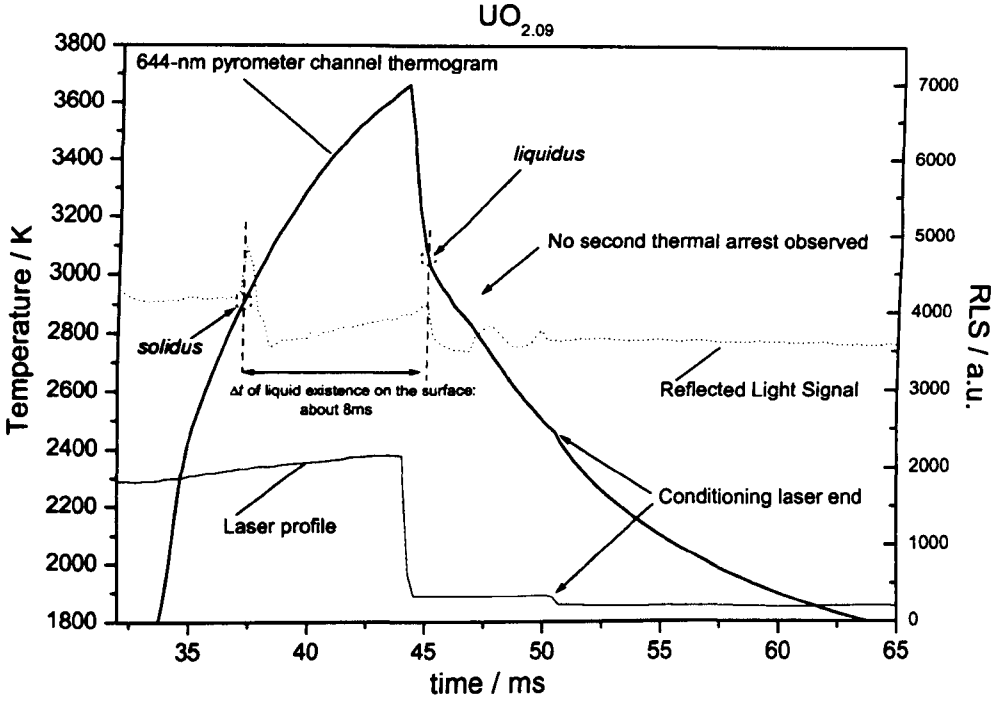

Fig 8.14: *Solidus – liquidus* measurement on the $UO_{2.09}$ sample of Fig. 8.13.

Actually, no "second thermal arrest" was observed in that thermogram, and, correspondingly, the centre of the re-frozen zone was flat, as mentioned previously. Thus the idea that the presence of such thermal arrest had to be linked to the solidification of the "swell" in the focal spot of the pyrometer on the surface was confirmed in this example.

The example of Fig. 8.15 would further corroborate the exposed interpretation. Fig. 8.15a shows a thermogram recorded during a melting / freezing experiment performed on a $UO_{2.11}$ sample. In this case, the pyrometer was focused on the molten zone, but slightly aside the centre. Thus, the pyrometer spot did not coincide with the "central swell" (Fig. 8.15b). In this thermogram, the *liquidus* thermal inflection was less pronounced, and the second thermal arrest was *not visible at all.*

Of course the proposed explanation is tentative only, and more experimental evidence would be needed in order to confirm it. Alternatively, or possibly combined with the movement of the molten mass, evolution of oxygen gas (bubbles) in the liquid could also lead to the formation of the observed swell, although no evidence of this kind of effect could be

observed. In any case, it is clear that out-of-equilibrium phenomena occurred in samples with O/U > 2.03 before the complete freezing, determining the shape of the final part of the recorded thermograms.

In summary, two important conclusions could be drawn from this analysis based on the simulation results and the post- melting ceramographic characterisation for UO_{2+x} samples with $2.03 < O/U \leq 2.10$:

- The measurement of melting point of stoichiometric and *liquidus* of hyperstoichiometric uranium dioxide by thermal analysis could be considered reliable.
- The melting- freezing process could be considered one-dimensional, justifying the use of a one-dimensional simulation to calculate thermograms, in the first part of the experiment only, i.e., until the crossing of the *liquidus* point during the cooling stage.

Therefore, the *solidus* in samples with O/U > 2.03 was preferably measured by means of the reflected light signal technique rather than by thermal analysis (see Chapter 7).

8.3.2 Samples with O/U > 2.10

Apart from the different shape of empirical and simulated thermograms on the final part of the cooling stage, in highly- oxidised samples the experimental curves could not be well reproduced even in the vicinity of the *liquidus* thermal inflection. According to the simulation results, in these samples, at the onset of solidification, oxygen concentration on the surface ($z = 0$) exceeded the original one by a quantity larger than the uncertainty of the sample starting composition itself. Fig. 8.16 shows, as a function of the initial composition, the deviation in the simulated *liquidus* arrest temperature with respect to the experimental *liquidus*. Such deviation was, obviously, systematically negative, as the surface enriched in oxygen started freezing at a lower temperature, according to the inputted *liquidus* line.

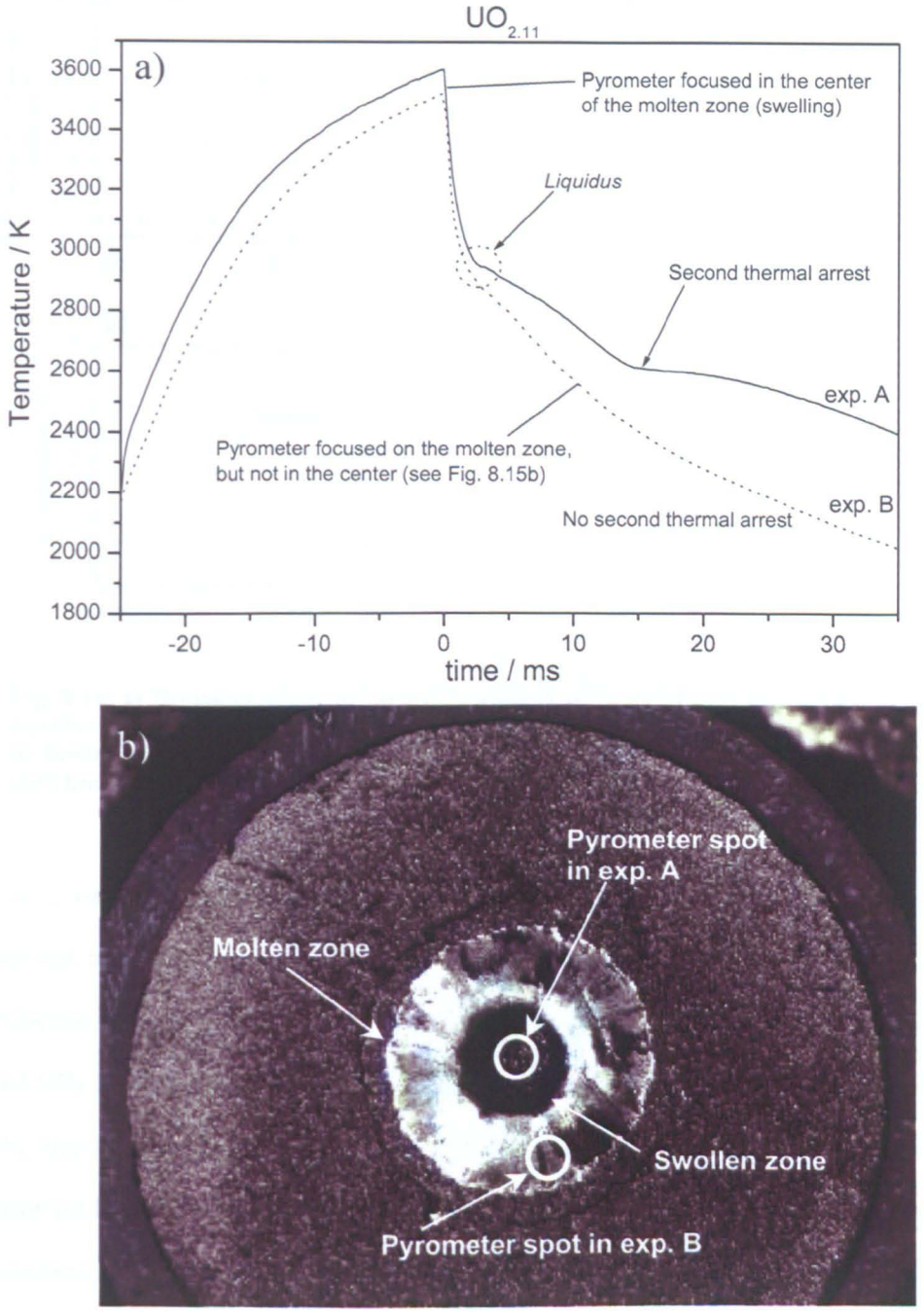

Fig. 8.15a: Thermograms recorded during melting/freezing experiments performed on $UO_{2.11}$ samples. Experiment A was a "standard" one, with the pyrometer focal spot in the very center of the molten zone. In experiment B, the pyrometer was focused on the molten zone, but slightly aside the centre, out of the "central swell" (Fig. 8.15b). In thermogram B the *liquidus* thermal inflection was less pronounced, and the second thermal arrest was *not visible at all.*

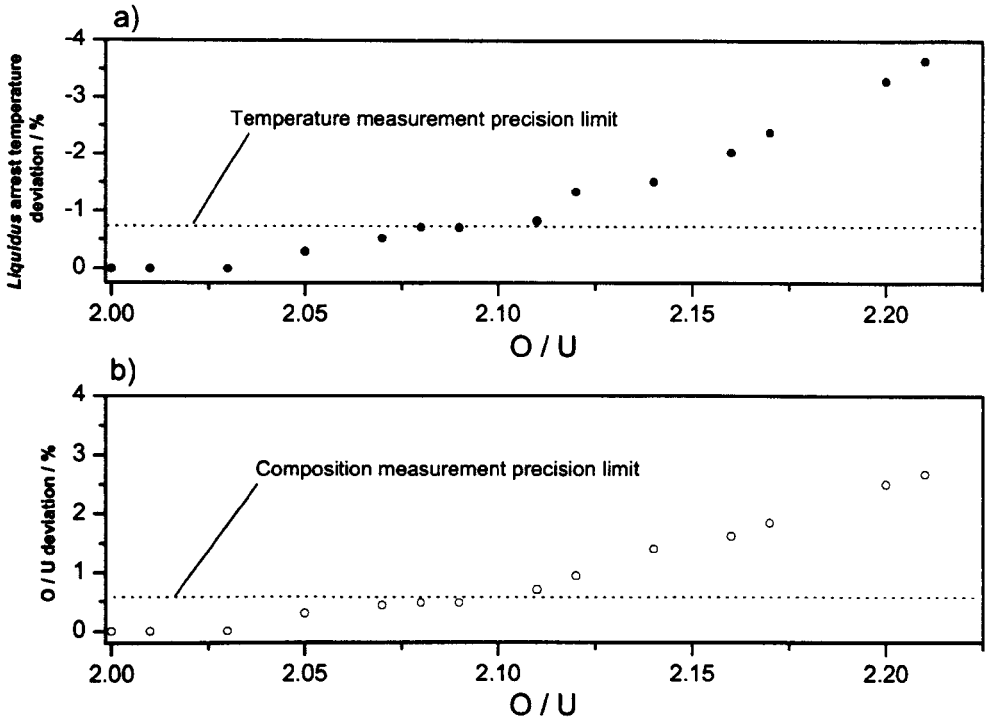

Fig. 8.16: a) Deviation of the simulated *liquidus* arrest temperature from the experimental *liquidus* as a function of the initial sample composition.
b) Deviation from the original sample oxygen content on the surface, induced by oxygen enrichment in the liquid during the melting/freezing process.

$UO_{2.10}$ was observed as the threshold- oxidation level, beyond which the disagreement, induced by oxygen enrichment in the liquid, between calculated and empirical *liquidus* inflection was larger than the measurement precision. In the most oxidised specimens, $UO_{2.2}$ and $UO_{2.21}$, the discrepancy would exceed 100 K, meaning a relative error of approximately 4%. Hence, according to the simulation results, the input *liquidus* line of Fig. 8.2, may be incorrect for O/U > 2.10. Since the curve was based on the experimental results obtained, the simulation could indicate that the experimentally determined *liquidus* points were also affected by a systematic error. The empirical *liquidus* line should be corrected approximately as indicated in Fig. 8.17.

However, one should not forget that a one-dimensional model is quite limited in simulating the extreme conditions taking place in the highly oxidised samples during the pulse- melting experiments.

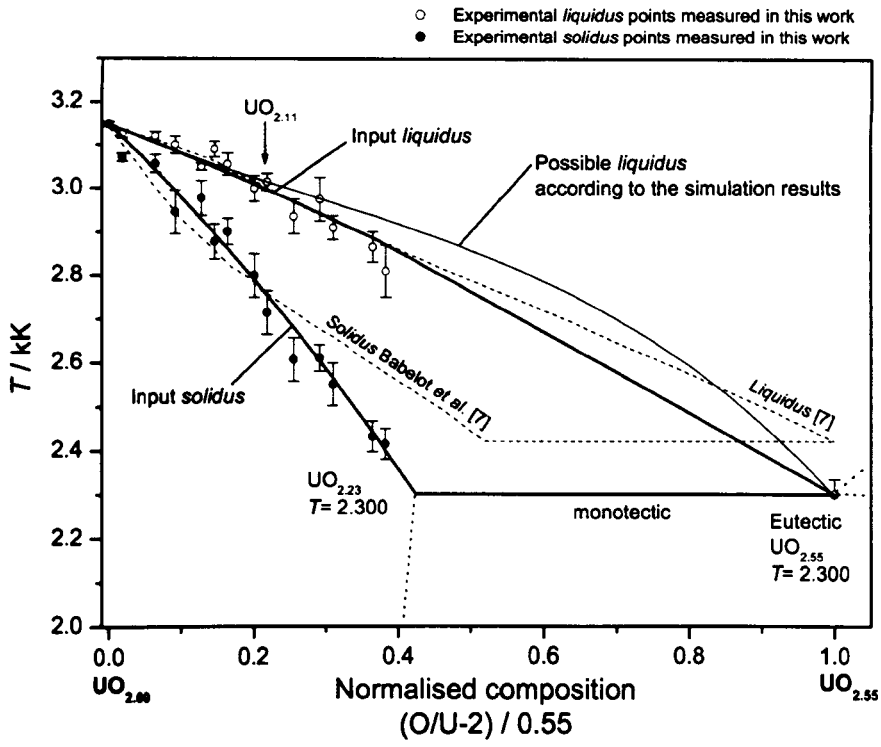

Fig. 8.17: Corrections to the phase diagram of Fig. 8.2 according to the results of the simulation.

In this case, better evidence of the reliability of empirical results should be sought in some experimental verification. Thus, melting- freezing experiments of very short duration were performed on samples with O/U > 2.10. An example measurement of this kind is reported of in Fig. 8.18. The *liquidus* points measured in these experiments by means of the reflected light signal analysis were in agreement (within the uncertainty limit of the method) with those measured in experiments of longer duration. This would not have been the case, if the error induced by the time- dependent oxygen distribution in the liquid had been decisive.

Finally the empirical *liquidus* line was not changed, although a large systematic error towards more oxidised compositions was associated with the experimental points at composition O/U > 2.10, in order to take into consideration the results of the simulation.

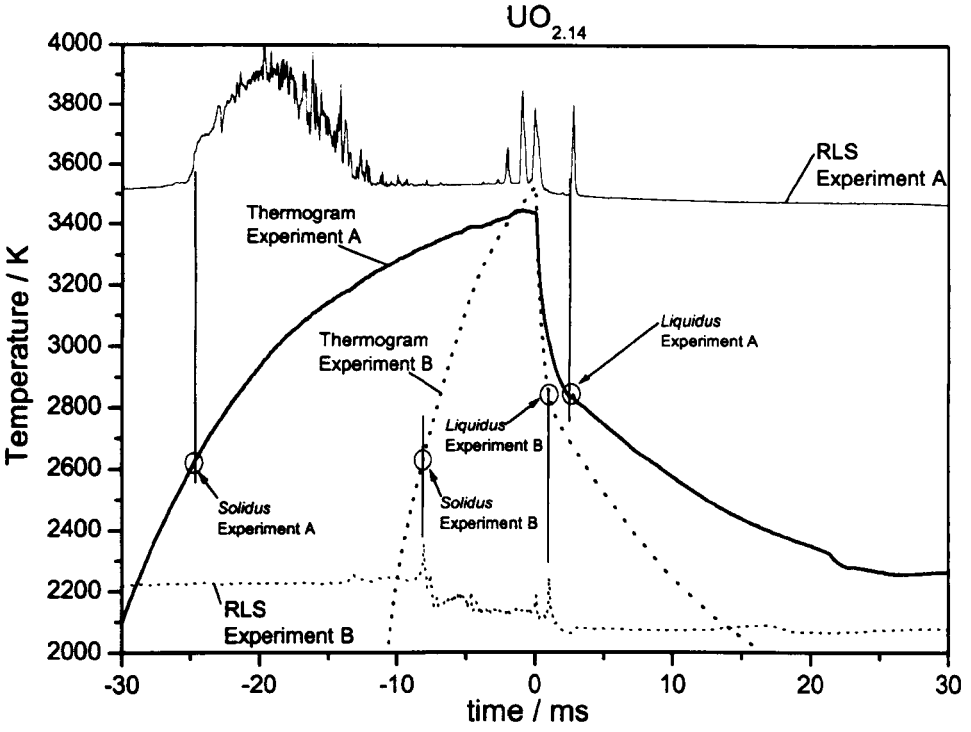

Fig. 8.18: Comparison between two melting point measurements performed on a $UO_{2.14}$ sample with different time regimes. In experiment A, the sample surface was kept over the melting point (*solidus*) for several tens of milliseconds, whereas in experiment B the existence of the liquid phase was limited to about 12 ms. *Solidus* and *liquidus* points measured by means of reflected light signal (RLS) analysis agreed in the two cases, whithin the uncertainty limits indicated by solid circles.

8.4 Summary and conclusion

The one- dimensional simulation presented in this chapter provided useful results, permitting a better understanding of the empirical thermograms presented in Chapters 6 and 7.

Good agreement between calculated and experimental thermograms was achieved, in stoichiometric and slightly non-stoichiometric (O/U ≤ 2.10) uranium dioxide specimens, up to the first thermal inflection observed on the cooling flank of the thermograms. This confirmed the reliability of the measured *solidus* and *liquidus* points.

On the other hand, the partial disagreement observed between simulated and empirical thermograms in the ending part of the curves revealed the actual influence on the measurements of out-of-equilibrium phenomena during the freezing process, such as high concentration gradients, displacement of the liquid mass in the radial direction and, possibly,

evolution of oxygen gas in the liquid. The effect of such phenomena was more extensive in highly oxidised samples (O/U > 2.10). Although one-dimensional simulation results could not be considered as fully representative in this range of compositions, the increased disagreement between calculated and empirical thermograms suggested that a larger uncertainty band should be associated to *liquidus* points measured in this part of the phase diagram.

It is however important to emphasize that uranium dioxide *solidus* and *liquidus* points were measured within the current research in a manner almost independent of the presence of any uncontrollable out-of-equilibrium effect. In fact, the *liquidus* was determined by means of thermal (§ 7.1.1) and reflected-light-signal (§ 7.1.2) analyses before the onset of the complex freezing process. The *solidus* could be determined during the heating stage by means of both post-melting visual examination and reflected-light-signal analysis (§ 7.2.2), during a stage where the sample was structurally stable. The set of procedures used for the experimental investigation of the melting behaviour is illustrated in the synopsis of Fig. 8.19.

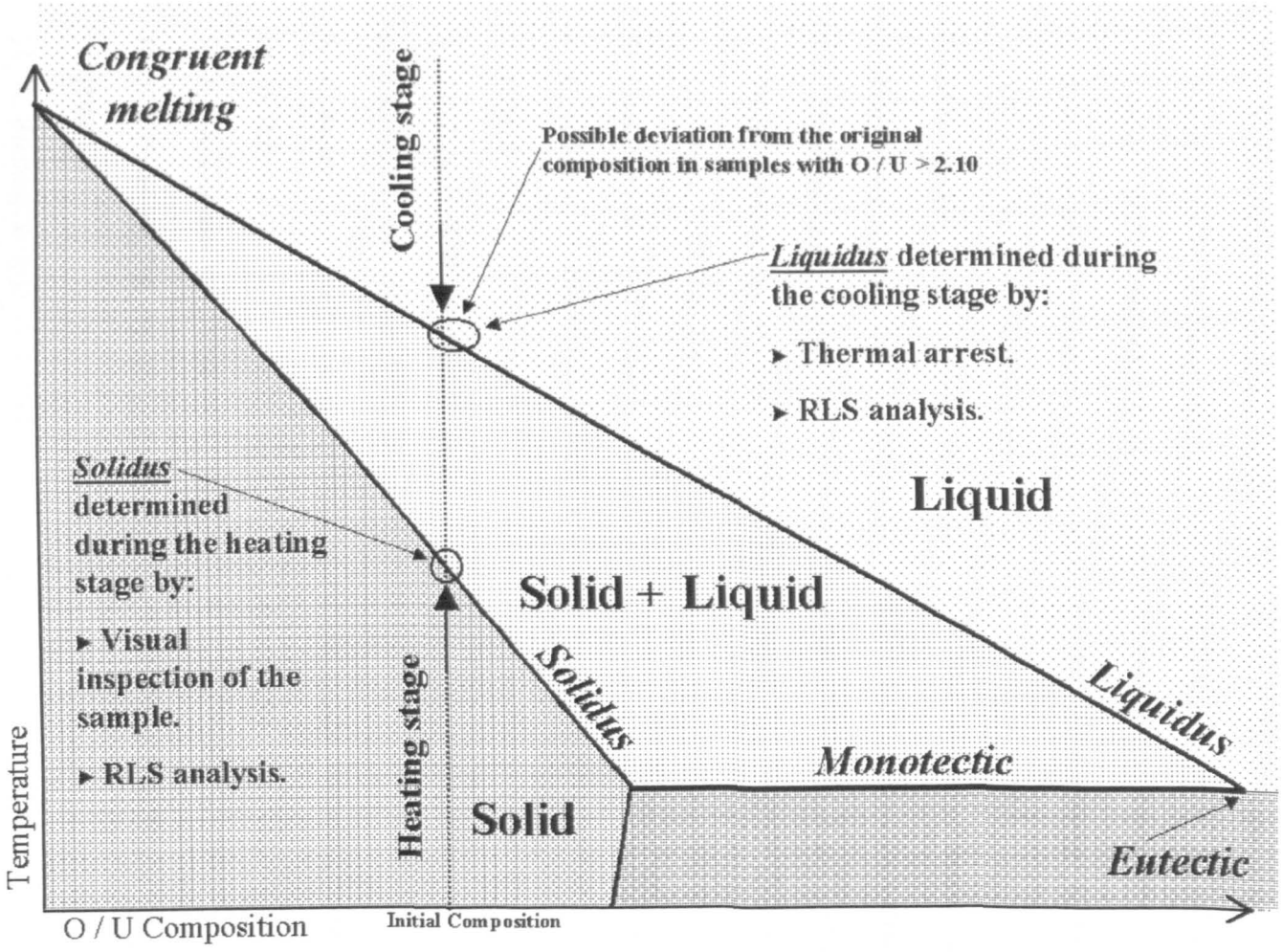

Fig. 8.19: Synopsis illustrating the whole procedure used for the experimental investigation of uranium dioxide melting behaviour. Solid circles around the phase transition points indicate the experimental uncertainties. In the case of *liquidus* determination, the uncertainty circle is deformed towards higher oxygen contents, indicating that the results in highly oxidised samples were possibly affected by oxygen enrichment of the liquid.

References Chapter 8

1. V.V Atrazhev, M.V. Brykin, *"Numerical Simulation of Melting and Solidification of Binary Mixtures in Laser Heating Pulses (Non-Congruent Phase Transition Solid-Liquid)"*, Study Contract N. 17644-2001-03F1SC KAR RU Final Report (ITU).
2. R.W. Cahn editor (University of Sussex, England): "*Physical metallurgy*" Chapters VI – XII, XXII. North – Holland Publishers Company – Amsterdam, 1965.
3. M.V. Brykin, V.S. Vorobiev, B.V. Sheluchaev *"Parameters of vapour near an evaporating surface"*, Teplofisika Vysokich Temperature **25** (1987), 2 (in Russian).
4. *"Thermophysical Properties of High Temperature Materials"*. Vol. 4, p. 2: *"Oxides and Their Solutions and Mixtures"*. Thermophysical Properties Research Center, Purdue University, 1967. Y.S. Touloukian Editor.
5. Gmelin Handbook of Inorganic Chemistry, Springer Verlag Berlin 1986, *Helium*.
6. C. Guéneau, M. Baichi, D. Labroche, C. Chatillon, B. Sundman, J. Nucl. Mater. **304** (2002), 161.
7. J.F. Babelot, R.W. Ohse and M. Hoch, J. Nucl. Mater. **137** (1986), 144.
8. J.K. Fink, J. Nucl. Mater. **279** (2000), 1.
9. C. Ronchi, M. Sheindlin, M. Musella and G.J. Hyland. J. Appl. Phys. **85** (1999), 776.
10. M. Bober, H.U. Karow and K. Muller, High Temp. – High Press. **12** (1980), 161.
11. R.J. Ackermann, P.W. Gilles, R.J. Thorn, J. Chem. Phys. **25** (1956), 1089.
12. J. S. Punni and P.K. Mason, "*UO_2 Oxidation and Volatilisation*", AEAT-1277, ST: MP (1997), 1.
13. W. Breitung, J. Nucl. Mater. **74** (1978), 10.
14. E. Yakub, I. Iosilevski and C. Ronchi, "*Defects interaction and order-disorder transitions in non-stoichiometric ionic solids*", 11th Int. Workshop on the Physics of Non- Ideal Plasmas, Valencia (Spain), June 1998.
15. E. Yakub, private communication.

16. L.S. Darken, Trans. AIME **175** (1948), 184.

17. K.W. Lay, J. Amer. Cer. Soc. **53** (1970), 369.

Chapter 9

Discussion of the UO_{2+x} phase diagram

Experimental data on the melting behaviour of stoichiometric and hyperstoichiometric uranium dioxide were obtained in this work as described in Chapters 6 and 7. Empirical results were then analysed in Chapter 8 with the help of a one- dimensional simulation.
The present chapter summarises the information yielded in this work on the system UO_{2+x}, and places the results in the scenario of the ongoing research described in Chapter 2.

9.1 Phase diagram of hyperstoichiometric uranium dioxide

The complete experimental database obtained in this work on the melting behaviour of uranium dioxide is summarised in Table 9.1. The dependence on buffer gas pressure of data measured for stoichiometric UO_2 specimens was accurately measured in the range 0.01 GPa $\leq P \leq$ 0.25 GPa (Chapter 6). In the same pressure range, the external-pressure-dependence of the *solidus* and *liquidus* points obtained for hyperstoichiometric UO_{2+x} samples was proved to be negligible compared to the precision of the measurements themselves (Chapter 7).

9.1.1 Solidus / liquidus lines for the system UO_{2+x}

Melting point measurements were performed with the experimental system presented in Chapter 4 on samples spanning several UO_{2+x} compositions, with $0 \leq x \leq 0.21$.

Tab. 9.1: Results obtained in this work in the determination of *solidus* and *liquidus* points in hyperstoichiometric uranium dioxide.

Nominal composition / O / U	**Number of samples investigated**	**Pressure / GPa**	***Solidus* / K**	**δT *solidus* / K**	**δx *solidus***	***Liquidus* / K**	**δT *liquidus* / K**	**δx *liquidus***
2	19	0.1	**3147**	± 20	± 0.005	**3147**	± 20	± 0.005
2.01	6	0.1	**3071**	± 20	± 0.005	**3135**	± 20	± 0.005
2.03	6	0.1	**3055**	± 25	± 0.005	**3130**	± 20	± 0.005
2.03	3	0.15	**3060**	± 25	± 0.005	**3115**	± 25	± 0.005
2.05	8	0.1	**2964**	± 50	± 0.005	**3098**	± 20	± 0.005
2.07	5	0.05	**2948**	± 40	± 0.005	**3028**	± 40	± 0.005
2.07	11	0.1	**2958**	± 40	± 0.005	**3070**	± 20	± 0.005
2.07	4	0.2	**2954**	± 40	± 0.005	**3063**	± 40	± 0.005
2.08	12	0.1	**2886**	± 25	± 0.01	**3075**	± 20	± 0.01
2.09	9	0.1	**2901**	± 49	± 0.005	**3056**	± 25	± 0.005
2.11	8	0.1	**2793**	± 40	± 0.005	**2995**	± 20	-0.005 + 0.015*
2.12	9	0.1	**2699**	± 25	± 0.01	**3008**	± 20	-0.01 + 0.02*
2.12	3	0.12	**2696**	± 25	± 0.01	**3020**	± 25	-0.01 + 0.02*
2.14	7	0.1	**2607**	± 25	± 0.01	**2930**	± 40	-0.01 + 0.03*
2.16	5	0.1	**2606**	± 30	± 0.01	**2920**	± 30	-0.01 + 0.035*
2.17	3	0.05	**2528**	± 50	± 0.005	**2887**	± 50	-0.005 + 0.04*
2.17	5	0.1	**2550**	± 50	± 0.005	**2891**	± 25	-0.005 + 0.04*
2.17	3	0.2	**2530**	± 50	± 0.005	**- a)**	**- a)**	**- a)**
2.2	12	0.1	**2438**	± 35	± 0.005	**2865**	± 30	-0.005 + 0.055*
2.21	10	0.1	**2410**	± 25	± 0.005	**2795**	± 60	-0.005 + 0.059*

Notes:

* Uncertainty in the sample composition including the possible enrichment in oxygen according to the simulation of Chapter 8.

a) Unsuccessful measurement.

N.B.: Additional melting points measured on stoichiometric samples in the range 0.01 GPa ≤ P ≤ 0.25 GPa are reported in Chapter 6.

The best results were obtained at 0.1 GPa, where three to twelve specimens of each composition were investigated. *Liquidus* and *solidus* lines measured at this pressure are shown in Fig. 9.1, and can be considered as representative of the melting behaviour of UO_{2+x} with $0 \leq x \leq 0.21$ and 0.01 GPa $\leq P \leq$ 0.25 GPa.

Liquidus points in Fig. 9.1 were obtained as a weighed average between experimental points measured with the RLS technique and experimental temperatures obtained with the thermal arrest technique. However, due to the limitations exposed in § 7.1.3, thermal arrest data were discarded in cases where the disagreement with RLS data was larger that the experimental uncertainty, and otherwise given a lower statistical weight in the analysis.

Solidus points are the weighed average between RLS analysis data and post- melting visual examination data. RLS analysis data were given a larger statistical weight because they were affected by smaller experimental uncertainty.

The horizontal error bands associated with each experimental point represent the uncertainty in the exact composition of an individual specimen. Vertical uncertainty bands correspond to the standard deviation in the reproducibility of each experimental datum.

Due to the fast non-congruent evaporation taking place at low pressures and high temperatures, the melting behaviour of uranium dioxide could not be experimentally studied under stable conditions at $P <$ 0.01 GPa. This would suggest that solid/ gas and liquid/gas boundary lines should also be considered in a correct representation of the phase diagram at pressures close to atmospheric (10^{-4} GPa). The correct description and validation of a model including both melting and sublimation evaluation would require knowledge of the triple line of hyperstoichiometric urania. In fact, a "triple" point exists at each composition, where solid, liquid and vapour coexist in equilibrium. If P^x_t is the pressure of the triple point at the composition UO_{2+x}, no liquid can be formed from the solid at $P < P^x_t$. The locus of all the triple points at different compositions is called "triple line", and is not yet known for the system UO_{2+x}. However, the results obtained in the present work can be seen as an upper limit for this triple line.

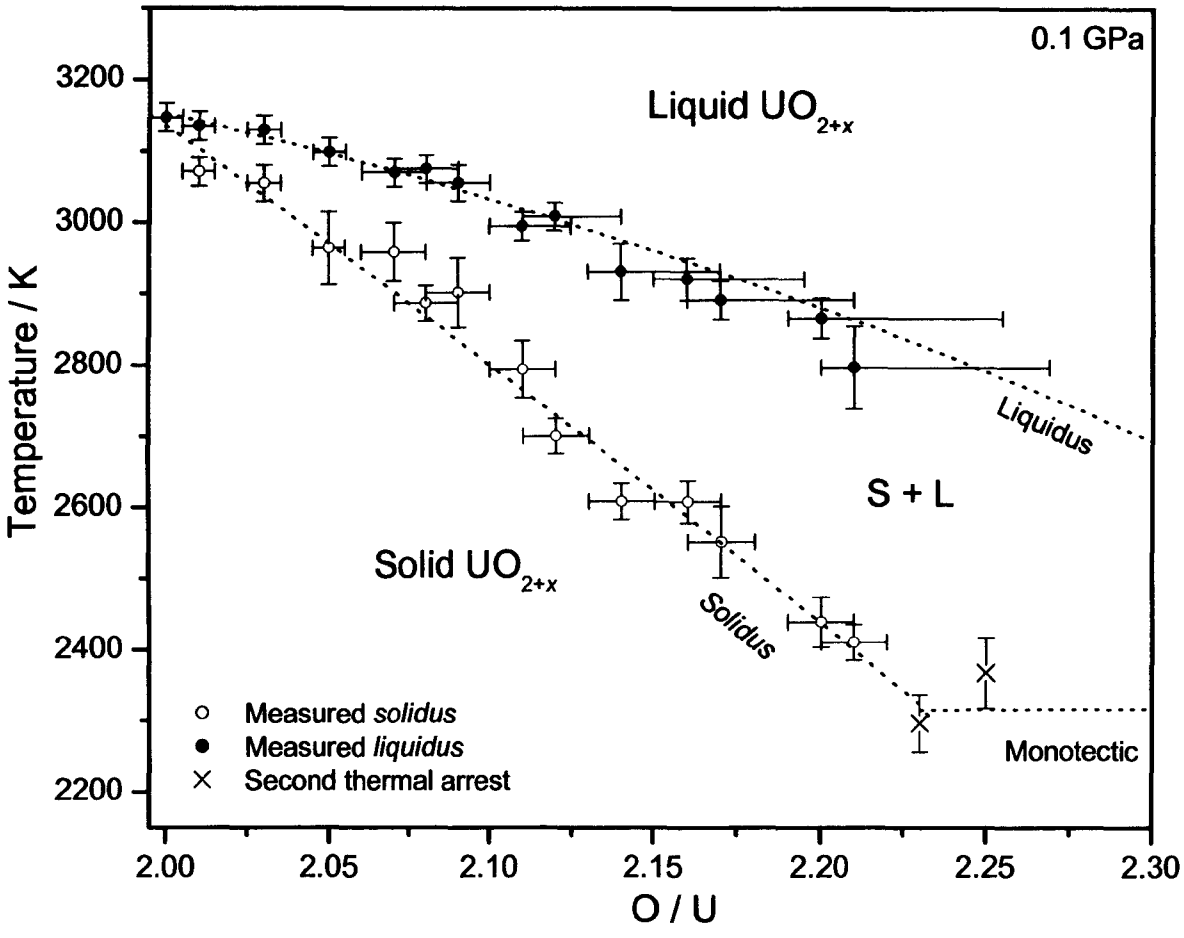

Fig. 9.1: *Liquidus* and *solidus* points measured in this work on samples spanning several UO_{2+x} compositions, with $0 \leq x \leq 0.21$.
The dotted straight lines, plotting second- order polynomial fits of the experimental points, serve as guide for the eye only. The expermental points plotted as „X" in the lower part of the graph correspond to the „second thermal arrest" temperatures observed in the most oxidised samples, at the composition given by post-melting TG measurements on molten- refrozen zones.

The triple point of the stoichiometric oxide certainly occurs at a pressure lower than atmospheric, as several authors unambiguously observed formation of liquid stoichiometric urania at ambient pressure. For compositions O/U > 2.03, one might expect an increase of the triple point pressure up to some MPa, anyway below the minimum buffer gas pressures under which molten oxide was obtained in the current research. In principle, the validity of the condensed phase diagram measured in this work should extend, within the experimental uncertainty, up to pressures close to the triple line.

9.1.2 Estimate of the monotectic transformation parameters

As mentioned in sections 2.1 and 7.2, a monotectic transformation solid UO_{2+xs} / liquid UO_{2+xl} / solid U_3O_8 (or vapour UO_y) was predicted in the hyperstoichiometric region by several theoretical investigations of the U - O phase diagram. A corresponding *monotectic* line, estimated on the basis of our results, is plotted in Fig. 9.1. In models without vapour phase the monotectic line is expected to start at a composition between $UO_{2.21}$ and $UO_{2.3}$ approximately, at a temperature between 2400 K and 2750 K. The same transformation is predicted at a higher temperature, and starting at a lower degree of oxidation, by models including the presence of the vapour phase. As for this work, parameters of the monotectic transformation can only be estimated on the basis of the observed "second thermal arrest" in the cooling stage of melting experiments performed on highly hyperstoichiometric samples. As explained in section 7.2 and § 8.1.4, the "second thermal arrest" temperature (2300 ± 50 K) recorded for the most oxidised samples investigated ($UO_{2.20}$ and $UO_{2.21}$) constituted the lowest point at which liquid UO_{2+x} was ever observed. Therefore, such temperature could be seen as an upper bound for the monotectic transformation under high external pressure. The 2300 ± 50 K value would be significantly lower than any monotectic temperature calculated prior to this research. As for the solid UO_{2+x} monotectic composition, the value $UO_{2.23}$ was obtained by extrapolating to 2300 K

the measured *solidus*. This composition for the molten- refrozen zone of $UO_{2.20}$ was also obtained in post- melting thermogravimetric measurements (§ 5.3).

In summary, parameters like temperature and solid composition of the hyperstoichiometric urania monotectic transformation could be estimated from empirical data obtained in the present work. However, a more precise study of such transformation would require further information on the melting point of specimens with higher oxidation state (e.g.U_3O_8).

9.2 Discussion of the experimental *solidus* / *liquidus* lines

9.2.1 Comparison with other experimental data

The only experimental points available prior to the current investigation are those due to Latta and Fryxell [1], whose research was described in Chapters 2 and 3. In Fig. 9.2 Latta and Fryxell's curves are compared with those measured in this work.

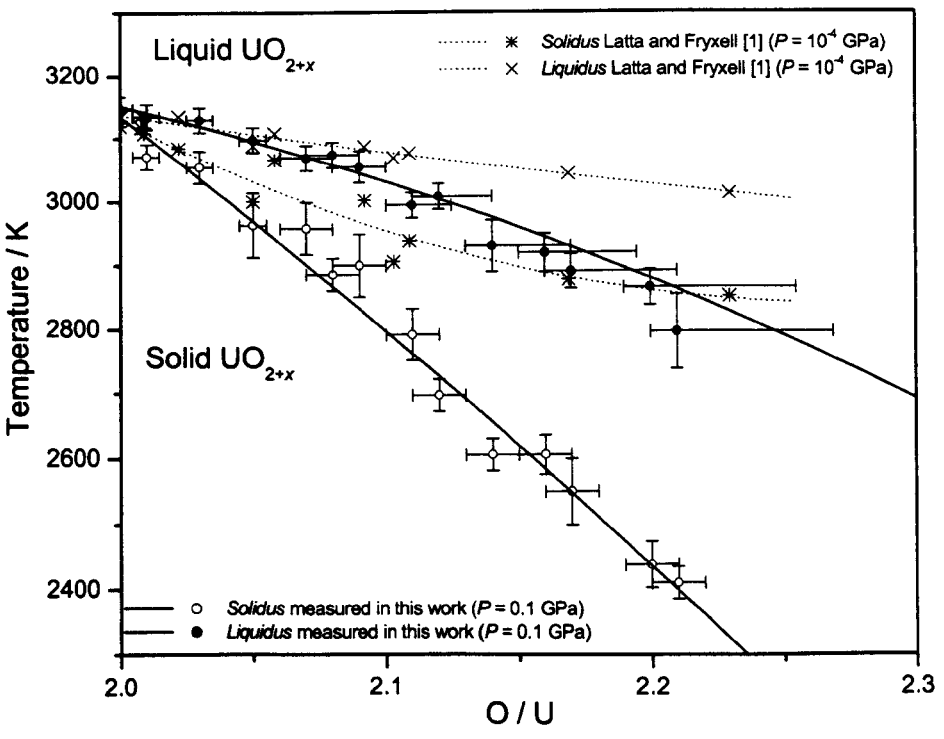

Fig. 9.2: UO_{2+x} phase diagram obtained in the current research compared with the experimental *solidus* and *liquidus* curves measured by Latta and Fryxell [1].

Solidus and *liquidus* temperatures measured in [1] are generally higher than those herein proposed for compositions O/U > 2.05. The disagreement extends beyond any experimental uncertainty for samples with O/U > 2.10. However, data measured in [1] for hyperstoichiometric compositions are strongly affected by contamination of the samples with the crucible material (W or Re) and by significant losses of the excess oxygen (see § 3.2.5). Both effects were likely to result in phase transition points higher than those of uncontaminated hyperstoichiometric urania would have been. The unreliability of Latta and Fryxell's results would constitute a further confirmation of the point that simple melting transitions cannot be measured at atmospheric pressure in urania samples with O/U > 2.10, where solid / gas and liquid / gas transformations occur.

9.2.2 Comparison with calculated phase diagrams

Figs. 9.3, 9.4, 9.5 and 9.6 show the experimental *liquidus-solidus* lines of Fig. 9.1 compared with other calculated phase diagrams proposed in literature for the system UO_{2+x}.

The work of Guéneau et al. [2]

In fig. 9.3 the phase boundaries calculated by Guéneau *et al.* [2] are plotted. In [2], the system UO_{2+x} is described by means of a compound energy model. In such model, solid urania is considered as an ionic three- sublattice structure, with one sublattice for U^{n+} cations, one for O^{2-} anions in normal sites and one for interstitial O^{2-} anions. The liquid phase is treated as an ionic two-sublattice (anionic and cationic) compound. The model permitted a calculation of both the phase diagram and the oxygen potential in the whole composition range from pure U to pure O by means of a consistent set of parameters. Such parameters were calibrated on the basis of a set of selected experimental data. In particular, for the *liquidus* and *solidus* lines Latta and Fryxell data were used, corrected using Raoult's

cryoscopic law to take into account the dissolution of tungsten in the liquid during the melting experiments. The parameters of the liquid were optimised in order to fit the experimental data over the whole phase diagram. Gibbs free energy calculations were performed in [2] at atmospheric pressure taking into account the liquid / gas and solid /gas phase transitions.

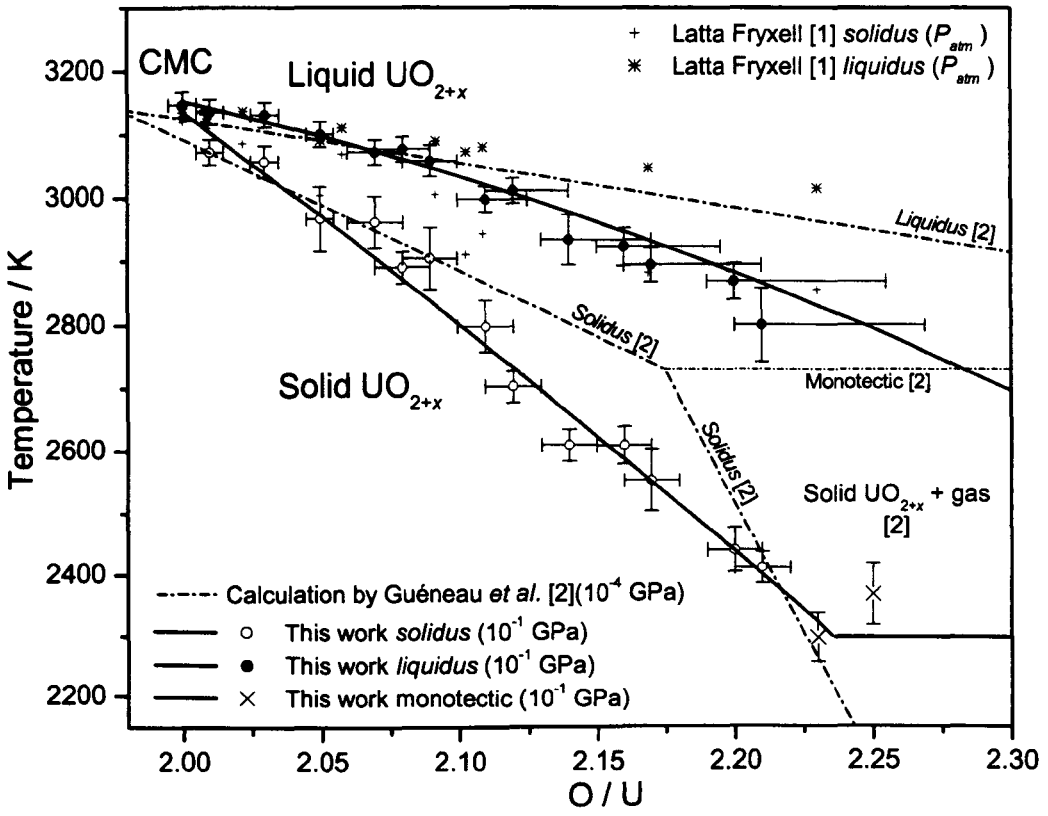

Fig. 9.3: Comparison between urania *solidus* and *liquidus* lines measured in the present work at 0.1 GPa and the same phase boundaries calculated by Guéneau *et al.* [2] at atmospheric pressure. Latta and Fryxell data [1] are plotted too, for comparison.

Guéneau *et al.* obtained a monotectic transformation $UO_{2.17}$ (s) / $UO_{2.55}$ (l) / UO_7 (g) at 2727 K. Of course, this type of transformation is unlikely to take place under an external pressure by several orders higher than atmospheric, as in the current investigation. The phase boundaries calculated in [2] and the experimental results of the present work are in a rather good agreement in samples with O/U < 2.1. The discrepancy for compositions

O/U > 2.1 can be partly attributed to the particular conditions under which our experiments were performed, in particular to the presence of high external pressure.

The congruent melting composition (CMC) differs slightly in the two cases, but the disagreement is still within the experimental uncertainty affecting the composition of the nominally stoichiometric oxide (O/U = 1.99 ± 0.01). The current experimental results provide no evidence that congruent melting occurs at a slightly hypostoichiometric composition, due to the limited precision in determination of O/U ratio in the samples.

The work of Chevalier, Fisher and Cheynet [3]

The current results on the melting behaviour of uranium dioxide are compared with the calculations performed by Chevalier, Fisher and Cheynet [3] in Fig. 9.4. In [3], solid urania is represented by a three-sublattice model similar to the one used by Guéneau *et al.* The liquid is supposed to be a mixture of pure species ($U_{(L)}$ and $O_{(L)}$) and associated species ($UO_{2\ (L)}$), according to the associate model [4, 5]. Under these assumptions, the hyper-stoichiometric field is described by the interaction parameter between $O_{(L)}$ and $UO_{2\ (L)}$ in the liquid in correlation with the UO_{2+x} solid solution model. The phase diagram at atmospheric pressure was calculated both with and without the gas phase. This latter condition corresponds to a situation closer to the one of the experiments reported in this research. Under this assumption, a monotectic $UO_{2.25}$ (s) / U_3O_8 (s) / UO_3 (l) was obtained at approximately 2750 K (though the exact co-ordinates of invariant points of this transformation are not very clear in [3]). If the condensed phase / gas transitions were taken into consideration, a monotectic transformation $UO_{2.07}$ (s) / $UO_{2.12}$ (l) / $UO_{3.35}$ (g) was obtained at 3077 K. In describing the $UO_{2+x} \rightarrow$ Liquid transition, free energy parameters were calibrated using Latta and Fryxell data. As a consequence, *liquidus* and *solidus* lines proposed in [3] follow almost perfectly the experimental points measured in [1] in the range $UO_{2.00}$ – $UO_{2.25}$, and are therefore in disagreement with the phase boundaries observed in

this work. On the other hand, the calculated phase diagram changes significantly when the condensed phase / gas transitions are taken into account, indicating that such transformations should be considered while studying the melting behaviour of uranium dioxide at pressure close to atmospheric.

The rather large disagreement between the parameters of the monotectic condensed phases / gas transition reported in [2] and [3] gives an idea of the uncertainty that still affects the few (calculated only) data available in this part of the phase diagram.

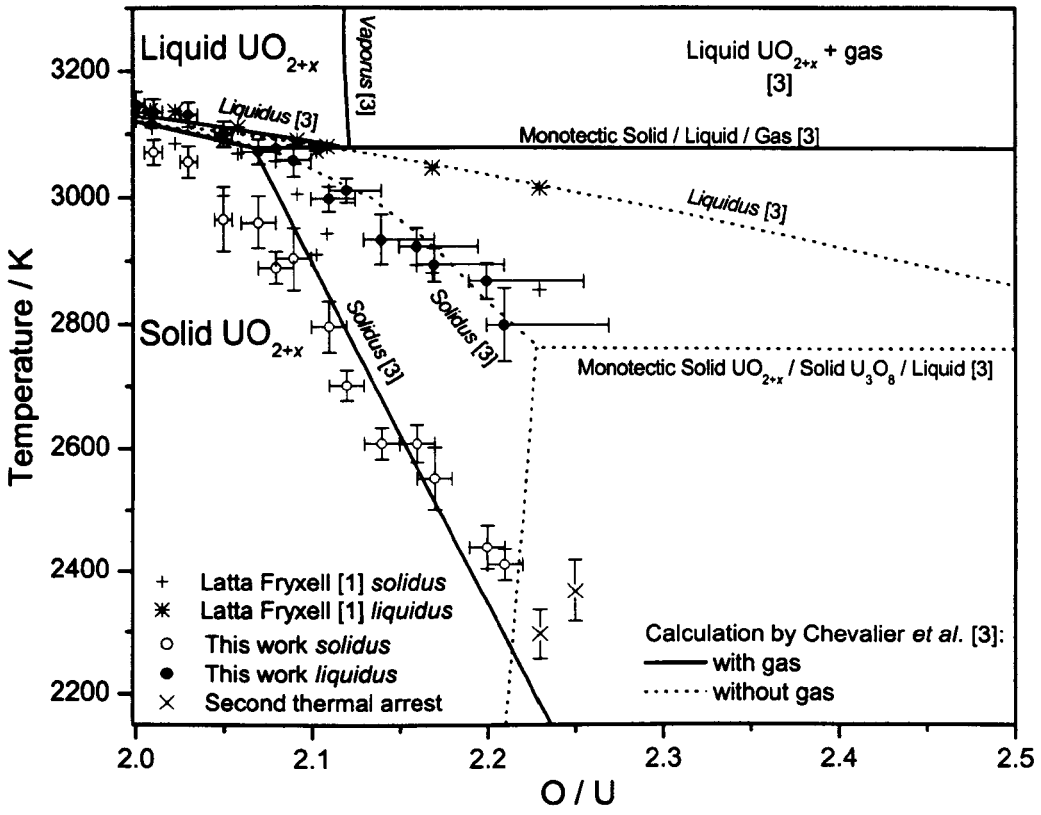

Fig. 9.4: Comparison between experimental data and the phase diagram calculated by Chevalier *et al.* in [3].

The work of Babelot, Ohse and Hoch [6]

Liquidus and *solidus* lines determined in this research are in rather good agreement with those calculated by Babelot *et al.* [6]. These latter lines are shown in Fig. 9.5.

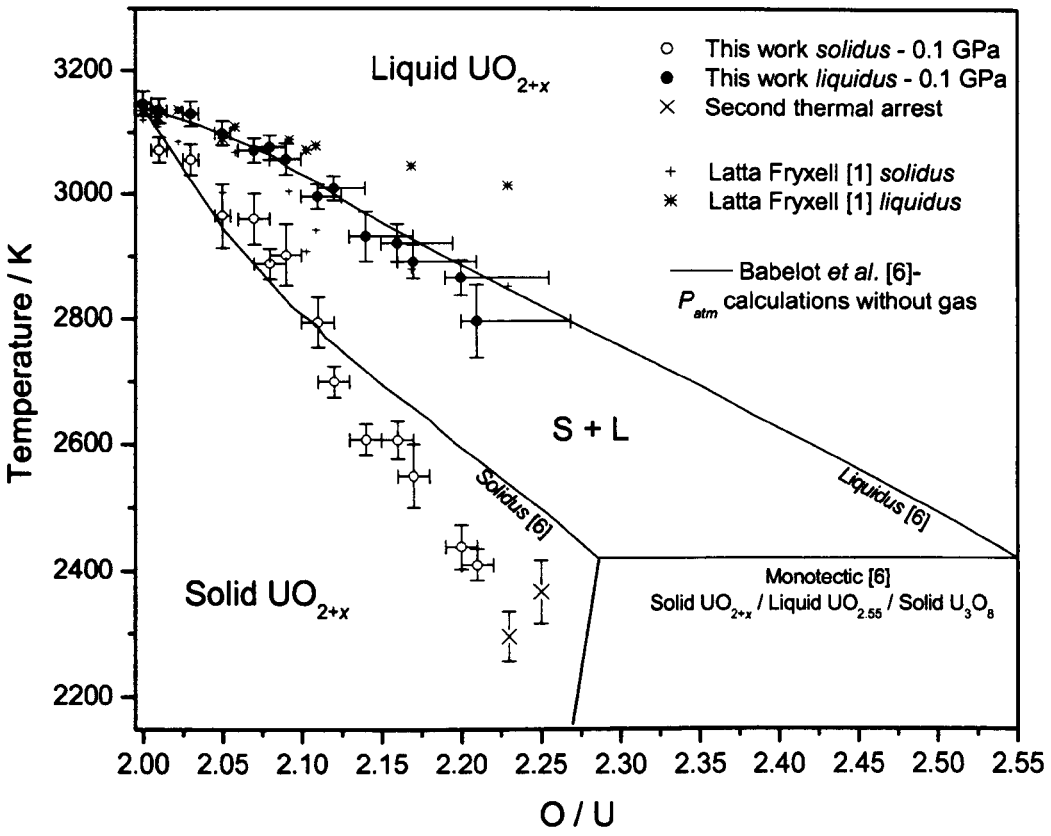

Fig. 9.5: Comparison between experimental data obtained in the present research and in [1] and the calculated UO_{2+x} phase diagram proposed by Babelot *et al.* in [6].

The system U-O is represented in [6] as a mixture of the three species U, UO_2 and UO_3. In particular, hypostoichiometric UO_{2-x} and hyperstoichiometric UO_{2+x} are considered as mixtures U / UO_2 and UO_2 / UO_3 respectively. For these phases, with large homogeneity, the Hoch- Arpshofen interaction model [7] was used to calculate the free energy of the solid mixture and of the liquid over the whole phase diagram. For compositions close to stoichiometric UO_2, the Schottky – Wagner disorder model [8] was used in order to calculate the concentration of U and UO_3 in UO_2. Latta and Fryxell data [1] were employed in the analysis of the hypostoichiometric urania phase diagram for the optimisation of the free energy parameters describing the solubility of liquid U in solid UO_2. For hyperstoichiometric urania, the phase boundaries were taken from the recommendations of Rand *et al.* [9]; free energy of mixing was calculated on the basis of existing oxygen potential measurements. UO_3 melting point and melting enthalpy were also needed to

complete the model. These latter data were estimated by comparison with the properties of the oxides MoO_3 and WO_3.

Finally, the system U-UO_3 was represented in [6] at atmospheric pressure, with no solid / gas and no liquid / gas transitions.

Despite the apparently strong approximations used in the data optimisation, the calculations presented in [6] constitute the best reference with which the results obtained in the present research should be compared for at least two reasons:

-Condensed phase / gas transitions are not considered. This assumption gives a meaningful extrapolation to atmospheric pressure of the phase diagram measured here at P = 0.1 GPa, where evaporation is practically absent.

-Unlike the work of Chevalier *et al.*[3], free energy calculations of *liquidus* and *solidus* in [6] were *not* calibrated using Latta and Fryxell's data, which, due to the experimental limits explained in § 9.2.1, systematically disagree with the results presented here.

The agreement between experimental data from the current work and calculations reported in [6] is satisfactory for the *liquidus* over the whole investigated composition range, and even excellent for $2 \leq O/U \leq 2.15$. For the *solidus*, the accord is good for $2 \leq O/U \leq 2.1$. *Solidus* points measured in this work have temperatures significantly lower than those calculated in [6] for the more hyperstoichiometric samples. However, one should not forget that for compositions $O/U > 2.1$ also calculated results are more uncertain, due to the progressively stronger extrapolations needed, and also experimental measurements are somewhat more difficult. Finally, according to the experimental results presented in this research, the theoretical approach to the UO_{2+x} phase diagram suggested in [6] looks to be the most realistic one, at least in the composition range $2 \leq O/U \leq 2.2$. This conclusion is of course meaningful only in the absence of condensed phase / gas transitions, i.e. in the assumption that evaporation is somehow suppressed.

The work of Gryzanov, Iosilevski, Hyland, Ronchi and Yakub [10, 16, 17]

Calculations of phase boundaries concerning the melting transition in UO_{2+x} have been performed (the related work is still in progress) within an international project supported by INTAS (International Association for Promotion of Cooperation with Scientists from the New Independent States of the Former Soviet Union) aimed at constructing a new equation of state (EOS) for uranium dioxide. In such a project a novel theoretical approach to the EOS of liquid and gaseous urania has been used. Such an approach, described by Iosilevski *et al.* in [10], constitutes a quite ambitious attempt, as it aims at describing the whole UO_{2+x} system starting from first principles. A so-called "chemical model" has been used, describing, with the help of the thermodynamic perturbation theory, a multi-component mixture of chemically reactive interacting neutral and charged molecules and atoms. A "hard- spheres mixture" approximation [11] has been employed along with a modified Lennard- Jones potential in order to describe the interaction between molecules and atoms. A simplified version of the Verlet and Weiss expressions [12] has been assumed for the first– order thermodynamic perturbation theory short- range attractive contributions. A superposition of the so- called "mean spherical approximation" and the Debye- Hückel approximation for charged sphere [13, 14] within the one- fluid approximation [15] has permitted a calculation of the non- ideality correction due to Coulomb long-range ionic interaction. Model parameters have been adjusted in [10] on the basis of well-established properties of stoichiometric liquid UO_2 only, such as density, Gibbs free energy, heat capacity, compressibility and oxygen potential. Therefore, the behaviour of the developed EOS in the broad temperature (2000- 11000 K) and composition ($1 \leq O/U \leq 7$) range investigated depends on the physical fundamentals of the model only. The model has been applied to the solid solution UO_{2+x} also [16], but work in this perspective is still in progress. Fig. 9.6 shows the *liquidus* and *solidus* lines calculated by Iosilevski *et al.* in [17] for

hyperstoichiometric urania compared with the experimental points measured in this research and in [1].

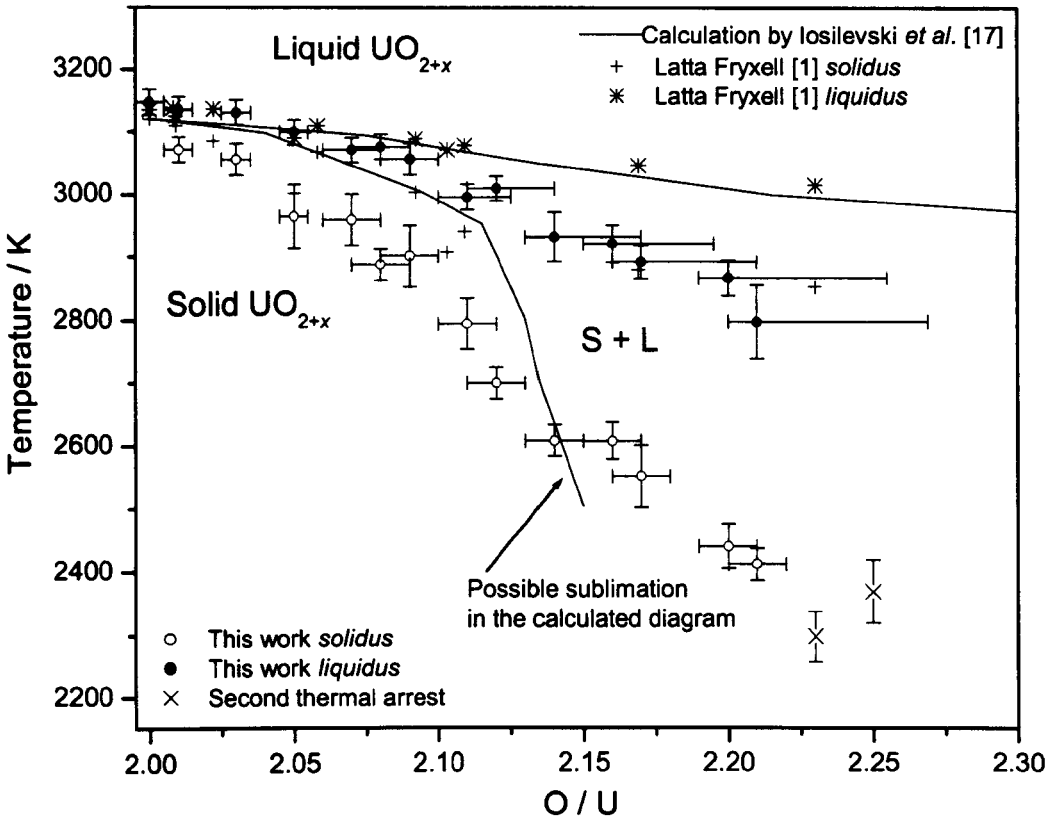

Fig. 9.6: *Liquidus* and *solidus* lines calculated by Yakub *et al.* for hyperstoichiometric urania [16], along with the experimental points measured in this research and in [1].

In [17], Latta and Fryxell's empirical curves were corrected for the experimental uncertainty and successively used to calibrate the model in the vicinity of the melting transition. The model for the solid solution is still to be assessed and validated. In particular, sounder experimental data for *solidus* and *liquidus* points and for the oxygen potential along these phase boundaries are needed. The results obtained in the present research can constitute a valuable reference in this perspective. In Fig. 9.6 one can see that for $0 \leq O/U \leq 2.12$ the curves calculated in [17] are in good accord with those measured by Latta and Fryxell, on which the model parameters were calibrated. Agreement between calculated phase diagram and the present results is acceptable in the vicinity of the stoichiometric composition only

(O/U ≤ 2.05). For O/U > 2.12, the calculated *solidus* line shows a marked increase of slope, whereas the calculated *liquidus* stays in accord with Latta and Fryxell's results over all the investigated composition range. The behaviour of the calculated *solidus* line depends on the nature of the fluid phase formed at each composition, since the model, as presented in [17], does not distinguish between liquid and gas phases. The pronounced inflection visible in the calculated *solidus* around $UO_{2.12}$ could correspond to the composition at which gas starts being produced at atmospheric pressure instead of liquid. If this assumption were correct, the *solidus* and *liquidus* lines calculated in [17] would be similar to those reported in [3]. In this case, only the experimental points measured in this work at compositions close to stoichiometry could be used to calibrate the model proposed in [17]. On the other hand, at compositions O/U > 2.1 the atmospheric- pressure physical model would be too far from the experimental conditions produced in the measurements at high- pressure, where evaporation is practically absent.

9.3 Summary and conclusions

The experimental results obtained in this work provide a considerable amount of information on the behaviour of stoichiometric and hyperstoichiometric uranium dioxide around the melting transition.

The data obtained permitted an improved definition of part of the $UO_{2\pm x}$ phase diagram around the melting transition at a pressure of 0.1 GPa, where *solidus* and *liquidus* lines were accurately measured in the composition range $UO_{2.00}$ - $UO_{2.21}$. In addition, the experimental results obtained provided information on a hyperstoichiometric oxide monotectic transformation. The *liquidus* and *solidus* lines measured were proven to be only slightly dependent on the external pressure in the range 0.05 – 0.2 GPa. The melting line of stoichiometric UO_2 was precisely determined in the range 0.01 – 0.25 GPa.

A comparison of the obtained experimental data with theoretical predictions, summarised in Table 9.2, suggests that the measured phase diagram should be valid up to pressures close to the UO_{2+x} triple line. On the other hand, the onset of massive evaporation, observed at atmospheric pressure and at temperature close to the melting point, indicated that realistic theoretical descriptions of the system UO_{2+x} at atmospheric pressure *should* take into account also the formation of gas from the condensed phases.

Phase diagrams calculated on the basis of the whole thermophysical and thermodynamic experimental databases of uranium dioxide are in rather good agreement with the empirical results presented here. Calculations only based on the few melting point measurements available prior to the present research yield UO_{2+x} melting transition temperatures higher than those measured here. Such a discrepancy clearly stems from the disagreement between our results and those of Latta and Fryxell [1], used as a reference by many authors.

Finally, the results obtained in this work can be used in the validation of theoretical models aimed at describing the whole U-O system through a suitable EOS.

Table 9.2: Synopsis of experimental and calculated results on the UO_{2+x} phase diagram in the hyperstoichiometric range.

Work	Type of research	Gas formation	$UO_{2.00}$		$UO_{2.05}$		$UO_{2.10}$		$UO_{2.15}$		$UO_{2.20}$		Monotectic-triple point	
			Solidus	*Liquidus*	*Solidus*	*Liquidus*	*Solidus*	*Liquidus*	*Solidus*	*Liquidus*	*Solidus*	*Liquidus*	Temperature	Composition
This work	*Exp.*	*Absent*	3147 K	3147 K	2964 K	3098 K	2850 K	3025 K	2605 K	2910 K	2438 K	2865 K	2300 K	$UO_{2.23}$
Latta and Fryxell [1]	*Exp.*	*Present*	3123 K	3138 K	3000 K	3095 K	2910 K	3050 K	2900 K	3080 K	2860 K	3025 K	-	-
Guéneau *et al.* [2]	*Comp.*	*Considered*	3130 K	3130 K	2990 K	3095 K	2890 K	3020 K	2780 K	3000 K	2520 K	2990 K	2727 K (*slg*)	$UO_{2.175}$
Chevalier *et al.* [3]	*Comp.*	*Not considered*	3130 K	3130 K	3095 K	3110 K	3050 K	3100 K	2960 K	3065 K	2825 K	3030 K	2760 K	$UO_{2.23}$
Chevalier *et al.* [3]	*Comp.*	*Considered*	3130 K	3130 K	3095 K	3110 K	2900 K	3100 K	2620 K	3077 K (*)	2340 K	3077 K (*)	3077 K (*slg*)	$UO_{2.067}$
Babelot *et al.* [6]	*Comp.*	*Not considered*	3130 K	3130 K	2975 K	3100 K	2810 K	3020 K	2698 K	2978 K	2590 K	2880 K	2420 K	$UO_{2.28}$
Gryzanov *et al.* [10, 16, 17]	*Comp.*	*Not considered*	3130 K	3130 K	3080 K	3105 K	2988 K	3080 K	2505 K	3050 K	-	3000 K	-	-

Notes and abbreviations:
(*) = Monotectic triple line.
(*slg*) = Monotectic solid / liquid / gas line.
Exp. = Experimental work.
Comp. = Computational work.

References Chapter 9

1. R.E. Latta, R.E. Fryxell, J. Nucl. Mater. **35** (1970), 195.
2. C. Guéneau, M. Baichi, D. Labroche, C. Chatillon, B. Sundman, J. Nucl. Mater. **304** (2002), 161.
3. P.-Y. Chevalier, E. Fischer, B. Cheynet, J. Nucl. Mater. **303** (2002), 1.
4. F. Dolezalek, Z. Phys. Chem. **64** (1908), 727.
5. I. Prigogine and R. Defay, Editors, "*Thermodynamique Chimique*", Dunod, Paris (1950).
6. J.F. Babelot, R.W. Ohse and M. Hoch, J. Nucl. Mater. **137** (1986), 144.
7. M. Hoch and I. Arpshofen, Z. Metallk. **75** (1984), 23.
8. C. Wagner and W. Schottky, Z. Phys. Chemie **B11** (1931), 163.
9. M.H. Rand, R.J. Ackermann, F. Groenvold, F.L.Oetting, A. Pattoret, Rev. Int. Hautes Tempér. Réfract. Fr. **15** (1978), 355.
10. I. Iosilevski, G.J. Hyland, C. Ronchi and E. Yakub, Int. J. Thermophys. **22** (2001), 1253.
11. G.A. Mansoori, N.F. Carnahan, K.E. Starling and T.W. Leland, J. Chem. Phys. **54** (1971), 1523.
12. L. Verlet and J. –J. Weiss Mol. Phys. **26** (1976), 1013.
13. E. Waisman and J. Lebowitz, J. Chem. Phys. **56** (1973), 3086.
14. M. E. Fisher and Y. Levin, Phys. Rev. Lett. **71** (1993), 3286.
15. V. Gryzanov, I. Iosilevski, E. Yakub, V. Fortov, G. J. Hyland and C. Ronchi, „*Strongly Coupled Coulomb Systems*", G. Kalman, K. Blagoev and M. Rommel editors (Plenum, New York, 1999), 147.
16. E. Yakub, I. Iosilevski and C. Ronchi, "*Defect interaction and order- disorder transitions in non- stoichiometric ionic solids*", 11th Int. Workshop on the Physics of Non- Ideal Plasmas, Valencia, Spain, March 21-25, 2003.

17. V.K. Gryzanov, I. L. Iosilevski, E.S. Yakub, „*Equation of State of Non-Stoichiometric $UO_{2\pm x}$: Validation of the ITU- INTAS Model in the Vicinity of the Liquidus / Solidus with Emphasis on the Interval {-0.10 < x <+0.25}*", Final Report of the Study Contract 7644-2001-03 FISC KAR RU, „*Construction of an Equation of State of Uranium Dioxide in Solid, Liquid and Vapour Phases*", Moscow 2002.

Chapter 10

Conclusions

The work presented in this Thesis encompassed the successful development and application of a novel experimental method for measurement of the melting behaviour of refractory and chemically unstable substances. In particular, the whole research project was conceived for the study of the high- temperature properties of nuclear materials.

Thus, the present research can be considered particularly innovative in two different domains:

- advances in experimental techniques aimed at investigating the high- temperature behaviour of refractory materials, also chemically unstable;
- the study of nuclear fuel properties, a field closely linked to the analysis of hypothetical severe reactor accidents.

10.1 Developments in the experimental techniques

10.1.1 Achievements of the current project

The empirical technique presented in this work is quite innovative in the experimental study of thermophysical, thermodynamic and optical properties of complex, unstable or chemically non- invariant substances.

The use of "double-pulse" laser heating enabled good control of the heating and cooling-rates in the investigated specimens.

The duration of one experiment was of the order of tens of ms, a range where good balance among contrasting factors was obtained (reaching the local thermodynamical equilibrium, avoiding convection in the buffer gas etc.).

Temperature was precisely measured on the sample surface by means of a fast pyrometer. The surface emissivity was obtained by analysing the thermal radiation emitted by the sample and recorded by an innovative multichannel pyrometer.

The novel "reflected light signal" (RLS) analysis method was particularly effective in the direct determination of the *solidus* and *liquidus* transitions by observing variations induced by the phase transition on the reflectivity of the sample surface.

Besides the results obtained in this project on the U-O system, the experimental method developed in this work has been used for materials such as tungsten, graphite, zirconia and urania alloys. The same method could be employed to investigate other refractory materials showing fast evaporation or chemical instability (e.g.: nitrides, carbides).

10.1.2 Future progress

Improvements of the presented techniques may result in a broadening of the achievable temperature- pressure range, and in a better determination of the sample surface emissivity.

Further development of the high- pressure system is currently in progress that will lead to maximum attainable buffer gas pressures around 1 GPa.

The planned implementation of a high- power laser with programmable time profile would replace the "double- pulse" technique, significantly improving the controllability on the heating and cooling rates produced during an experiment.

A possible employment of low- temperature pyrometers would increase the number of substances that could be studied. Better emissivity measurements would be feasible by employing a multi-channel pyrometer with higher time resolution.

Finally, a completion of the experimental apparatus with a high- speed camera is planned, which would provide *in situ* images of the sample surface during a melting/freezing experiment.

10.2 Nuclear Fuel Properties

10.2.1 Summarised results

The melting behaviour of uranium dioxide, nowadays the most used nuclear fuel, has been widely and accurately investigated for compositions both stoichiometric and hyperstoichiometric. The atmospheric-pressure melting point determined in the stoichiometric compound slightly differed from other literature values, which were probably affected by uncertainty in the sample composition due to non- congruent evaporation. For the stoichiometric compound, the melting line T_m *(P)* was also measured. The agreement of the observed melting slope with the one given by the Clausius – Clapeyron equation confirmed that thermodynamic equilibrium was reached locally during the measurements and that melting occurs in stoichiometric UO_2 without molecular change.

The same dependence of melting point on pressure could be partly confirmed, but with a considerably larger uncertainty, for hyperstoichiometric samples. Measurement of the melting point of hyperstoichiometric uranium dioxide with O/U > 2.10 at pressures close to atmospheric was inhibited by the onset of strong, non- congruent evaporation. This experimental evidence suggested that the compound UO_{2+x} with $x > 0.10$ is probably unstable, at atmospheric pressure, with respect to the gas phase formation; this latter should therefore be considered in an accurate description of the U-O phase diagram.

Under external pressures higher than 10 MPa approximately, the formation of liquid was unambiguously observed, without any significant production of gas, even in highly oxidised samples, according to the expected *solidus / liquidus* scheme. *Solidus* and *liquidus* were

observed at temperatures significantly lower than those so far recommended, especially in the samples with the highest oxygen content, confirming that previous measurements were possibly affected by uncontrolled evaporation and contamination of the sample with the containing material.

Some parameters of the monotectic transformation predicted in hyperstoichiometric uranium dioxide were also estimated on the basis of the measurements presented here, obtaining an empirical monotectic temperature lower than previously quoted.

Data measured on the behaviour of the hyperstoichiometric oxide are of great interest in the analysis of hypothetical accidents. Actually, uranium dioxide could be significantly enriched in oxygen during a mishap, in case the fuel came into contact with water, which is employed as coolant in the majority of the reactors in use.

The results presented in this work indicate that, during an accident in which high temperatures were reached, the fuel enriched in oxygen could either decompose into gas or melt, depending on the total pressure produced inside the reactor core. In both cases, the fuel would risk collapsing at temperatures significantly lower than so far reported in literature. Thus the results presented would also influence the definition of the limiting power for a reactor element.

10.2.2 Future Work

A considerable amount of experimental information is still needed for correct definition of the phase diagram of uranium dioxide, especially in the hyperstoichiometric domain. Data of this kind would also be fundamental for the validation of advanced formulations of the uranium dioxide EOS.

In particular, investigation of the melting transition in hyperstoichiometric urania samples with O/U > 2.2, as well as in higher uranium oxides (e.g. U_3O_8 and UO_3) would be of the

greatest importance. Such measurements may be performed by means of the experimental apparatus devised in this work.

The results presented also suggest that sound experimental data would be needed on gas formation above hyperstoichiometric urania, especially at temperatures close to the melting point and at pressures close to atmospheric.